

See discussions, stats, and author profiles for this publication at: <https://www.researchgate.net/publication/51820731>

# Advanced Nanoarchitectures for Solar Photocatalytic Applications

ARTICLE *in* CHEMICAL REVIEWS · NOVEMBER 2012

Impact Factor: 46.57 · DOI: 10.1021/cr100454n · Source: PubMed

---

CITATIONS

645

READS

1,246

## 3 AUTHORS:



[Anna Kubacka](#)

Spanish National Research Council

89 PUBLICATIONS 2,136 CITATIONS

[SEE PROFILE](#)



[Marcos Fernández-García](#)

Spanish National Research Council

257 PUBLICATIONS 8,395 CITATIONS

[SEE PROFILE](#)



[G. Colón](#)

Spanish National Research Council

131 PUBLICATIONS 4,434 CITATIONS

[SEE PROFILE](#)

## Advanced Nanoarchitectures for Solar Photocatalytic Applications

Anna Kubacka,<sup>†</sup> Marcos Fernández-García,<sup>\*,†</sup> and Gerardo Colón<sup>\*,†</sup>

<sup>†</sup>Instituto de Catálisis y Petroleoquímica, CSIC, C/Marie Curie 2, 28049-Madrid, Spain

<sup>\*</sup>Instituto de Ciencia de Materiales de Sevilla, Centro Mixto CSIC-Universidad de Sevilla, C/Américo Vespucio, 49, 41092-Sevilla, Spain

### CONTENTS

1. Introduction: Toward a Sunlight-Driven Photocatalyst	1555
1.1. Scope of the Review	1555
1.2. TiO <sub>2</sub>	1556
1.3. Solar-Light Based Systems: Beyond TiO <sub>2</sub>	1561
2. TiO <sub>2</sub> -Based Photocatalysis: Doped and Composite Systems	1562
2.1. Structural Description of TiO <sub>2</sub> -Based Systems	1562
2.1.1. Composite Systems	1563
2.1.2. Single-phase anatase systems	1564
2.2. Electronic Description of TiO <sub>2</sub> -Based Systems	1567
2.2.1. Composite Systems	1568
2.2.2. Single-Phase Anatase Systems	1570
3. Third Generation Photocatalysts: A <sub>x</sub> B <sub>y</sub> O <sub>z</sub> and New Nonoxidic Photocatalysts	1573
3.1. Perovskite Structure	1574
3.2. Perovskite-Related Structures	1576
3.3. Aurivillius Phases	1576
3.4. BIVO <sub>4</sub> Scheelite Structure	1578
3.5. Other Structures	1579
4. New Photocatalysts for Water Splitting	1580
5. New Photocatalysts for CO <sub>2</sub> Reduction	1583
6. Light Handling Aspects	1585
6.1. TiO <sub>2</sub> -Based Systems	1585
6.1.1. Composite Systems	1587
6.1.2. Single Phase Anatase Systems	1591
6.2. A <sub>x</sub> B <sub>y</sub> O <sub>z</sub> and Nonoxidic Photocatalysts	1593
7. Sunlight-Based Photocatalysis: Current and Future Perspectives	1595
7.1. The Quest for New Materials	1595
7.1.1. Single-Phase Materials	1595
7.1.2. Composite Materials	1598
7.2. A Summary of Present and Forthcoming Ideas	1602
Author Information	1604
Biographies	1604
Acknowledgment	1604
References	1604

### 1. INTRODUCTION: TOWARD A SUNLIGHT-DRIVEN PHOTOCATALYST

#### 1.1. Scope of the Review

Since they were first described in the scientific literature, photoinduced processes have been studied with a view to developing

several industrially oriented applications. Despite differences in their character and proposed utilization, most of the photoinduced processes that have been successfully exploited have the same origin. For example, a semiconductor can be excited by light energy higher than the band gap which results in inducing the formation of energy-rich electron–hole pairs. In using the term photocatalysis, it is commonly understood that we are referring to any chemical process catalyzed by a solid where the external energy source is an electromagnetic field with wave numbers in the UV–visible-infrared range.<sup>1–10</sup> Photocatalysts are usually solid semiconductors which are (i) able to absorb visible and/or UV light, (ii) chemically and biologically inert and photostable, (iii) inexpensive and (iv) nontoxic. The importance of this field is exemplified by a simple search of the ISI web database using the terms “photocat” and “oxide/semiconductor”; from 2000 more than 1000 publications per year can be found.

The semiconductors TiO<sub>2</sub>, ZnO, SrTiO<sub>3</sub>, CeO<sub>2</sub>, WO<sub>3</sub>, Fe<sub>2</sub>O<sub>3</sub>, GaN, Bi<sub>2</sub>S<sub>3</sub>, CdS and ZnS can all act as photoactive materials for redox/charge-transfer processes due to their electronic structures which are characterized by a filled valence band and an empty conduction band. Among these heterogeneous semiconductors, TiO<sub>2</sub> is the most widely used photocatalytic material because it fulfills all of the above requirements as well as exhibiting adequate conversion values.<sup>11</sup> However, in spite of its high conversion values, the calculated quantum yield for the reactions studied is appreciably low: certainly well below 10% for most degradation and synthesis processes.<sup>12</sup> TiO<sub>2</sub> occurs in nature in three crystallographic phases: rutile, anatase and brookite. Anatase is the most commonly employed in photocatalytic applications due to its inherent superior photocatalytic properties.<sup>8,11,13</sup> Anatase is the least thermodynamically stable TiO<sub>2</sub> polymorph as a bulk phase, although, from energy calculations, it appears as the most stable phase when the grain size is below 10–20 nm.<sup>14,15</sup> High surface TiO<sub>2</sub> materials should, therefore, consist of the anatase polymorph as a general rule. The crystalline structure of the TiO<sub>2</sub> oxides can be described in terms of TiO<sub>6</sub> octahedral chains. These differ by the distortion of each octahedron and the assembly pattern of the resulting octahedral chains. Although the Ti–Ti distances in the anatase structure are greater than in rutile, the Ti–O distances are shorter.<sup>16</sup> These structural differences cause different mass densities and lead to different electronic band structures. The anatase phase is 9% less dense than rutile. It presents more pronounced localization of the Ti 3d states and, therefore, a narrower 3d band. Also, the O 2p–Ti 3d hybridization is different in the two structures. Anatase exhibits a valence and conduction band with more pronounced O 2p–Ti 3d character

Received: December 28, 2010

Published: November 22, 2011

and less nonbonding self-interaction between similar ions (e.g., anion–anion and cation–cation interactions).<sup>17</sup> The importance of the covalent vs ionic contributions to the metal–oxygen bond has already been discussed in a more general context for Ti oxides.<sup>18</sup> It could be said that these anatase vs rutile differential structural features are likely responsible for the difference in the mobility of the charge carriers upon light excitation.

Among the simple oxides (e.g.  $\text{TiO}_2$ ,  $\text{ZnO}$ ,  $\text{WO}_3$ ,  $\text{Fe}_2\text{O}_3$ ), anatase- $\text{TiO}_2$  is the dominant structure employed for sunlight applications mostly due to its charge carrier handling properties.<sup>1–12</sup> In the quest to optimize the photoactivity of anatase- $\text{TiO}_2$  systems, several research paths have been pursued. One methodology, central to current research, considers the extension of the solid light absorption spectrum to the visible region. This should facilitate the use of sunlight as an inexpensive, renewable energy source, for the excitation energy of the photocatalytic processes.  $\text{TiO}_2$  is a UV-absorbing material with a band gap energy in the 3.0–3.4 eV range. It is dependent on several physicochemical parameters such as primary particle size and shape and surface characteristics among others. If the band gap energy is decreased to about 2.5 eV or certain localized midgap states having adequate (excitation) energies are present, these would fulfill the two main requirements for generating valuable sunlight-driven photosystems. These are, first, an increase of the absorption power into the visible region and, second, an acceptable potential energy of the photogenerated carriers to limit the loss of degradation/transformation power with respect to the use of a UV excitation wavelength.

The majority of studies involving  $\text{TiO}_2$ , with respect to the improvement of optical absorption and photocatalytic performance, are focused on anatase modification by cation and/or anion doping.<sup>1,5,7,8,19</sup> Almost from the very beginning of photocatalytic research, the photoactivity of anatase- $\text{TiO}_2$  systems was typically enhanced by the addition of noble metals such as Pt, Pd, Ir, and Ag at the oxide surface. These act as electron trapping centers. Also anatase–oxide contact using  $\text{WO}_3$ ,  $\text{SnO}$ ,  $\text{ZrO}_2$ , or other systems aiming at influencing the electron–hole charge separation process was attempted.<sup>1,7,8,20–22</sup> A judicious choice of metal or oxide displaying absorption power into the visible region, together with adequate electronic interface characteristics, can thus lead to the development of useful systems within the context of this work. There are additional alternatives, mainly based on the use of all-solid Z-schemes (polymeric materials, molecular sensitizers, hypothetical cubic-type  $\text{TiO}_2$  polymorphs) or the use of some non-Ti inorganic solids (e.g. oxides, sulfides, nitrides, carbon nanostructures) either in the presence or in the absence of  $\text{TiO}_2$ . These have all been tested in pursuit of this goal.<sup>1–12,22–24</sup> In sections 2 to 5 of this review we will present an overview of the advanced nanoarchitectures currently employed to transform solar into chemical energy. As listed in the outline, these sections attempt to cover the so-called second and third generation photocatalysts as well as other exciting novel approaches mainly related to Z-schemes or phase-coupling schemes and/or nonoxide photocatalysts. Section 2 covers  $\text{TiO}_2$ -based systems while novel semiconductor formulations, other than conventional oxides such as  $\text{TiO}_2$  or  $\text{ZnO}$ , will be discussed in section 3. These two sections concern systems that demonstrate valuable activity in decontamination and/or partial oxidation processes. Section 4 describes systems involving hydrogen production and section 5 those active in  $\text{CO}_2$  reduction. Section 6 is specifically devoted to light–matter interaction phenomena. Attempts are made to interpret the physical grounds

giving support to the exceptional photochemical properties shown by the most interesting solids. A comparative analysis of the systems discussed and their future projection as environmentally friendly photocatalytic systems will conclude the review.

It should be pointed out that this review will emphasize the optimization of useful systems under sunlight-type excitation; operation both under UV and under visible light excitations are considered. Previously the fruitful use of sunlight has been pursued with the development of specific reactor setups,<sup>25</sup> typically with the help of high surface, nanostructured materials having adequate morphological and physicochemical (including optical) properties. An analysis of both current and future developments from a solid state point of view, which would take into account nanostructure, seems therefore mandatory. In this context, it should be mentioned that, as recently evidenced in the study of anion-doped anatase systems, a significant number of systems can display enhanced activity under visible light with respect to well-defined photocatalytic reference systems such as Degussa P25, TS01 or Millennium PC500. However, the number of successful systems compared to those using sunlight-type excitation is certainly not only less significant but, moreover, even scarce.<sup>5–7</sup> It seems obvious that any real alternative must outperform P25 or other well-defined reference systems using sunlight in order to create attractive technologies for the future.

This review will, therefore, concentrate on novel, nanostructured materials that demonstrate useful activity under solar excitation in fields concerned with the elimination of pollutants, partial oxidation and the valorization of chemical compounds, water splitting and  $\text{CO}_2$  reduction processes. There are already a significant number of reviews covering such subjects<sup>1–13,26,27</sup> but here the emphasis will be on analyzing photoactive materials from a solid state point of view. Our emphasis will be on the influence that morphological variables, e.g. primary particle size but also particle shape as well as secondary particle size, surface area and porosity, all have on photocatalytic activity.

## 1.2. $\text{TiO}_2$

Improving high-surface, nanoparticulated anatase- $\text{TiO}_2$  materials requires a basic knowledge of  $\text{TiO}_2$  performance as well as the main operating parameters. Although a detailed analysis of the photoexcitation and further elemental processes leading to the chemical treatment of contaminants is beyond the scope of this review,<sup>1–12</sup> we will, however, summarize the main issues and highlight the main framework indicating the fields where anatase- $\text{TiO}_2$  may be modified or adapted to pave the way toward developing highly efficient sunlight-driven systems. Modern photocatalysts are usually high surface area materials, consisting of nanometric particle sizes below 100 nm and typically around 10 nm. Therefore, the inter-related size and defect chemistry, inherent to oxide nanomaterials, play a key role in understanding the phenomenological behavior of such anatase systems upon light excitation.<sup>5–7</sup>

Before proceeding to a more in-depth analysis it is pertinent to undertake a short revision of the primary size/shape and defect structure characteristics typical of nanoanatase materials. The number of publications concerning these topics is overwhelming, so for the sake of brevity we will only mention the most relevant review articles which should be read in order access the complete literature. Although both the shape and surface morphologies of anatase particles can be analyzed by microscopy,<sup>28,29</sup> we still essentially lack a unified view of shape change as a function of size. Some valuable reports, however, present size/shape changes

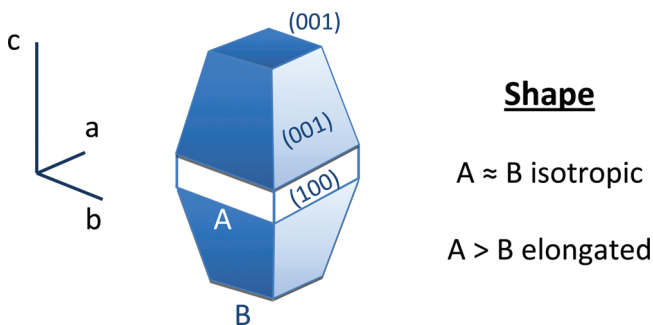


Figure 1. Morphology of anatase nanocrystals.

as a function of several experimental variables.<sup>15</sup> Essentially, although truncated bipyramidal shapes are expected for anatase nanoparticles, some very recent studies show unexpected shapes for “molecular” (e.g., below 1.5 nm)  $\text{TiO}_2$  entities.<sup>30</sup>

Anatase is the thermodynamically stable phase below 10–15 nm.<sup>15</sup> Due to the inherent heterogeneity and low crystallinity of these materials, for particle sizes well below 10 nm other analytical techniques may have significant advantages over microscopy methods. One recent example is where joint density functional theory (DFT) and IR spectroscopy studies made it possible to accurately predict surface morphologies.<sup>31</sup> Such a correlation is based on the O–H stretching frequencies of surface-adsorbed entities or water molecules which only give information at a local level. The analysis of such local OH species provides evidence of the morphology of anatase nanoparticles. Their study from an amorphous-like precursor state showed anatase-type surface terminations are formed well below the onset of nucleation. Originally the more stable (101)-surface termination is developed. Subsequently this is followed by the (100)- and, for some samples, (001)-type surface terminations.<sup>15,32–36</sup> These results are also supported by theoretical predictions.<sup>15,37,38</sup> Figure 1 shows that anatase nanoparticles can have two main or “extreme” morphologies: first, the elongated (along the *c* crystallographic axis) ones dominated by (101) and (100) faces, and second, the more isotropical ones with certain additional main contribution from the (001) faces. The joint analysis of this data set should indicate that situations with an aspect parameter above 0.6 may be possible. However, the importance of surface-alien stabilized species, such as F, needed to reach such an objective needs further clarification (see sections 6 and 7 for a complete discussion).

Typical anatase nanoparticle morphologies can be thus represented by an aspect parameter as shown in  $B/A$  in Figure 1. These usually consist of values of 0.3–0.4 and can display a maximum value of up to 0.57.<sup>38</sup> Modulation or control of the *c*-axis elongation of the particle through the presence of alien surface species, such as fluoride ions, during preparation<sup>39</sup> and morphology control with the formation of nanostructures having a dominant presence of the (001) facets<sup>40–45</sup> have both been recently reported. Recent work indicates that particle morphology, that is, the primary particle size and shape, is governed by thermodynamic as well as kinetic parameters of the anatase genesis process.<sup>36</sup> Specifically the initial local order, around 3–6 Å, in the solid precursor state of the oxide at nucleation states seems key in controlling size. Other variables such as the surface OH density and net charge (e.g., hydration of surface layers) together with the number of kinks/edges may strongly influence shape as well as size growth after nucleation.<sup>37,38,46–48</sup> In the case

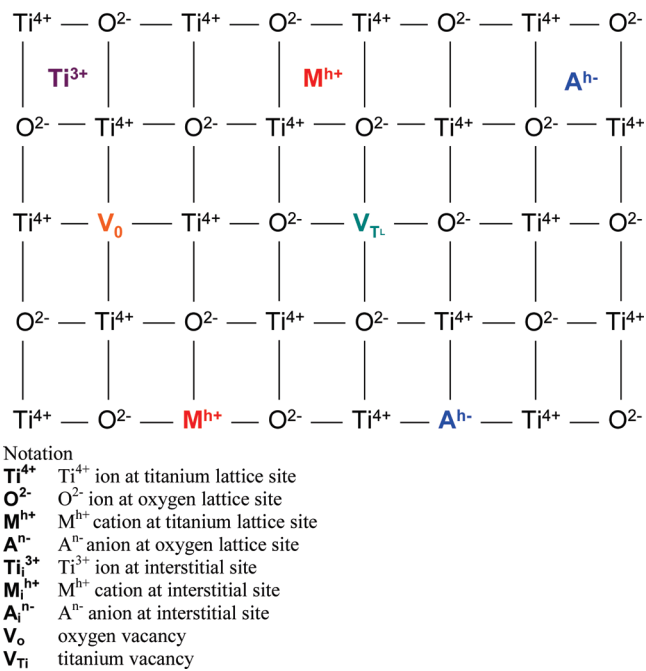


Figure 2. Schematic representation of the possible point defects present at the  $\text{TiO}_2$  lattice.

of OH species, they can be envisaged as controlling the elongation along the *c* axis (e.g., particle shape).

Nanoparticulated systems display a significant number of defects. The study of defects is important because, as shown below, they are intimately involved in charge trapping and recombination processes, both of which affect photoactivity in a dramatic manner.<sup>5–7</sup> A summary of the known point defects present in nanoparticulated anatase is shown in Figure 2. The (101) surface presents both 5-fold- and 6-fold-coordinated titanium atoms, as well as 2-fold- and 3-fold-coordinated oxygens. The first titanium and oxygen species display undercoordination with respect to the bulk. The studies performed over the (001) surface reveal the presence of 5-fold-coordinated titanium atoms, next to 2-fold- and 3-fold-coordinated oxygen atoms.<sup>49–51</sup> Amorphization of the structure, which most likely happens for sizes below 3–4 nm, may allow the presence of edge-type, tetracoordinated Ti atoms. These are otherwise energetically unstable. In fact, for particles below 10 nm, Luca recently postulated a significant amorphization of the surface layer, with a natural increase in the number of undercoordinated atoms with respect to “bulk-type” terminations.<sup>52</sup> Of course, undercoordinated atoms are protonated/hydroxylated while in surface positions in samples which are in contact with air and hence, in some cases, recover the bulk-type coordination. Punctual defects deviating from an  $\text{O}/\text{Ti} = 2$  stoichiometry are typically present for primary particle sizes below ca. 20 nm. These were usually ascribed to oxygen vacancies, which upon growth trigger both ordering and the presence of oxygen-defective phases, such as Magnelli and other phases described in the corresponding Ti–O phase diagram.<sup>53,54</sup> Specific preparation methods lead to the so-called oxygen-deficient (or self-doping) anatase nanoparticles. These have  $\text{O}/\text{Ti}$  ratios as low as 1.8 and a significant number of subsurface oxygen vacancies.<sup>55–57</sup> However, recent studies show increasing evidence of the presence of Ti vacancy in nanosized anatase materials. This means a Ti occupancy of between

0.95 and 1 for, respectively, 5–10 nm anatase nanoparticles. These are presumably stabilized (e.g., charge neutrality) by the presence of protons forming hydroxyl species with neighboring lattice oxygen ions.<sup>58,59</sup> Theoretical calculations indicate that both oxygen and titanium vacancies, as well as Ti interstitials, are energetically feasible in anatase.<sup>60</sup> The coexistence of oxygen and titanium vacancies is hardly possible for energetic reasons alone. The predominance of one of these is a function of a significant number of variables, among which the preparation conditions (oxygen-poor conditions drive toward oxygen vacancies while oxygen-rich conditions lead to titanium vacancies) and size appear to be key factors; this is further discussed below in the context of their electronic effects. Experimental and theoretical results thus indicate that the most frequent isolated or punctual defects are oxygen and Ti vacancies and  $\text{Ti}^{n+}$  interstitials.<sup>53–60</sup> Such centers can be present at both the surface (or near surface) and bulk positions.

It seems obvious, that as the surface area/primary particle size increases/decreases, the number of defective anion and cation surface centers increases. In a simple approximation, this is a function of size and shape. While size may display a rough  $r^{-2}$  dependence of the number of defects above 4–5 nm, we can expect a larger number of defects in isotropic with respect to elongated shapes as the number of undercoordinated Ti atoms per surface area unit should be larger in the last case. This simple approximation is valid at least for sizes above 3–4 nm. Below this the number of kinks/edges (which should display an  $r^{-3}$  behavior) becomes important and amorphization of the anatase structure seems likely.<sup>48,52</sup>

The boundary region between the anatase nanoparticles should also display specific structural characteristics, namely, the presence of undercoordinated local structures not present in surface free terminations as well as some amorphization. Already this has been detailed in the case of other oxides such as ceria.<sup>61</sup> In the case of anatase, Alimohammada et al.<sup>62</sup> analyzed the attachment of well-defined nanoparticle surfaces. They observed oriented interfaces (e.g., attachment) driven by electrostatic forces between the (001) local planes and undercoordinated atoms along the edges of two (101) planes of other nanoparticles. Data regarding local order detail within such interfaces requires further input. In systems that exist with more than one phase, they can display differences with respect to the single phase system, particularly at boundary regions. As will be detailed below, in the case of anatase/rutile interfaces, in particular, for Degussa P25, attachment has been thoroughly analyzed.

From the previous discussion, it should be clear that nanocrystalline anatase has two electronic differences with respect to the bulk anatase material. These are associated with the two main physicochemical parameters already mentioned: size (more generally speaking morphology) and defects.<sup>54</sup> Quantum-size confinement effects on band structure essentially arise from the presence of discrete, atomlike states. These states can be considered as being a superposition of bulklike states with a concomitant increase in oscillator strength. The natural consequences of these size-induced electronic phenomena are first the band narrowing and then the subsequent changes in band energy and gap. Although still the subject of discussion, the best experimental work seems to indicate that such a material only exhibits quantum size effects (more precisely strong confinement effects) for very small sizes, below 2–3 nm.<sup>29,63,64</sup> According to theoretical expectations, however, surface effects derived for undercoordinated atoms (where the local structure is in turn

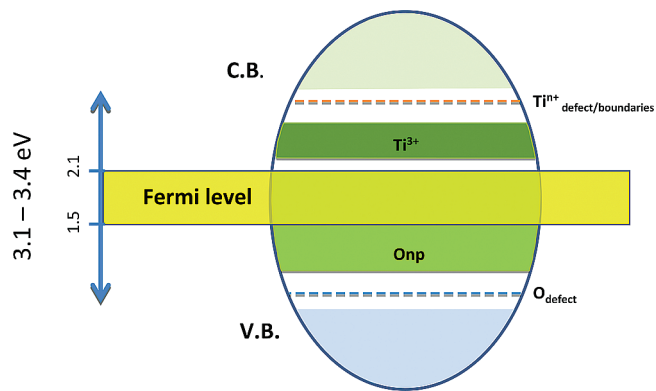


Figure 3. Main electronic characteristics of nano-TiO<sub>2</sub> (15 nm > particle size > 4–5 nm). See text for details.

related to the hydrated/dehydrated state of the surface) plus amorphization can in fact counteract the expected quantum blue shift of the band gap energy for particle sizes around 2–3 nm.<sup>65</sup> It should be noted that, within this size range, the anatase particle structure may be strongly perturbed. There are structural characteristics, such as 4-fold-coordinated Ti ions, which are not present in particles greater than 4–5 nm. Of course, in a nanoparticulated material, no band bending occurs at the surface of the material. In the case of anatase, there is always the question of whether the first allowed band gap indirect transition of the bulk material has a “vanishing” intensity in nanosized materials. Hence, the direct band gap energies lying slightly above the bulk indirect ones (all appearing between 3.0 and 3.5 eV) could be observed in specific cases.<sup>52,66</sup>

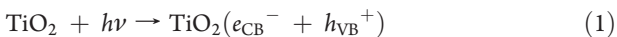
The electronic states associated with defects are not easily summarized. But from recent reports through the use of a suite of analytical techniques such as strain–stress XRD measurements, Raman analysis of peak width, impedance, electron spin and photoluminescence spectroscopies and other measurements based on the use of electron/hole scavengers and/or surface reactive molecules, a consistent picture has started to evolve.<sup>2–7</sup> We can speak of shallow or deep donor levels that are energetically near or below the conduction band whereas acceptor ones are located either near or above the valence band. Exponential and/or Gaussian-like distributions with a width proportional to the number of defects can be created.<sup>67,68</sup> It should be noted that this terminology has a slightly different physical meaning than that typically describing alien cations or anions in the anatase structure as donor/acceptor species. Essentially we are talking of more or less localized states for pure anatase, which are schematically depicted in Figure 3. The localization of the charge is essentially driven by the broad energy distribution. A typical number of defects range from  $10^{-1}$  to  $10^{-3}$  atom basis. As the density of states (DOS) varies over 0.5–1.0 eV (typical cases as discussed below), electronic carriers (that is electrons and holes, present in these levels) are found to be permanently localized in most cases.<sup>67</sup> There are, however, indications for high levels of defects (for example Ti vacancies above  $5 \times 10^{-2}$  atom basis) in 5 nm anatase particles.<sup>58</sup> This suggests that, below such size, defect-electronic states may have some extended, nonlocalized “band-type” midgap electronic structure. However, as repeatedly mentioned, at sizes below 4–5 nm a strong amorphization of the anatase structure may result which greatly limits our current understanding of the situation.

The density of states or electronic distribution of these vacancy-related midgap energy levels have been obtained experimentally,<sup>7,69–72</sup> which allows a comparison between different samples. Care must be exerted, however, in considering that the corresponding electronic level distribution is strongly influenced by the difference in dielectric constants between the semiconductor nanoparticle and the neighboring medium.<sup>73</sup> Above the Fermi level, the electronic levels display distributions ranging from 0 to 1.5 eV from the corresponding flat band potential with maxima (or depth) located sometimes at 60–100 meV<sup>65,69,72</sup> and in other cases around 0.4–0.6 eV<sup>65,69,71</sup> or 0.7–1.4 eV.<sup>69,74</sup> All the shallow levels are rather complex to assign. But the interparticle grain boundary and/or surface defective (e.g., undercoordinate) cation with  $Ti^{n+}$  ( $n > 3$ ) are structural situations which are assumed to generate such states.<sup>5,65,69–76</sup> The deep levels ( $>0.7$  eV) are exclusively ascribed to  $Ti^{3+}$  states arising from oxygen vacancies and/or interstitial Ti species.<sup>77–80</sup> The predominance of oxygen vacancies vs interstitial cations is generally assumed.<sup>1–10</sup> Some recent work of Besenbacher, however, may indicate a more prominent role of the Ti cations than has been previously assumed.<sup>78</sup>

There are also localized electron acceptor levels below the Fermi level. Some of these are shallow ones close to the valence band edge and other deep states located ca. 0.7–1.3 eV above that limit.<sup>5–7,69–74</sup> Shallow acceptor levels are customarily identified with defective, undercoordinated lattice  $O^{2-}$  ions. These are either at the surface or, what is less likely but also known to be present, at the bulk, called  $O^{*-}$  after hole capture. Deep levels are more difficult to assign unequivocally but typically appear for small primary sizes, below 10 nm, and/or for poorly crystallized samples. This appears to indicate that certain nonpunctual or associated defects and/or amorphization (typically induced concomitant to the presence of bulk OH species) may be the origin of these electronic states.<sup>5–7,69–75,81,82</sup> Some authors highlight the resemblance of these deep trap levels (as well as the other localized electronic states described previously) with the so-called color centers observed in ionic oxides.<sup>6,75</sup>

To summarize, it is clear that the nature of the midgap electronic levels in anatase is still to be fully clarified. In spite of this, Figure 3 schematically depicts midgap levels for a particle size in the ca. 5–15 nm range following the main guidelines discussed previously. The particle size decrease and concomitant presence of gap states raise the Fermi level position. Below 5 nm, the significant presence of Ti vacancies and the strong alteration of the anatase structure (together with the fact that the majority of these samples are subject to preparations that very likely allow the presence of C-containing impurities in large amounts) lead to a very different scenario than that described in Figure 3. The dominance of anion or cation (substitutional) vacancies is important as this would drive to n- or p-type conduction, respectively. The n/p-type conduction in turn would affect the ease by which the different charge carriers are generated and trapped and reach the surface.

From basic quantum mechanisms, it is known that the absorption of light with energy higher than the band gap promotes electrons into the conduction band (CB); this leaves holes in the valence band (VB), as shown in reaction 1.



This is the so-called “charge separation phenomenon”, which follows the well-known Fermi golden rule under the dipole

approximation.<sup>68</sup> The electron–hole pair which is formed after the absorption of light is called the exciton. This phenomenon occurs on the time scale of femtoseconds, below 100 fs.<sup>83–85</sup> For  $TiO_2$  and other oxides, absorption leads to the formation of singlet exciton states. Strong spin–orbit coupling with cation orbitals facilitates intersystem crossing to the triplet exciton states; this latter is presumably longer-lived and has the potential to undergo further physical/chemical transformations. Due to quantum confinement and in accordance with the electronic structure of nanoparticulated solids, the absorption of light becomes discrete-like and size-dependent. For nanocrystalline semiconductors, both linear and nonlinear optical (absorption included) properties arise as a result of transitions between electron and hole-discrete or quantized electronic levels. Depending on the relationship between the radius of the nanoparticle ( $r$ ) and the Bohr radius of the bulk exciton ( $R_B = \epsilon\hbar^2/\mu e^2$ ;  $\mu$ , exciton reduced mass, and  $\epsilon$ , dielectric constant of the semiconductor), the quantum confinement effect can be divided into three regimes: weak, intermediate and strong confinement regimes. These correspond to  $r \gg R_B$ ,  $r \approx R_B$ , and  $r \ll R_B$ , respectively.<sup>86</sup> The effective mass theory (EMA)<sup>87</sup> is the most elegant and general theory for explaining the size dependence of the optical properties of nanometer semiconductors (of course above a certain size where “molecular” behavior is not observed, typically 2 nm). Of course other theories such as the free-exciton collision model (FECM)<sup>88</sup> or those based on the bond length–strength correlation<sup>89</sup> have been developed also to account for several deficiencies or as alternatives to the EMA theory. For the onset of light absorption, e.g. the optical band gap, as well as for all the electronic transitions present in the optical absorption spectrum, the EMA theory predicts an  $r^{-2}$  dependence, with a main  $r^{-1}$  correction term in the strong confinement regime, while FECM gives an  $\exp(1/r)$  behavior. The Bohr radius of  $TiO_2$  is 1–2 nm. This indicates the size region where strong quantum confinement effects are expected in the band gap energy of such materials and, thus, in the chemical potential of charge carriers. In such a simplified view, which omits surface effects on the band structure,  $TiO_2$  anatase, greater than 3–4 nm, does not display size-dependence in valence/conduction band flat edge and band gap energies. This leaves “free” carriers modified (with respect to the bulk material) by secondary effects connected with the discretization/narrowing of the valence and conduction levels.

Once the electron–hole pair can be stabilized, both charge carriers should diffuse to the surface of the particle in order to generate chemistry. A rough approximation of the diffusion coefficient ( $D$ ) can be obtained by using the Frohlich theory.<sup>90</sup> From this, a (random walk) calculation of the time required ( $t = r^2/\pi^2 D$ ) to reach the surface of spherical  $TiO_2$  nanoparticles with characteristic size below 10 nm indicates that the electron diffusion process will last, at most, a few picoseconds. The corresponding transition time for holes would be below 100–300 fs.<sup>91–93</sup> The time response of electrons is obviously dependent on the energy of excitation as well as the presence of shallow traps which are roughly in thermal equilibrium with the free electrons. However, estimations of average lifetimes indicate that these would not exceed a few hundred picoseconds.<sup>93</sup> Apart from the inherent limitations of applying the Frohlich theory to nanoparticulated systems,<sup>7</sup> another important point is that electron and hole transport are known to be trap-limited in nanosized  $TiO_2$ .<sup>85</sup> Modern theoretical frameworks allow the interpretation that the electron/hole diffusion coefficients decrease proportionally with the number of (deep) traps present

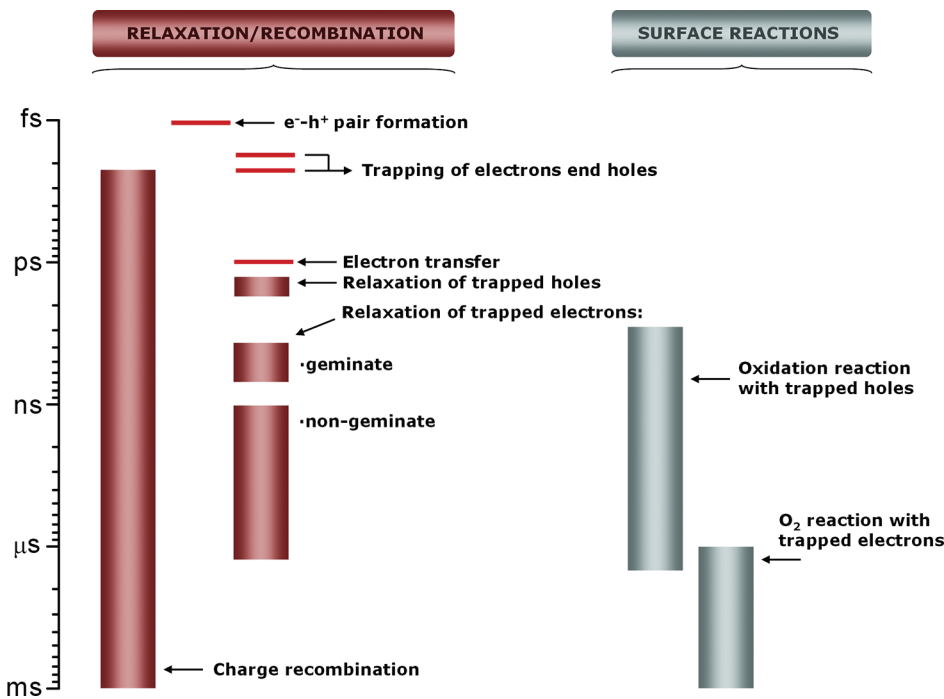


Figure 4. Time scales of “elemental steps” occurring in a prototypical photocatalytic process.

(i) in the particle<sup>67</sup> and/or (ii) created by the network morphology (porosity, secondary particle size) at interfaces of the porous material.<sup>94,95</sup> These trapping phenomena (more correctly speaking, trapping and relaxation, e.g. multiple trapping) occur over a broad time scale. These range from picoseconds to milliseconds or even a fraction of second and always compete with the charge recombination process. From an experimental point of view, an important result was first reported by Cornu et al. They showed that the charge carrier dynamics in the temporal region below the microsecond appears to be “irrelevant” with respect to anatase surface chemistry.<sup>96,97</sup> Hole trapping, relaxation and transfer (to surface species) processes all appear to be significantly faster and occur in the pico- and nanosecond region.<sup>85,91–93,98</sup> These experimental results also highlighted the facts that (i) electron trapping species with shorter lifetimes than a few microseconds are largely of importance in relation to their contribution to the charge recombination step; those having longer lifetimes, on the other hand, can be involved in the surface chemistry steps that are directly linked to the degradation or transformation of organic molecules; and (ii) holes interacting or recombining with multi-trapped electrons (with respect to anatase these are typically bulk species) control the diffusion process of the charge carrier species to the surface in nanosized TiO<sub>2</sub> under light excitation. These studies also indicate that free-like or shallow-trapped electrons most likely accumulate in the interior part of the particle (for particles with sizes greater than 5 nm) while both trapped charge species are generally located at the surface of the nanometer TiO<sub>2</sub> particles.<sup>98,99</sup> Long-lived (e.g., deeply trapped) electrons (and of lesser importance holes) are recombination centers if located within the bulk or innermost part of the nanoparticle. As discussed in section 6, under reaction conditions, holes at the surface may be trapped by hydroxyl radicals and/or directly transferred to the pollutant while electrons are initially trapped by anion-related traps and/or by gas phase oxygen.<sup>1–11</sup> Recent results indicate that hydroxyl and oxygen-containing radicals

move freely through the gas/liquid-catalyst interface and are not strictly retained at the surface.<sup>100</sup> Whereas, as previously mentioned, hole trapping and surface reaction(s) are quite fast, electron trapping kinetics (by gas phase oxygen), on the other hand, is in the micro- to millisecond range. Once again this indicates the dominant contribution of multiple-trapping electrons to this surface-chemical process.<sup>5,7</sup> A schematic view of the time scale of the different charge carrier-related phenomena just discussed is included in Figure 4.

Charge carriers formed in TiO<sub>2</sub> nanostructures upon absorption of light (reaction 1) can relax or recombine in both radiative or nonradiative ways, according to reactions 2 to 5.



Here the subindexes CB, VB and Tr stand for conduction and valence bands and trapped charge carriers, respectively. It should be noted that charge carrier energy relaxation or de-excitation in bulk semiconductors is dominated by nonradiative interactions with longitudinal optical phonons. These lead to fast (as described in the previous section, typically near picosecond or sub-picosecond) carrier cooling dynamics.<sup>101</sup> This is the so-called “Frohlich interaction”,<sup>90</sup> which is used to calculate diffusion coefficients. However, in nanometer systems, whether or not in weak or strong confinement regimes, the charge carrier relaxation mediated by interaction with phonons is drastically hindered because of the restrictions imposed by energy and momentum conservation. This leads to a phenomenon called “phonon bottleneck”. It appears that relaxation is in fact dominated by a

"non-phonon" energy-loss mechanism mediated by Auger-type electron–hole energy transfer phenomena.<sup>101,102</sup> Auger-recombination in a semiconductor is a nonradiative multiparticle process which leads to electron–hole pair recombination via energy transfer to a third particle (electron or hole) which is re-excited to a higher energy state. In nanometer systems, confinement-induced enhancement in Coulomb interactions and relaxation in translation momentum conservation should lead to increased Auger rates with respect to bulk systems. The atomic-like structure of the energy levels should hinder the Auger process because of a lower availability of final states.<sup>103</sup> As a result, Auger recombination can only occur in nanometer systems with the participation of a phonon (as a four-particle process) or with the involvement of a final state from the continuum of states outside the nanocrystal.<sup>104</sup> This analysis supports the idea that a major number of the electrons and holes would recombine using nonradiative channels. These might involve interparticle de-excitation and thus can be influenced not only by primary particle size but also by other morphological parameters such as porosity and secondary particle size.

Direct recombination models describe the reaction of the geminate ion pair in the lattice before any transfer to trapping sites.<sup>105</sup> This type of recombination takes place below the picosecond region. Serpone et al. found that this process could be the only (radiative) absorption decay in ca. 2 nm TiO<sub>2</sub> particles. It has a characteristic time of 10 ns. In addition, it dominates (ca. 90%) in 10–25 nm particles and has a decay time that decreases with increasing particle size.<sup>106</sup> The significant differences with the 2 nm sample can be attributed to the low crystallinity degree of the anatase phase in such small particles. Other charge carrier decay kinetics are observed after 1–10 ps. Depending on sample and experimental conditions these can extend to the subsecond domain. Such recombination processes are called nongeminate recombination and include contributions with at least one previously trapped charge species. Two typical nongeminate recombination processes are observed in anatase. These are ascribed to interaction of deep-trap electrons with valence band holes or conduction band/shallow-trap or free electrons with deep-trap holes, respectively.<sup>69–71,75</sup> Their non-exponential decay kinetics indicate multiple-trapping processes, which are mainly related to deep-trapped species, as discussed above.<sup>5,67,75,107</sup>

In summary, the work concerning nanoparticulated TiO<sub>2</sub> electron/hole dynamics indicates that there are several factors in photoelimination reactions which need to be carefully tuned in order to obtain active solids. Nonradiative recombination appears to be the main de-excitation channel for such systems. It seems to be connected with a significant number of morphological properties of the solid including porosity and secondary particle size. Primary particle size diminishing seems to produce two adverse key contributions associated with nonradiative recombination: (i) enhancement of the geminate recombination and (ii) the presence and subsequent role of bulk electron traps. Particle shape affects the photoactivity through the involvement of the OH groups in (at least) some degradation processes as well as affecting the variation of surface cation (Ti) and kink/edge defect number.

Hence, these three morphological parameters, primary and secondary particle size and particle shape, all need to be carefully engineered in order to control the photoactivity. Their simultaneous optimization must be capable of controlling the defect surface/bulk densities, with a view to accomplishing a number of

objectives. First, it is necessary to minimize light to chemical energy conversion losses by either nonradiative means (the main de-excitation pathway) or geminate radiative recombination; this occurs mainly through control of primary and secondary particle size. Second, it is necessary to minimize nongeminate recombination through control of the number of bulk traps. This is particularly relevant to electron traps since this charge carrier suffers an acute multitrapping process and, in the case of n-type semiconductors, accumulates at the bulk. This is intimately linked with primary particle size although it appears that this mostly occurs through a dependence on the surface to volume ratio for reasons that are not clear at the moment.<sup>108</sup> Finally, the third consists of modulating deep-trap chemistry of the holes and surface electrons. Thus, just limiting the attention to primary particle size, it defines three important regions because of the different nature of the defects. The first is roughly located above and below the 4–5, 12–15 nm cutoff edges. The second cutoff is more imprecise mainly due to the significant variety of surface effects which exert a strong influence on the structural/electronic properties.

### 1.3. Solar-Light Based Systems: Beyond TiO<sub>2</sub>

As has been known for several decades, an improvement in TiO<sub>2</sub> activity requires the simultaneous control of both morphology and defect structure. According to the previous discussion, it is possible to speculate that an elongated shape (aspect ratios clearly below 0.4; Figure 1) for nanometric particles greater than ca. 4–5 nm but less than 12–15 nm, with simultaneous minimization of the bulk defect number, should maximize anatase-TiO<sub>2</sub> photoactivity upon UV excitation. However, this behavior is not typically observed as the (001) anatase plane is known to be highly reactive,<sup>7,40–45</sup> this will be discussed further in more depth in section 6. The limitation of primary particle size at the nanometric range clearly leads to high reaction rates, inherent to the high surface area of the material, but also will maximize specific photoactivity rates per surface area unit if the whole morphology (not only the primary particle size) and defect chemistry of the material are adequately handled.

The requirement of using sunlight as the excitation source for the degradation reaction demands, as a principal requirement, the modification of the electronic characteristics of a UV-absorber system such as anatase-TiO<sub>2</sub>. Two main potential modifications may be envisaged: a decrease in the band gap or the presence of more or less localized midgap states. Although these will lead to different scenarios each with well differentiated structural/electronic characteristics, both possibilities have been explored almost from the beginning of research into photocatalysis using dopand ions. The approach involving doping ions (plus the corresponding charge neutrality defects) needs to accommodate simultaneously their influence in (i) charge trapping and recombination processes, (ii) morphological properties (primary and secondary particle size and particle shape), and (iii) the surface chemistry. This mainly involves OH and/or other alien species which are related to the acidity and basicity properties. As discussed below, some of the most critical issues affecting TiO<sub>2</sub>-based systems are so strongly affected by the presence of doping ions that they need to be very carefully formulated in a context far from that discussed above for unmodified anatase. However, knowledge and a good understanding of the pure anatase-TiO<sub>2</sub> system is a necessity in order to develop new optimized materials capable of displaying optimum photoactivity on sunlight excitation. A third possibility using anatase-TiO<sub>2</sub>

requires the incorporation of an external visible-light absorber, sometimes called a sensitizer. Solid-state sensitizers (as opposed to adsorbed molecules) are the only ones that can ensure long-term stability over a wide range of reaction conditions. Here we will briefly discuss the three most thoroughly analyzed pathways. These are the semiconductor-anatase system, the metal–anatase two-phase systems and finally other 3-component systems, in particular Z-schemes which simulate naturally occurring ones. With respect to sunlight excitation, a few words concerning carbon-nanotube-TiO<sub>2</sub>, polymer-TiO<sub>2</sub>, and other less well explored systems will be also included. All these TiO<sub>2</sub>-based systems will be presented in section 2 of this review.

As an alternative approach, exciting novel developments generally imply the absence of anatase as a solid photocatalyst and instead try to exploit new architectures in order construct novel photocatalysts. In section 3 we will review the main structures known to date which are important in the transformation/oxidation/elimination of pollutants. Sections 4 and 5 are, respectively, devoted to photocatalysts involving hydrogen generation and CO<sub>2</sub> reduction processes.

## 2. TiO<sub>2</sub>-BASED PHOTOCATALYSIS: DOPED AND COMPOSITE SYSTEMS

In the context of photocatalysis, research into the doping process of TiO<sub>2</sub> was initiated with the aim of improving titania performance under UV light. Choi et al.'s<sup>109</sup> exhaustive work used nanoparticulated anatase sized below 5 nm and tested the catalytic performance at 0.1–0.5 atom % doping levels for 24 cations. Systems containing Fe<sup>3+</sup>, Mo<sup>5+</sup>, Ru<sup>3+</sup>, Os<sup>3+</sup>, Re<sup>5+</sup>, V<sup>4+</sup>, and Rh<sup>3+</sup> showed increasing activity with respect to the titania reference systems. However, they also exhibited a complex dependence on dopant concentration, state in the lattice and/or surface/bulk, d-electron configuration, light intensity and other physicochemical variables. Using sunlight-type excitation, Fuerte et al. published another general test using 9 different cations over a broad range of concentrations (1–25 atom %) for single phase anatase materials. They found that the photoactivity can be increased from that of the titania reference systems (P25 or nanosized anatase) in the case of V<sup>4+</sup>, Mo<sup>6+</sup>, and W<sup>6+</sup>. However, in this case, the above-mentioned variables also appear to play a complex role. The d-electron configuration, the band gap modification and the lattice state are the principal ones.<sup>19,110–112</sup> Similarly, Anpo et al. demonstrated that the improved performance of Fe<sup>3+</sup>, Cr<sup>3+</sup>, and V<sup>4+</sup> anatase-type systems on sunlight-excitation. In these cases the alien cations were hosted into deep positions of the samples as a result of the magnetron sputtering preparation.<sup>2,113</sup> The structural complexity and, therefore, the number of structural and electronic variables influencing photoactivity are even greater for composite systems having 2 or 3 phases.<sup>21,22,114,115</sup> The examples just discussed are simple but illustrative examples of those that led to the key conclusion reached from hundreds of such studies: namely, there are a number of structural and electronic variables involved in the anatase photoactivity modulation in the presence of alien species or phases.

In spite of the complexity of these systems, recent work has contributed significantly to clarifying the situation. It has become increasingly obvious that the first step in the rationalization of the performance of TiO<sub>2</sub>-based systems requires a careful and complete structural and electronic characterization of such systems. Ideally this should be jointly carried out with an analysis

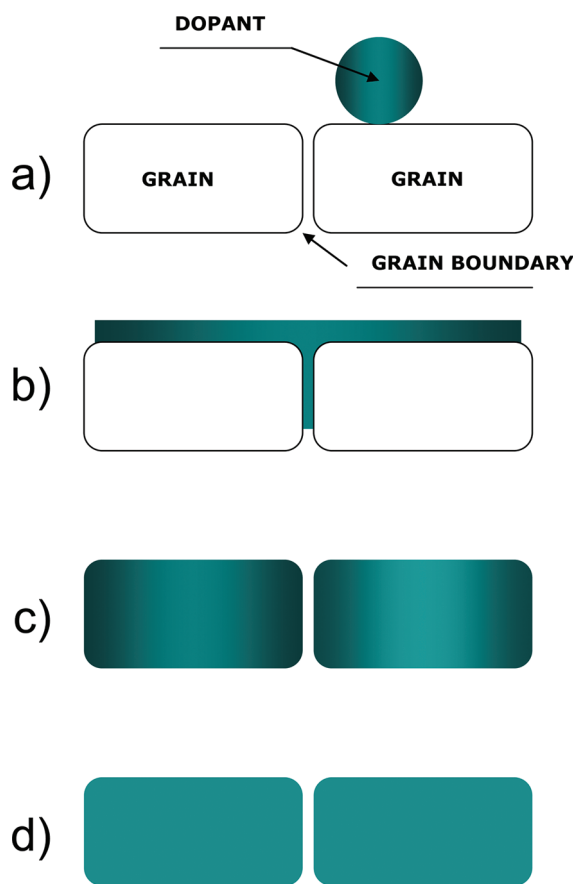


**Figure 5.** Main structural situations encountered in titania-based systems prepared in the presence of an alien species.

of both the photoactivity and charge carrier behavior. Taking into account such a conceptual scheme and with a view to rationalizing the literature, it is pertinent to first present an outlook of the main structural state that occurs with the introduction of alien species or phases. The study of the main electronic effects derived from well-defined structural situations is also a requirement. The importance of these structural and electronic modifications in light handling processes and photoactivity will be considered in section 6.

### 2.1. Structural Description of TiO<sub>2</sub>-Based Systems

Figure 2 depicts the main structural states connected to the presence of punctual defects which are in turn associated with doping. The anion (A species in the plot) and cation (M species in the plot) are characterized by two main structural parameters: (i) the presence at the surface or bulk of the particle and (ii) the presence at substitutional or interstitial positions of the anatase lattice. Although this simple classification considers the M or A alien species as isolated centers, the connectivity with the neighboring anatase ions is also relevant. The presence or absence of [M–O–M/Ti], [A–Ti–O/A] or [Ti/A–O–Ti/A] bonds needs to be considered in order to describe, in a simple yet reasonable (and experimentally achievable) way, the local order of a TiO<sub>2</sub>-containing solid.

A graphical representation of all structural states is displayed in Figure 5. When the M/A alien species is exclusively at the surface of the material, the result is the formation of composite systems. The M/A-containing phase may be present as patches of reduced

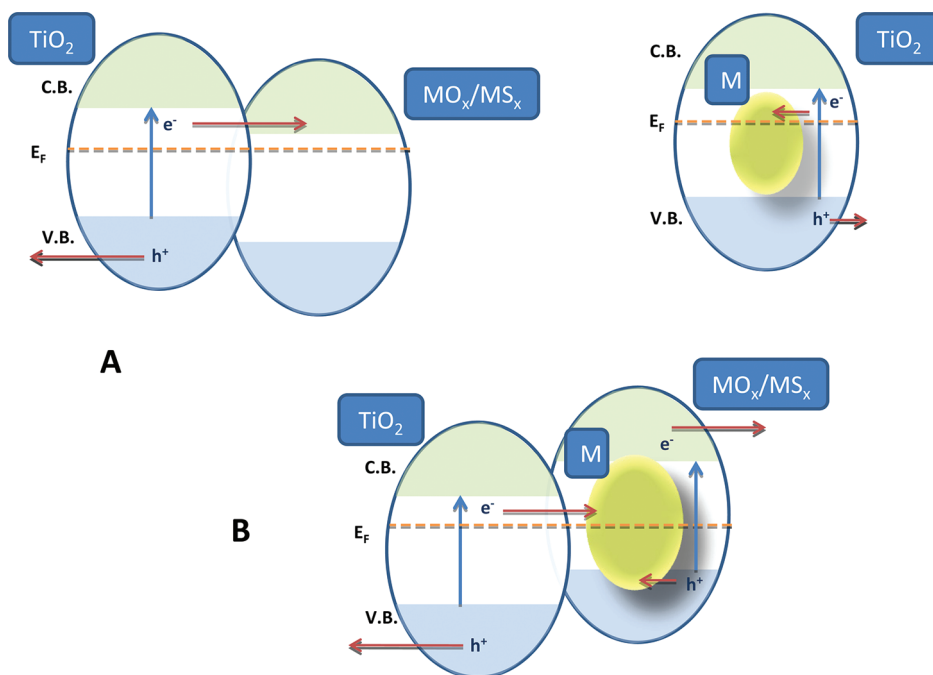


**Figure 6.** Illustrative representation of binary (A)  $\text{MO}_x(\text{MS}_x)$  or metal/ $\text{TiO}_2$  coupled or core–shell and (B) ternary  $\text{MO}_x(\text{MS}_x)$ /metal/ $\text{TiO}_2$  systems under UV and/or sunlight excitation.

dimensionality (Figure 5a) or completely encompassing the surface (Figure 5b). The chemical nature of the M/A species will lead to semiconductor-anatase or metal-oxide composite (multiphasic) systems. First these two structural situations leading to composite systems will be detailed. In these cases,  $\text{TiO}_2$  remains unaltered and maintains the same physicochemical properties or characteristics discussed in section 1.2 for the unmodified oxide.

**2.1.1. Composite Systems.** Semiconductor–anatase systems consist of three different useful types within the context under discussion: oxide–anatase, phosphate–anatase, and chalcogenide–anatase materials. Archetypical examples are the rutile–anatase ( $\text{TiO}_2\text{--TiO}_2$ ),  $\text{SnO}_2\text{-}$ ;  $\text{ZnO}\text{-}$ ;  $\text{ZrO}_2\text{-}$ ;  $\text{Bi}_2\text{O}_3$ ;  $\text{Fe}_2\text{O}_3\text{-}$ ;  $\text{Fe}_3\text{O}_4\text{-}$ ;  $\text{WO}_3\text{-}$ ;  $\text{CeO}_2\text{-}$ ;  $\text{Cu}_2\text{O}\text{--TiO}_2$  and  $\text{Bi}_2\text{S}_3\text{-}$ ;  $\text{PbS}\text{-}$ ;  $\text{CdS}\text{-}$ ; and  $\text{CdSe}\text{--TiO}_2$  systems.<sup>21,22,69,114–124</sup> However, the list is shortened when limited to active and reasonably stable systems in connection with sunlight-excitation:  $\text{WO}_3\text{-}$ ;  $\text{Cu}_2\text{O}\text{-}$ ;  $\text{BiO}_x\text{Cl}_y\text{-}$ , as well as specific geometrical configurations of  $\text{CdS}\text{-}$ ; and  $\text{CdSe}\text{--TiO}_2$  systems. Other useful candidates could be  $\gamma\text{/}\alpha\text{-Fe}_2\text{O}_3\text{--TiO}_2$  and  $\text{CeO}_2\text{--TiO}_2$ , but these are somewhat limited since apparently there are only a few reports with sunlight although there are several with UV or visible light sources. Recently, some complex oxides such as  $\text{FeTiO}_3$ ,<sup>125</sup>  $\text{NiTiO}_3$ ,<sup>126</sup>  $\text{LaVO}_4$ ,<sup>127</sup> and Bi-based oxides,<sup>128</sup> or oxohalides,<sup>129</sup> have been also tested in contact with  $\text{TiO}_2$ . Other less explored but yet important systems are the polyoxometalates and hetopolyacid-TiO<sub>2</sub>,<sup>100,130–133</sup> phosphate-TiO<sub>2</sub>,<sup>114</sup> multiwall carbon-nanotube-TiO<sub>2</sub>,<sup>134</sup> or polymer-TiO<sub>2</sub> systems.<sup>135–138</sup> In these latter cases, the nonoxidic component but also the interface play a capital role in the absorption of visible light photons. Rutile-anatase ( $\text{TiO}_2\text{--TiO}_2$ ) is interesting because the ion-doping of any of these phases leads to visible-light active materials. Also of interest are the 3-phase Z-type schemes using Au/Pt/Rh. These are a direct extension of the chalcogenide–anatase systems where Au/Pt/Rh acts as an electron modulator which is in physical

contact with both semiconductor phases in order to render effective photocatalytic systems.<sup>23,139</sup> A parallel scheme which allows practical use of  $\text{MS}_x$  nanostructures in elimination reactions considers the use of  $\text{MS}_x$ /polymer nanocomposites with adequate electronic structures to permit a fast drain of holes produced on the inorganic semiconductor upon light excitation. This limits the auto-reduction process.<sup>140</sup> In addition, both direct and indirect Z-schemes incorporating  $\text{TiO}_2$  have been pursued in order to physically or spatially separate the reduction and oxidation reactions.<sup>141,142</sup>

Figure 6 depicts a schematic representation of all the 2/3-phase structural situations commonly explored in the literature and based on “external” phase-coupling or “internal” core–shell geometries for multiphase contact. Rutile-anatase interfaces are the structural states subjected to the most intense structural research. In the case of the P25 system, it is well-known that nanometric (smaller than 20 nm) anatase patches are supported on larger rutile particles (ca. 25–30 nm). To summarize somewhat simplistically, the Ti and O surface sites appear to complete their coordination at the interfaces, reaching, respectively, 6- and 3-fold coordinations characteristic of the bulk. This occurs at a narrow interface layer (less than 0.5 nm) with some general disorder with respect to the bulk oxides.<sup>116,143</sup> In addition, novel punctual defects seem to appear. It has been postulated that this is the case of tetrahedral  $\text{Ti}^{4+}$  species.<sup>99,116,118</sup> As previously discussed, 4-fold-coordinated Ti species are rather uncommon on pure anatase surfaces. They are believed to be of importance for particle size smaller than 5 nm only. Focusing on the case of surface growth of anatase on larger rutile particles, it appears that structurally similar rutile (20–30 nm)–anatase (5–10 nm) 2-phase systems demonstrate that the optimum anatase content for maximizing the photoactivity appears close to 20%.<sup>144</sup> The surface contact between the two oxides is, however, strongly dependent on the preparation method. A fundamental rationalization of the anatase content leading to maximum photoactivity

as a function of both anatase–rutile particle size and the degree of interface contact<sup>145</sup> has been published.

Figure 7 brings together the data necessary to produce a correct rationalization of the anatase–oxide contact as a function of size. The analysis must take into consideration that the strong structural/electronic differences in anatase for particle sizes both smaller and larger than 5 nm would display, respectively, p- and n-type conductivity. As mentioned previously, this could be driven by a change in the main point defect on going from anionic to cationic nature. According to recent reports, such differences are not observed in rutile.<sup>52</sup> Due to polydispersity, anatase–anatase nanoparticle contact also has the potential to display several electronic contacts within the same single phase sample.<sup>7</sup>

Figure 7 also summarizes  $\text{WO}_3$ ,  $\text{Cu}_2\text{O}$ , or  $\text{Fe}_2\text{O}_3$  single-oxide electronic features as a function of size. Unfortunately, details about the structural interfaces between oxides such as  $\text{WO}_3$ ,  $\text{Cu}_2\text{O}$ , or  $\text{Fe}_2\text{O}_3$  with anatase are essentially unknown from a structural point of view. Nanosized  $\text{WO}_3$  is frequently crystallized into monoclinic ( $\text{P}2_1/n$ ) or orthorhombic ( $\text{Pnma}$  or  $\text{Pban}$ ) phases whereas  $\text{Cu}_2\text{O}$  presents a cubic structure.  $\text{Fe}_2\text{O}_3$  can exist as three polymorphs  $\gamma/\alpha/\epsilon$ . However, an understanding of the relative stability of these phases in the nanometer range (below 20–15 nm) is much less clear than for titania. Although some works suggest the  $\alpha$  as the most stable,<sup>146</sup> the gamma polymorph is typically pointed out as the stable phase for size below ca. 15 nm.<sup>147</sup> The presence of several W oxidation states, anion vacancies, and corresponding  $\text{WO}_3$  surface phases (with a certain degree of amorphization) on anatase gives an idea of the complexity of the situation that can be encountered in such cases.<sup>148,149</sup> The presence of CuO at the surface layers of nanoparticulated  $\text{Cu}_2\text{O}$  is also well established.<sup>150</sup> A critical point when dealing with oxide–oxide systems is the modification of surface area and properties, in particular acidity. The reason for this is that the photocatalytic elimination (oxidation) of most pollutants requires the presence of somewhat moderate acidic sites, the number of which is directly proportional to the photoactivity of particular samples under UV excitation.<sup>151,152</sup>

Other oxides can also be useful in the context of sunlight; in the case of simple oxides,  $\text{CeO}_2$  and  $\text{Bi}_2\text{O}_3$  were previously pointed out as representative examples. Due to the relatively limited performance observed for the former and the low stability of the latter, they (or other oxide-containing systems) will not be described here. However, a brief mention of the corresponding oxide– $\text{TiO}_2$  composite materials will be presented in section 6.

Chalcogenide (mainly sulfide)–anatase systems have the potential for making well-defined systems due to the current opportunities for achieving high morphological (size/shape) control of the chalcogenide materials. As detailed below, and in spite of the fact that not much interface structural detail is known, the influence of sulfide particle size and other morphological characteristics on photoactivity has been explored.<sup>21,22,114,115,120</sup> Most sulfide systems, in particular  $\text{CdS}$ , suffer deactivation by oxygen-induced photocorrosion under reaction conditions. This leads to ion leaching in solution and the formation of an elemental sulfur layer at the surface of the particle. As mentioned above, this problem has been solved using several approaches: (i) contact with an electron-drain system such as Au or Rh upon a Z-contact scheme,<sup>23,139</sup> (ii) contact with a quick drain hole polymeric system,<sup>140</sup> or (iii) the creation of core–shell structures where the sulfide is protected by a limited number of anatase shells.<sup>153</sup>

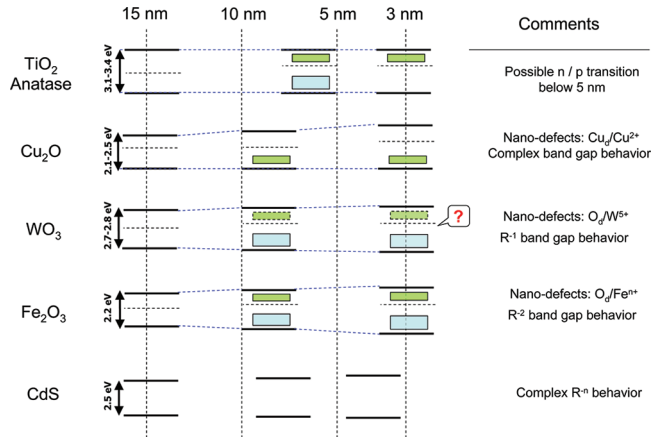


Figure 7. Size dependence of the main physicochemical properties of several semiconductors. Valence and conduction bands are represented by the corresponding top and bottom edges, respectively.

Metal–anatase composite systems have been analyzed from the starting point of the photocatalysis research field; typical metals investigated are Cu, Ag, Pt, Pd, Ru, Ir and more recently Au.<sup>1,20–22,154</sup> Metal–anatase–silica ternary systems with the metal bridging the contact between the two oxides are also utilized.<sup>155</sup> Similar to the semiconductor–anatase case, the design of metal–anatase nanostructures is based on two main models which correspond to phase-coupled or core–shell geometries. These are schematically summarized in Figure 6. From a structural point of view, the joint analysis of DFT (density functional theory) calculations and STM (scanning transmission microscopy) experimental data show that metals are deposited over oxygen vacancies or surface edge sites. Both the oxygen vacancies and the surface edge sites act as nucleating centers on the anatase surface. All the metals listed above tend to form 3D islands over anatase surfaces.<sup>53,156,157</sup> Metals and, particularly, noble metals are expected to undergo morphology (sometimes including size) changes after prolonged exposure to light under liquid-phase reaction conditions.<sup>9,154</sup> The size-dependence of the metal–anatase interface characteristics has been reported.<sup>21,22</sup> But due to the fact that it is mostly concerned with electronic parameters, its description is delayed until section 2.2.

The simultaneous presence of noble metals (Pt, Ru, Pd, Rh) and metal oxides ( $\text{NiO}$ ,  $\text{RuO}_2$ ) as cocatalysts for  $\text{TiO}_2$ -based systems also merits attention. In this case, reduction and oxidation semireactions of the photocatalytic process take place without the direct intervention of the anatase surface.<sup>158</sup> Finally, it should be pointed out that recently  $\text{WO}_3$ -supported metal-promoted systems appear to be highly active compared with M-promoted N-containing  $\text{TiO}_2$ -based systems under sunlight-type excitation. Hence, they may prove attractive for future photoactive alternatives.<sup>159,160</sup>

**2.1.2. Single-phase anatase systems.** Figure 5c and 5d exemplify the two other main structural states encountered in the presence of alien species. These two extreme situations are a result of the presence of alien doping species located into the anatase structure. The first (Figure 5c) represents a system with a radial concentration gradient of the alien species. This leads to either surface depletion or enrichment of one of the cations (Ti or M) or anions (O or A). This is a unique yet relatively common case resulting from local ordering inhomogeneities derived from the energetic prevalence of  $\text{M}–\text{O}–\text{M}/\text{A}–\text{M}–\text{A}$  vs  $\text{M}–\text{O}–\text{Ti}/\text{A}–\text{M}–\text{O}$  bonds. The complete picture can take into consideration

The figure shows a standard periodic table with several elements highlighted in orange, blue, and yellow. Orange highlights are placed on Scandium, Titanium, Vanadium, Chromium, Manganese, Cobalt, Nickel, Zinc, Gallium, Germanium, Indium, Tin, Antimony, Tellurium, and Iodine. Blue highlights are placed on Calcium, Strontium, Barium, Lanthanum, Cerium, Praseodymium, Neodymium, Promethium, Samarium, Europium, Gadolinium, Terbium, Dysprosium, Holmium, Erbium, Thulium, Ytterbium, and Lutetium. Yellow highlights are placed on Boron, Carbon, Nitrogen, Oxygen, Fluorine, Neon, Silicon, Phosphorus, Sulfur, Chlorine, Argon, Potassium, Sodium, Magnesium, Rubidium, Cesium, Francium, Radium, Thorium, Protactinium, Uranium, Neptunium, Plutonium, Americium, Curium, Berkelium, Californium, Einsteinium, Fermium, Mendelevium, Nobelium, and Lawrencium.

IA	IIA	VIII A
1 H Hydrogen 1.00797	4 Be Boron 9.0122	2 He Helium 4.0026
3 Li Lithium 6.939	11 Na Sodium 22.9898	5 B Boron 10.811
12 Mg Magnesium 24.312	19 K Potassium 39.102	6 C Carbon 12.0115
37 Rb Rubidium 85.47	20 Ca Calcium 40.08	7 N Nitrogen 14.0067
55 Cs Cesium 132.905	21 Sc Scandium 44.956	8 O Oxygen 15.9994
87 Fr Francium (223)	22 Ti Titanium 47.90	9 F Fluorine 18.9984
88 Ra Radium (226)	23 V Vanadium 50.942	10 Ne Neon 20.183
90 Th Thorium 232.038	24 Cr Chromium 51.998	13 Al Aluminum 26.9815
91 Pa Protactinium (231)	25 Mn Manganese 54.9380	14 Si Silicon 28.086
92 U Uranium 238.03	26 Fe Iron 55.847	15 P Phosphorus 30.9738
93 Np Neptunium (237)	27 Co Cobalt 58.932	16 S Sulfur 32.064
94 Pu Plutonium (242)	28 Ni Nickel 58.71	17 Cl Chlorine 35.453
95 Am Americium (243)	29 Cu Copper 63.548	18 Ar Argon 39.948
96 Cm Curium (247)	30 Zn Zinc 65.37	
97 Bk Berkelium (247)	31 Ga Gallium 69.72	
98 Cf Californium (251)	32 Ge Germanium 72.59	
99 Es Einsteinium (254)	33 As Arsenic 74.9216	
100 Fm Fermium (257)	34 Se Selenium 78.98	
101 Md Mendelevium (258)	35 Br Bromine 79.904	
102 No Nobelium (259)	36 Kr Krypton 83.80	
103 Lr Lawrencium (260)	50 Sn Tin 118.69	
	51 Sb Antimony 121.75	
	52 Te Tellurium 127.60	
	53 I Iodine 126.9044	
	54 Xe Xenon 131.30	
	55 Cs Cesium 132.905	
	56 Ba Barium 137.34	
	57 La Lanthanum 138.91	
	58 Ce Cerium 140.12	
	59 Pr Praseodymium 140.907	
	60 Nd Neodymium 144.24	
	61 Pm Promethium (145)	
	62 Sm Samarium 150.35	
	63 Eu Europium 151.98	
	64 Gd Gadolinium 157.25	
	65 Tb Terbium 158.924	
	66 Dy Dysprosium 162.50	
	67 Ho Holmium 164.930	
	68 Er Erbium 167.26	
	69 Tm Thulium 168.934	
	70 Yb Ytterbium 173.04	
	71 Lu Lutetium 174.97	

**Figure 8.** Periodic table highlighting doping elements with small (orange), intermediate (blue) and high (yellow) solubility limit at the anatase structure.

the possible existence of M- or A-enriched local patches either at the surface or in the bulk of the anatase material.<sup>19,112</sup> Of course, the presence of alien-species enriched patches at the surface which are of a well-defined nature has already been represented in Figure 5a. So here we will consider situations where there is a certain presence of a binary phase and not just a “simple” phase/compound (e.g., a pure oxide, sulfide, nitride). Finally Figure 5d displays a true solid solution with a (more or less) constant chemical composition throughout the particle size.

As summarized in Figure 8, the tendency for surface segregation of M cations in anatase mixed-oxide materials has been studied. Typically it has been observed for V, Ca, Sr, Ba, Mn, Zn, Sb, Fe, La and In and occasionally detected for Cr, Co, Ni, Mo, Zr, Sn, Ce or Nd, while other cations such as Ta, Nb or W do not show any appreciable tendency to accumulate at the surface layer.<sup>19,54,109–111,113,161–180</sup> This is a direct consequence of the corresponding M solubility limit into the anatase structure. This is relatively low (below 5 atom % in  $Ti_{1-x}M_xO_{2\pm\delta}$ ) for V, Fe, Mn, La and In; intermediate (ca. 5–12 atom %) for Mo, Cr, Co, Ni, Sn, Zr, Ce or Nd; very high (near or above 20 atom %) for the remaining cations mentioned. Ca, Sr and Ba may display high solubility limit(s) but concomitant amorphization of the titania structure occurs above ca. 5 atom %.<sup>163</sup> M cations can additionally show differences in terms of their location into the anatase lattice as most of the cations tend to occupy substitutional positions. Only a few such as Nd, V and Fe (and the noble metals) can favor partial (as they are additionally present at substitutional positions in most cases) occupation of interstitial positions.<sup>54,165,170,176,181</sup> There is some uncertainty with respect to Ce as well as Ni, Mn, Cr and/or Co on the doping level. These are typically either below or above 5 atom % which is attributable to the range of conditions driven by the multitude of experimental preparation methods. In the case of Ce, this can be related to the presence of additional phases such as  $CeTiO_4$  or the pyrochlore-type  $Ce_2Ti_2O_4$  which because they display limited crystallinity escape detection by conventional techniques. In addition, the presence of such phases would result in photoactivity and hence render the study of these Ce–Ti binary

systems much more difficult.<sup>182,183</sup> Other, even more complex cases, such as Cr or Fe, are discussed in detail below.

The presence of a  $M^{n+}$  cation with  $n \neq 4$  at the anatase lattice necessarily implicates the presence of defects in order to achieve charge neutrality.<sup>184</sup> Although very few studies deal with the structural topic at both local and long order ranges in detail, it is somewhat surprising that the few studies where the structure of the nanosized mixed oxide has been rigorously analyzed at both local/long ranges show the presence of cation vacancies irrespective of whether the M oxidation state is above or below 4.<sup>165,170</sup> For  $M^{n+}$  with  $n < 4$ , the charge valence is achieved with the additional presence of hydroxyl groups.<sup>165</sup> Stabilization of cation defects on the  $Ti_{1-x}M_x[\cdot]_zO_{2-w}(OH)_w$  stoichiometry (where  $[\cdot]$  represent a cationic vacancy) through partial replacement of the oxide ions by hydroxyl groups is a common feature with cation-defective anatase nanomaterials with limited size (below 5 nm).<sup>59</sup> Other studies, however, showed the expected anion vacancies such as in the case  $n < 4$  (Fe) and nanosized materials.<sup>185</sup> More complex structural defects with the prevalence of anion vacancies independent of primary particle size can nevertheless occur in cases such as Cr. Here two oxidation states either above or below 4,  $Cr^{6+}$  and  $Cr^{3+}$ , can exist simultaneously.<sup>186</sup> Oxygen vacancies efficiently release strain in the anatase structure, and their existence in nanosized materials would be thus a function of the  $M^{n+}/Ti^{4+}$  radius ratio, being favored as the ratio departs from 1. In the case of  $n = 4$ , systems with an anatase structure, these are found to display anion vacancies only.<sup>152,175,176</sup>

The predominance of cation vs anion vacancies could, therefore, be a function of (i) primary particle size; according to the situation on unmodified titania, cation vacancies would be favored at low particle size (as described previously); and (ii) the  $M^{n+}/Ti^{4+}$  radius ratio and the corresponding structural strain. A large  $M^{n+}/Ti^{4+}$  radius and strain favor the presence of anion vacancies. It is clear that the  $M^{n+}/Ti^{4+}$  radius invokes another physicochemical variable, namely, the M oxidation state. In some cases, such as V, this differs from the surface (+5) to the bulk (+4) positions. This can display multiple values in the same

sample as would occur with Cr, Co or Mn, or cannot have a single oxide counterpart (e.g., unique electronic structure) such as is the case for Nb.<sup>19,174,186,187</sup> Thus cations with the potential for oxidation state variability are those presenting the greatest differences; this is the result of the numerous preparative methods used for obtaining anatase-based mixed oxides.

Another case where increasingly complex structural states exist is that of Fe. Here either the presence or absence of  $\text{Fe}-\text{O}-\text{M}/\text{Fe}-\text{O}-[]$  ( $\text{M} = \text{Ti}, \text{Fe}$ ) localized arrangements and/or the presence of iron surface enrichment can be detected depending on the experimental preparative conditions employed.<sup>109,110,165,169</sup> Localized to middle range ordering is therefore the last variable which controls defect formation. Strong local ordering effects with the appearance of M – cation vacancy pairs are observed in anatase-based systems such as W-doped systems.<sup>170,188</sup> For highly loaded samples (above ca. 10–15 atom %), nonpunctual defects, based on the collective handling of cation vacancies, seem active and appear to accumulate at the nanoparticle/grain boundaries.<sup>170,179</sup> The available data indicates that first a well-defined local ordering is probably a constant in doped anatase systems which display cation vacancies but also that, in order to get the complete picture, analysis of the local structural detail beyond the first coordination shell is also required. So, in order to complete the long-range order overview of a nanosolid, an accurate description of the local-middle order must be carried out. A full rationalization of the structural states originating from cation doping will nevertheless only be possible in the future. This is largely due to the lack of detailed local and long-range simultaneous/cooperative information in the nanometer range from 4 to 20 nm. Some novel techniques which are capable of describing the complete local and long-range order, such as those derived from X-ray total scattering approaches (e.g., XRD-PDF), are without doubt the key to accomplishing this objective.

We can thus conclude that the anatase cation solubility limit is a function of the primary particle size,  $\text{M}^{n+}/\text{Ti}^{4+}$  radius and the structural strain. The structural strain in turn is influenced by important variables such as the M oxidation state as well as local-middle long-range effects (both of the M and defect sites). Simple yet useful numerical equations have been put forward to qualitatively evaluate the importance of the role of these variables in the energetics of the anatase lattice.<sup>186</sup> Although Figure 8 summarizes the trends observed with respect to solubility limits observable from the periodic table, there is still a lack of information concerning size-dependence. The previous discussion suggests that different energy vs size effects are expected for systems which have cation or anion vacancies as charge neutral defects. It is also clear that complete short, middle and large structural views are required in order to further progress the understanding of the solubility limits on cation-doped  $\text{TiO}_2$  materials. Achieving a M concentration near the corresponding (thermodynamic, size-dependent) solubility limit is frequently related to the preparation method. This, in a rough approximation, should allow control of both the structural homogeneity and the primary particle size.<sup>54</sup> Cations with low or intermediate solubility limits commonly segregate at the surface and form M-enriched binary patches. In addition, with increasing concentrations single pure  $\text{MO}_x$  phases are formed. These are independent of the preparation method. Highly soluble cations can, however, be differentiated. Among these are those which have a tendency to form M–O–M bonds such as is the case with Nb. In others such as W, this trend is much less pronounced.<sup>19,179,188</sup>

The anion-doping of anatase appears to be controlled by a generally significantly inferior solubility limit. The best studied case involves doping with nitrogen. Here it appears that very few preparative methods are capable of giving a N content above 2.5 atom % ( $\text{Ti}_{1-x}\text{O}_x\text{N}_z$ ). Apparently doping levels as high as ca. 10 atom % are only obtained using exclusively nucleophilic substitution chemistry or magnetron sputtering.<sup>189,190</sup> These are, however, only nominal doping levels since almost all the materials synthesized (at least by chemical methods) contain adsorbed (e.g., surface) N-containing species. This appears to indicate somewhat lower solubility limits than those typically quoted in the literature, estimated using chemical analyses.<sup>6,75,191</sup> Physical methods such magnetron sputtering, on the other hand, produce heterogeneous materials with the presence of either undoped or doped particles as a function of the “penetration” spatial coordinate.<sup>190</sup>

The range of surface species present in N-doped  $\text{TiO}_2$ -based materials is enormous but typically contains N–O, N–H and/or N–C bonds.<sup>6,7,29,75</sup> The chemical species present within the anatase lattice are also numerous. Of the key features of N-containing  $\text{TiO}_2$ -based systems it should be mentioned that (i) generally, the materials synthesized do not contain a single N-containing species and (ii) the chemical nature of the species varies with the preparation method. So, with the aid of XPS, EPR, DRIFTS and DFT calculations, the presence of substitutional  $\text{N}^{n-}$  ( $2 < n \leq 3$ ) or  $(\text{NO}_x)^{n-}$  species and interstitial  $\text{NH}_x$  ( $0 < x \leq 2$ ) or  $\text{NO}_x$ -type species have all been detected.<sup>5,29,75,191,189,192–201</sup> In addition, the presence of negatively charged  $(\text{CN})^{n-}$ , and positively charged  $(\text{NH}_x)^{n+}$  species have been identified as being present at anion or interstitial positions.<sup>191,201–203</sup> Possibly, the most complex assignment corresponds to oxygen-containing  $\text{NO}_x$ -type species. Here N has a positive charge  $(\text{NO}_x)^{n-}$ , and their presence at both anion substitution positions and interstitial positions has been claimed but with no obvious consensus in the literature.

Due to the relatively complexity of the N-doping process it is a challenge to describe in detail the associated defects which allow charge neutrality. Nevertheless, XPS, XAS and DFT analyses showed the presence of anion vacancies in samples containing both substitutional and interstitial N-containing doping species without the concomitant existence of  $\text{Ti}^{3+}$  species (the latter would indicate some depopulation of the typical  $\text{Ti}^{3+}$  levels already described for pure nano- $\text{TiO}_2$ ). The creation of oxygen vacancies into the anatase lattice is strongly favored by the presence of the N-containing impurities. This is particularly well documented from theoretical calculations in the case of substitutional doping. Interstitial doping generates strong local rearrangements of the anatase structure leading to charge neutrality vacancies which are not fully understood. The total number of oxygen vacancies present in a real sample is, however, difficult to ascertain due to the variety of the N-impurity species. But it seems higher than that expected from “simple” charge neutrality requirements based on the N-content of the solid measured using chemical analysis.<sup>193,198–201,203–207</sup> This suggests a more complex structural situation than the simplest ones currently being considered.

In addition to N, C,<sup>5,29,208–215</sup> F,<sup>29,216–220</sup> S,<sup>29,221–226</sup> and to a lesser extent B,<sup>227–230</sup> Cl, Br,<sup>220,231</sup> P<sup>232–234</sup> and I<sup>220,235–238</sup> have all been tested as anion dopants of anatase systems. The codoping processes have also been frequently analyzed. Typical examples are the combined use of N/F,<sup>239–243</sup> N/Cl,<sup>191</sup> N/I,<sup>244,245</sup> N/B<sup>246–249</sup> or N/C.<sup>250</sup>

With respect to carbon, experimental approaches indicate the presence of surface carbonate and carbonaceous species, as well as lattice-bound carbon species.<sup>208–210,214</sup> Due to the expected dominant contribution of surface species to the total carbon content, it is not clear what the maximum amount of carbon that can be present at the anatase lattice can be. Carbon doping of anatase has also been addressed theoretically. Results showed the potential presence of substituted C in both anion and cation lattice positions as well as interstitial positions. Under normal catalytic preparative conditions (oxygen-rich conditions), substitution of an anion lattice position is not likely but the concomitant creation of oxygen vacancies is strongly favored and thus makes the whole process possible.<sup>213</sup> These anion-substitution doping centers promote minimal disturbance of the lattice and seem to be responsible for forming complex units with anion vacancies at interacting distances. These certainly form in-gap states, but they are not well understood at the moment.<sup>212,215</sup> Carbon at cation positions would have a carbonate-like chemical nature. It appears that overall carbon structural effects must be related to the simultaneous presence of cation (less likely anion) substitution carbon-containing entities. These would occur together with a complex interplay with the anion vacancies generated in order to achieve charge neutrality.<sup>208–214</sup> As mentioned above, C is also at the surface and the importance of these species as visible light sensitizers has been also pointed out.<sup>251,252</sup>

The case of fluorine is similar, at least concerning the simultaneous presence of surface species and those located within the anatase lattice. There is, however, conclusive evidence that fluorine is present exclusively in the anion lattice positions as F<sup>−</sup> with concomitant formation of Ti<sup>3+</sup> species for overall charge neutrality. The substitutional occupation of anion lattice positions seems to display a rather low concentration limit, possibly below 1–2 atom %.<sup>215–219</sup> Such solubility limits seem, however, easily overcome in the presence of N-containing species. In such a situation, a fluorine concentration as high as 8 atom % has been reported.<sup>241</sup> Theoretical studies of N<sub>x</sub>F-codoping indicate that, irrespective of whether N is in substitutional or interstitial anatase lattice positions, the simultaneous presence of both N and F doping anions significantly reduces the number of oxygen vacancies compared to N-doped systems.<sup>242</sup> As with fluorine, the sticking coefficient of other halide species onto oxide surfaces ensures their surface presence under almost all experimental conditions. In the case of iodine, (IO<sub>4</sub>)<sup>−</sup> groups are customarily observed at the surface. In contrast to fluorine, other halogen dopants such as iodine would present a more complex chemical behavior when located within the anatase lattice. The presence either of (IO<sub>4</sub>)<sup>−</sup>/I<sup>−</sup> pairs or I<sup>5+</sup> (the latter possibly at cation anatase positions) species has been mentioned as occurring in nanometric (5–10 nm) anatase samples.<sup>235,236</sup> There is also some evidence of differences with respect to the local ordering of iodine ions in anatase lattice positions.<sup>238</sup> Trends with respect to the halogen series ease in occupying either anion or cation positions have been also explored.<sup>220</sup>

Sulfur also exhibits the common characteristic of all anion-doping systems, e.g. its presence at the surface, typically as sulfate groups, and as the S<sup>4+</sup> species in lattice positions. The latter species appears to be of some significance in the anion positions of the anatase lattice. Possibly it has a limited maximum concentration below 4 atom %. The sulfur substitution of anion (O) lattice ions should take place with an important local rearrangement still to be fully unraveled.<sup>222,223,225,226</sup> Again, S-doping apparently creates a number of oxygen vacancies exceeding

that predicted from “simple” charge neutrality arguments.<sup>56</sup> Phosphorus also shows up as in the presence of phosphate species at the surface layers and P<sup>5+</sup> species of unknown chemical nature replacing Ti cations in lattice positions.<sup>233,234</sup> Finally, with respect to B, it should be noted that it is typically present as the dopant at both the surface and bulk anatase lattice positions. At the surface layers, the calcination step usually produces B<sub>2</sub>O<sub>3</sub> patches. The presence of B in the anatase lattice seems again to display a low solubility limit (possibly ca. 1 atom %).<sup>230</sup> Theoretical and experimental data indicate the presence of B at anion lattice and interstitial positions, the latter being preferred. Doping and charge neutrality appear to occur with strong local rearrangement of both O-anion and Ti-cation neighboring atoms.<sup>227–230</sup> The copresence of B and N produces two types of interstitial B with N at interacting distances.<sup>249</sup>

It is pertinent to include a small final paragraph that considers the simultaneous presence of two or more doping species in anatase samples. Although we already mentioned this in the case of N/F and other binary anion-doping combinations, some cation–cation examples, such as Cr–Sr,<sup>253</sup> Ni–Nb,<sup>254</sup> Sc–Nb,<sup>255</sup> W–Nb<sup>256</sup> and Sn–Eu,<sup>257</sup> as well as cation–anions, such as Li–F,<sup>258</sup> Zr–F,<sup>259</sup> Mo–C,<sup>260</sup> Ce–C,<sup>261</sup> Fe–N/C,<sup>262</sup> Fe–N,<sup>263,264</sup> V–N,<sup>265,266</sup> Mo–N,<sup>267</sup> In–N,<sup>268</sup> Sn–N,<sup>269</sup> Ce–N,<sup>270</sup> Eu–N<sup>271</sup> and W–N,<sup>267,272,273</sup> have been also studied. A detailed theoretical analysis of the anion–cation (V, Cr, Nb, Mo; N, C) doping process,<sup>274</sup> together with a comprehensive review,<sup>275</sup> has been recently published. Although a full understanding of the structural situation is less than clear due to the limited amount of information available, one useful contribution of codoping studies would be the subsequent ease in handling of the stoichiometry. This would make it possible to control defect formation as related to charge balance, at least as much as is possible. Structure strain, at least compared to the single doping situation, could also be controlled. However, no clear rationalization has been presented on whether the codoping would drive to additive or synergistic effects with respect to the stoichiometry/strain parameters. The poor understanding of structural/electronic effects in the case of codoped materials indicates the need for further analysis in order to test the potential of binary doped anatase-based photomaterials compared to single-doped materials. A brief statement on future perspectives concerning codoped systems will be presented in section 7.

## 2.2. Electronic Description of TiO<sub>2</sub>-Based Systems

In accordance with the structural states depicted in Figure 5, the electronic features of multiphase or single-phase systems which allow them to become active photocatalysts under sunlight excitation will now be discussed from a phenomenological point of view. Composite materials are multiphase materials, and the subsequent newly introduced electronic features, with respect to bare anatase, will be concerned with those brought about by the semiconductor or metal phases accompanying anatase, as well as the interface states derived from the presence of heterojunctions. In the case of doping, it is possible to distinguish between surface- and bulk-derived electronic features. Even more importantly, the substantial differences expected as a function of the doping level as they would lead to localized vs band edge electronic effects can also be distinguished. This has profound consequences on the light handling properties of doped anatase-based solids and should be at the core of light–matter interaction differences occurring in cationic vs anionic doping of the anatase structure.

**Table 1.** Band Gap and Approximate Conduction Band Flat Edge (with Respect to Vacuum Level) of Several Semiconductors at pH<sub>ZPC</sub>

semiconductor	band gap/eV	conduction band/eV
TiO <sub>2</sub>	3.1	-4.2
ZnO	3.2	-4.2
WO <sub>3</sub>	2.7	-5.2
Cu <sub>2</sub> O	2.2	-4.3
CuO	1.7	-4.1
Fe <sub>2</sub> O <sub>3</sub>	2.2	-4.8
CdS	2.4	-4.0
CdSe	1.7	-3.9

**2.2.1. Composite Systems.** Table 1 summarizes the main electronic information concerning the conduction and valence bands of the typical bulk solid semiconductors of interest in photocatalysis.<sup>276</sup> Figure 6 depicts the 2/3-phase structural states encountered with respect to composite materials. It also includes a simple picture of the Fermi level equilibration which occurs on contact between anatase and the semiconductor. Upon light excitation both materials can absorb light, albeit of different wavelength, as will be detailed in section 6. Since both phases are typically high-surface area nanometric materials, it should be noted that Figure 6 is clearly an idealization which can be drastically modified by the influence of three main factors: primary particle size, size distribution or polydispersity, and the defect electronic structure. The effect of size on single-phase compounds is addressed in Figure 7.

In section 1.2 the main structural/electronic effects of anatase derived from a nanometric particle size and the inter-related defect structure were described. For samples undergoing calcination or any other oxygen-rich synthesis step (e.g., hydro-treatment), three different situations as a function of primary particle size, defined by the 4–5 and 12–15 nm cutoffs, are possible. These situations are schematically depicted in Figure 7.

With respect to the semiconductors mentioned in Table 1, the situation is similar to that of anatase insofar as they also have electronic behaviors modulated by primary particle size and defect chemistry. The defect chemistry of WO<sub>3</sub> and Cu<sub>2</sub>O is remarkably rich. It includes the presence of anomalous oxidation (e.g., W<sup>5+</sup>/Cu<sup>2+</sup>) states which occur at the surface layers or defects; using current knowledge these cannot be rationalized as a function of size. Apart from the predominance of cation vacancies and defect-derived electronic states above the Fermi level, the p-type Cu<sub>2</sub>O semiconductor defect chemistry is relatively unknown in the nanometric range due to the complications derived from the presence of Cu<sup>2+</sup> at the surface layers. This is in addition to nonstoichiometry.<sup>150,277</sup> Some recent work suggested a size-driven p to n transition for Cu<sub>2</sub>O as the size decreases in the nanometer range, but the latest studies seem to indicate that this is simply triggered by the presence of alien (particularly chloride) ions.<sup>278</sup> The optical band gap shows confinement effects are not well established and are “affected” experimentally by the presence of Cu<sup>2+</sup> layers. In addition, they are poorly predicted by the EMA theory, particularly for sizes below 10 nm.<sup>54,279–281</sup> In the case of WO<sub>3</sub>, the presence of W<sup>n+</sup> ( $n < 6$ ) and oxygen vacancies are typical. Oxygen vacancies generate occupied/partially occupied levels near the valence band but also affect both the conduction and valence band through resonant states. The band gap energy in the nanometric

range behaves as an inverse function of the particle size ( $r^{-1}$ ).<sup>54,148,282,283</sup> Amorphization of the structure as the size decreases may be (at least in part) be the physical origin of the observed gap behavior (e.g., below 5 nm).<sup>284</sup> A few observations about Fe<sub>2</sub>O<sub>3</sub> are also pertinent; it appears that the alpha and gamma polymorphs should follow the EMA prediction with a main  $r^{-2}$  dependence of the band gap energy.<sup>285</sup> As in previous cases, surface vs bulk differences with respect to Fe oxidation/structural properties are described for nanometric samples in the literature.<sup>286</sup>

Contrary to nanooxides, extreme control of primary particle size is possible when nanometric chalcogenides are synthesized. The result is that the size-dependence of the band gap and the corresponding behavior with respect to anatase bands have been experimentally measured.<sup>21,22,114,115,120,287</sup> Due to the shell-like structure of most chalcogenides, the EMA predictions of optical observables for nanometer size specimens are not fully quantitative (although qualitatively correct and useful). However, current DFT theoretical calculations can make adequate predictions of band gap energy size-dependence with the help of the DFT+U method, and/or hybrid exchange-functionals, in which some parameters ( $U$  value in the former, the fraction of exact Hartree–Fock exchange in the latter) are adjusted in order to obtain a correct and precise description of the material under study. Recent studies indicate an approximate  $r^{-1}$  dominant term for the band gap energy behavior.<sup>288</sup>

A schematic picture of all localized and band-type states for anatase-TiO<sub>2</sub> and selected MO<sub>x</sub>/MS<sub>x</sub>/MSe<sub>x</sub> materials as a function of size is presented in Figure 7. The semiconductor-anatase “electric” contact leads to a single Fermi edge for any pair of nanostructures built up for each characteristic TiO<sub>2</sub> size while in contact with surface MO<sub>x</sub>/MS<sub>x</sub>/MSe<sub>x</sub> entities of limited size (below 15 nm). The resulting contact is, however, complex due to polydispersity; a TiO<sub>2</sub> oxide with relatively high morphological control will have a non-Gaussian particle size distribution with, at best, a 2–3 nm half-width at medium height. This clearly indicate that an average particle size of 7 to 12 nm will have significant contributions from particles above and below 5/10 and 9/15 nm. This indicates the presence of several electronic junctions for the same sample. In a first, rough approximation, 3 × 2 different situations as a function of primary particle size for a MO<sub>x</sub>/TiO<sub>2</sub> or MS<sub>x</sub>/TiO<sub>2</sub> sample are possible. Most composite samples contain a single 2-phase (structural/electronic) contact situation. But for anatase materials in the 3–8 and 10–15 nm intervals, in the simplest case two anatase interfaces (among the three states displayed for anatase in Figure 7) are simultaneously present.

As mentioned, the contact between MO<sub>x</sub>/MS<sub>x</sub>/MSe<sub>x</sub>-anatase phases requires the equilibration of the Fermi level. But this is not as simple as it may be guessed for nanometric samples. This is due to the fact that surface defect-derived and band-type charge carriers do not always equilibrate and two, separate apparent Fermi levels can be rigorously defined.<sup>289</sup> This is further discussed in section 6 of this review. In addition, the whole electronic density of the system is not a simple sum of the 2-phase electronic structure due to interface effects. While still poorly understood, according to current thinking (mostly based on rutile-anatase interfaces) oxide–anatase contact either eliminates or strongly modifies deep-trap anion-vacancy donor anatase levels since they are not capable of giving radiative recombination upon light excitation.<sup>69</sup> This may be in turn related to the strong rearrangement of the interface region

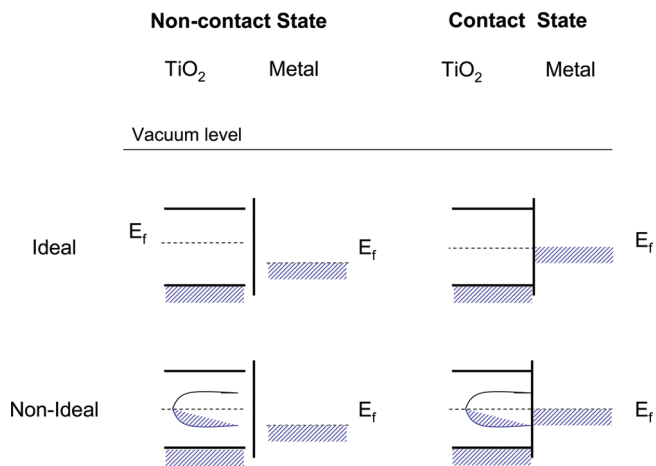


**Figure 9.** Electronic behavior of a metal–oxide nanocomposite system in either the presence or absence of surface states.

(0.5 nm) and the completion of the coordination spheres of the interface ions. Additionally, in the case of anatase/rutile contact, due to the presence of new anatase electron-trapping  $\text{Ti}^{4+}$  interface centers located below (0.8 eV), the conduction band seems also clear.<sup>99,116,118</sup> It can therefore be expected that such interfaces eliminate surface or near (0.5 nm) surface anion vacancies and produce new (4 fold-coordinated) Ti empty electronic states. As a result, appearance of midgap states is expected. This occurs together with the inherent (to amorphization) broadening of the electronic structure.<sup>82</sup>

The metal–anatase interface displays a somewhat simpler behavior than semiconductor-anatase systems. Typical noble metals such as Cu, Pt, Pd, Ag or Au maintain their metallic state when in contact with  $\text{TiO}_2$  surfaces irrespective of the metal particle size as long as it is in the nanometer range (e.g., >1 nm).<sup>21,22,53,154,156,157</sup> However, oxidation/corrosion and/or dissolution (the latter for liquid-phase reactions) of the noble metal particles during the photocatalytic operation are usually a problem for long-term use and stability.<sup>21,22,290</sup> Other metals (Cr, V, W etc.) albeit with uncertain oxidation states (mostly nonmetallic) have been also tested.<sup>291</sup> Similar to the chalcogenide–anatase systems, protection of the metal using core–shell nanoarchitectures containing  $\text{SiO}_2$  used to limit metal– $\text{TiO}_2$  direct contact and subsequent oxidation upon light excitation under reactive atmospheres have all been shown to be effective.<sup>155</sup> Nanometric metal particles absorb visible light through surface plasmon resonances in a quantized fashion. Their size dependence can be analyzed according to the Mie theory.<sup>292</sup> This allows the buildup of oxide (non- $\text{TiO}_2$ )-supported systems for running photocatalytic reactions using sunlight-type excitation.<sup>293</sup> As the result of an ideal contact with anatase, the (apparent) Fermi level of the nanocomposite undergoes equilibration as demonstrated in Figure 9. Due to the relative semiconductor and metal work functions, this happens as a result of electronic flow from the anatase toward the metal, ending in a local configuration where the surface of the metal acquires an excess negative charge while anatase exhibits an excess positive charge. A Schottky barrier forms between the anatase conduction band and the nanocomposite Fermi level. This can act as an effective charge trap upon illumination (section 6). In the presence of defect-associated gap states and typical surface states, the ideal Schottky behavior is not obeyed and the

deviation is measured in terms of the slope parameter  $S$  ( $S = d\Phi_b/d\Phi_N$ ; Figure 9). A phenomenological definition of the Schottky barrier height can be expressed by the following equation:

$$\Phi_b = S(\Phi_N - X_e) + (1 - S)\Phi_0 \quad (6)$$

In eq 6 the barrier height  $\Phi_0$  corresponds to the situation where the charge neutrality level of the continuum of defect states coincides with the Fermi level of the nanocomposite (at the interface),  $\Phi_N$  corresponds to the metal work function and  $X_e$  to the electron affinity of the semiconductor. This is turn is defined as the energy difference between the bottom of the conduction band and the vacuum level.<sup>294</sup> Limiting values occur for states exhibiting pure Schottky behavior ( $S = 1$ ) or when a pinning phenomenology occurs ( $S = 0$ ). Fermi level pinning ( $S \rightarrow 0$ ) is customarily tested by the constancy of the nanocomposite Fermi level position with respect to the vacuum level by varying either the work function or the Fermi level of the metal.

In addition to this, specific geometries where the metal is situated between two adequate oxides can show an effective enhancement of the electric field upon light excitation of the plasmon resonance with a significant oriented antenna-type characteristic at a local level. This can lead to a boosting of the photoactivity on condition there is correct handling of the phenomenon.<sup>155,295–297</sup> It should be noted that antenna effects require careful handling of the three-dimensional networking/assembly characteristics that occur among the components or particles of the materials in question. These effects promote the handling of the electric fields in such a way as to create strongly spatially oriented material light absorption and/or radiative de-excitation capabilities which are ruled by interparticle mechanisms. There are several geometries that are highly efficient in promoting light trapping by nanomaterials: (a) metals at surface positions emitting (scattered) light which is subsequently scattered and trapped in the semiconductor (if adequate multiple and high-angle scattering occurs, this causes an increase in the effective path length and hence leads to an enhanced absorption); those geometries leading to (b) light trapping through excitation of the surface plasmon polaritons at well-defined metal/semiconductor interface sites. This occurs in conjunction with a corrugated metal back surface (second metal phase) and allows the coupling of the incoming light with the “interface” (plasmon/photon) modes leading to propagation into the semiconductor. However, although these phenomena are known to occur in “ordered” systems and interfaces, their presence has not been proved rigorously in any high surface area, hence relatively “disordered”, materials. Further experimental studies and rationalization, as detailed in section 7, are needed in order to lead to a deeper understanding.

The correct assembly of the polymer–anatase interface can be also devised in order to allow sunlight absorption. This is achieved by not only using the polymer as a visible light sensitizer but, more specifically, creating adequate interface electronic states, e.g. electronic states of the nanocomposite (and not of the individual components) capable of absorbing visible light. This not only permits efficient sunlight absorption but also creates true “remote” photosystems. Such systems are capable of working without contact between the anatase phase and the pollutant mainly by transporting holes (the carrier leading to chemistry) throughout the nanocomposite system.<sup>135–138</sup> The potential of such “remote photocatalysts” remains, however, to be explored, particularly in the context of pollutant elimination or

partial oxidation, water or CO<sub>2</sub> valorization processes.<sup>298,299</sup> This will be briefly discussed in section 7.

**2.2.2. Single-Phase Anatase Systems.** M/A doping or impurity insertion into the anatase lattice generates two well-defined electronic situations as a function of the loading. The cutoff limit between these two situations is related to the modification of the essentially localized electronic levels obtained at low doping levels to the bandlike structure expected for samples where the overlap of many impurity electronic wave functions occurs. Complex structural situations, where a multitude of local geometries are possible, can lead to Urbach tails (typical of amorphous semiconductors)<sup>68</sup> which lie either above or below the conduction and valence band structures but without effective modification of the band gap. It is clear that a localized vs bandlike electronic density of states can have a strong differential effect on the charge carrier dynamics. Discussion regarding the specific situation after light excitation is in section 6 of this review.

The corresponding doping/impurity turning point on going from low to high doping level “regimes” can be reached in practice when the heteroion occupies a single position (e.g., high homogeneity) in the lattice and displays well-defined local order. In simple terms this can be expressed as specific M/A—O—M/A or A—Ti—A bonds at “interacting” distances (see below). Both conditions are only met as a result of a substitutional (not interstitial) doping process. It is only in this case that anatase samples showed a high solubility limit, as detailed earlier in section 2.1. The cutoff limit between these two “low/high loading” situations can be roughly estimated as being in the 2–5 atom % interval. Calculations for pure covalent semiconductors (Si, Ge) point to a concentration of ca. 1 atom %,<sup>300</sup> a value expected to be significantly higher for less covalent anatase oxide.

In the case of an extended or band-type density of states, the M/A-derived density of states produced by *N* impurity/doping ions is approximately Gaussian and proportional to *N*.<sup>68</sup> So, it is clear that in samples where the solubility limit can be as large as 10–20 atom %, the cutoff limit can be confidently reached. This situation is encountered with some M cations as outlined above. On the contrary, in the case of anion-doping processes, the low levels of doping, below 5 atom % in almost all cases, and the intrinsic heterogeneity of the samples, which always displays 2 or more substitutional/interstitial (the only exception is fluorine, which shows a solubility limit of ca. 1%), plus additional surface species, makes it almost impossible to achieve a dopant/impurity-derived band-type electronic density of states. As previously mentioned, specific preparative methods for N-containing samples as well as N,F-codoped and some S-doped materials appear to be the exceptions to this generalization.<sup>189,190,239–243</sup>

Generally speaking, apart from the localized or extended nature of the doping/impurity density of states, three additional general considerations must be taken into account when speaking about Ti—M/Ti—A/O binary solid solutions. First, when considering a M/A doping process, it is important to take into account that not only the M/A species contribute to a modified density of states with respect to anatase but also the entities corresponding to defects related to charge compensation. In some cases, the charge neutrality-derived defects can have their “own” electronic fingerprint, which can be easily distinguished from the corresponding M/A-derived density of states. As previously mentioned, this is occasionally observed when anion vacancies are created as charge compensation defects in the anatase lattice, particularly in the case of halogen-doping.

In general, interacting impurity-defect centers exist (e.g., are located at bonding distance below 5 Å) and a formal separation of the M/A and charge-compensation density of states is not possible. This appears to be particularly true in the case of cation doping where local M—O—[] ([] = cation vacancy) arrangements are detected; these indicate M—[] short interacting distances, well below 4 Å.

The second consideration concerns the structural homogeneity/heterogeneity of the sample. In the simple yet useful way of measuring heterogeneity within a single phase, the presence of M—O—M or A—Ti—A bonds or, in other words, of local order (described here simply as first order, second neighbor nature), must be considered in order to interpret the electronic effects derived from the doping/impurity process. With this in mind, an attempt to emphasize that local order beyond the first coordination shells appears to be the key to interpreting electronic structure in nanoanatase. It is clear that the presence of M—O—M or A—Ti—A bonds generates electronic states resembling the corresponding M- or A-containing-phases while this does not occur in highly homogeneous phases. Again, as a case study halogen (anion) doping is highlighted; here the simultaneous presence of A—O—A and A—O—Ti local arrangements has been shown to produce both unoccupied and occupied electronic states, respectively.<sup>238</sup>

The final general consideration concerns the presence of M or A at the surface. Even in the presence of a highly homogeneous binary anatase-type oxide, with no radial concentration profile, the presence of M/A isolated species at the surface generates a different surface chemistry. This is obvious, for example, in cases such as W or Mo cation-doping, where the presence of M=O bonds, not available for the single-phase anatase structure, is clearly detectable using Raman spectroscopy.<sup>19,112</sup> The presence of surface species in anion-doping materials acting as visible light sensitizers is another important example.<sup>248,251</sup> Speaking in a general way, the presence of M/A dopant/impurity species alters the surface chemistry and, most relevant to our context, the surface acidity/basicity. It is pertinent to add a brief note mentioning the case of ions suffering lixiviation and dissolution/readsoption processes in liquid-phase reactions. A typical case is that of Fe where such processes can add a “homogeneous” contribution to the photoactivity.<sup>301,302</sup>

**2.2.2.1. Low Doping Levels.** Several theoretical works have addressed the case of M-doping. Uebayashi et al. analyzed the substitutional doping process by first transition row elements (Figure 10).<sup>303</sup> Other recent studies of first-row (V, Cr, Mn, Fe)<sup>274,304–306</sup> second-row (Nb, Mo),<sup>274</sup> third-row (W),<sup>170,188</sup> lanthanide (Nd)<sup>307–309</sup> and other (Ge, Sn, Pb)<sup>310–312</sup> doping agents should be mentioned. For the first transition row, the states due to 3d dopants/impurities of importance in the context of this review shift to a lower energy as the atomic number increases. In the case of V, the impurity level is rather close to the conduction band and progressively moves apart up to Mn. Fe appears to modify the conduction band at low doping levels and both valence and conduction bands at high levels. Co “M—O” antibonding states appear to be close to the valence band, while in the case of Ni, this electronic state appears delocalized through the valence band. Both Mo and W occupy substitutional anatase positions and decrease the bottom end-ge of the conduction band by modifying the Ti 3d partial density of states (W) or by inducing new dopant-related (Mo) states.<sup>170,274</sup> Nd appears at substitutional positions and can modify the both the valence, but in particular the conduction, band end-ge.<sup>307,309</sup> Other metals such as Ca, Sn, Zr etc. are mostly irrelevant in the context of this

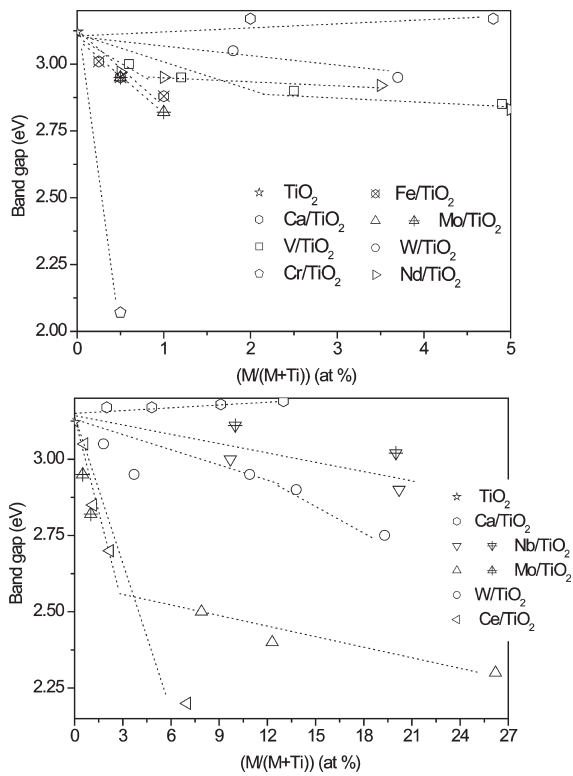


**Figure 10.** Low (top) and high (bottom) doping level effect on anatase band gap energy.

study as they do not alter or lead to a higher band gap energies than those corresponding to the bare anatase material. Sn may be a singular case as  $\text{Sn}^{2+}$  (not  $\text{Sn}^{4+}$ ) may produce localized gap levels near to or merging with the valence band.<sup>313,314</sup> The band gap modification seems, in any case, modest. In this low-doping level region, and taking into consideration that the new electronic states are essentially localized unless there is overlap with the main valence and conduction bands of the solid, the available theoretical information indicates that V, Ni, Mo, W and Nd are candidates able to “merge” adequately with the bare anatase electronic states. Fe is, as mentioned previously, a special case, due to the potential simultaneous presence of several structural states driven by the presence or absence of  $\text{Fe}-\text{O}-\text{M}/\text{Fe}-\text{O}-[]$  ( $\text{M} = \text{Ti}, \text{Fe}$ ) contacts and surface enrichment. The remaining cations already mentioned should lead to localized electronic states. It should be noted that a significant number of transition/lanthanide cations (e.g., Fe, Co, Cr etc.) could additionally display d–d or f–f intra-atomic transitions upon visible light excitation, but such processes are essentially irrelevant in the current context except for the decrease in the number of photons (light intensity) with potential for light to chemical energy conversion.

It can be deduced from experimental information that at low loading Ni produces localized gap states.<sup>177,315</sup> Only in the cases of V, Mo, W and Nd is there combined experimental/theoretical data that confirms that there is a reduction in the band gap. Where Fe, Cr, Nb and Mo doped systems are concerned, there is also experimental information available which, from a structural point of view, differs from the somewhat “simple” models considered by theoretical calculations. It is possible, therefore, to divide cations at low doping levels into two categories: those

that give rise to localized gap states and those leading to electronic states that merge with the anatase bands. As explained previously, the majority of ions would lie within the first category. Only in the case of V, Mo, W and Nd is there, at least to some extent, a complete experimental/theoretical range of information that allows a definitive allocation to the second category.

The anatase band gap measurements as a function of the M dopant/impurity concentrations are shown in Figure 10 (upper panel).<sup>19,113,162,163,170,172,174,177,178,309,316–319</sup> The oxidation chemical states of V ( $\text{V}^{4+}$ ), Fe ( $\text{Fe}^{3+}$ ), Nd ( $\text{Nb}^{5+}$ ), Mo ( $\text{Mo}^{6+}$ ), W ( $\text{W}^{6+}$ ) and Nd ( $\text{Nd}^{3+}$ ) that are present on the anatase lattice appear consistent with the rule that they all (with the exception of Nd) have similar ionic radii to  $\text{Ti}^{4+}$  (e.g., control of strain into the anatase structure). In all cases, however, the ions occupy substitutional positions. Doping with Nb requires the handling of the oxidation chemical state to give a formal charge approaching a +5 state. This particular electronic situation is not present in any single-phase Nb-oxide structures. Experimentally it was observed that V atoms located principally in the substitutional positions of anatase have a  $\text{V}^{4+}$  chemical state. Ions located at the surface, on the other hand, display a  $\text{V}^{5+}$  oxidation state. Cr, as previously mentioned, requires the involvement of two chemical states, namely, the  $\text{Cr}^{6+}$  and  $\text{Cr}^{3+}$ , together with the anion vacancies. Although Fe is also a complex case, the presence of a single oxidation state ( $\text{Fe}^{3+}$ ) and a near constant band gap value as a function of the doping level are typically observed. However, the differences between samples that are observed are mostly concerned with structural variables, as previously mentioned. In the presence of  $\text{Cr}^{3+}/\text{Fe}^{3+}/\text{V}^{4+}$  chemical states at substitutional positions, a strictly low solubility limit is assumed: well below 3 atom %. Expect for Cr and, possibly, Mo, a small band gap shift of less than 0.1–0.2 eV is always detected (Figure 10; upper panel). Nb, Mo and W display larger solubility limits but at low concentration levels these cations display the moderate band gap decrease trends as shown in Figure 10 (upper panel). The maximum band gap decrease roughly correlates to an absorption onset below 430 nm and a corresponding use of less than ca. 20% of the visible light content of the solar spectrum.

In the case of anion (A) doping, as mentioned previously, we are mostly dealing with a low loading level for substitutional/interstitial species. This means, therefore, that unless the appropriate mixture with anatase band electronic states occurs we are dealing with localized electronic states. Figure 11 summarizes the theoretically described electronic states for N, F, C, S, and N,F codoping in the presence of the corresponding vacancy/defects needed to ensure charge neutrality.<sup>193,212,213,215,219,221,222,225,229,242</sup>

As can be observed from the data shown in Figure 11, irrespective of whether or not they are in substitutional or interstitial positions, N-doping always produces occupied states responsible for electronic transitions with an energy 0.0–1.0 eV above the valence band. Essentially, up to three types of states at ca. 0.0–0.2, 0.5–0.6 and 0.8–1.0 eV can be observed in nitrogen-doped samples.<sup>75,193</sup> Asahi and co-workers suggested that the overlapping of some of these levels with the valence band can occur, but this does not appear to be the general case for all N-doped systems synthesized.<sup>192,320</sup> There is, however, a general consensus that substitutional species produce the low energy gap states. Experimentally, there is evidence of electronic states associated with nitrogen species but also with oxygen vacancies (and/or oxygen local structures).<sup>6,75,192–205</sup> In the cases of a solid having a significant number of anion-related defects, this number is not correlated with the N content of the solid.<sup>203–207</sup>

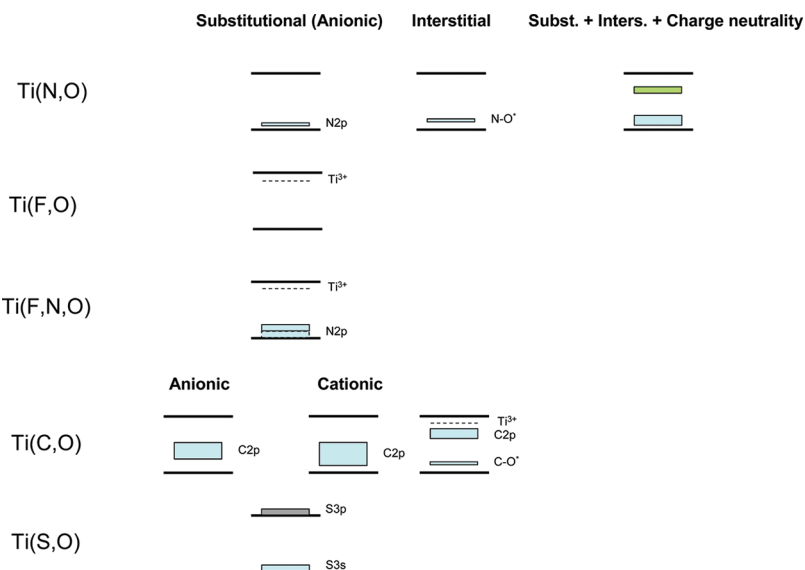


**Figure 11.** Electronic effects of N and/or F, C and S doping species on the anatase electronic structure. Valence and conduction bands are represented by their top and bottom edges, respectively.

The seminal work of Pacchioni, Serpone, Rodríguez and other groups essentially suggests the localized nature of the majority of the near valence band states.<sup>6,75,194,198,200,203,206</sup> On the other hand, others indicate the additional presence of quasi-continuum electronic states around/below ca. 2.5 eV from the top of the valence band.<sup>203,205,321</sup> It should be additionally noted that the absence of  $\text{Ti}^{3+}$ -type electronic states in N-doped samples is the most apparent difference compared with bare  $\text{TiO}_2$  materials. So, to summarize, it appears that both occupied nitrogen- and oxygen-vacancy related midgap states near the valence band as well as some empty or partially occupied states near the conduction band can be observed in N-doped anatase samples. Figure 11 ascribes the experimentally observed states to simple structural states although it should be noted that the fine details of such an assignment would require further work.

With fully occupied gap states C presents a somewhat similar situation to N.<sup>213,322</sup> As pointed out earlier, we lack a full understanding of C-derived electronic effects due to the strong interactions present between carbon impurities and the corresponding anion vacancies (derived from electroneutrality).<sup>212,215</sup> However, it appears that interstitial species can allow a decrease in the anatase band gap if the doping level is high enough.<sup>212–215</sup> Fluorine also introduces localized states,  $\text{Ti}^{3+}$  in nature, into the gap, close to the conduction band.<sup>218,219</sup> As discussed above, halogens (e.g., I) can induce in-gap states near both the valence and conduction bands. These are possibly in correspondence with two local ( $\text{I}-\text{O}-\text{I}$  vs  $\text{I}-\text{O}-\text{Ti}$ ) structural states and lead apparently to light absorption of up to ca. 800 nm.<sup>235–238</sup> In contrast to these cases, B-related levels seem to be buried at the bottom of the valence band. This is concomitant with an absence of noticeable effects on visible-light absorption properties.<sup>229</sup> The coexistence of B and N at interacting distances can, however, produce an effective decrease in the band gap if the adequate structural situation (mainly driven by B at interstitial positions) is reached.<sup>249</sup> A different case is encountered in the case of S-doping; here there is a strong overlap of S3s impurity-derived electronic states and the top of the valence band has been predicted for substitutional doping.<sup>222</sup> This appears to be the

only case where an effective modification of the valence band is observed upon anionic doping at relatively low concentration levels (ca. 4 atom %).

**2.2.2. High Doping Levels.** The introduction of a large number of dopants, always into substitutional positions, not only produces a Gaussian-like band-type electronic density of impurity-derived states but can concomitantly perturb the shape of the conduction and valence bands. Bonc-Bruyevich has shown the conduction band edge to “tail” into the forbidden band.<sup>323</sup> If the M cation is judiciously chosen to merge with either the conduction (most typical case) or valence band tails, a modulation of the band gap energy as a function of the M content of the solid is thus possible. This allows the engineering of anatase-type materials with adequate properties, particularly electronic ones, which, at the same time, display only limited modification with respect to the parent oxide.<sup>19,110,111,170</sup> This should, therefore, produce anatase-type materials with almost all the charge-handling properties of the unmodified oxide but also having a non-negligible absorption power into the visible region of the solar spectrum.

As detailed in section 2.1, those cations with solubility limits well above 5 atom % and thus able to produce band-type electronic states are Ni, Nb, Mo, Sn, Zr, W, Ce and Nd. All these cations are found in substitutional anatase positions. As discussed in section 2, although some other cations such as Ca, Ba or Sr can display high solubility limits, they also destroy the anatase structure. Ni, Mo, Ce and Nd-doped materials display variable solubility limits.<sup>110,171,177,178,182,183,324</sup> Also, as previously discussed, several structural (strain; local-middle ordering) and/or electronic (oxidation state) characteristics that define doped systems, as,  $\text{Fe}^{2+}$ <sup>317</sup> or Cr, respectively,<sup>186,325</sup> make such cases very difficult to decide whether real mixed oxides exist above the 5 atom % level. In spite of this fact, band gap decreases of 0.5 (Fe) or 0.9 (Cr) eV are claimed for samples containing a doping level of 6 (Fe) or 10 (Cr) atom %.<sup>304,325</sup> In the case of Cr, such doping levels require an exhaustive control of the oxidation state, but such a claim seems rather dubious for Fe-containing materials.

In the bottom panel of Figure 10 the experimental measurements for the corresponding anatase-type material band gaps as a function of the M (Ca, Sr, Ba, Ni, Nb, Mo, Sn, W, Ce and Nd)

content are presented.<sup>19,113,162,163,171,178,309,310</sup> Three different states can be encountered. Typically Ni is an example of the first as it produces midgap states.<sup>171,177</sup> The presence of gap states into the band gap region would open a two-photon (of relatively low energy; below 2 eV) scheme to optimize the absorption of sunlight. The second situation encloses cations, e.g. alkaline metals and Sn or Zr which produce a widening of the band gap and are thus not relevant in the current context. The remaining cations should lead to a reduction in the band gap energy. Typically Ce and Nd (again) raise doubts about the solubility limit (beyond 10 atom %) point. Nd does not significantly alter the anatase band gap at high concentration levels. The Ce (structural) case was discussed in more detail in section 2.1.2, but it should be noted that it can produce important effects on the band gap even for doping levels below 10 atom %. The remaining above-mentioned cations all diminish the band gap. According to theoretical calculations, they mostly achieve this by altering the conduction band end-ge.

In Figure 10 (bottom panel), Ce and Nb (and also Ca) appear to present a single linear region of the band gap energy as a function of the M content. On the other hand, Mo and W appear to present two. This behavior appears intimately linked with the structural characteristics of the Ti–M binary oxides. In the case of Nb, the structural situation appears to dismiss excessive changes as a function of the M content of the material due to the presence of strong local ordering effects. These favor the presence of Nb-rich entities at the bulk or surface (depending on the study and, for example, the preparative method used) of the material even for limited Nb concentrations (below 10 atom %). The Mo structural situation dramatically changes as a function of the M content due to the presence of surface enrichment for samples having a M content above 8–10 atom %. Finally, W only suffers the presence of a different local environment for samples having ca. 15 atom %; presumably this is due to a modest W local enrichment at the grain boundaries. The structure–electronic link seems, therefore, to manage the band gap behavior and predict the presence of one or two regions where the linear gap energy vs M content relationship is observed.<sup>19,112</sup> This is in agreement with the theoretical expectations based on the formation of a binary oxide with a unique local arrangement for the M cation in the substitutional positions of the anatase lattice. Small variations of this local arrangement seem to govern the slope variations. Therefore, structural information used to interpret the electronic information is concerned with not only the M lattice position as well as the charge compensation defects but also the local-middle order properties.

Varying the M content of the anatase-base solid it is therefore possible to manage the absorption power of the material in the visible part of the solar spectrum. Data for Nb alone shows a modest enhancement of the visible light absorption power, whereas Mo, W and Ce on the other hand all allow the absorption of photons with wavenumbers up to 500 or 550 nm. Considering therefore that the maximum of the solar spectrum into the visible region is at 500 nm, then these three cations appear to be the optimum cases, although, as pointed out, Ce may present a relatively “low” solubility limit for the anatase structure. The reduction of the conduction band end-ge can, therefore, be modulated as a function of both the nature and content of M in order to obtain the optimum visible-light absorption power. However, this has to be done without jeopardizing the formation of oxygen radicals. These are necessary in order to run oxidation reactions under continuous operation mode, through maintaining

the conduction band end-ge above the O<sub>2</sub> affinity level (O<sub>2</sub>/O<sub>2</sub><sup>-</sup>). This indicates that reducing the band gap below ca. 2.5–2.7 eV (ca. 470–480 nm) means loss of interest for general, practical applications. A simple approach which could minimize this problem relies on the use of (additional) isolated surface-ion species which may be able to capture electrons and thus can supply adequate redox potential for activating oxygen.<sup>326</sup>

As previously mentioned, some reports indicate the need for large doping concentrations (either close to or above 10 atom %) for N-doping in specific cases where notable changes in the valence band onset are subsequently observed.<sup>189,190</sup> The presence of such high dopant content leads to the concomitant formation of oxygen vacancies. In addition, gap states with significant chemical consequences on light absorption are typically produced. Figure 11 summarizes results with respect to the presence of localized states for substitutional/interstitial N-doping at low concentrations as well as the more “real world” situations. In the latter both types of species are present together with a number of oxygen-related empty states.<sup>190–207</sup> The potential for N (and also S and C) to be used in order to manage band gap energies at high doping levels has been theoretically addressed. Results show that anion-doping should be able to produce large energy variations (near 1 eV).<sup>327</sup>

It appears that those cases where high loaded samples are customarily obtained correspond to cases involving N,F-codoping and, to a lesser extent, S-doped materials, whereas the remaining systems apparently lead to localized gap states as described in Figure 11. Theoretical reports dealing with the N,F system indicate the presence of fully occupied N-derived gap states close to and/or merging with the valence band as well as the additional presence of Ti<sup>3+</sup> states near the conduction band.<sup>242</sup> The electronic structure resembles that of N-doped systems although here some incipient bandlike characteristics are expected for the impurity-derived electronic density of states near the valence band.<sup>239–242</sup>

As described in Figure 11, sulfur doping is also expected to lead to band gap modification for the higher impurity levels achievable (4 atom %). But to date, the only unquestionable confirmation for this is theoretical data due to the well-known heterogeneity of the anion-doped materials.<sup>225</sup> Finally, an alternative to anion-doped materials could be a two-photon absorption process, but the complex structural situation encountered in such materials limits any clear statement at this point.

### 3. THIRD GENERATION PHOTOCATALYSTS: A<sub>x</sub>B<sub>y</sub>O<sub>z</sub> AND NEW NONOXIDIC PHOTOCATALYSTS

As already stated, solar photocatalysis is expected to be the ideal green technology for several environmental areas and particularly for the sustainable management of a range of waste materials. A visible-light photoactive material has long been anticipated and pursued over recent decades. Recent TiO<sub>2</sub>-based attempts to tackle this challenge were evaluated in the previous sections. Although the actual doping method and the nature of the nanocomposite systems appear to be serious alternatives, they are not without drawbacks as efficient visible-light-responsive TiO<sub>2</sub>-based photocatalysts. Therefore, new and/or more efficient visible-light photocatalysts are being sought with a view to meeting the requirements of future environmental and energy technologies driven by solar energy.

As Kudo et al. pointed out, suitable band engineering is needed in order to develop new photocatalysts for visible light

applications.<sup>328</sup> The band tailoring of inorganic semiconductors can be undertaken using different approaches: (i) the creation of discrete electronic levels between the valence and conduction bands (this is normally achieved by doping or codoping in the case of oxides); (ii) the creation of a new valence band through the synthesis of novel compounds; (iii) the formation of solid solutions exhibiting band gap values intermediate between those of the parent materials. Within this context, a research strategy has emerged in recent years that considers a new set of materials unrelated to TiO<sub>2</sub>. Generally speaking, single phase photocatalysts are more stable than the corresponding doped ones. On the other hand, they might be expected to possess fewer defects and therefore fewer potential electron–hole recombination centers. The result is that these single phase systems would be expected to be more effective for carrier separation and migration to the surface and the subsequent generation of the necessary chemistry.

In this context, and contrary to the traditional TiO<sub>2</sub>-based photocatalysts, surface area does not represent a determinant parameter. This is a common feature for most of the systems discussed in this section. In contrast, the structural and electronic configurations of these alternative photocatalysts emerge as the key characteristics.

A large number of alternative photocatalysts, incorporating the above-mentioned features and exhibiting a great variety of compositions and structures, have been proposed. Most of these novel systems have also been used for water splitting and H<sub>2</sub> production.<sup>329</sup> In addition, many results indicate good photocatalytic behavior for pollutant degradation. In a first analysis, as has been already mentioned, the principal difference with respect to doped TiO<sub>2</sub> is the role of the surface area and its minimal influence on the photocatalytic activity. On the other hand, another important point that should be stressed is that in most cases the photocatalytic experiments reported were carried out using only visible radiation ( $\lambda > 400$  nm) rather than UV or sunlight. Thus, the comparison with TiO<sub>2</sub>-based systems becomes difficult. It becomes, therefore, somewhat complicated to ascertain whether or not these single phase photocatalysts are in fact a real alternative to TiO<sub>2</sub> for solar applications. Hence, both issues will be discussed in sections 6 and 7.

In brief, the types of new materials under investigation for photocatalytic applications exhibit different crystalline structures. Among these are perovskite (A<sup>2+</sup>B<sup>4+</sup>O<sub>3</sub>), perovskite-related materials, A<sup>3+</sup>B<sup>5+</sup>O<sub>4</sub> compounds with scheelite structures (such as some tungstates, molybdates or vanadates) and even iron spinels (AB<sub>2</sub>O<sub>4</sub>). In particular, perovskite-like compounds are stable structures which form solid solutions with a range of metal ions. Hence they are considered promising solids for the chemical substitution of TiO<sub>2</sub> with a view to achieving the appropriate band engineering and consequent band gap lowering required.<sup>330,331</sup> Furthermore, new nonoxidic structures such as nitrides and sulfides have emerged as promising alternatives for TiO<sub>2</sub> for both photocatalytic oxidation and water splitting reactions.

The availability of such a great variety of compounds and structures opens up a wide range of possibilities for visible light driven photocatalytic applications. In this section we endeavor to present the scope of alternative photocatalysts in terms of their crystalline structures. A brief and necessary description of each structure together with synthesis protocols as well as their photocatalytic behavior will be included.

### 3.1. Perovskite Structure

The perovskite oxide structure with the general formula ABO<sub>3</sub> is a frequently encountered structure in inorganic chemistry. This

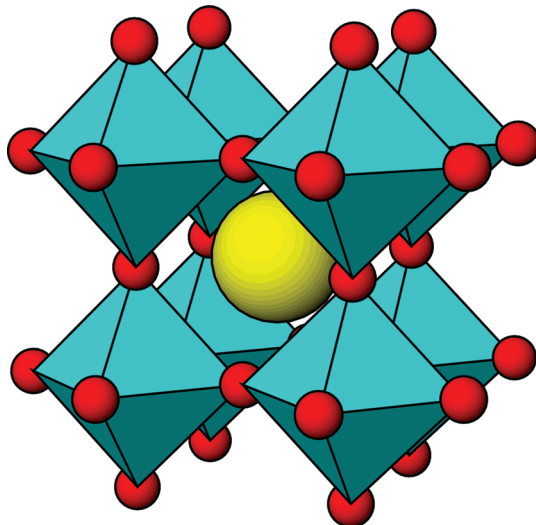


**Figure 12.** Ideal cubic perovskite structure for ABO<sub>3</sub> (cyan, BO<sub>6</sub> units; yellow, A atoms).

structure can accommodate most of the metallic ions in the periodic table together with a significant number of other anions. An ideal perovskite structure has an ABO<sub>3</sub> stoichiometry and a cubic crystal structure (Figure 12). The cubic cell is composed of a three-dimensional framework of corner-sharing BO<sub>6</sub> octahedra. The B-site cation is a transition-metal element.<sup>332</sup> The A-site cation occupies the 12 coordinate position formed by the BO<sub>6</sub> network and often consists of an alkaline-earth metal element or a rare earth element. For this geometrical configuration the following relationship can be proposed:

$$(r_A + r_O) = \frac{\sqrt{2}}{2} a = \sqrt{2}(r_B + r_O) \quad (7)$$

Although the primitive cube is the idealized structure, the differences in radii between both cations can in fact distort the structure. This normally involves tilting the BO<sub>6</sub> units (octahedral tilting). Goldschmidt's tolerance factor describes the deviation of the perovskite cubic basic structure.

$$t = \frac{(r_A + r_O)}{\sqrt{2}(r_B + r_O)} \quad (8)$$

For an ideal cubic perovskite,  $t = 1$  and the A–O and B–O bond distances perfectly matched. Most perovskites have  $t < 1$ , and hence the structures are distorted. Thus, perovskite-related structures arise from the loss of one or more of the symmetry operators of the basic cubic structure. The substitution of multiple cations into the A- or B-sites would expand the compositional space that can be explored. Such substitutions can alter the symmetry of the pristine structure and hence the physical properties. Because of this great flexibility inherent in the perovskite structure, there are many different types of distortions of the ideal structure. These include octahedral tilting (tilting of the octahedra), displacement of the cations out of the center of their coordination polyhedra and distortions of the octahedra driven by electronic factors (i.e., Jahn–Teller distortions). Many of the physical properties of perovskites depend crucially on the precise details of these distortions. In particular, the electronic,

magnetic and dielectric properties, which are so important for many of the applications of perovskite materials, are affected.<sup>333</sup>

A multitude of examples can be found in the recent literature concerning the use of perovskite compounds in photocatalytic degradation reactions. One interesting example is related to bismuthate compounds. Bismuth can be stabilized in its highest oxidation state by using binary metal oxides such as  $\text{MBiO}_3$  ( $\text{M} = \text{Li}, \text{Na}, \text{K}, \text{Ag}$ ). In most cases these will have the perovskite structure. Recently, Kako et al.'s group investigated the photocatalytic decomposition of organic compounds such as methylene blue using  $\text{NaBiO}_3$  under visible light irradiation.<sup>334</sup> They claim that  $\text{NaBiO}_3$  is relatively stable under visible light irradiation even in aqueous solution. The compound  $\text{BaBiO}_3$  reported by Tang et al.<sup>335</sup> exhibits an ordered perovskite structure (monoclinic space group  $I\bar{1}2/m1$ ) with two kinds of distorted octahedra, namely,  $\text{Bi}'\text{O}_6$  and  $\text{Bi}''\text{O}_6$ . Bismuth is present in these and has 3+ and 5+ valencies coexisting in the same compound.<sup>336</sup> The absorption of this material increases until 650 nm. Although the specific surface area is extremely low ( $1.2 \text{ m}^2/\text{g}$ ), the photoactivity for methylene blue degradation is significantly higher than for  $\text{TiO}_2$  under visible irradiation. This photocatalyst also demonstrated high stability in gas phase reactions but photocorroded in aqueous solutions.

Other examples of perovskite-structured materials are related to the ferrite family ( $\text{LaFeO}_3$ ,  $\text{SrFeO}_3$ ,  $\text{BaFeO}_3$  and  $\text{BiFeO}_3$ ).<sup>337–340</sup> Lanthanum ferrite was synthesized by means of a traditional sol–gel method.<sup>339</sup> After calcination at 500 °C this “soft” method yields a relatively high surface area ( $21 \text{ m}^2/\text{g}$ ). The best photocatalytic behavior for rhodamine B degradation is obtained for this calcination temperature; it decreases as the calcination temperature increases. Results from surface photovoltage (SPS) and photoluminescence spectroscopies (PL) clearly indicate that the weaker the SPS and PL signals obtained, the higher the photocatalytic activity. In this case, the surface area, together with an adequate structural and electronic configuration of the catalysts, leads to the best photocatalytic behavior. The strontium ferrite was obtained using a combustion method followed by sintering at 800 °C. Yang et al. described its photocatalytic properties in methyl orange degradation. They related the observed properties to the existence of  $\text{FeO}_6$  units with  $\text{Fe}^{4+}$ .<sup>338</sup> However, they also reported the instability of such units under UV irradiation with concomitant formation of the corresponding carbonates. Another ferrite example is the bismuth ferrite ( $\text{BiFeO}_3$ ). This has been synthesized using different methods such as microwave, sol–gel and hydrothermal methods. Syntheses lead to nanocubes of about 50–200 nm size and a band gap of 2.1 eV.<sup>340–342</sup> It should be noted that these kinds of materials exhibit an important magnetic ordering which leads to interesting multifunctionality. In this context, Li et al. demonstrated that both magnetic and optical properties seem to depend on the morphology and size of the particles.<sup>342</sup> Therefore, it is possible to propose  $\text{BiFeO}_3$  microcrystals as a multifunctional “device” which combines magnetic, electronic and optical properties. In synthesizing  $\text{BiFeO}_3$ ,  $\text{Bi}_2\text{Fe}_4\text{O}_9$  was frequently observed as being present as an impurity phase. Its structure is orthorhombic, and it belongs to the family of mullite-type crystal structures.<sup>343,344</sup> The  $\text{Bi}_2\text{Fe}_4\text{O}_9$  unit cell contains two formula units with evenly distributed  $\text{FeO}_6$  octahedral and  $\text{FeO}_4$  tetrahedral forms. The  $\text{Bi}^{3+}$  ions are surrounded by eight oxygen ions with mutually orthogonal shorter  $\text{BiO}_3$  and longer  $\text{BiO}_5$  units. It is well-known that the material  $\text{Bi}_2\text{Fe}_4\text{O}_9$  is a semiconductive material with gas sensing and catalytic properties. Recently some authors

reported the photocatalytic performance of such compounds in the degradation of organic contaminants under visible irradiation.<sup>345,346</sup> In both cases, different morphologies can be achieved by controlling the parameters of the hydrothermal synthesis. Thus, microplatelets and nanosheets can be obtained by controlling the  $\text{Bi}^{3+}/\text{Fe}^{3+}$  molar ratio as well as the  $\text{NaOH}$  concentration. The most interesting result, reported by Ruan et al., refers to the differential photocatalytic behavior observed as a function of the final morphology. So, while microplatelet and nanosheets appear to be photoactive under UV irradiation, nanosheets produce a higher photocatalytic performance under visible irradiation.<sup>345</sup> Similarly, Sun et al. reported the preparation of flowerlike  $\text{Bi}_2\text{Fe}_4\text{O}_9$  using a hydrothermal method. It exhibited visible photoactivity in phenol degradation.<sup>346</sup> They confirmed that the flowerlike particles preferentially grow along the [100] plane. This anisotropic growth can be ascribed to the specific  $\text{Bi}_2\text{Fe}_4\text{O}_9$  structure. From the classic model for crystal shape equilibrium, the Gibbs–Curie–Wulff theorem suggests that the shape or morphology of a crystal is determined by the relative specific surface energy of each face or facet of the crystal. Accordingly, the growth rate of a particular facet is inversely proportional to the atom density of the respective plane. The orthorhombic structure for  $\text{Bi}_2\text{Fe}_4\text{O}_9$  clearly demonstrates that the [100] planes present the highest atom density so the growth rate along this direction would be the slowest leading to the platelike structure (mentioned above), with preferentially exposed [100] planes. This particular morphological structure seems to be related to the enhanced photoactivity shown.

Even more complex systems can be derived from substitutional perovskite structures. From the initial perovskite structure a double perovskite can be developed by the substitution of one of the original perovskite cations (A or B); this leads to either the  $\text{AA}'\text{BO}_3$  or  $\text{ABB}'\text{O}_3$  structures. This kind of cationic substitution can of course alter the photophysical properties of the system and enhance the visible absorption. This is the situation for the  $\text{Ba}(\text{M}_{0.5}\text{Sn}_{0.5})\text{O}_3$  system as reported by Borse et al.<sup>347</sup> The incorporation of Ti, V, Cr, Zr and Ce into the Sn position is found to produce a clear improvement in the photocatalytic features, and a band gap even lower than 2.5 eV is achieved in some cases. The presence of 3d, 4d, 4f or 6s orbitals, depending on the substitution, contributes to the bottom of the conduction band, which in turn leads to a narrowing of the band gap of the unmodified  $\text{BaSnO}_3$ . A similar approach was reported by Hur et al. for  $\text{BaInO}_3$  perovskite. They substituted the indium cations by Sn, Pb, Nb and Ta forming a complex structure of the type  $\text{Ba}(\text{In}_{1/3}\text{M}_{1/3}\text{M}'_{1/3})\text{O}_3$  ( $\text{M}, \text{Sn}, \text{Pb}; \text{M}', \text{Nb}, \text{Ta}$ ).<sup>348</sup> In this case, the incorporation of electronegative non-transition metal cations into a wide-band gap material such as  $\text{BaInO}_3$  leads to a narrowing of the band separation. From a study of the MB and 4-chlorophenol photocatalytic degradation reactions they concluded that the Pb-substituted perovskite showed the highest photoactivity under UV–vis and visible irradiation. The higher electronegativity of the  $\text{Pb}^{4+}$  cation is directly responsible for the lowest band gap value. This is due to the participation of Pb 6s in the conduction band. On the contrary, tin-substituted or pristine  $\text{Ba}(\text{In}_{1/2}\text{M}'_{1/2})\text{O}_3$  showed no photocatalytic activity under visible irradiation.

Another structural possibility corresponds to quadruple perovskites structures. Here both the A and B cations of the structure can be substituted by equivalent cations resulting in a perovskite with the empirical formula  $\text{AA}'\text{BB}'\text{O}_3$ . One example of this structure was reported by Wang et al.<sup>349</sup> They examined

the photocatalytic behavior of the Sr and Ti substituted  $\text{AgNbO}_3$  materials ( $(\text{Ag}_{1-x}\text{Sr}_x)(\text{Nb}_{1-x}\text{Ti}_x)\text{O}_3$ ) in the decomposition of acetaldehyde under visible light ( $\lambda > 400 \text{ nm}$ ). In spite of the pronounced low specific surface area (approximately  $1 \text{ m}^2/\text{g}$ ) shown by this system, a calculated quantum yield of 1.48% (at  $\lambda = 440 \text{ nm}$ ) was observed. As mentioned previously, a low surface area value is a common feature of most of these novel systems.

### 3.2. Perovskite-Related Structures

In addition to the “ideal” perovskites just discussed, there are other relevant perovskite-related compounds that are derived from the presence of either anion excess (Dion–Jacobson phases), anion deficiency (brownmillerite,  $\text{A}_2\text{B}_2\text{O}_5$  as  $\text{Sr}_2\text{Fe}_2\text{O}_5$  or  $\text{Ca}_2\text{Fe}_2\text{O}_5$ ) or even the incorporation of other components into the structure (Ruddlesden–Popper and Aurivillius phases).

Within this perovskite-related family, a number of layered variants of the perovskite structure are also known. The most common layered perovskites are the Aurivillius phases (with the general formula  $(\text{A}_{n-1}\text{B}_n\text{O}_{3n+1})^{2-}$ ), the Ruddlesden–Popper phases (with the general formula  $\text{A}_{n+1}\text{B}_n\text{O}_{3n+1}$ ; Figure 13) typified by  $\text{Na}_2\text{La}_2\text{Ta}_3\text{O}_{10}$ ; and the Dion–Jacobson phases (with the general formula  $\text{A}_{n-1}\text{B}_n\text{O}_{3n+1}$ ; Figure 14) as  $\text{RbLaNb}_2\text{O}_7$ , where, in all cases,  $n$  represents the number of the perovskite-like layers.

Some ion-exchangeable layered perovskites, Dion–Jacobson-type niobates and Ruddlesden–Popper-type titanates (and their reduced-charge forms) are known to show photocatalytic activity in water splitting as well as  $\text{H}_2$  and/or  $\text{O}_2$  evolution from water containing sacrificial reagents.<sup>350–352</sup>

Among these perovskite-related classes, Aurivillius phases can be considered the most successful in providing significant photocatalytic results. For this reason Aurivillius structures will be described separately.

### 3.3. Aurivillius Phases

The Aurivillius phase was first reported by Aurivillius in 1949 and consists of  $n$  perovskite-like layers ( $\text{A}_{n-1}\text{B}_n\text{O}_{3n+1})^{2-}$ ) sandwiched between fluorite-like A–oxygen sheets ( $\text{A}_2\text{O}_2)^{2+}$ <sup>353</sup> (Figure 15). The A and B sites can accommodate a great variety of cations from (A) Na, K, Ca, Sr, Ba, Bi, etc. to (B): Fe, Cr, Ti, Ga, Nb, V, Mo, W, etc.

More recently, many Aurivillius-based compounds have been reported which exhibit interesting properties suitable for photocatalytic applications. Of these,  $\text{Bi}_2\text{WO}_6$ <sup>354–358</sup> is the simplest and probably the most studied example within this family. In this bismuth tungstate, the perovskite-like structure is defined by  $\text{WO}_6$  units which form a layer perpendicular to the 100 direction and sandwiched between the  $(\text{Bi}_2\text{O}_2)^{2+}$  units.

A hydrothermal synthetic procedure has been widely reported in the literature as an alternative to traditional solid state reactions for obtaining  $\text{Bi}_2\text{WO}_6$  Aurivillius-phase compounds.<sup>359,360</sup> The exact experimental conditions employed in the hydrothermal synthesis as well as the use of surfactants have been shown to exert a great influence on the morphology and shapes of the particles obtained. Flowerlike, tirelike, sheet or square nanoplates can all be created. It is clear that this new synthetic route provides compounds with better photocatalytic behavior, although, in certain cases, the specific surface areas are not significantly higher with respect to those obtained by solid state pathways. Interestingly, further calcination after the hydrothermal step leads, in almost all cases, to a dramatic loss in the surface area. Thus, the formation of 3D or 2D superstructures appears to be responsible for the enhancement in the photocatalytic performance.<sup>356,358,361,362</sup>

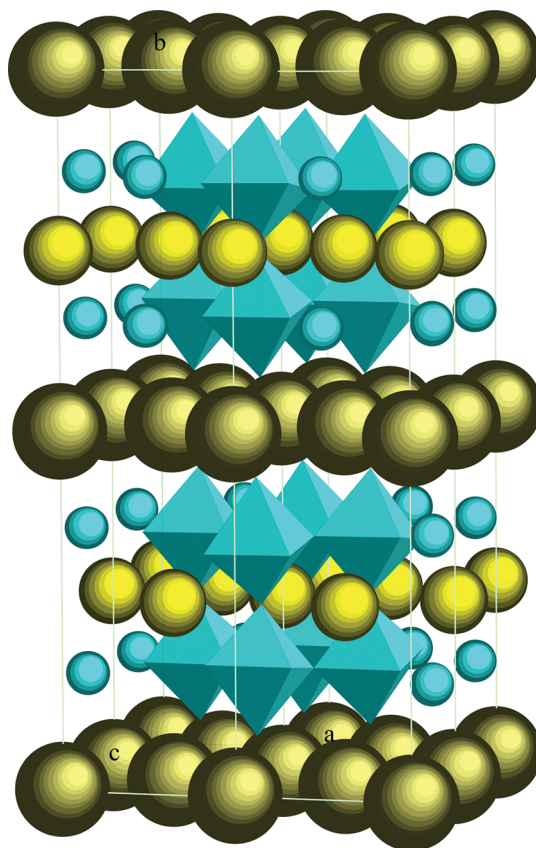
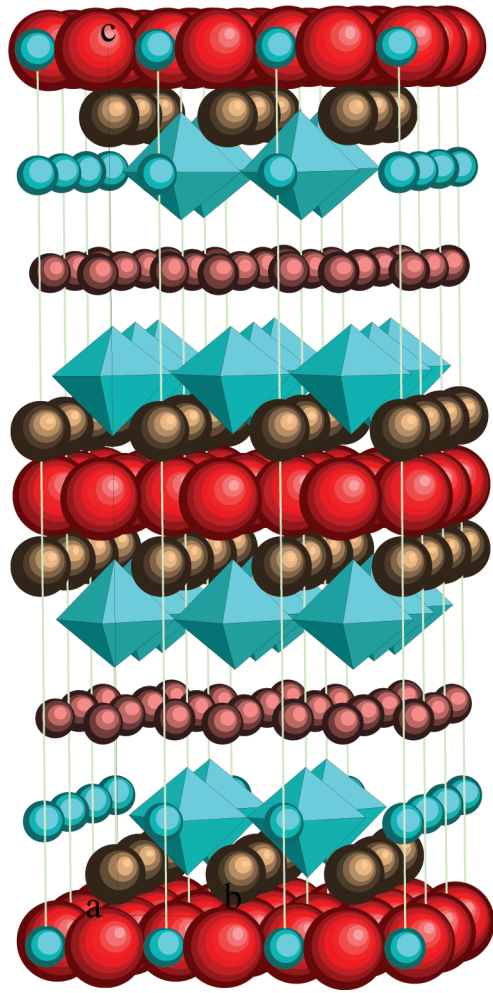


Figure 13. Representation of the  $\text{RbLaNb}_2\text{O}_7$  Dion–Jacobson phase (cyan,  $\text{NbO}_6$  units; dark yellow, Rb atoms; light yellow, La atoms).

These results indicate that  $\text{Bi}_2\text{WO}_6$  shows acceptable photodegradation rates for both liquid and gas phase reactions under visible irradiation ( $\lambda > 400 \text{ nm}$ ), all with higher values compared to  $\text{TiO}_2$ . In addition, the photoelectrocatalytic performance of such systems immobilized into conducting supports for the degradation of 4-chlorophenol under visible irradiation is also promising.<sup>363</sup> In a recent study, Saison et al. proposed that the relevant photocatalytic activity of such materials was related to their strong surface acidity. They provided an interesting discussion, related to the lateral facets in these platelike structures, on the origin of such acidity.<sup>364</sup>

In order to improve the photocatalytic performance of these Aurivillius structures, it has been recently proposed that the assembly of a  $\text{Bi}_2\text{WO}_6$  nanostructure with  $\text{Bi}_2\text{WO}_6$  quantum dots dispersed on crystalline nanosheets has potential.<sup>365</sup> Using this approach, the authors aim to balance all the benefits of nanoparticles, nanoplates and nanostructures. The reported enhanced photocatalytic activity for RhB degradation appears to be justified. Among other structural and surface features, the interesting homojunction between the quantum dot and nanosheet substrate is significant. Along the same lines, the incorporation of  $\text{TiO}_2$  units into the  $\text{Bi}_2\text{WO}_6$  structure leading to a homogeneous heterostructured material has shown that this new photocatalyst can in principle function under sunlike irradiation conditions.<sup>366,367</sup> This new system gave interesting results for the degradation of RhB under UV–vis that clearly exceeds any previous results.

The second candidate with Aurivillius structure that has been reported in recent years is  $\text{Bi}_2\text{MoO}_6$ .<sup>368–373</sup> The crystalline



**Figure 14.** Representation of the  $\text{Li}_2\text{CaTa}_2\text{O}_7$  Ruddlesden–Popper phase (cyan,  $\text{TaO}_6$  units; brown, Ca atoms; pink, Li atoms; red, O atoms).

structure of this compound is similar to that described above but the  $\text{W}^{6+}$  cation is substituted by  $\text{Mo}^{6+}$  in the perovskite-like layer. Man et al. discuss the relationship between the physical properties, the photocurrent response and the preparation conditions of  $\text{Bi}_2\text{MoO}_6$  coatings prepared by dip-coating of the amorphous polymeric precursor.<sup>374</sup> They reported that the  $\text{Bi}_2\text{MoO}_6$  films exhibited a visible-light response. In addition, a detectable photocurrent was generated under visible-light ( $\lambda > 400$  nm) irradiation. Photodegradation studies of rhodamine B demonstrated that such compounds can be considered as a good alternative for visible photocatalysis. These authors obtained the Bi–Mo Aurivillius phase using a traditional solvothermal method. It exhibited well-crystallized nanorods with a diameter of about 30 nm and up to a few micrometers in length. In this case, the specific surface areas achieved using this method were relatively higher; reaching in some cases  $30 \text{ m}^2/\text{g}$ . Nevertheless, the reactivity results appear to be correlated not with this feature but to crystallinity and morphology. The same conclusion is reached by Zhou et al. in the case of  $\text{Bi}_2\text{MoO}_6$  prepared by an ultrasonic assisted method.<sup>375</sup> Furthermore, Zheng et al. provide interesting results which also support Zhou's assumption.<sup>376</sup> The  $\text{Bi}_2\text{MoO}_6$  systems were prepared using simple solution methods. With preferentially exposed [010] surfaces they exhibited enhanced

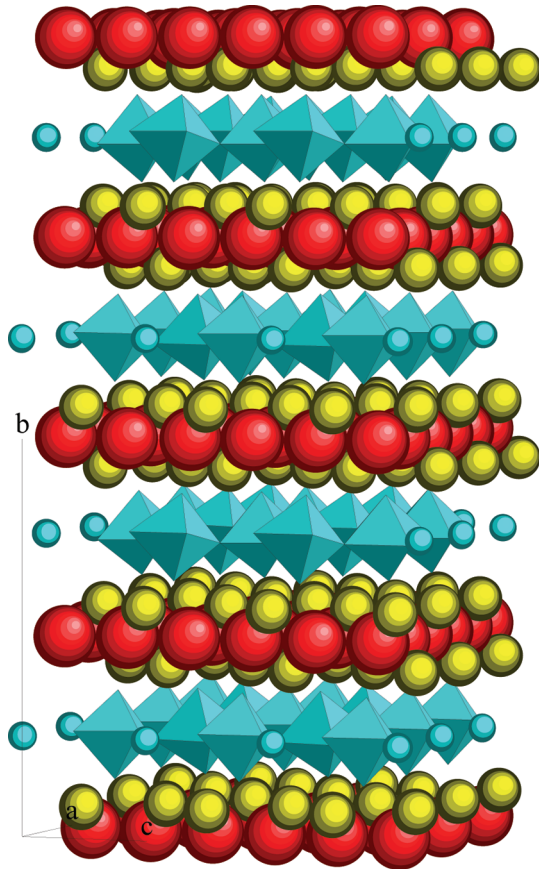


**Figure 15.** Representation of an  $\text{Bi}_2\text{WO}_6$  Aurivillius phase (cyan,  $\text{WO}_6$  units; yellow, Bi atoms; red, O atoms).

photoactivity over other catalysts. By favoring the formation of large sheet morphologies, the preferential exposition of plane [010] was observed. The analysis of these [010] surface planes indicates the existence of distorted  $\text{MoO}_6$  octahedra which lead to an oxygen-deficient surface which enhances the concentration of  $\text{OH}^\bullet$  and/or  $\text{OOH}^\bullet$  radicals.

With respect to the Aurivillius phases it is also necessary to mention Sillén structures. Compounds with these structures can be described as resulting from the intergrowth of  $\text{PbO}$ -type blocks ( $\text{M}_2\text{O}_2$ )<sup>+</sup> and one (the simplest  $\text{X}_1$  structure), two and even three layers of halide ions  $\text{X}^-$  (i.e., Bi-based oxychlorides such as  $\text{BiOCl}$ ,  $E_g = 3.50$  eV, and  $\text{Bi}_3\text{O}_4\text{Cl}$ ,  $E_g = 2.80$  eV) (Figure 16). Compounds with the general formula  $\text{MBi}_2\text{O}_2\text{X}$  ( $\text{M} = \text{Pb}$  or  $\text{Cd}$ ) and  $\text{MBi}_3\text{O}_4\text{X}_2$  ( $\text{M} = \text{Li}$  or  $\text{Na}$ ) are designated as  $\text{X}_1$  and those with general formula  $\text{MOX}$  ( $\text{M} = \text{Bi}$ ,  $\text{Ln}$ ) as  $\text{X}_2$ .

Layered-structure Bi-based oxychlorides such as  $\text{BiOCl}$ ,  $\text{Bi}_3\text{O}_4\text{Cl}$ ,  $\text{Na}_{0.5}\text{Bi}_{1.5}\text{O}_2\text{Cl}$ ,  $\text{Bi}_4\text{NbO}_8\text{Cl}$  and  $\text{MBi}_2\text{O}_2\text{Cl}$  ( $\text{M} = \text{Ca}$ ,  $\text{Sr}$ ,  $\text{Ba}$ ,  $\text{Cd}$ ,  $\text{Pb}$ ) can also be used as efficient photocatalysts. Most of them have been synthesized using solid state reactions, and they have demonstrated good photocatalytic activity in the degradation of selected dyes. The literature results often show that the UV-induced photocatalytic performances of these novel oxychloride catalysts are better than or comparable to that of anatase- $\text{TiO}_2$ .<sup>377</sup> The open crystalline structure and the indirect optical transition of  $\text{BiOCl}$  have been shown to be responsible for the excellent photocatalytic activity. In addition, the high photocatalytic performance of these Bi-based oxychlorides has been ascribed to the presence of strong internal static electric fields

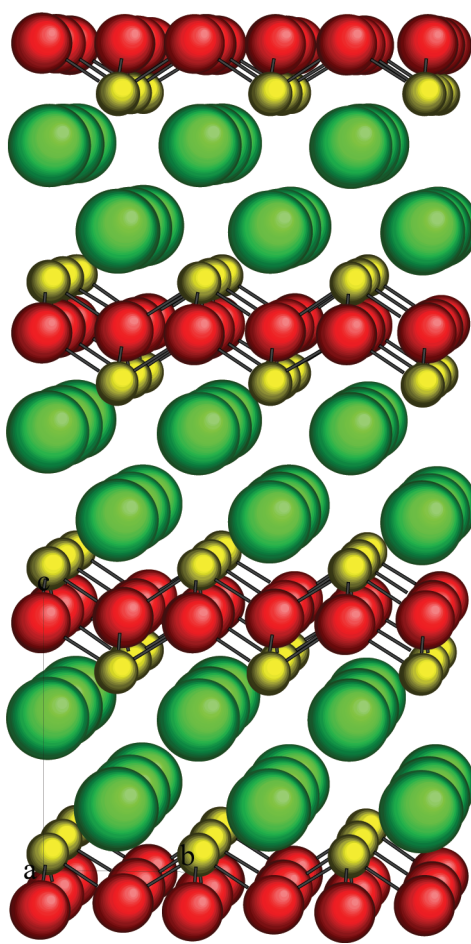


**Figure 16.** Representation of a  $\text{BiOCl}$  Sillén structure (green, Cl atoms; yellow, Bi atoms; red, O atoms).

between the layers. Alternatively, Ye et al. considered that the high oxygen atom density in [001] facets could be key for the increase of the UV-induced photoactivity, probably due to the creation of oxygen vacancies in the crystal lattice.<sup>378</sup>

However, more recent efforts have focused on the observation that similar structures demonstrate visible absorption. This is the case for  $\text{Bi}_3\text{O}_4\text{Cl}$  ( $E_g = 2.79$  eV),  $\text{Na}_{0.5}\text{Bi}_{1.5}\text{O}_2\text{Cl}$  ( $E_g = 3.03$  eV) and  $\text{PbBiO}_2\text{Cl}$  ( $E_g = 2.45$  eV) which all exhibit visible-light photoactivity.<sup>377,379,380</sup> For such materials, the composition of the valence and conduction bands determine the lower band gap values. Indeed, the valence band consists of Cl 3p, O 2p and Bi 6s hybridized orbitals. The photocatalytic performance of  $\text{Bi}_3\text{O}_4\text{Cl}$  and  $\text{Na}_{0.5}\text{Bi}_{1.5}\text{O}_2\text{Cl}$  for methyl orange degradation is better than that of  $\text{TiO}_2$  under both UV and visible irradiation conditions.

Also related is the fact that other oxyhalides have been proposed which have acceptable photoactivities in the visible range. Oxybromide and oxyiodides such as  $\text{BiOBr}$ ,  $\text{PbBiO}_2\text{Br}$ ,  $\text{BiOI}_{x}\text{Br}_{1-x}$  or  $\text{BiOI}_{x}\text{Cl}_{1-x}$  possess good visible light responsive abilities.<sup>381,382</sup> The band gaps of the sheet-shaped compounds  $\text{BiOX}$  ( $X = \text{Cl}, \text{Br}$  and  $\text{I}$ ) were 3.44, 2.76 and 1.85 eV, respectively.  $\text{BiOBr}$  showed the highest photocatalytic activity in degrading rhodamine B.<sup>383</sup> In a recent paper, the modification of  $\text{BiOI}$  with an ionic liquid was reported.<sup>384</sup> The modification of  $\text{BiOI}$  with  $[\text{bmim}]\text{I}$ , which acts as iodine source also, clearly improves the photocatalytic activity for MO degradation under visible light.

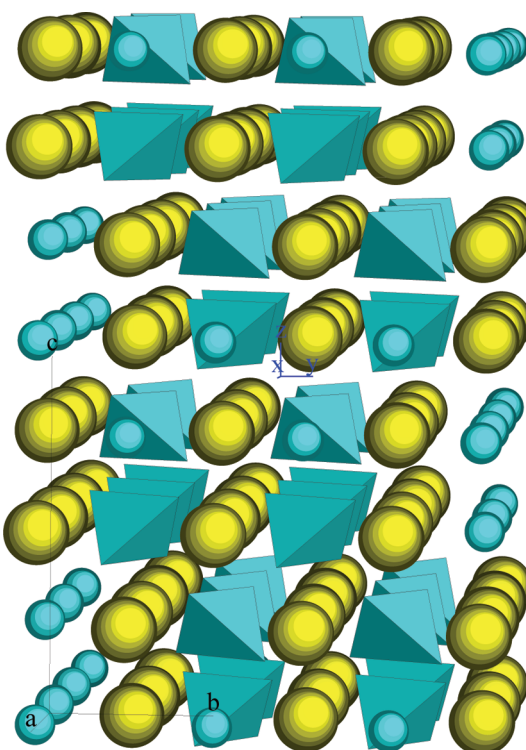


**Figure 17.** Representation of the  $\text{BiVO}_4$  scheelite structure (cyan,  $\text{VO}_4$  units; yellow, Bi atoms).

This enhancement was ascribed to the capability of  $[\text{bmim}]$  molecules to trap photoexcited electrons.

The combination of an Aurivillius phase with a Sillén intergrowth gives rise to the so-called Sillén–Aurivillius interwoven materials. The most common examples of these types of structures are the Bi-based oxychlorides. Among these  $\text{Bi}_4\text{NbO}_8\text{Cl}$  is of particular interest because it has a reddish yellow color ( $E_g = 2.38$  eV) and therefore a reasonable visible light-response ability.<sup>385</sup> The nominal composition of this Bi–Nb oxychloride can be rewritten as  $[\text{Bi}_2\text{O}_2\text{Cl}][\text{Bi}_2\text{NbO}_6]$  where the Sillén and Aurivillius structures are clearly denoted. In this case, the reported photoactivities clearly indicate that the Bi–Nb oxychloride obtained by the solid state reaction method behaves better than  $\text{TiO}_2$ , but only under visible irradiation ( $\lambda > 400$  nm).

### 3.4. $\text{BiVO}_4$ Scheelite Structure

Where  $\text{AMO}_4$  compounds are concerned, the scheelite structure type is favored when A is a big electropositive ion (generally an alkali metal, alkaline earth or lanthanide ion) and M is a smaller cation in a high oxidation state (e.g.,  $\text{W}^{6+}$ ,  $\text{Mo}^{6+}$ ,  $\text{Re}^{7+}$ ,  $\text{Ru}^{7+}$ ,  $\text{I}^{7+}$ ) (Figure 17). Of the members of this family of compounds, bismuth vanadate,  $\text{BiVO}_4$  ( $E_g = 2.30$  eV), is one which has been widely reported as exhibiting good photocatalytic properties.  $\text{BiVO}_4$  has three main crystalline structures, zircon-tetragonal, scheelite-tetragonal and scheelite-monoclinic,<sup>386</sup> and can be prepared using different synthetic routes.<sup>387–389</sup> It is possible to selectively make one of the above-mentioned structures and morphologies by judicious choice of the preparative method.<sup>390,391</sup> Regarding the scheelite-like compound, the monoclinic structure is usually obtained by means of a solid state and melting reaction at high temperatures. On the other hand, the tetragonal form is usually formed by aqueous media methods in low temperature processes. From the literature data,

it appears that the most photoactive phase is the monoclinic phase. Clearly therefore, attempts at achieving this crystalline phase are of great importance. Thus, a simple coprecipitation method using mild calcination temperatures such as 200 °C was proposed and successfully led to the photoactive monoclinic structure.<sup>392</sup> An interesting effect of cetyltrimethylammonium bromide (CTAB) on the crystallization is reported by Yin et al.<sup>393</sup> They showed that the presence of CTAB induces the appearance of BiOBr during the synthesis at 80 °C using an aqueous method. This intermediate seems to favor the crystallization of BiVO<sub>4</sub> as monoclinic polymorphs. In addition, it appears that the use of hydrothermal treatments for the preparation of BiVO<sub>4</sub> leads to the appearance of the monoclinic phase at mild temperatures. These have smaller crystallite sizes compared to those obtained from the solid state reaction.<sup>391,394,395</sup> Thus, Zhang et al. proposed the synthesis of monoclinic BiVO<sub>4</sub> nanosheets by means of a hydrothermal method assisted by a morphology-directing agent.<sup>387</sup> These nanosheet-shaped materials exhibit much higher photocatalytic activities for the solar photodegradation of rhodamine B than the corresponding bulk material. Subsequently, an m-BiVO<sub>4</sub> structure with high surface area was also obtained using K<sub>2</sub>SO<sub>4</sub> as the inorganic crystal-controlling additive.<sup>396</sup> Recently, Xi et al. reported a novel hydrothermal synthetic procedure for obtaining m-BiVO<sub>4</sub> nanoplates which showed preferential exposition of the [001] facets.<sup>397</sup> Similar to the Bi<sub>2</sub>MoO<sub>6</sub> systems, this preferentially exposed facet seems to produce an enhanced photoactivity for the degradation of organic contaminants as well as for the photocatalytic oxidation of water to O<sub>2</sub>. When compared to m-BiVO<sub>4</sub> nanorods with a [100] growth direction, the nanoplates showed notably higher photoactivity in spite of having a lower surface area with respect to the nanorods. Li et al. reported the preparation of BiVO<sub>4</sub> with surface exposed (004) facets.<sup>398</sup> They demonstrated the correlation between the extent of (004) facet exposure and the photocatalytic activity for O<sub>2</sub> evolution. The existence of multiatomic BiV<sub>4</sub> centers at this facet seems to be the origin of the observed high activity. This appears to confirm that in this material the photoactivity is more closely related to the surface (or shape) structure than to the actual surface area or other physical properties. In addition, using a similar procedure Zheng et al. employed a Gemini surfactant and produced a 3D hierarchical structure.<sup>399</sup> The influence of the specific morphology of a particular material is also referred to by Zhou et al.<sup>400</sup> They reported that the preparation of monoclinic BiVO<sub>4</sub> microtubes particles which formed flowerlike structures resulted in a distinct improvement in the photocatalytic activity. It can be safely concluded that such noteworthy visible photoactivity appears to be attributable to the presence of a distinctive morphology. Another approach consists of the substitution of M cations to form structural MO<sub>4</sub> tetrahedra. Applying this, Yao et al. proposed the substitution of Mo<sup>6+</sup> into the V<sup>5+</sup> sites to form a BiV<sub>0.98</sub>Mo<sub>0.02</sub>O<sub>4</sub> compound.<sup>401</sup> The modified material, obtained by a solid state reaction method, exhibits a well-crystallized monoclinic scheelite structure and similar band gap values (2.39 eV). Methylene blue degradation under visible light irradiation was found to be significantly improved by the incorporation of even this small amount of Mo. The higher adsorption affinity toward the organic molecule due to the enhanced surface acidity was reported as the reason for the improved photocatalytic performance. In a subsequent work, Park et al. proposed a codoped BiVO<sub>4</sub> system in which the incorporation of W and Mo would lead to an improved

electron–hole separation.<sup>402</sup> The consecutive doping with W and Mo induces the crystal symmetry shifting from monoclinic to tetragonal, without a significant change of the band gap or the material's optical properties. This symmetry deformation seems to be the reason for an effective charge separation.

### 3.5. Other Structures

Pyrochlore is a generic term for the pyrochlore crystal structure (*Fd*3*m*) which describes materials of the type A<sub>2</sub>B<sub>2</sub>O<sub>6</sub> and A<sub>2</sub>B<sub>2</sub>O<sub>7</sub>. Here the A and B species are generally rare-earth or transition metal species.<sup>403</sup> The pyrochlore structure is a super structure derivative of the simple fluorite structure (AO<sub>2</sub> = A<sub>4</sub>O<sub>8</sub>, where the A and B cations are ordered along the ⟨110⟩ direction). These compounds are predominantly cubic and ionic in nature and, provided the ionic radius and charge neutrality criteria are satisfied, lend themselves to a wide variety of chemical substitution at the A, B and O sites. A<sub>2</sub>B<sub>2</sub>O<sub>7</sub> compounds exhibit a wide range of interesting physical properties. This is because the B element can be a transition metal with variable oxidation states or a post transition metal. The A element can be a rare earth (Ln) or an element with an inert lone-pair of electrons. Recently, some Nb-containing photocatalysts with a pyrochlore-type structure have also been reported; examples are Bi<sub>2</sub>MNbO<sub>7</sub> (M = Al, Ga, In and Fe) and Bi<sub>2</sub>RNbO<sub>7</sub> (R = rare earth elements). However, one thing that they all have in common is that all these systems have been reported for water splitting reactions under UV irradiation.<sup>404,405</sup> Among the family members of this group, certain tantalate compounds with pyrochlore structures (Bi<sub>2</sub>LaTaO<sub>7</sub> and Bi<sub>2</sub>YTaO<sub>7</sub>) have been shown to also exhibit visible photocatalytic activity in the degradation of methylene blue.<sup>406</sup> In relation to this, Luan et al. pointed that the best photocatalytic performance shown by the La structure can be explained by taking into account the structure distortion due to the rare earth ion substitution and the consequent displacement of the band edge. A related tantalum compound (K<sub>2</sub>Ta<sub>2</sub>O<sub>6</sub>) has been reported as suitable for the degradation of rhodamine B under UV irradiation.<sup>407</sup> Zhu et al. also reported the nitrogen doped K<sub>2</sub>Ta<sub>2</sub>O<sub>6</sub>.

The compound AgSbO<sub>3</sub> which has a pyrochlore structure is also reported as having photocatalytic activity for 2-propanol degradation under visible irradiation.<sup>408</sup> The crystal structure of AgSbO<sub>3</sub> can be depicted as a combination of AgO<sub>6</sub> and SbO<sub>6</sub> octahedra with a band edge at around 480 nm (E<sub>g</sub> = 2.6 eV). This band narrowing was attributed to the hybridization of the Ag 4d and O 2p orbitals which form the top of the valence band.

Spinels have a common structural arrangement shared by many oxides of the transition metals. Their formula is AB<sub>2</sub>O<sub>4</sub>, and the oxide anions are arranged in a cubic close-packed lattice. The cations A and B occupy some or all of the octahedral and tetrahedral sites in the lattice. Some compounds with this structure have been used for the photodegradation of organic pollutants under visible irradiation.<sup>409–412</sup> Tang et al. first reported the photocatalytic activity of CaIn<sub>2</sub>O<sub>4</sub> for methylene blue degradation using visible radiation.<sup>409</sup> In addition, these authors report the effect of alkaline earth ion substitution into the structure leading to the following photoactivity order: CaIn<sub>2</sub>O<sub>4</sub> > SrIn<sub>2</sub>O<sub>4</sub> > BaIn<sub>2</sub>O<sub>4</sub>. The complex structure of BaIn<sub>2</sub>O<sub>4</sub>, which exhibits an InO<sub>x</sub> polyhedral network, was identified as being responsible for this compound exhibiting the lowest photoactivity. The smaller ionic radii of the Ca and Sr cations provide a higher oxidative ability and therefore better photocatalytic performances.<sup>410,412</sup> In other words, the different electronegativities

of the cations directly affect the final band structure and hence the subsequent photocatalytic activity.

#### 4. NEW PHOTOCATALYSTS FOR WATER SPLITTING

Taking into consideration the current socioeconomic and environmental situation, it is widely believed that hydrogen will play an important role in this system since it is considered the ultimate clean energy carrier. At present, H<sub>2</sub> is mainly produced from CO and CH<sub>4</sub> from fossil fuels by a steam reforming reaction. However, the ultimate future effective depletion of fossil fuels as well as the serious environmental problems associated with CO<sub>2</sub> production has inspired the development of viable alternatives. Of these, the solar photocatalytic water splitting reaction in which sunlight and water are used as the hydrogen source is a highly appreciated alternative. In a process that mimics photosynthesis, solar energy can also be used to convert water into hydrogen and oxygen.

Over the last three decades the overall photocatalytic water splitting process has been extensively studied.<sup>413–417</sup> Regarding this field of research, however, it must be said that the earliest research focused more on developing good photocatalysts than on actually understanding the process itself.<sup>418</sup> Recent advances in the tailoring of new photocatalysts for solar water splitting pass through the comprehension of the band electronic structure which subsequently would lead to improvements using band engineering.<sup>329,419</sup> Consequently this is currently considered the primary research approach and hence will be now described in more detail.

With respect to the formal electronic structure of a potential water splitting photocatalyst, there are two important requirements: (i) The band gap should be  $1.23 \text{ eV} < E_g < 3.26 \text{ eV}$ . (ii) The band positions should be located as follows: the bottom of the conduction band should be more negative than the redox potential of H<sup>+</sup>/H<sub>2</sub> (0 V vs NHE). Meanwhile the top of the valence band should be more positive than the redox potential of O<sub>2</sub>/H<sub>2</sub>O (1.23 V). Thus, from a thermodynamic point of view the water splitting reaction should be easily achieved using a photoinduced catalytic process involving any materials which satisfy the above conditions.

However, the overall photocatalytic water splitting reaction is an endothermic reaction with a large positive change in Gibbs free energy ( $\Delta G^\circ = 238 \text{ kJ/mol}$ ). This means that, in order to overcome such an energy barrier, photons of higher energy are needed. Moreover, the inverse reaction, water formation, strongly competes with the desired hydrogen formation (surface back reaction). There are two main approaches to suppressing the reverse reaction: either the use of sacrificial reagents or the creation of a physical separation between the corresponding photoactive sites on the surface of the photocatalyst. With respect to this second approach, the separation of the photoactive sites would require surface separation of the photogenerated electrons and holes. In this context, some transition metals oxides and noble metals (Pt,<sup>420</sup> Rh,<sup>421</sup> Au, NiO and RuO<sub>2</sub>) are suitable as cocatalysts for the improvement of the H<sub>2</sub> evolution reaction by suppressing the water forming back reaction. The presence of the cocatalyst plays a crucial role in the water splitting mechanism. It induces the photogeneration of carriers, facilitates the charge transfer, constructs the catalytic sites and reduces the activation energy for gas evolution. In the majority of cases, the presence of a cocatalyst enables or increases the water splitting activity. Although it has been reported that noble metals improve the water

reduction reaction in order to generate H<sub>2</sub>, these particular cocatalysts have been shown to be inadequate for water splitting reaction because effectively they favor the back reaction. This together with their high cost makes it essential to develop novel less expensive ones, and in fact alternative cocatalyst systems have been proposed. Zong et al.<sup>422</sup> have shown that the rate of H<sub>2</sub> evolution was significantly improved by using Mo<sub>2</sub>S as the cocatalyst. The photoactivity reported was even higher than that for the Pt-loaded catalyst. Following on from this, other compounds such as those proposed by Leung et al., materials such as Ni and Mo alloys, Mo<sub>2</sub>C, or W<sub>2</sub>C, are potential candidates for cocatalysts since they have shown a low overpotential for hydrogen evolution.<sup>423</sup>

However, other metal oxides such as NiO<sub>x</sub> or RuO<sub>2</sub> have been mainly used as cocatalysts for the decomposition of pure water into H<sub>2</sub> and O<sub>2</sub>.<sup>424–427</sup> Domen's group has extensively studied the effect of cocatalysts for this water splitting reaction.<sup>428,429</sup> From recent studies where NiO<sub>x</sub> cocatalysts were developed, their particular core–shell structure is crucial for the remarkable improvement in water splitting. Thus, Ni@NiO structures would act as selective reaction centers in which the NiO shell successfully suppresses the back reaction by limiting the diffusion of oxygen into the Ni core. On the other hand, the Ni core can act as an electron drain site accessible to H<sup>+</sup>, which then enables the H<sub>2</sub> formation.<sup>416</sup> Recently, a variation of this NiO<sub>x</sub> cocatalyst has been proposed based on a Cr<sub>2</sub>O<sub>3</sub> shell covering different cocatalyst cores (NiO<sub>x</sub>, RuO<sub>2</sub>, Rh<sub>2</sub>O<sub>3</sub>, Rh, Pd, Pt). It showed remarkable quantum efficiencies for the H<sub>2</sub> evolution reaction.<sup>430–432</sup> In this case, the method consisted of the deposition of Rh and Cr by simultaneous photoreduction. This simultaneous deposition leads to the formation of a core–shell structure consisting of a metallic Rh core and a Cr<sub>2</sub>O<sub>3</sub> shell.

From these latest results, it can be concluded, therefore, that the selection of the appropriate cocatalyst is critical for achieving enhanced efficiencies for the overall water splitting reaction.

To date, more than 130 potential materials have been proposed for use either in the overall water splitting reaction or for the water oxidation/reduction half-reaction in the presence of external sacrificial agent. These UV-based systems can be classified into four groups: (i) d<sup>0</sup> metal oxides (such as Ti<sup>4+</sup>, Zr<sup>4+</sup>, Nb<sup>5+</sup>, Ta<sup>5+</sup>, W<sup>6+</sup>); (ii) d<sup>10</sup> metal oxides (In<sup>3+</sup>, Ga<sup>3+</sup>, Ge<sup>3+</sup>, Sn<sup>4+</sup>); (iii) f<sup>0</sup> metal oxides (Ce<sup>4+</sup>) and finally (iv) nonoxidic photocatalysts.<sup>415</sup> Using UV light all of these potential systems can lead to "photon efficiencies" as high as 30–50%. Thus, the conclusion reached from reading the huge amount of published papers is that the real challenge now refers to the low quantum efficiencies achieved in UV and especially in visible light-induced processes.<sup>418</sup> Some authors have identified the goal for competitive photocatalytic water splitting as the development of photocatalysts with low band gaps. This would make the visible process possible with quantum yields of 30% at 600 nm.<sup>328</sup> This efficiency should constitute about 5% of solar energy conversion.

Until the 1980s the first systems studied for the photoassisted water-splitting reaction were based mainly on TiO<sub>2</sub> derived catalysts. After that, a new approach emerged involving other complex systems such as layered (Dion–Jacobson and Ruddlesden–Popper) and pillared structures. A titanium-based layered perovskite in the form La<sub>2</sub>Ti<sub>2</sub>O<sub>7</sub>, which is formed by TiO<sub>6</sub> unit slabs separated by La<sup>3+</sup> ion layers, showed a 3.8 eV band gap energy. Doping with NiO and even more so with BaO leads to UV high photocatalytic activity for water splitting.<sup>433</sup> One of the most representative systems of this period is the layered niobate family (K<sub>4</sub>Nb<sub>6</sub>O<sub>17</sub> and Rb<sub>4</sub>Nb<sub>6</sub>O<sub>17</sub>).<sup>352</sup> Their unique layered structures

which are composed of two different interlayer spaces lead to efficient water decomposition. However, the large band gap values exhibited by these materials (ca. 3.3 eV) introduce a significant handicap which unfortunately renders the overall process unfeasible. Further approaches to developing a visible light-active niobate involved the incorporation of an alkaline metal at the interlayer space (i.e.,  $\text{RbPb}_2\text{Nb}_3\text{O}_{10}$ ). Ion-exchangeable layered perovskites with general formula  $\text{A}_{2-x}\text{La}_2\text{Ti}_{3-x}\text{Nb}_x\text{O}_{10}$  ( $\text{A}$  = interlayer cations such as K, Rb, Cs) showed interesting photocatalytic behavior under visible irradiation.<sup>434</sup>

Further trials for highly active systems centered on layered tantalates. Because of their large band gap, UV irradiation is needed and the addition of a cocatalyst ( $\text{NiO}$ , Pt or  $\text{RuO}_2$ ) for improving the photocatalytic activity. In this context, it has been reported that  $\text{NiO}/\text{NaTiO}_3$  is the most active for water splitting among the tantalate family. The use of such cocatalysts as active sites is a justified strategy for improving the localizing effect of the protons for the formation of hydrogen gas.<sup>435</sup> Recently, Hu et al. demonstrated that the incorporation of small amounts of  $\text{NiO}$  (below 3 wt %) should lead to the formation of a solid solution transition zone between the  $\text{NiO}$  and  $\text{NaTaO}_3$ .<sup>436</sup> Using high-resolution transmission electron microscopy (HRTEM) data they reported that this interface is formed by the interdiffusion of  $\text{Ni}^{2+}$  and  $\text{Na}^+$  cations. This interdiffusion should generate a reduction in the depletion width. Subsequently this should allow a charge tunneling through the interface barrier and result in markedly enhanced  $\text{H}_2$  evolution rates under UV illumination. The doping of the  $\text{NiO}/\text{NaTiO}_3$  with  $\text{La}^{3+}$  also significantly improves the efficiencies of this particular photocatalyst by increasing the lifetime of the photogenerated electrons.<sup>437</sup> Other tantalate structures such as  $\text{LnTaO}_3$  ( $\text{Ln} = \text{La, Ce, Pr, Nd}$ ) present a variable band gap depending on the lanthanide cation. However, only  $\text{NiO}$ -modified  $\text{LaTaO}_3$  shows UV photocatalytic activity for overall water splitting.<sup>438</sup>

Furthermore, it has been reported that doping  $\text{NaTaO}_3$  with transition metal ions such as Mn or Fe also leads to visible absorption.<sup>439</sup> Because the ionic radius of Mn and Fe (0.67–0.72 Å) is close to that of  $\text{Ta}^{5+}$  (0.64 Å), the substitution for  $\text{Ta}^{5+}$  is strongly feasible. In this situation, the Fe and Mn 3d-like states would contribute not only to the CB but also to the VB, making the band gap much smaller than that of pure  $\text{NaTaO}_3$ . Using density of state calculations (DOS), these authors proposed that Mn-doped  $\text{NaTaO}_3$  is expected to be active only for photooxidation while Fe-doped  $\text{NaTaO}_3$  can be an active material for overall photocatalytic splitting of water under visible light.

As already mentioned in the previous section, band engineering strategies for the tailoring of competitive visible active systems for water splitting reactions approach the creation of systems with modified band structures through the incorporation of doping ions or new solid solution systems. After the initial considerations about the water splitting mechanism, it appears that it would be quite difficult to attain the water cleavage reaction under visible light since efficient photocatalysts must have a narrow band gap and suitable band positions for the simultaneous evolution of  $\text{H}_2$  and  $\text{O}_2$ .

The creation of a visible active system within the tantalates was achieved by developing an  $\text{InTaO}_4$  system doped with  $\text{NiO}$  and  $\text{RuO}_2$ .<sup>440,441</sup> In fact, the band gap of the perovskite tantalates strongly depends on the cations participating. Hence lanthanide doping seems to notably increase the photocatalytic activity. In a similar way, the incorporation of Ni into the perovskite structure diminishes the  $E_g$  value to 2.3 eV for  $\text{In}_{0.9}\text{Ni}_{0.1}\text{TaO}_4$ .

Oxynitrides and oxysulfide materials also have potential as interesting water-splitting photocatalysts.<sup>329,442</sup> Among the oxynitrides reported in the literature showing interesting photocatalytic behavior are those containing transition-metal cations of  $\text{Ti}^{4+}$ ,  $\text{Nb}^{5+}$  and  $\text{Ta}^{5+}$  which have the  $d^0$  electronic configuration.<sup>329</sup> It should be noted that oxynitrides exhibit high photocatalytic activity for  $\text{O}_2$ -evolution. Materials with a  $d^{10}$  electronic configuration also exhibit photocatalytic activity under visible light. The main difference with respect to the  $d^0$  configuration is the fact that the lower end of the conduction band is composed of hybridized s and p orbitals. Such conduction band mixed orbitals exhibit a large dispersion leading to higher mobility of the photogenerated electrons and thus higher photoactivity.<sup>329</sup> As has been previously mentioned,  $\text{Ge}_3\text{N}_4$  and  $\text{GaN}$  show large band gap energies and exhibit photoactivity under UV light.<sup>443,444</sup> The combination of such nitrides with  $\text{ZnO}$  to form a solid solution such as  $(\text{Ga}_{1-x}\text{Zn}_x)(\text{N}_{1-x}\text{O}_x)$  leads to a lower band gap energy (2.4–2.8 eV).<sup>445</sup> Although  $(\text{Ga}_{1-x}\text{Zn}_x)(\text{N}_{1-x}\text{O}_x)$  with a  $\text{ZnO}$  concentration greater than 75% can absorb long-wavelength visible light, only  $\text{GaN}$ -rich  $(\text{Ga}_{1-x}\text{Zn}_x)(\text{N}_{1-x}\text{O}_x)$  with a  $\text{ZnO}$  concentration below 22% exhibited activity for overall water splitting.<sup>446</sup> The modification of this oxynitride material with  $\text{Rh}_{2-x}\text{Cr}_x\text{O}_3$  as the cocatalyst and the use of silver nitrate as a sacrificial electron acceptor led to improved performance.<sup>447</sup> Similarly, a solid solution of zinc oxide and germanium nitride  $(\text{Zn}_{1+x}\text{Ge})(\text{N}_2\text{O}_x)$  has also been demonstrated as being an active photocatalyst for overall water splitting under visible light.<sup>448</sup>

Regarding oxysulfide materials, DFT calculations have shown that the relative stability of such compounds compared to sulfides with respect to oxidation reactions is due to the difference in their band structures. The O 2p and S 3p orbital mixing which forms the valence band is reported as being the main reason for such stability toward oxidation. Thus, Ishikawa et al. reported that  $\text{Ln}_2\text{Ti}_2\text{S}_2\text{O}_5$  ( $\text{Ln} = \text{Sm, Gd}$ ) behave as stable photocatalysts for the  $\text{H}_2$  and  $\text{O}_2$  evolution reaction in the presence of an electron donor (methanol,  $\text{Na}_2\text{S}-\text{Na}_2\text{SO}_3$ ) and acceptor ( $\text{Ag}^+$ ), respectively.<sup>449</sup> The improvement in the photocatalytic activity was achieved by raising the sulfidation temperature to 850 °C. It was found that this induces a higher degree of crystallinity. In addition, Ogisu et al. report La–Ga-based oxysulfides which exhibit photocatalytic activity for  $\text{H}_2$  evolution in the presence of Ru or Pt cocatalysts, whereas with  $\text{IrO}_2$  loading this system promotes  $\text{O}_2$  evolution reaction.<sup>450</sup>

Due to their suitable electronic band structures sulfide photocatalysts have been extensively studied for their photocatalytic water splitting potential.<sup>451</sup> Some of the attempts to improve the stability of metal sulfide involved the following: (i) the loading of a noble metal onto the surface of  $\text{CdS}$ , (ii) the incorporation of metal sulfide nanoparticles into the interlayer photocatalysts or (iii) mixing with wide band gap semiconductors of chalcogenides such as  $\text{ZnS}$ . Thus, it was reported that Cu or Ni doping onto  $\text{ZnS}$  leads to an active photocatalyst for the hydrogen evolution reaction under visible irradiation. Kudo et al. first reported an interesting example of visible photoactivity for  $\text{H}_2$  evolution by the Ni–ZnS system. On the other hand, Cu-doped  $\text{ZnS}$  with a composition of  $\text{Zn}_{0.957}\text{Cu}_{0.043}\text{S}$  was reported to be an efficient photocatalyst for  $\text{H}_2$  evolution from water in the absence of any cocatalyst.<sup>451</sup> The results indicate that, although the band gap is narrowed by forming donor levels from the Cu 3d orbitals located in the forbidden band, the high conduction band potential of the  $\text{ZnS}$  host semiconductor remains effective for the separation of charges and the reduction of water.

Such systems overcome the harmful instability of the previously proposed CdS system which suffered photocorrosion. Later, Xing et al. showed that the solid solution  $\text{Cd}_{1-x}\text{Zn}_x\text{S}$  which exhibits modulated band gap values gives efficient and stable photocatalytic behavior for water splitting.<sup>452</sup> Other solid solutions such as  $(\text{Zn}_{0.95}\text{Cu}_{0.05})_{1-x}\text{Cd}_x\text{S}$ ,  $\text{Cd}_x\text{Cu}_y\text{Zn}_{1-x-y}\text{S}$ ,  $(\text{AgIn})_x\text{Zn}_{2(1-x)}\text{S}_2$  and  $\text{ZnS}-\text{CuInS}_2-\text{AgInS}_2$ , which contain sacrificial reagents such as  $\text{S}^{2-}$  and  $\text{SO}_3^{2-}$ , have all been investigated and show photocatalytic activity for  $\text{H}_2$  evolution under visible light.<sup>453,454</sup> A more complex heterostructure based on sulfide materials was recently described by Amirav and Alivisatos.<sup>455</sup> They reported a multicomponent nanoheterostructure composed of a platinum-tipped cadmium sulfide rod with an embedded cadmium selenide seed. The metal tip is designed to “drain out” the electrons while the holes would be three-dimensionally confined to the CdSe nanoparticle. By adopting this arrangement, an effective charge carrier separation is achieved that can be modulated by tuning the physical length of the CdS rods.

Comparing a range of these sulfide systems, it emerges that the catalyst with a moderate doping concentration of Cu results in the best  $\text{H}_2$  evolution performance while maintaining good stability. Zhang et al. reported that the photoactivity can be enhanced by a factor of around 20-fold after adding up to 11 mol % of Cu during the synthesis to form a Cu-rich surface.<sup>456</sup> They argued that  $\text{Cu}^{2+}$  remains at the surface forming 3d impurity levels that can perform as noble metal cocatalysts, thus increasing the photocatalytic activity for water splitting. Unfortunately, binary sulfide solid solutions are unstable for water oxidation to form  $\text{O}_2$ . This is attributed to the prevalence of the more favorable  $\text{S}^{2-}$  oxidation by photogenerated holes.<sup>139</sup>

The so-called biomimetic Z-scheme was also proposed as a means of enhancing the photocatalytic efficiency of water splitting. The first artificial Z-scheme was proposed by Arakawa et al. and consisted of a  $\text{WO}_3$  photocatalyst and an  $\text{Fe}^{2+}/\text{Fe}^{3+}$  redox mediator.<sup>457</sup>

A further innovative approach which also relied on the Z-scheme consisted of the development of a two-photon process-based reaction using two different photocatalysts. Using this novel configuration, Abe et al. proposed a two-step photoexcitation.<sup>458</sup> In this kind of reaction, the redox water splitting half-reactions ( $\text{H}_2$  and  $\text{O}_2$  evolution reactions) progress with the aid of two different photocatalysts working as a coupled redox system: Pt-loaded anatase- $\text{TiO}_2$  for  $\text{H}_2$  evolution and rutile- $\text{TiO}_2$  for  $\text{O}_2$  evolution. Clearly, the study of the  $\text{H}_2$  and  $\text{O}_2$  evolution reaction is important not only for a greater understanding of the mechanism involved in the overall water splitting reaction but also in order to develop a coupled photocatalytic system. An indirect Z-scheme mechanism, similar to that occurring in the photosynthesis of green plants, is proposed for such configurations. This novel concept for the photocatalytic water splitting was first introduced by Bard in 1979.<sup>459</sup> To summarize, the indirect Z-scheme is thus composed of an  $\text{H}_2$ -evolution photocatalyst, an  $\text{O}_2$ -evolution photocatalyst and an electron mediator (Figure 18a).<sup>414,458,460</sup>

Hence in the context of such Z-schemes, a photocatalyst that is active for one of the water splitting half-reactions can be employed for the construction of the complete Z-scheme.<sup>461</sup>  $\text{TiO}_2$ -based systems are suitable for UV irradiation, while  $\text{SrTiO}_3$ -based compounds combined with Pt- $\text{WO}_3$  systems provide good  $\text{H}_2$  and  $\text{O}_2$  evolution under visible conditions. With respect to the electron-mediator system, the redox couples  $\text{IO}_3^-/\text{I}^-$  and  $\text{Fe}^{3+}/\text{Fe}^{2+}$  are usually employed. An optimized system has recently

been proposed by Domen's group. It consists of a  $\text{Pt/ZrO}_2-\text{TaON-Pt/WO}_3-\text{NaI}$  coupled system.<sup>462</sup> The modification of TaON with  $\text{ZrO}_2$  appears to be the key factor for the resulting improved photocatalytic performance. Thus, it appears that the incorporation of  $\text{ZrO}_2$  reduces the electron–hole recombination on TaON. The authors concluded that, although oxynitride presents a low activity for the  $\text{H}_2$  evolution reaction, appropriate modification should lead to a high potential for photocatalytic water splitting.

In a recent development, the electron-mediator redox couple is avoided by introducing an interparticle electron-transfer using a nanojunction system. This leads to the so-called direct Z-scheme (Figure 18b).<sup>463</sup> In contrast to the indirect Z-scheme process, the electron-transfer process takes place as a result of the isolation of stronger oxidative holes and reductive electrons on a different semiconductor by directly quenching the weaker oxidative holes and reductive electrons at the solid heterostructure interface.<sup>464</sup> Therefore, using this configuration it appears to be unnecessary to involve a redox mediator solution. From time-resolved fluorescence emission decay spectroscopy it was found that the synergistic effect is the origin of the high photoactivity of the  $\text{ZnO:CdS}$ -coupled system. Thus, while the lifetime of carriers in single semiconductor systems is ca. 60 ns, for heterostructure systems this changed to 220 ns. This fact is evidence for the real charge transfer between the two semiconductors and the delay in the recombination process.<sup>464</sup> In relation to this, Sasaki et al. demonstrated that by improving the effective contact between the  $\text{Ru/SrTiO}_3:\text{Rh-BiVO}_4$  photocatalysts participating in the Z-scheme it is possible to perform overall water splitting under visible light irradiation without the need for an electron mediator.<sup>465</sup> The apparent quantum yield of the  $(\text{Ru/SrTiO}_3:\text{Rh})-(\text{BiVO}_4)$  system was reported as being 1.7% at 420 nm. Similar results were reported for a  $\text{Cr/Ba}_2\text{In}_2\text{O}_5:\text{In}_2\text{O}_3$  system.<sup>466</sup> Yun et al. recently proposed a combination of two visible light active photocatalysts as a highly active Z-scheme system.<sup>467</sup> Thus, the combination of CdS and carbon doped  $\text{TiO}_2$  to form a  $\text{CdS/Au/TiO}_{1.96}\text{C}_{0.04}$  heterojunction, in which CdS/Au has a hemispherical core–shell structure, leads to an important  $\text{H}_2$  evolution. These results provide evidence that a suitable preparative route leading to intimate contact between both components is critical for producing efficient solar  $\text{H}_2$  production.

Currently the problem with photolytic Z-schemes is that catalytic activities and efficiencies are still low. However, taking into account the versatility of such coupled systems, it is anticipated that Z-schemes will be the focus of intense investigation in the future. The challenge for such coupled heterostructures is the need to find suitable semiconductors and to construct an adequate interface connection to realize the direct Z-scheme electron process.

After this brief discussion on the most relevant systems, it is clear that the best result reported so far for overall water splitting, that is for  $\text{Rh}_{2-y}\text{Cr}_y\text{O}_3/\text{GaN-ZnO}$  (quantum efficiency of ca. 6% at 420–440 nm), is still far from what is considered the “flashpoint” for practical applications (up to 30% at 600 nm). Therefore, as has been widely discussed, the main drawbacks are still the issues of recombination process as well as the back reaction. The overcoming of these problems appears crucial in order to develop a practical photocatalyst for  $\text{H}_2$  production from water. Due to low efficiencies and the absence of adequate scaling-up studies, the lack of industrial application is not surprising. However, Jing et al. have recently designed a compound parabolic collector photocatalytic reactor for solar light

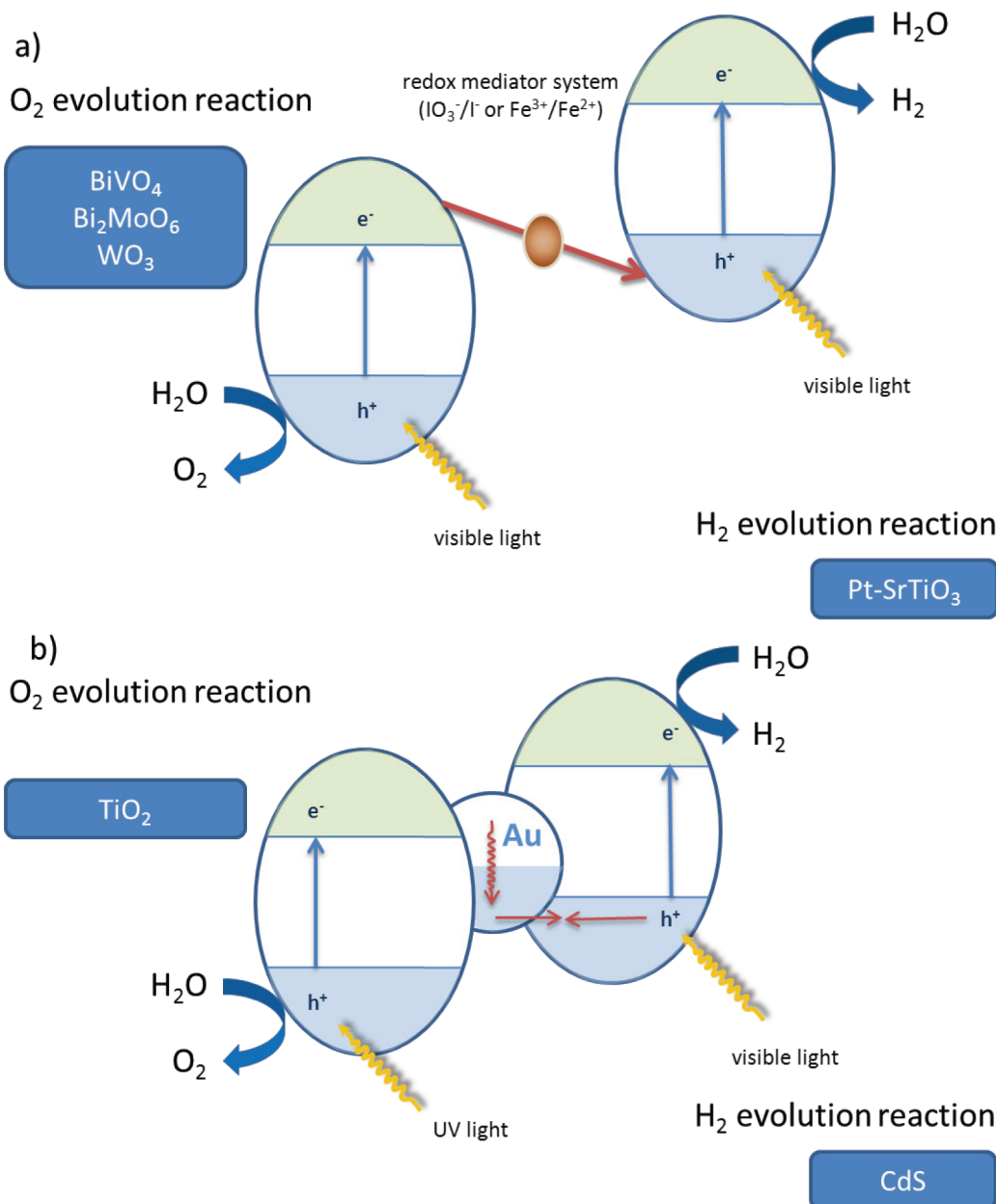


Figure 18. Z-scheme diagram for the photocatalytic water splitting reaction.

hydrogen production.<sup>468</sup> This first attempt clearly opens up new perspectives in the large scale application of the water splitting reaction.

## 5. NEW PHOTOCATALYSTS FOR CO<sub>2</sub> REDUCTION

It is widely accepted that atmospheric CO<sub>2</sub> is the most abundant greenhouse gas arising from various human activities such as energy production and transport. Currently after the Kyoto protocol ratification by many countries, the development of an adequate method for the removal of this gas from the atmosphere has attained great importance in order to control climate change. Among the CO<sub>2</sub> reduction methods should be mentioned the following: the capture and geological storage underground of the gas to form stable carbonates, absorption into several functionalized materials and large-scale forestation.

However, even though they appear attractive approaches, those solutions are in fact energy intensive and costly. An alternative and preferable way could be the valorization of CO<sub>2</sub> emissions toward fuel feedstock using a cheap and abundant energy source such as solar energy. In 1979, Inoue and co-workers examined the use of semiconductor powders for CO<sub>2</sub> reduction. These included TiO<sub>2</sub>, ZnO, CdS, SiC and WO<sub>3</sub>, suspended in CO<sub>2</sub>-saturated water illuminated by a Xe lamp.<sup>469</sup> Small amounts of formic acid, formaldehyde, methyl alcohol, and methane were produced, although it is clearly evident that one critical constraint on solving the problem of CO<sub>2</sub> is that any energy source used must not produce any more CO<sub>2</sub>. Taking this into consideration, there has been an increasing interest to tackle this problem by photocatalytic methods using solar energy.<sup>470–472</sup>

The first consideration which must be taken into account refers to the thermodynamic aspects of the reaction. The energetic

**Table 2.** Representative CO<sub>2</sub> Reduction Steps and Potentials Occurring during the Photochemical Valorization of the Molecule

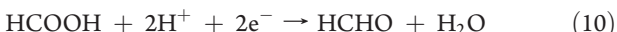
reaction	E° (V) vs SCE at pH = 7
CO <sub>2</sub> + 2H <sup>+</sup> + 2e <sup>-</sup> → CO + H <sub>2</sub> O	-0.77
CO <sub>2</sub> + 2H <sup>+</sup> + 2e <sup>-</sup> → HCOOH	-0.85
CO <sub>2</sub> + 4H <sup>+</sup> + 4e <sup>-</sup> → HCHO	-0.72
CO <sub>2</sub> + 6H <sup>+</sup> + 6e <sup>-</sup> → CH <sub>3</sub> OH	-0.62
CO <sub>2</sub> + 8H <sup>+</sup> + 8e <sup>-</sup> → CH <sub>4</sub>	-0.48

stability of the CO<sub>2</sub> molecule ( $\Delta G^\circ = -394 \text{ kJ mol}^{-1}$ ) with respect to the desired products ( $\Delta G^\circ = -51 \text{ kJ mol}^{-1}$  for methane and  $\Delta G^\circ = -159 \text{ kJ mol}^{-1}$  for methanol) appears to be a strong limitation.<sup>473</sup> This fact makes CO<sub>2</sub> reduction a highly endothermic process, even more so than the water splitting reaction ( $\Delta G^\circ = -228 \text{ kJ mol}^{-1}$ ).

Regarding the electronic requirements for the catalysts, several semiconductors exhibit adequate band gap energies for the photocatalytic reduction of carbon dioxide (ZnS, CdS, ZrO<sub>2</sub>, MgO and ZnO). Although all of these photocatalysts possess conduction band energies sufficiently negative compared to the reduction potential of CO<sub>2</sub>, the one most frequently applied is wide band gap TiO<sub>2</sub>. This is largely due to its stability and low cost.

Finally, and taking into consideration the electronic mechanism of CO<sub>2</sub> reduction, the direct process proceeds by a thermodynamically uphill one-electron transfer to form CO<sub>2</sub><sup>•-</sup>. This is highly unfavorable and exhibits a formal reduction potential of -2.14 eV.<sup>474</sup> Therefore, the most favorable pathway consists of a multiple electron transfer. This needs more than one photon to produce each of the final products (Table 2).

As can be deduced from the data presented in Table 2, photocatalytic CO<sub>2</sub> reduction would form energy-bearing products such as carbon monoxide, formic acid, formaldehyde, methanol or methane. This multistep mechanism was first proposed by Inoue,<sup>469</sup> and the different reduction products are sequentially formed:



In order to understand the complexity of the photoreduction process we will now present a brief description of the proposed mechanism that would lead to the different reduction products. The first logical step consists on the hydrogenation of CO<sub>2</sub> molecule to formic acid. The activation of CO<sub>2</sub> would be a result of a simultaneous attack of a nucleophilic metal hydride at a carbon atom and a Brønsted acid H<sup>+</sup> at the oxygen atom. The result of this simultaneous attack consists of a heterolytic process that adds H<sup>-</sup> to carbon and H<sup>+</sup> to oxygen. The next step consists of the deoxygenation of formic acid to form formaldehyde. This step proceeds through a similar mechanism based on the addition of H<sup>-</sup> to the carbon atom and a H<sup>+</sup> to the OH group of the formic

acid molecule. The third step, that is the formaldehyde reduction to methanol, proceeds by a completely different mechanism. This could involve direct hydrogen addition to the C=O, which implies a double bond cleavage.

Therefore, the design of a catalyst that can exploit the metal–H reactivity could be the basis of the development of an appropriate candidate for the CO<sub>2</sub> photoreduction reaction. This photocatalyst would have to overcome important mechanistic challenges which involve (i) the multistep, multielectron chemical transformation; (ii) coupled electron and atom transfer reactions; (iii) strongly endothermic kinetic processes; (iv) interrelationships with different catalytic sites. This complex scenario would require a complex assembly including hybrid catalysts, hierarchical nanostructured systems and multiple (active)-site catalytic materials.

At present, all the photocatalysts reported thus far exhibit low performances and/or require the use of sacrificial reducing agents. A thorough understanding of how to efficiently manage the water oxidation reaction to give oxygen turns out to be a critical requirement for achieving the efficient photochemical reduction of CO<sub>2</sub> in the absence of other sacrificial electron donors such as hydrogen.<sup>475</sup>

Since the earliest report of Inoue and co-workers, many photocatalytic systems have been proposed. All of these exhibit more or less efficiency under UV or solar irradiation conditions.<sup>471</sup> The first systems were based on GaP and GaAs semiconductors yielding methanol and formic acid–formaldehyde mixtures respectively as the main products.<sup>476,477</sup> Sulfides have been also proposed as suitable photocatalysts for the CO<sub>2</sub> splitting reaction. Egging et al. reported the formation of 2-carbon acids (glyoxylic, formic and acetic acids) using CdS.<sup>478</sup> The use of ZnS has been also explored for this reaction. It gives formic acid and methanol as the final products.<sup>479,480</sup> In spite of these cases, most of the research still focuses on TiO<sub>2</sub>-based materials due to the low cost, stability and performance.<sup>481–486</sup> In spite of the ongoing research, clearly the process still suffers from low conversion rates. In order to enhance this low performance, Ooman et al. proposed the following strategies: (i) enhancement of the catalyst surface area to facilitate efficient charge transfer of the photogenerated carriers to the surface; (ii) tailoring of the semiconductor band gap to improve light absorption; (iii) modifying the catalyst with adequate cocatalysts to allow absorption of the reactants and help the redox process. A step by step optimized pathway is essential because the photoreduction consists of a heavy photon-consuming process, involving a multistep mechanism with different reaction intermediates.

Following this strategy, some attempts have been reported where efforts have been made in order to enhance the surface area of the photocatalysts. The deposition of TiO<sub>2</sub> over a high surface area is one currently interesting and advantageous approach for this particular reaction. For example, in one particular study the authors report that highly dispersed tetrahedrally coordinated TiO<sub>2</sub> species incorporated into mesoporous MCM-type supports exhibited higher performances for CO<sub>2</sub> reduction to CH<sub>3</sub>OH and CH<sub>4</sub> compared to TiO<sub>2</sub> nanoparticles.<sup>487</sup> More recently, Yang and co-workers reported CO<sub>2</sub> splitting over TiO<sub>2</sub> dispersed on a SBA-15 support.<sup>488</sup> In addition, the high catalytic performance leading to CH<sub>3</sub>OH formation was also associated with a synergistic effect of the well-dispersed nanocrystalline anatase on the mesoporous matrix.

As referred to in previous sections, one challenge central to current research is to extend the absorption capability of the

catalyst in order to exploit a wider range of the solar spectrum and produce a higher amount of photogenerated carriers. In this context, Varghese et al. studied the photocatalytic solar conversion of CO<sub>2</sub> and H<sub>2</sub>O to hydrocarbons using N-TiO<sub>2</sub> nanotubes with Pt and/or Cu as the cocatalysts.<sup>489</sup> Recently Pan et al. proposed an InTaO<sub>4</sub> catalyst for visible CO<sub>2</sub> reduction.<sup>490</sup> This material has excellent potential since it is already widely used for water splitting under visible irradiation. Recently other visible light-responsive semiconductors have been reported as alternative photocatalysts for the CO<sub>2</sub> reduction reaction. BiVO<sub>4</sub> has been studied and found to lead to the selective formation of ethanol under visible light conditions.<sup>491</sup> Another approach would be the development of heterojunction structures formed by two nanostructured semiconductors with different band gaps. An example of this is the case of the CdSe quantum dot-sensitized TiO<sub>2</sub> system proposed by Yang and co-workers.<sup>492</sup> Using visible light, this heterostructured catalyst is capable of reducing CO<sub>2</sub> to CH<sub>4</sub> as the major product, with CH<sub>3</sub>OH, H<sub>2</sub> and CO as secondary products.

To summarize, it appears essential, as is the case for water splitting, that an adequate cocatalyst is employed. Its role in the active sites, which in turn are involved in reactant adsorption as well as in the redox process, is critical.<sup>489</sup> Also, the selectivity, which determines the final products, is strongly influenced by the participation of the specific cocatalyst. As stated earlier, the use of a Cu species as the cocatalyst has been widely reported for the CO<sub>2</sub> photoreduction process.<sup>482,493–497</sup> In all the reported cases, the formation of methanol was clearly favored. This indicates that the participation of copper is crucial in the redox process. From these studies, the conclusion is that the presence of isolated Cu<sup>+</sup> is the primary active site for photoreduction.

In a recent paper, Carpenter et al.<sup>498</sup> reported on one of the most researched processes of this field. It is one which mimics plant photosynthesis by coupling the photochemical splitting of water with the reduction of carbon dioxide with the aim of creating useful fuels. Their new strategy consisted of making the reducing agent recyclable instead of seeking to eliminate the use of an external reducing agent altogether. However, as Michl has pointed out, this is not a practical system. In spite of this, Carpenter's group has introduced a new concept that must be further developed before a commercially viable "artificial leaf" can be proposed.<sup>499</sup>

As outlined in the above strategies, the efficient photoreduction of CO<sub>2</sub> with H<sub>2</sub>O is fast becoming one of the most challenging tasks involving environmental catalysts. However, in practice the efficiency of CO<sub>2</sub> reduction has been demonstrated as being low when water is used as the reductant. It appears that greater detail of the mechanisms behind this reaction remain to be clarified. Within this context, Yang et al. had proposed a critical discussion on the CO<sub>2</sub> photoreduction process questioning the "fact or fiction" of this process.<sup>500</sup> After an in-depth and interesting spectroscopic study, they concluded that carbonaceous residues at the surface could participate in the formation of the primary products of the CO<sub>2</sub> reduction which would lead to an overestimation of the reaction rate. In summary, it appears that the conversion efficiency of CO<sub>2</sub> into valuable energy-bearing hydrocarbons is still in its infancy and much work remains in order to bring this technology to reality. A thorough understanding of the reaction mechanisms is indispensable for the design of high-efficiency and highly selective catalysts. Once this objective has been achieved, the morphology (besides surface area) as well as other important physicochemical effects can be addressed.

## 6. LIGHT HANDLING ASPECTS

### 6.1. TiO<sub>2</sub>-Based Systems

In the previous sections we detailed the effects of the two key physicochemical parameters involved in the control of TiO<sub>2</sub> structural and electronic characteristics: first, morphology, which is a complex variable that includes size, shape and secondary particle, porosity variables, and second, defect structure. As summarized earlier, two limiting situations were identified. These were a function of the best known morphological variable, namely, size, and concern the range 4–5 and 12–15 nm where differences in defect structure lead to distinctive electronic consequences. These, however, are concerned with localized, gap states without the influence of band structure. Below 5 nm, as a result of cation vacancies and amorphization, a p-type behavior may be suggested. On the other hand, above that point n-type bulklike behavior can be expected. In addition, it appears that, above 15 nm, the defect structure would be exclusively concerned with the surface. This contains ca. 5% of the atoms, and essentially, it could be envisaged that bulk behavior would result.

Shape is the other morphological variable with a known influence on the defect structure. There appears to be an increase in the number of undercoordinated surface atoms from elongated to isotropic geometries. For particles with a size greater than 5 nm a beneficial effect on the photocatalytic activity, derived from presence of (001) surfaces, is generally reported.<sup>40–44,501,502</sup> This indicates that elongated shapes would be detrimental for photoactivity with respect to isotropically shaped ones or any other shape that maximizes the presence of (001) surfaces. The photocatalytic influence of this (001) surface may be a trade-off of two opposing facts: the larger the chemical reactivity of the more open surface and the higher charge recombination expected by a higher surface/near-surface density of defects. There is, however, the question of whether the presence of alien (mostly fluoride) species which stabilize such (001) surfaces may contribute to the high photocatalytic performance observed. Recent studies support both possibilities. Some suggest that the fluoride contribution may not be dominant<sup>503</sup> while others tend to support the key catalytic role of fluoride.<sup>504</sup> Also the influence of the defect nature and number in the electronic properties and photoactivity of (001) surfaces is under debate.<sup>505</sup>

After light excitation both intraparticle and interparticle effects are important for the interpretation of the behavior of TiO<sub>2</sub> nanomaterials. Intraparticle effects are rationalized in terms of both the structural and electronic characteristics summarized in previous paragraphs. In addition, interparticle effects, particularly secondary particle size and porosity, appear to be important variables as well.<sup>506</sup> Size, shape and porosity thus appear to be key variables to control (i) light absorption vs dispersion and (ii) fast nonradiative and geminate-radiative de-excitation pathways, favored as size decreases and dominant de-excitation channels in the nano (e.g., below 15 nm) region.

Nongeminate radiative losses, and hence charge carriers with potential for the correct chemistry, are usually found in the visible range above 2 eV. For example, within the high energy region of the visible spectra, up to three processes are triggered by photons of ca. 2.0–2.2, 2.5 and 2.8–2.9 eV. Systems can involve either one, two or the three processes depending on the method of preparation and other so-far unknown variables. Decay pathways that occur below an energy of about 2.0 eV are usually ascribed to Ti(III) centers.<sup>80</sup> The interpretation of the electronic structure behind these three

de-excitation processes that is relevant to this work is, as described in section 2, not universal.<sup>69,71,85,91–93,96,97,106,507–510</sup> In spite of the lack of a unified interpretation, it is clear that minimizing the number of defects, more specifically the anion bulk vacancies, appears essential for enhancing photocatalytic activity for both UV and visible light excitations. Where the anion vacancies are concerned, their final role is linked to their structural/electronic energy dispersion properties. As discussed in section 2, a localized nature of their electronic states and ultimately their performance as recombination centers is the most likely case when they are located at bulk positions. In contrast, when anion bulk vacancies produce quasi-continuum states, the positive or negative role on charge recombination is likely related to their initial electronic occupation (or in other words to the number of defects and the corresponding electronic state energy position with respect to the Fermi edge).<sup>55–57,203,205,321,511</sup>

It should be noted also that the electronic consequences of these defect structures after light excitation can be complex. In the case where the electron transfer from surface defect states to surface chemical compounds results in a higher reaction rate than the detrapping step, the occupancy of the corresponding localized states would be much less than that derived from the Fermi level of the system and Fermi–Dirac statistics.<sup>289</sup> This leads to the creation of a pseudo-Fermi edge that can control the defect-derived electron behavior with subsequent consequences in the dynamic behavior of the charge carriers. This can occur, for example, on metal–oxide contact or in other situations. As described previously, this appears to be important for electron-related defects because of the fact that oxygen is a rather efficient scavenger; superoxide ions display long lifetimes of milliseconds.

With respect to nanosized semiconductors there is another relevant aspect, namely, carrier multiplication. As shown by Klimov et al., one photon with an excess of energy (over the band gap) can produce not one but multiple excitons. Up to 4 excitons per photon are possible for high energy photons. While the exact mechanism for this enhancement is still a subject of debate, high multiexciton yields in nanocrystals are likely due to factors such as the close proximity between interacting charges, reduced dielectric screening, and relaxation in translation-momentum conservation.<sup>512</sup>

Interparticle, or more generally speaking media effects, appear to be as important as intraparticle effects for the interpretation of light–matter interactions even in pure anatase nanomaterials. Due to the relatively poor control of particle size and morphology in crystalline oxide systems, materials with an average primary particle size in the 5–10 nm range can possess two heterosize contact structures with particles either above or below 5 and 12 nm. The first possibility is rather important since this would lead to a p–n union between any particles of a size below or above 5 nm. Here the Schottky barrier acts as a charge accumulation center and allows long-lived charge carriers with the potential to undergo chemical processes (Figure 19). Such p–n contacts have been previously mentioned with respect to other oxides such as ZnO,<sup>513</sup> but further experimental evidence is desirable. This type of complex interparticle contact that occurs around 5 nm, together with the fact that in nanomaterials nonradiative recombination is a multiparticle process that dominates the charge carrier relaxation process, supports the view that morphology variables such as size, shape, secondary particle size and porosity play a key role in controlling light–matter interactions. The second critical state is for sizes around 12 nm. Here the importance is in relation to the effect of surface states

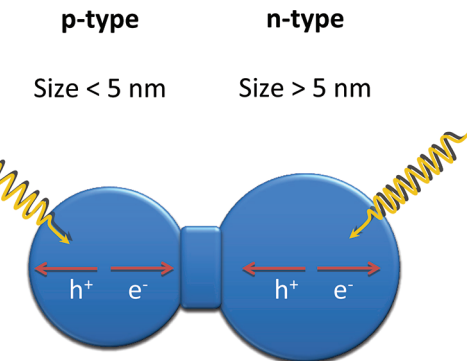


**Figure 19.** Charge dynamics after light excitation as a result of a p–n contact present in nano-TiO<sub>2</sub> as an inherent effect of polydispersity.

(as mentioned above). The heterocontact can potentially lead to a low energy state for electrons located in the smallest particle. Such an electronic state may display its own “separate” electron dynamic behavior.

Finally from a fundamental point of view the medium is also important in liquid reactions. This is due to the fact that, for both semiconductors and metals, the charged particles produced after light excitation display strong polarity-induced effects in the Fermi level position through solvation effects produced by a particular solvent. This effect needs to be considered in conjunction with the particle size effects in order to predict the chemical behavior on light excitation.<sup>73,514</sup>

The combination of intraparticle and interparticle effects discussed so far clearly emphasizes the fact that all the morphological variables concerning primary particle size and shape, particle size distribution (or, in other words, polydispersity) as well as secondary particle size and porosity are important in any description of the photoactivity of TiO<sub>2</sub> materials. Since complete morphological information is essentially unavailable in any reports published to date, it is not unexpected that the structure–activity link for photoactive materials remains in question. For example, the size-dependent contributions reported so far can be classified into three different groups.

The first group includes works which report an optimum primary size well below 10 nm. These are the gas phase photo-oxidations of 1-butene,<sup>515</sup> trichloroethylene,<sup>516</sup> and toluene,<sup>517</sup> as well as the liquid-phase hydrogenation of CH<sub>3</sub>CCH,<sup>518</sup> the photooxidation of rhodamine B<sup>519</sup> or the polymerization of a trisacrylate ester.<sup>520</sup> Although not fully explained, these studies infer that a strong quantum size effect dominates the catalytic properties. Two main factors are responsible: the first is the change in the redox potential suffered by both charge carriers as the band gap of the samples experiences a blue shift with decreasing particle size. As previously discussed, however, there is limited support of this theory for particle sizes above 3–4 nm. The second factor concerns the existence of midgap states associated with the surface charge-trapping centers. These have either a positive or negative effect depending on numerous experimental variables (as explained below). Both of these factors depend on primary size but also on other morphological parameters.

The second group of reports supports a size-dependence with a maximum of about 10–15 nm: the gas-phase photooxidation of CHCl<sub>3</sub>,<sup>521</sup> or the liquid-phase of acetone,<sup>522</sup> as well as the gas-phase reduction of CO<sub>2</sub>,<sup>523</sup> are examples. Finally, the third group consists of systems with photoactivity maxima well above a

limiting size where quantum confinement effects can play a role. The gas-phase photooxidation of trichloroethane<sup>524</sup> and hexane<sup>525</sup> and the liquid-phase of 2-propanol,<sup>526</sup> phenol,<sup>527</sup> methylene blue<sup>528</sup> and methyl orange,<sup>529</sup> are illustrative examples. In all these cases, the authors claim that the dominant effect of the recombination rate on the chemical reaction kinetics, which presumably should increase as size decreases, is not balanced by any of the positive effects coming from size confinement in the nanometer range.

Apart from the morphological properties mentioned above which affect photoactivity, one of the studies already described gives evidence of the importance of surface hydroxylation. The behaviors of two samples with rather similar morphological properties are analyzed.<sup>522</sup> A link between surface acid/base and particle size has been recently published indicating that an increase of acidity with decreasing size can be attributable to bridging hydroxyls.<sup>47</sup> Another recent study also emphasizes the role of acidity in regenerating the Ti surface sites after photoreaction as well as closing the catalytic cycle (enhancing activity but with no effect on selectivity).<sup>530</sup> Surface properties and particularly, acid/base properties are thus important.

After sunlight excitation, three important factors for modified  $\text{TiO}_2$ -based materials compared to  $\text{TiO}_2$ -alone nanomaterials emerge. These factors add complexity to the already briefly reviewed situation characteristic of  $\text{TiO}_2$  anatase-pure nanocatalysts. These concern visible light absorption and the corresponding charge-carrier handling (trapping and recombination), as well as surface modification. The first two factors are intimately connected with the doping/defect distribution. Of particular importance is the anion-derived defect distribution, whereas the third factor relates mainly to the acid/base properties and to a lesser extent to local properties of the surface active centers. The influence of such a set of properties on composite and single phase materials is therefore the main objective of the following subsections.

**6.1.1. Composite Systems.** The structure–electronic relationship in composite materials containing anatase as one of the components has already been described previously. Hence this section will try to answer two main questions arising from the structure–electronic effects specifically related to (i) UV vs visible photon absorption and (ii) the corresponding de-excitation processes. Following the scheme described in section 2, we distinguish between three main composite systems, namely, metal–anatase, oxide–anatase, and chalcogenide–anatase materials.

For metal–anatase systems, it has been firmly established that an electron transfer process occurs with UV light. This leads to the excited electrons leaving anatase and being collected at the metal phase. Upon light excitation, the metal Fermi level suffers a displacement to more negative potentials and becomes closer to the anatase conduction band, as schematically depicted in Figure 20. A more negative Fermi level shift indicates an improved charge separation and more reductive power of the composite system.<sup>21,85,514</sup> Alternatively a transfer of photons from the metal to the semiconductor via radiative decay of the surface plasmon states to excite semiconductor electrons could be proposed.<sup>155</sup> But this would not be a general phenomenon under UV light. In any case, the electron transfer is presumed to be a fast process which occurs in a few picoseconds, and depletes geminate (radiative) recombination by as much as 50%.<sup>84</sup> However, there is evidence that nongeminate trapped electrons also suffer the same type of process.

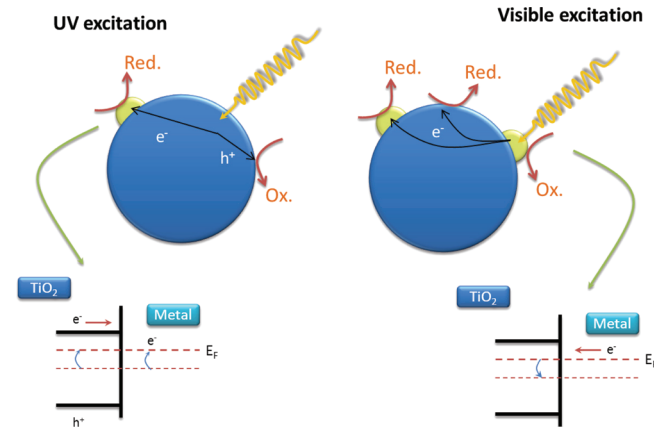


Figure 20. Scheme representing main electronic events for a metal/ $\text{TiO}_2$  nanocomposite system upon UV and visible light excitation.

Essentially, in the presence of a metal, it appears that geminate recombination is diminished and displays shorter lifetimes (the faster geminate recombination processes are less affected by presence of the metal). In addition it appears that trapped electrons are strongly affected by both anatase and metal particle size. The corresponding electron transfer of previously trapped charge carriers occurs typically in the nanosecond to microsecond region and seems to be disfavored by a decrease in the anatase primary particle size. The importance of surface states as the anatase particle size decreases and the potential effect on the surface-related pseudo-Fermi leveling (this is different from that of the nanocomposite) are invoked in order to interpret both the microsecond charge carrier lifetime domain and the adverse effects of nanometric anatase size.<sup>531,532</sup> In fact, it is well-known that photocatalytic reactions involving weak adsorbates (such as phenol) may be rationalized using such particle size premises. However, the presence of strong adsorbates and their concomitant influence on surface states may exert a more dominant effect in explaining photocatalytic performance than anatase particle effects exclusively related to size.<sup>154,533</sup> The metal particle size would also be expected to tune the nanocomposite Fermi level; the discrete electronic structure of the nanoparticles indicates that the shift in the Fermi level would be expected to be larger as the metal particle size decreases. It is, however, obvious that, in addition to size, other (morphological) properties of the metal distribution are also important if metal–metal electric interaction (e.g., distance between particles below 1 nm) is allowed. Hence, preparation variables are critical.<sup>21,85</sup> In fact, the crucial role of the Fermi level handling in charge recombination, electron chemical potential and photocatalytic properties has been demonstrated by using different metals.<sup>534</sup> Finally it should be mentioned that a pinning phenomenon may be present with nano- $\text{TiO}_2$  which limits charge transfer phenomena as well as any size-dependence phenomenon/influence among phases.

After visible light excitation, light absorption also occurs but through the metal surface plasmon resonance, as detailed in section 2.2.1. The excited metal nanoparticles are relaxed to the ground state within a sub-nanosecond domain. The electronic gas thermalizes through electron–electron collisions and electron–phonon coupling before being externally cooled by phonon–phonon coupling. But metal to anatase electron density transfer will also occur in ca. 50 ps with a yield (per photon absorbed) as high as 10–50%.

The effect of the anatase particle size has been addressed and showed no effect in the injection. It does, however, apparently influence recombination; it is faster as the anatase size decreases. This is attributed to the back electron transfer from anatase to gold process as well as the differences in electron diffusion within the anatase nanoparticle.<sup>535</sup> While this is not the general case expected for the metal–semiconductor contact,<sup>120</sup> it may be rationalized in terms of the absence of anatase band-position quantum size effects for sizes above 2–3 nm.

Effects of metal particle size and shape (and secondary particle or aggregation state) are primarily observed in the plasmon resonance energy. They can allow tuning of the absorption in the visible light photon range. This is particularly of interest for sunlight excitation in the 400–550 nm range because of the subsequent useful chemical consequences.<sup>536–538</sup> Recently, Kowalska et al.<sup>538</sup> reported the action spectra for different Au–TiO<sub>2</sub> systems with varying gold and TiO<sub>2</sub> sizes for the isopropanol oxidation reaction. They demonstrated that under plasmonic excitation a direct relationship between the gold size with the photocatalytic activity can be established. Thus, under visible irradiation, the greater the gold particle size (e.g., broader particle size distribution with larger mean and higher moments, particularly the variance), the higher the efficiency exhibited due to the larger number of photons absorbed. On the contrary, under UV conditions, smaller gold particles clearly produce higher photoactivities. Furthermore, the photocatalytic reaction rate strongly depends on the properties such as particle size, surface area and crystalline form of the titania. However, the TiO<sub>2</sub> influence on photoactivity only occurs through an effect on the morphological and/or physicochemical features of the gold particles. Although these results are an apparent contradiction of previous results by Du et al.,<sup>535</sup> they appear to agree with those of Robel et al. for CdS QD sensitized TiO<sub>2</sub>.<sup>115</sup>

Electron transfer from the (visible-light) excited metal particle to anatase will activate oxygen at the oxide surface. This potentially leads to radical species formation and/or the production of electron-deficient metal particles capable of attacking organic molecules (Figure 20). The positive charge produced at the metal particle is most likely stabilized by interaction with the anatase surface states.<sup>296,297</sup> Such a general view, supported by the previous discussion, has been recently challenged with respect to certain details. Theoretical simulations of the plasmonic effect suggest that a local metal–titania interaction, involving surface localized gap states of the TiO<sub>2</sub>, could be responsible for the photocatalytic activity enhancement using visible light. This is in contrast to the accepted charge transfer phenomenon involving the band states of the semiconductor.<sup>539</sup> We have already discussed (section 2.2.1) the presumed positive influence that cooperative or antenna effects may have on light handling and photoactivity. But at the moment current difficulties in controlling nanointerfaces prohibit any further progress with respect to real, high surface area materials. A statement considering future perspectives will be given in section 7.

From an applied point of view, upon sunlight excitation, processes triggered by UV and visible light photons occur simultaneously. A schematic representation of these charge transfer processes after UV and visible light excitation is depicted in Figure 20. The sunlight photon intensity distribution curve, however, indicates that visible light photon phenomena may in fact dominate when adequate metal-loaded photocatalysts are used. It could, therefore, be that electron transfer processes from metallic to titania phases are thus dominated. This of course

dismisses the “domino” effect of the carrier multiplication process potentially occurring in anatase nanoparticles on UV excitation. Within such limits, oxidation processes would, however, be expected to occur predominantly within the metallic nanoparticles. On the other hand, reduction processes can occur at both titania and/or metallic surfaces.<sup>21,22,507,540</sup> Such an explanation obviously requires the consideration of metallic redox states, a likely event occurring at the metal–titania interface as shown with the help of X-ray absorption techniques.<sup>541</sup> There is also the practical problem related to corrosion and/or dissolution of the metal by continuous use under some reaction conditions, particularly in liquid phase reactions. But, as previously pointed out, this is typically mitigated by the use of core–shell or three-component materials. On the other hand, it should be remembered that Naya et al. recently reported a wavelength-switchable function of the photocatalyst. The plasmonic excitation of an Au–TiO<sub>2</sub> system by visible light leads to the selective oxidation of thiol to disulfide while UV light irradiation leads to the reverse reduction reaction.<sup>542</sup> From these results it appears that the appropriate use of the light wavelength for noble metal-supported systems opens up the possibility for “a la carte” selective oxidation and/or reduction reactions. Finally, it should be mentioned that while we are discussing the contact between metals, typically noble metals such as Cu, Ag, Pd, Pt, Ir or Au, and titania there is also the possibility of photocatalytic effects of other elements (Cr, Fe, etc.) which seem to display a dominant ionic state at semiconductor surfaces which do not always produce a positive effect on the photoactivity.<sup>291,543</sup>

More complex situations occur when the titania semiconductor displays an altered band gap energy because it also allows visible light absorption by such phases. As previously mentioned, useful titania modifications can drive light absorption up to 550 nm, and on sunlight excitation this therefore leads to the opposite situation, namely, the dominance of charge carrier-handling phenomena which occur principally at the semiconductor instead of in the metallic phase. In this case, there are some reports indicating that the presence of noble metals at surfaces may not always lead to a favorable scenario with an enhancement of the photoactivity.<sup>544</sup> The metal state at the interface also seems to be of some importance here, and the stability of the oxidized states may favor activity.<sup>545</sup> The metal–oxide interface contact for anion-doped anatase materials has been recently addressed using theoretical methods.<sup>546</sup>

In addition to the metal–anatase system, the oxide–anatase system corresponds to another of the most broadly applied composite materials in the field of photocatalysis. For sunlight applications Cu<sub>2</sub>O/CuO and WO<sub>3</sub> oxides are among the more interesting, while Fe<sub>2</sub>O<sub>3</sub> is also extensively used but typically with visible light. These, together with the anatase–rutile system where one or both of the components are doped, complete the list of photocatalysts displaying stability and potential long-term use. Figure 21 describes the main charge carrier interphase flow expected for these nanocomposite materials on illumination. Discussion will be limited to anatase nanoparticle contact for particles greater than 5 nm and only for anatase–rutile systems the contact with anatase particles smaller than 5 nm is considered. The electronic states for the single oxides have been discussed previously in section 2.2.1 (Figure 7). The cartoon is clearly an oversimplification of the real processes in that it ignores pinning and other complex phenomena (e.g., multiple excitons per photon production) which can occur. It should be noted that our current understanding of this field is far from complete.

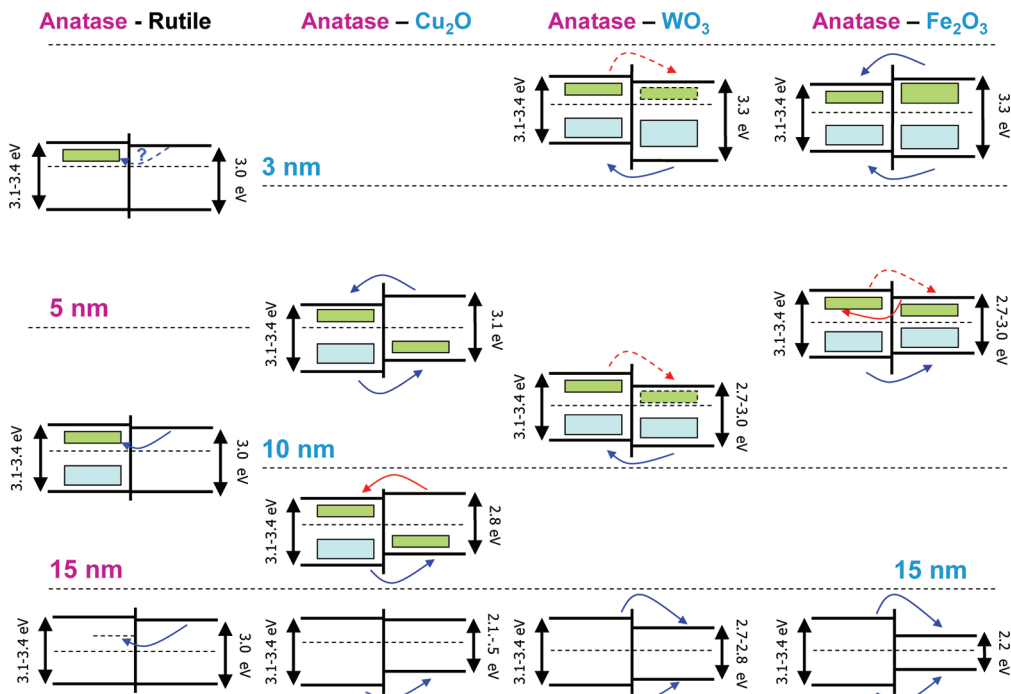


**Figure 21.** Size dependence of the electronic structure of several oxide–oxide nanocomposite systems. Valence and conduction bands are represented by the corresponding top and bottom edges, respectively. Blue/red arrows describe UV/visible light induced charge transfer processes.

Moreover, with the exception of the anatase–rutile nanocomposite system, basic research concerning charge creation and annihilation on light excitation, as previously summarized for the metal–anatase system, is essentially lacking in this field.

Probably, the best known anatase–rutile contact occurs with the Degussa P25 materials. Here structural and electronic interfacial characteristics have been thoroughly analyzed.<sup>99,116–118,143</sup> In P25, both anatase and rutile display large particle size (greater than 15 nm) and would therefore be expected to display a bulklike structural/electronic behavior. Small differences related to the rather limited band bending at the interface would, however, also be expected. However, the structural interface effects detailed in section 2.1.1 and which described both the absence of anion vacancies and the presence of localized states ascribed to tetracoordinated Ti species may drastically influence the interface electron flow between anatase and rutile as depicted in Figure 21. Thus, for a bulk-type contact (e.g., particle size above 15 nm), the electron flow depicted in this figure is the opposite to the currently accepted convention, justified on bulk band energy considerations.

In anatase–rutile systems, size effects concern exclusively the anatase phase and delineate the two regions, below 5 and 15 nm, respectively, where some differences with the bulk situation are expected. Below 15 nm, since the band gap is essentially constant and the existent punctual oxygen vacancies mostly (although not exclusively; see section 2.2.2) generate  $\text{Ti}^{3+}$ -type localized states, a relatively limited alteration of the bulk situation would be expected. However, the main difference is the surface vs bulk nature of the localized states associated with the (anatase–rutile) interface and the above-mentioned (both surface/interface and bulk) defect distribution. This, as previously discussed for unmodified  $\text{TiO}_2$ , may affect the Fermi level and charge trapping/recombination behavior as key differential properties. The Fermi level could suffer an excursion to higher energies as the size

grows; the Fermi edge is roughly at 1.5 eV from the valence band edge for 15 nm and 2.1 eV for 5 nm as depicted in Figure 21. Below or around 5 nm the situation is somewhat different. Here for thermodynamic reasons the raising of the Fermi level with respect to the anatase component compared to the previous situation would probably diminish the electron transfer from rutile. In contrast, such electrons would have an enhanced chemical potential due to the more negative energy values of the corresponding electronic states. It should be remembered that this is an oversimplification since the real structural/electronic information for particle sizes below 4 nm is still rather limited. As roughly represented in Figure 21 this could very well imply a completely different defect nature and distribution. Concerning modified materials for adequate handling of sunlight, potential ways to produce efficient anatase–rutile sunlight-active systems could involve either (i) the doping of the rutile phase with cations allowing visible photon absorption, modification of the conduction band and promotion of electron transfer to anatase defect-derived states or (ii) N,F-codoping of anatase. Again, this allows visible light absorption, modification of the valence band and promotion of hole transfer to rutile. A combination of these two strategies has been explored recently.<sup>547</sup>

The bulk-type contact between anatase and  $\text{Cu}_2\text{O}/\text{CuO}$  (e.g., the presence of CuO at the surface layers) has not been well-studied, but the band energy leveling would be adequate for enhancing charge separation only on UV illumination.<sup>276</sup> Size, however, drastically changes the situation. Around 10 nm, the modification of the  $\text{Cu}_2\text{O}$  band gap and the nanocomposite Fermi level position provide an effective way to transfer visible-light excited electrons from the copper oxide to anatase and promote electron–hole separation.<sup>150,279–281</sup> This should lead to highly active sunlight-driven photocatalysts which, however, to date have been minimally analyzed.<sup>548,549</sup> Below 10 nm, the band gap is expected to reach a value close to 3.0 eV which limits

the absorption of visible light photons. One such case as illustrated in Figure 21 would indicate the adequacy of the Cu<sub>2</sub>O–TiO<sub>2</sub> contact for UV excitation. It is worth noting that holes at Cu<sub>2</sub>O can be used for pollutant attack or, what is less likely due to kinetic constraints at room temperature, to oxidize Cu<sub>2</sub>O to CuO in the presence of water (particularly for liquid-phase reactions). Nevertheless, it appears that, irrespective of the initial Cu<sup>2+</sup>/Cu<sup>+</sup> state of the oxide, the Cu<sup>+</sup> state is the stable one under reaction conditions using sunlight.<sup>550</sup> In a Cu<sub>2</sub>O material, shape can also play an important role if this phase plays a catalytic role. This is a result of the neutral/positive electrostatic nature of the (100)/(111) faces and their subsequent effects on the reactant molecules.<sup>551</sup>

The case of WO<sub>3</sub> is another complex one as several polymorphs, such as the monoclinic *P2*<sub>1</sub>/*n* and orthorhombic *Pnma*, have been detected on contact with anatase.<sup>148,149</sup> Considering a band gap of ca. 2.7–2.8 eV, typically ascribable to the monoclinic polymorph,<sup>276</sup> Figure 21 indicates that the bulk contact between anatase and WO<sub>3</sub> allows energy and exciton transfer between components but would be rather inefficient in promoting charge separation for both UV and sunlight excitation. For WO<sub>3</sub> particles below ca. 10 nm, the band modification of the solid should allow efficient hole transfer from WO<sub>3</sub> to anatase upon light absorption. But the WO<sub>3</sub> band gap energy is large enough to severely limit visible photon absorption. The presence of gap states may allow electron transfer from TiO<sub>2</sub> to WO<sub>3</sub> and adequate charge separation. As depicted in Figure 21, using a dashed line the thermodynamic reasons appear to favor the case where WO<sub>3</sub> particles are close to 10 nm. For particles well below 10 nm, WO<sub>3</sub> is considered to be mainly amorphous and hence the capability to absorb visible photons and handle charge carriers to produce useful chemistry is essentially lost. Thus, in the WO<sub>3</sub>–anatase system, a strong size effect is expected for sunlight excitation and positive effects arising from interphase charge transfer can only be envisaged in a narrow size domain mainly governed by WO<sub>3</sub> characteristics. Correlation with the experimental result is, however, far from trivial. Both UV<sup>552,553</sup> and visible<sup>554–556</sup> light excitation produce positive effects on the photocatalytic elimination of phenol and methylene blue for samples where WO<sub>3</sub> is mostly amorphous. In this case, the main factor governing the photoactivity enhancement appears to be related to an optimum acidity. This is obtained with a tungsten content of around 4 wt % for all cases. Samples either above or below this point present lower photoactivities. WO<sub>3</sub> is therefore a case where surface properties, particularly acidity, most likely rule or at least constitute one of the important factors controlling the photocatalytic activity enhancement. A full analysis of surface vs electron–hole recombination as a function of the particle size remains, however, part of future studies.

Contact with bulk alpha Fe<sub>2</sub>O<sub>3</sub> lacks adequate electronic characteristics to efficiently separate the charge carrier for visible light excitation. The only positive effect might be derived from UV-excited electrons on anatase which may be efficiently transferred to the Fe<sub>2</sub>O<sub>3</sub> phase. Apparently, some changes can be expected when contact among nanometer oxides occurs with a Fe<sub>2</sub>O<sub>3</sub> material having a primary particle size greater than 3–4 nm. As Figure 21 illustrates, visible photon-excited electrons can be transferred to the anatase phase with the adequate defect derived density of states. However, systematic studies of the anatase–hematite contact as a function of the particle size are missing from the literature in the context of its use for light excitation. Only a few reports analyze this nanocomposite system

for visible<sup>557</sup> or UV/visible<sup>558,559</sup> light excitation. The latter studies indicate that defect-rich nanosized FeO<sub>x</sub> patches/clusters in fact transfer visible-light-excited electrons to the anatase phase. This is schematically depicted in the central panel of Figure 21 (anatase–Fe<sub>2</sub>O<sub>3</sub> column). This indicates that charge transfer is strongly affected by defect-derived states and limits the utility of models exclusively based on band structure energy analysis. The corollary is that although Figure 21 illustrates the present knowledge of oxide–oxide contact, clear deficiencies are expected to explain light handling phenomena through interfaces.

Other oxides such as CeO<sub>2</sub><sup>560</sup> or Bi<sub>2</sub>O<sub>3</sub><sup>121,128</sup> are useful in the context of their interaction with titania. The latter is particularly well suited as valence/conduction relative band positions should promote (visible-photon generated) electron transfer from Bi<sub>2</sub>O<sub>3</sub> to anatase and (UV-photon generated) hole transfer from anatase to Bi<sub>2</sub>O<sub>3</sub>. However, only Bi-containing oxychloride phases display stability under photoelimination conditions.<sup>381,382</sup> The use of FeTiO<sub>3</sub> as a material closely related to Fe<sub>2</sub>O<sub>3</sub> can be also mentioned as it should allow visible-photon excited hole transfer to anatase.<sup>125</sup> Other complex oxides such as LaVO<sub>4</sub> or Bi oxyhalides are also very useful in this context. This is because, similar to Bi<sub>2</sub>O<sub>3</sub>, they lead to an efficient electron–hole charge separation on sunlight-excitation.<sup>127,129</sup>

Finally another composite system which has been carefully investigated concerns chalcogenide–anatase. CdSe, CdS, PbS, PdS, and PbSe are among the most used chalcogenides which, however, lack stability in specific environments due to anodic photocorrosion by holes and the subsequent release of cations into the media.<sup>21,22,115,120,561,562</sup> To limit this problem, core (chalcogenide)–shell (anatase)<sup>563</sup> architectures or structures maximizing interaction between phases (like anatase nanosheets supporting CdS nanoparticles)<sup>564</sup> have been synthesized. A more satisfactory solution is found for a three-component anatase and Au/CdS core–shell contact. This system protects the chalcogenide from photocorrosion by a constant electron supply through the metal phase which minimizes hole attack.<sup>139,565</sup> Alternatively, polymer–MS<sub>x</sub> nanocomposites can effectively drain holes produced at the chalcogenide.<sup>140</sup> Figure 7 displays the typical band gap behavior vs size for several chalcogenides (CdSe, PbS) and indicates the potential and tunability of these systems to absorb/handle visible light.<sup>21,22,114,115</sup> Under visible light, the anatase–chalcogenide charge separation works by the initial absorption of visible photons by the chalcogenide; electrons generated can be transferred to the anatase phase for chalcogenide sizes above 2 nm. Here the gap approaches the UV region.<sup>21,22,115,120,566</sup> Moreover, the detailed analysis of Kamat and co-workers showed that the driving force of the electron transfer is, as expected, the energy difference between the conduction band energies of the two phases involved. This means that by decreasing the particle size of the chalcogenide the transfer is strongly favored. Differences of 3 orders of magnitude in going from 8 to 3–2.5 nm particles are displayed.<sup>120,566</sup> In liquid-phase reactions, modulation of the TiO<sub>2</sub> conduction band-edge can be reached by tuning the pH. This produces changes in the electron transfer of about 1 order of magnitude.<sup>567</sup> Charge recombination shows an expected strong dependence on light intensity, with charge transfer between phases favored with a light intensity below the one corresponding, roughly, to 1 photon per particle.<sup>561</sup> Under such conditions, an optimum charge separation coverage of the TiO<sub>2</sub> surface typically requires a relatively low content of the chalcogenide.<sup>568</sup>

For other cases this does not appear to be the key to controlling activity.

**6.1.2. Single Phase Anatase Systems.** As has been detailed previously, when considering single-phase doped materials there are three main relevant factors that alter the behavior with respect to nano-TiO<sub>2</sub>. The importance of the first of these is often dismissed and concerns the surface effects which in turn are related to the adsorption of pollutants as well as the thermodynamics and kinetics of the reaction. Changes with respect to pure anatase-TiO<sub>2</sub> reference systems with similar morphological properties (primary particle size or shape and porosity) can be based either on the introduction of new species such as, for example, strong M=O bonds originating in alien species like Mo or W<sup>19</sup> or in acidity/basicity variations.<sup>530</sup> Important surface-related reaction rate effects on the photocatalytic activity of Zr, W, Mo-containing anatase materials have already been mentioned.<sup>152,291</sup> The other two factors are intimately related to the electronic effects generated by the presence of doping species, and these take into account the change in light absorption as well as the charge carrier fate/properties. The relative importance of electronic vs surface chemistry effects can be roughly estimated using UV vs visible light excitation, and these exhibit the corresponding enhancement factors with respect to an adequate anatase single-phase sample. Surface “chemical” effects should be roughly independent of the photon energy.

In earlier sections we separated the cases for low and high doping levels since the electronic effects depend primarily on the localized/delocalized nature of the doping-induced states. It should be noted that strictly speaking localized levels can be present at low doping levels while delocalized ones can be present for both levels. Delocalized, electronic defect-derived density of states at low doping levels can occur when a strong overlap takes place between the original solid (anatase) bands and the impurity-derived density. Of course, the strong mixing of “partial” electronic densities means that, according to quantum chemistry rules, no strict correspondence exists between the doping plus anatase “isolated/initial” electronic densities and the total electronic density of the solid. The isolation of the component electronic wave functions in the “final”, multicomponent system is only possible in an ionic bonding situation. This requires, for example, an absence of covalent contribution to the cation–anion bond.

Since doping strongly promotes disorder in the anatase nanoparticles, any having a primary particle size below 5 nm can be considered essentially as disordered materials just like the original, pure TiO<sub>2</sub> nanoparticles of such sizes that already have a strong degree of disorder. This means that the zone below 5 nm is even more complex to explore in doped-TiO<sub>2</sub> materials than in pure, nano-TiO<sub>2</sub> ones. For this reason, the discussion will be limited to sizes above the cutoff limit. Our focus will be on the nm range between ca. 5 (strong amorphization below this point is expected) and 12–15 (bulklike behavior above such point). It should be remembered that anatase particles with sizes around 7 or 10–12 nm should lead to “heterogeneous” physicochemical properties. This is explained by the typical variance of the particle size distribution which implies the presence of a certain fraction of entities either above or below the two cutoff (5/15 nm) limits. As has just been explained for unmodified TiO<sub>2</sub>, real oxides therefore bring about a complex scenario for the interpretation of the experimental observables.

**6.1.2.1. Low Doping Levels.** As discussed in previous sections such as section 2 of this review, typical cations can lead to two

well-differentiated situations. The first is characterized by the presence of localized gap states derived from the cation and/or the charge neutrality states. On the contrary, other cations are able to interact with the anatase valence or, more frequently, the conduction bands. It must be emphasized that apart from the cation states it is rather important to consider whether charge neutrality leads to cation or anion vacancies. In addition, the nature of the gap states, either localized or band-type, must also be considered.

Within this simple structural framework light absorption can be interpreted. Size and, more generally speaking, morphology effects have been described for both cation and anion stoichiometry defect situations in section 2. Some general structure–electronic links and consequences as a result of light absorption were described for nanosized materials.<sup>19,110,111,113,165,169,170,172</sup> To summarize, for all cation low content doping cases and assuming primary particle sizes above 5 nm, size effects should mostly be related to charge handling and would be essentially minor for light absorption. This is true for example for a constant band gap if we assume the same behavior as observed for the bare anatase oxide. Gap states and polydispersities in the 5–15 nm range would, however, play a different role for specific cation-doped materials than that driven by the size-dependence described in Figure 7 for pure, nano-TiO<sub>2</sub>. A reasonable parallel with bare TiO<sub>2</sub> material (a situation explored at the beginning of section 6.1) is only applicable to systems where it is implied that anion vacancies exist as stoichiometry defects. The case of V (isovalent with Ti) can be highlighted as an example of a system which leads to band gap modification by doping where anion-defects are generated exclusively by size. The representative example of Cr is a case of a multiple oxidation cation (as occurs also with Co and Mn) which leads to anion vacancies. No general trend concerning the band gap modification of anatase has been discussed for these cases. Another possibility such as the presence of cation stoichiometry defects on anatase would result in a relatively simple situation due to the high uniformity expected at both local and long-range order(s). In such cases, there is little evidence of the presence of localized gap states (as would be expected if structural heterogeneity such as is found in Fe appears). It appears that a modification of the gap is encountered in most cases such as for Mo and W, and possibly also in well-ordered Fe. Hence, this is responsible for the corresponding light absorption modifications.

Charge handling aspects are the next to be considered. As initially discussed by Bahnemann et al.,<sup>569</sup> we must consider that the localized gap states with respect to bulk species are essentially recombination centers. Their presence at the surface can be either beneficial or detrimental depending on two main factors. The first is the relative energy with respect to the anatase bands. As addressed in Irie et al.’s work, for ions grafted at the anatase surface, localized states lying below, but close to, the anatase conduction band are capable of trapping excited electrons and active oxygen as a result of visible light excitation.<sup>326,570</sup> The second relates, obviously, to the nature of the reaction. Whereas efficient electron capture is required for the elimination of pollutants (mostly produced by a hole-related species attack), it may prove detrimental if a reduction reaction (CO<sub>2</sub>) needs to be performed. On the other hand, “nonlocalized” band-type states located at the gap may allow two-photon processes but, as mentioned previously, there is, to our knowledge, no single experiment in the literature concerning high-surface anatase materials which describes this situation. As stated earlier, another

situation which also needs to be analyzed is the result of cations leading to a merging of alien electronic states with adequate anatase (mostly conduction band) states. In such cases, a narrowing of the gap is expected for relatively low concentrations (possibly above 2–3 atom % but definitely around 5 atom %). With respect to charge handling, size and morphology effects are numerous. However, in the early part of section 6.1, we outlined the general framework in which their influence in de-excitation or relaxation channels can be described for unmodified anatase. As discussed below, only rather limited information is available for cation-doped materials.

Experimental measurement of charge carrier lifetimes is usually focused on UV-excited low-doped anatase nanomaterials. But as a starting point, it is possible to distinguish between those systems having either surface or bulk species. In all cases it appears, however, that the only charge carriers with a direct involvement in the chemistry of the system are those with lifetimes near or above a microsecond; this was originally proposed for pure anatase<sup>96,97</sup> but has also been claimed for doped samples.<sup>571,572</sup> We can thus speculate that doping species can have an influence on different temporal regions of the charge carrier recombination phenomenon with subsequent influence on the chemistry, or not, as the case may be. An increase in the charge carrier lifetime in the microsecond region has been experimentally observed for cases where Sm and Gd<sup>572</sup> are surface species, and for Fe<sup>573</sup> and Cr/Sb<sup>573</sup> as (co)doped bulk species. Positive effects on time scales longer than a microsecond were also reported by Gratzel et al. for Fe<sup>3+</sup> and V<sup>4+</sup>.<sup>574</sup> Negative effects on surface species have been observed for Cr and Mo by Wilke et al.,<sup>162</sup> Co, Cr, Cu, Fe, Mo Mo, V and W by Palmisano and co-workers,<sup>291,575</sup> and in the case of V, Fe, Cu, Zr and W bulk-doped species by Nagavendy et al.<sup>169</sup> So, even for cases where the doping ion at low content is the same and the structural situation is relatively well-defined (at least in terms of presence either at the surface or the bulk), very different results are experimentally observed. This is closely connected with the fact that after light absorption there are a multitude of relaxation channels and the fact that they depend to a great extent on the intra- and interparticle morphological properties. As discussed earlier for pure nano-TiO<sub>2</sub> (section 6.1), nonradiative recombination appears to be the main de-excitation channel for anatase-based nanosystems. This process seems to be connected with a significant number of morphological properties of the solid including porosity and secondary particle size.

In spite of these problems, we can detail the case of Fe as the most studied doping cation. As a general rule, positive effects on the photoactivity at very low loadings, below 0.5–1 atom %, are typically observed. This can be justified, as mentioned earlier, on the basis of the potential of this species to capture both electrons and holes, thus playing a direct, positive role on recombination rates. This particular case is highlighted here since it is the only one where some systemic studies can be found which address the optimum content of Fe vs particle size. Although these are, of course, for UV excitation, they can be roughly applied to visible light and sunlight as far as the size effects on the main charge carrier recombination events are concerned. Figure 22 summarizes the results for the optimum Fe doping content as a function of particle size.<sup>109,317,318,576–580</sup> Although to describe the system morphology using the particle size is, as explained earlier, only a rough approximation, we can still see that in a number of cases there is a trend to lower optimum concentrations as the primary particle size increases. Since no differential

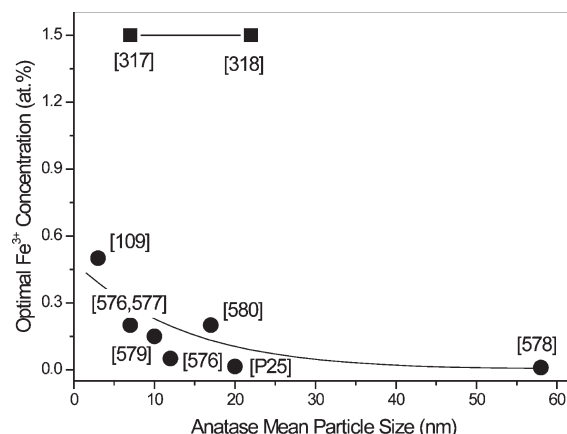


**Figure 22.** Optimal Fe<sup>3+</sup> concentration (atom %) in nano-TiO<sub>2</sub> as a function of particle size under UV irradiation. Numbers refer to original data publications or the Degussa P25 material data sheet.

effect of (the nature of) anion vacancies as a function of size is expected in the Fe–TiO<sub>2</sub> system, and assuming a similar local order in all systems, we clearly see the effect of the mean free path of the charge carriers on the optimal Fe concentration. Therefore, an exponential decay due to the effect of the mean free path on recombination rate up to ca. the 15 nm size can be envisaged. Here, as has been previously stated, the influence of size on the electronic properties becomes negligible. Experimental data are, however, not always in agreement with this trend, and some examples of conflicting reports are included in Figure 22. The presence of two different trends may be grounded in differences in local structural properties since it is well-known that Fe can produce a variety of structural situations. As stated previously, the presence of Fe–O–Fe contacts and the heterogeneous distribution of Fe with increasing concentration at the surface are typical of “heterogeneous” samples even at rather low content (>0.5 atom %).

It should be mentioned that Fe–TiO<sub>2</sub> is a prototypical system where the presence of a variable surface chemistry has been well established. This can be considered in terms of surface concentration and local (acid/base and OH-related) properties which arise as a function of the preparation method.<sup>317,580</sup> Also, the presence of Fe in the liquid medium though lixiviation is well-known. Once extracted from the solid, readsorption/desorption surface Fe species are observed in numerous aqueous reactions (mainly in the presence of carboxylic acids). These could very well add a non-negligible “homogeneous” contribution to the activity.<sup>301,302,581</sup> Finally, and again depending on the preparation method, it is not uncommon that Fe doping ends up at an Fe/TiO<sub>2</sub>:TiO<sub>2</sub> composite heterojunction, with subsequent influence on the photoactivity.<sup>582</sup> All such phenomena must be jointly considered when interpreting the activity, as well as the morphology dependence of the activity, for Fe-doped TiO<sub>2</sub> samples.

In the case of low-dopant loading, visible light absorption occurs differently in anion-doped materials. As discussed previously, only in the N/F case and a few synthetic methods for N is there some experimental evidence of high doping levels for anatase networks. In the case of S, it could be borderline between high and low doping levels, although, since electronic effects appear not to be localized, this particular case will not be discussed now. The remaining cases are characteristic of low

doping levels and should, as a general rule, generate localized states. The most analyzed system is N-TiO<sub>2</sub>. Here it has already been mentioned that there is prevalence of impurity-derived states near the valence band. Their coalescence (or not as the case may be) with the valence band has also been previously addressed. But it is pertinent to mention the presence of, generally speaking, three types of localized states around 0–0.2, 0.5–0.6 and 0.8–1.0 eV above the valence band. The nature of these states has been discussed in section 2, and these states together with those states observed near the conduction band were schematically depicted in Figure 7.<sup>6,73,193,194,198,200,201,203,508,583,584</sup> Majima's group carried out the majority of the experiments concerning charge carrier behavior in N-doped anatase materials.<sup>100,585</sup> They suggested that hole attack to most of the pollutants can be thermodynamically inhibited and only electron-derived O<sub>2</sub><sup>-</sup>, O<sub>2</sub> and (subsequent) •OH radicals can lead to the degradation of the organic molecules. It appears that UV light can give rise to all these radicals while visible light can only produce the O<sub>2</sub><sup>•</sup> radical. We also recall here, as described in previous sections, the importance of surface species (more precisely surface sensitization) on visible-light induced photoactivity for N and/or C-containing systems.<sup>251,252,586</sup>

A relatively similar case occurs with I-TiO<sub>2</sub> nanomaterials. However, these materials display localized states near both the conduction and valence bands of anatase.<sup>235–238</sup> In fact, as mentioned earlier, the presence of two local environments (A–Ti–A vs A–Ti–O or A–O–A vs A–O–Ti) or two, separate (localized) densities of states for doping and charge neutrality species is possible. This could be frequently the case in anion-doping systems (at least with respect to cation-doping ones) and may lead, as in the I-TiO<sub>2</sub> system, to localized states near both the conduction and valence bands of the anatase. In spite of the different electronic situations with respect to N-TiO<sub>2</sub>, the hole attack at the pollutant molecules again seems inhibited for thermodynamic reasons and only the oxygen path appears available.<sup>237</sup> The limited availability of holes to produce the desired chemistry using visible light seems, in any case, a universal constant for all N, I, and C low-level doped anatase materials.<sup>100,237,585,587</sup>

**6.1.2.2. High Doping Levels.** The presence of some impurity-derived density of states merged mostly with conduction bands at “low doping levels” as well as the bandlike structure of all states expected for cation loadings around or above ca. 5 atom % will be treated in more detail here. In the case of “low doping levels”, although these are known to lie well below 5 atom %, their cutoff levels are poorly established. Probably they lie somewhere around above 2–3 atom %. The first case may be typical of V if it is present at the bulk, i.e. in the V<sup>4+</sup> state.<sup>174</sup> As previously mentioned, most successful approaches to generating high photoactivity for highly loaded materials appear to be connected to cations such as W, Mo. Although currently less well-defined in the literature, Nd and Ce can merge with the anatase bands (conduction band), and drive toward an adequate red shift of the band gap. Simultaneously, they can present high structural order and the absence of local ordering effects. Ca, Zr and Sn (Sn<sup>4+</sup>) generate a blue instead of a red shift probably as a consequence of amorphization and Ce can additionally present several poorly crystallized phases together with anatase. The red shift of the anatase band gap has been measured as a function of the heteroatom content, and Figure 10 summarizes the published information. Differential effects with nano-TiO<sub>2</sub> can be minimal with respect to charge carrier handling and recombination. This

appears to be because these metals (in the high doping region) are expected to omit participation in trapping processes since their electronic d-states are delocalized in the conduction band. Although, to the best of our knowledge, there is no experimental information available about charge carrier dynamics for these high doping level systems, apparently, there is a correlation between the presence of local heteroatom ordered structures (M–O–M) and a potential increase in the recombination process. In some cases, therefore, local middle-order range-favoring homocation bonding situations would be expected to drive the creation of localized gap states. Such local structures appear to occur in varying quantities or with different probabilities, with the increasing heteroatom content for all the doping cations mentioned above. However, they appear inherent to systems such as Nb, which also display high solubility limits.<sup>19</sup> The large band gap decrease together with the limited potential influence on recombination can explain the high photoactivity observed for some cation-doped systems (Mo, Nd or W) after sunlight excitation.

With respect to anion-doped materials, the high doping level region has more or less been dismissed from the interpretational analysis of the charge carrier dynamics. It is only in the case of S-doped nanomaterials that there appears to be some information available.<sup>587,224</sup> S-doping alters the valence band through an important O 2sp–S 3s orbital mixing. This occurs independently of the anion loading. We are thus considering a system where the valence band is modified, and, at least from a theoretical perspective, a red shift of up to 1 eV can be obtained.<sup>327</sup> This should allow efficient use of the visible part of the sunlight spectrum, but, again, the inability of holes to oxidize organic species is observed. It should be noted that S may play a major role as a surface sensitizer in visible-excited systems.<sup>224</sup> If this is generally the case, then the electronic effects on band gap would consequently play a minor role.

## 6.2. A<sub>x</sub>B<sub>y</sub>O<sub>z</sub> and Nonoxidic Photocatalysts

Any improvement in the photocatalytic activity as a result of visible absorption may involve both structural and electronic aspects. As previously described, the photoactivity of these A<sub>x</sub>B<sub>y</sub>O<sub>z</sub> materials is essentially not related to their surface area values. This is clearly in contrast to oxide-based, particularly titania, photocatalysis. In a recent review Zang et al. analyzed the effects of micro and nano structuration of Bi<sub>2</sub>WO<sub>6</sub> photocatalysts.<sup>588</sup> As widely discussed in early sections, Bi<sub>2</sub>WO<sub>6</sub> superstructures including flower/sphere-like, nest/tire/helix-like and nanocage assemblies are constructed by nanosubstructures. As summarized in the above-mentioned review, such diversity of shapes clearly affects the final photocatalytic behavior.<sup>588</sup>

A further analysis of the efficiency values obtained, for example, for materials useful in the water splitting reaction (section 4) was recently reported in a comprehensive review article.<sup>415</sup> Values in the range from nearly 0 to ca. 95% were reported. This fact together with the existence of rather high quantum efficiencies or even marked differences for the same material (for a reaction where morphological parameters are expected to weakly affect photoactivity) means it is worth presenting some general considerations. First, as is well-known, some physical phenomena such as photon scattering and non-radiative and geminate-radiative recombination processes must affect the quantum yield values since they diminish the number of chemically efficient absorbed photons. As discussed above for anatase, which is the most intensively studied material, the

geminate recombination process dominates radiative recombination for nanosize materials by about 90%.<sup>106</sup> As detailed in section 2, the dominance of nonradiative and geminate deexcitation processes in nanosized materials can be generalized based on the fact that anatase is one of the best systems performing light to chemical energy conversion. Consequently any apparent quantum yield values higher than 20–30% might reasonably be questioned. It can be safely concluded, therefore, that the correct settlement of either the overall or the apparent quantum yield in order to allow comparative analysis of the different results reported turns out to be crucial. Clearly this still needs to be addressed. While it appears that morphology effects could be of limited influence in justifying the broad range of quantum efficiencies reported, it is also possible that the differences reported for the same material may in fact have physical grounds in specific cases. These could account for the defect distribution in nanometer solids. Generally speaking, and as previously pointed out, for sunlight-operated photocatalysts, there are several common approaches for the development of visible light active photocatalysts that need to be considered: ion doping, synthesizing new compounds through substitutional doping or the formation of solid solutions.

In order to achieve these it is necessary to classify the chemical elements for the development of visible light handling materials into four groups.<sup>329</sup>

- (i) Chemical elements participating in the crystalline and electronic structure of a single phase: metal cations exhibiting  $d^0$  or  $d^{10}$  electronic configuration ( $Ti^{4+}$ ,  $V^{5+}$ ,  $Nb^{5+}$ ,  $Ta^{5+}$ ,  $Mo^{6+}$ ,  $W^{6+}$ , ...). Such materials present a conduction band composed of d or hybridized sp orbitals. Meanwhile the valence band is mainly formed by an O 2p orbital in the case of oxidic catalysts. In other cases, using Se, S or N instead of O could lead to selenide, sulfide or nitride-based catalysts.
- (ii) Elements that participate in the crystal structure but not in the energy level construction. For example, they merge with the pre-existing band structure in relatively nonimportant energy regions: these sets of elements normally affect the crystalline structure by stabilizing certain crystalline phases. For example,  $Y^{3+}$  and  $La^{3+}$  are widely used for the stabilization of crystalline structures during sintering. This leads to higher crystallinity and smaller crystal size.<sup>589</sup>
- (iii) Ions forming impurity gap levels as dopants.
- (iv) Elements acting as cocatalysts.

Taking these into consideration, a huge number of materials have been recently proposed that exhibit interesting visible light photoactivity as a result of tailoring the visible light absorption power. Within this context and as has been shown before, bismuth-based materials constitute a good alternative for visible photocatalysis. The hybridization of the Bi 6s orbital with the O 2p leads to a higher position of the valence band top-end. However the individual structure clearly affects the configuration of the bands. Hence, different crystalline structures result in a different participation of the Bi orbital in the valence band and this subsequently leads to different band gap values. As mentioned above,  $BiVO_4$  mainly exists in three crystalline phases with the monoclinic structure being the more photoactive. Its different photoactivity can be explained by considering the electronic aspects. It has been reported that the tetragonal and monoclinic structures present a significant band gap variation. This is due to an unequal participation of the Bi 6s orbital in the valence band.

In the meantime, for the tetragonal  $BiVO_4$ , which is a UV-absorber, the top of the valence band is composed of only the O 2p orbital. In the case of the monoclinic form, the Bi 6s and O 2p orbitals hybridize and contribute to the valence band.<sup>590</sup>

The same Bi 6s + O 2p hybridization and the subsequent band gap narrowing can be observed in other Bi-based materials such as  $CaBi_2O_4$ ,  $Bi_2WO_6$  and  $Bi_2MoO_6$ .

Another band gap tailoring approach might be achieved by modifying the conduction band. In this case, the contraction of the band gap would be completed by lowering the bottom of the conduction band. This is the scenario for  $NaBiO_3$  where the bottom of the conduction band is created by mixing the Na 3s and O 2p orbitals. This band tailoring leads to the visible activity of this material. Thus, sodium bismuthate has exhibited good performance in the photooxidation of 2-propanol in the gas phase at  $\lambda \geq 460$  nm as well as for methylene blue (MB) bleaching in the liquid phase at  $\lambda > 400$  nm.<sup>334</sup> Other authors report the photodegradation of acetaldehyde using  $NaBiO_3$  that reaches about 80% and a full degradation of methylene blue within one hour using  $\lambda \geq 440$  nm and  $\lambda \geq 420$  nm, respectively.<sup>335</sup> Another example of conduction band modeling is the complex hybridization found in  $In_{12}NiCr_2Ti_{10}O_{42}$ . Here, the conduction band is composed of the mixed Ti 3d + In 5s + Cr 2d and Ni 3d orbitals.<sup>591</sup> Conduction band engineering would also be affected by the electronegative character of the cation participating in the orbital mixing.<sup>348,412</sup> Thus, the more electronegative the cation, the lower the location of the conduction band and therefore the lower the band gap values.

Using synchrotron diffraction data in combination with DFT calculations, it is reported that, in  $Sm_2Ti_2S_2O_5$  oxysulfides, the overlap of the O 2p and Ti 3d orbitals is responsible for the covalent bonds between the T and O atoms. In addition, the presence of S 3p orbitals overlapping with the O 2p and Ti 3d states results in the dispersion of the valence band. This complex orbital mixing leads to the elevation of the valence band making the visible light response possible.<sup>592</sup> In this context, remarkable quantum efficiencies in the range 9.6–19.8% at 420 nm were achieved for  $CuS(y)-Zn_xCd_{1-x}S$  (where  $0.3 \leq x \leq 0.8$ ,  $0\% \leq y \leq 15.8\%$ ) photocatalysts without noble metals for  $H_2$  production.<sup>593</sup>

In addition to the band tailoring which affects the absorption process, and which is described above, the other key property that is influenced by the nature of the orbital hybridization and band configuration is the mobility of the photogenerated carriers. The existence of efficient charge transport routes that connect the bulk with the surface of the material constitute the ultimate key requirement for a successful photocatalytic process.

In the case of  $CaBi_2O_4$ , the hybridization of the Bi 6s and O 2p levels renders the valence band largely dispersed. This favors the mobility of the photoholes in the band which subsequently enhances the oxidation reaction.<sup>594</sup> Similarly, the photoactivity of the  $d^{10}$  metal oxides and nitrides has been associated with the fact that the conduction bands of hybridized sp orbitals are associated with broad dispersions that are able to generate photoexcited electrons with enhanced mobility. On the contrary,  $BaTi_4O_9$ , which has a band gap of 2.84 eV, shows an extremely small mixing of the Ti 3d with the O 2p orbital.<sup>595</sup> Thus, the degree of hybridization in the valence and conduction bands was found to be negligible. The resulting dispersion is quite small for the  $BaTi_4O_9$  conduction band. This significant effect can be clearly observed for the photocatalysts  $Zn_3V_2O_8$  and  $Mg_3V_2O_8$ . The hybridization of the Zn 3d and O 2p orbitals in  $Zn_3V_2O_8$  does not alter the valence band and does not produce any change

in the band gap value. Nevertheless, the fact that a pd hybridization exists between the Zn 3d and O 2p orbitals favors the mobility of photoinduced holes for  $Zn_3V_2O_8$  compared to the situation for  $Mg_3V_2O_8$ . Here the valence band is mainly composed of the more localized O 2p orbital. The result, therefore, is that  $Zn_3V_2O_8$  shows a notably improved photoactivity with respect to  $Mg_3V_2O_8$  for  $O_2$  evolution, even though the latter showed a stronger absorption of visible light than the former.<sup>596</sup> This indicates that the mobility of the photoexcited electrons is low. These facts indicate that structural effects must play an important role in photocatalysis.<sup>597</sup> Likewise, in the case of  $BaTi_4O_9$ , the existence of distorted  $TiO_6$  octahedra is believed to be the principal reason for the improved electron–hole separation due to the dipole moment that is generated.

The cases described above should prove useful references when considering new materials that could trigger visible absorption by means of engineered orbital mixing. An additional way to achieve visible light photoactivity is through the use of solid solution systems such as the well-known GaN–ZnO system.<sup>443,598</sup> The solid solution  $(Ga_{1-x}Zn_x)(N_{1-x}O_x)$  exhibits hybridization of the Zn 3d and N 2p orbitals at the upper end of the valence band.<sup>599</sup> On the other hand, the bottom of the conduction band is formed by the 4s4p hybridized orbital of Ga. The interpretation of the visible absorption for these systems has been extensively discussed using different theoretical models that consider both stoichiometric and nonstoichiometric situations.<sup>600–603</sup> In the first instance, the origin of the visible light absorption was explained by the band gap narrowing due to p–d repulsion between the Zn 3d and N 2p electrons in the upper valence band. However, recent studies combining photoluminescence spectroscopy and theoretical DFT analysis of the electronic structure of GaN-rich  $(Ga_{1-x}Zn_x)(N_{1-x}O_x)$  materials described in more depth the electronic configuration of GaN–ZnO solid solutions.<sup>604</sup> The authors discussed the origin of the visible light absorption on the basis of (i) the O donor level formed at the bottom of the conduction band, (ii) the broad Zn acceptor level at the top of the valence band and (iii) the midgap deep Ga vacancy levels present in the solid solution.

In addition, the modification of this particular oxynitride material with  $Rh_{2-x}Cr_xO_3$  as a cocatalyst and using a silver nitrate as a sacrificial electron acceptor increased the quantum efficiency to 5% at 420–440 nm.<sup>447</sup> This illustrates that the judicious choice of a cocatalyst can play a positive role arising from the chemical (reaction center) and/or the charge handling (electron) effects (as described in section 4).

## 7. SUNLIGHT-BASED PHOTOCATALYSIS: CURRENT AND FUTURE PERSPECTIVES

This section is intended to provide an overview of the main systems and ideas already analyzed throughout the review but in addition it will detail future perspectives based on systems/ideas currently being explored, even if in a rather limited extension. This information has not been previously presented in this contribution since it is still clearly evolving. But since it corresponds to exciting, new perspectives with enormous potential to become relevant research directions of the future, it deserves to be mentioned here.

To simplify the discussion, we will first review current efforts aiming at developing *new materials* and in a second subsection, the *new ideas* concomitantly generated. In the first section we will identify whether the materials being discussed correspond either

to (i) current well-known technologies, (ii) those that have undergone limited exploration or (iii) novel future alternatives. Again we stress the fact that, although the emphasis here is on sunlight-excited photosystems, when required the importance of both UV and the visible excitation spectrum on catalyst performance will be presented separately.

The second section will summarize the main ideas for future developments extracted from an analysis of the capabilities of the different materials. The overall analysis of the basic ideas sustaining photoactivity is intended to summarize the key information presented throughout this review. The final section will start with a summary of morphology effects on photoactivity. Subsequently, there will be a brief overview of the importance of (i) complex structures as well as (ii) some advanced applications based on remote, dark and other capabilities that some specific materials might have on the future of the field.

### 7.1. The Quest for New Materials

**7.1.1. Single-Phase Materials.** *7.1.1.1. Current Systems.* Among the “simple” or single-phase materials currently being explored, those systems resulting in successful applications for sunlight use mostly correspond to doped and/or nanoforms of several semiconductors. Among these  $TiO_2$  and GaN are mentioned as prototypical examples related, respectively, to photocatalytic elimination and the partial oxidation of pollutants/molecules and water splitting. The doping of such phases is the current key technology to producing nanomaterials with adequate electronic characteristics for sunlight operation applications.

Semiconductor doping can lead to localized or bandlike electronic states dependent on a range of physicochemical variables. Among these the key ones are doping percentage and structural distribution (both local and long ranges) and bonding characteristics. More precisely, the covalent or ionic nature of the host lattice which, in a simple approximation, commands the mixing degree between the Ti/Ga and O/N electronic states is critical. We stress that by the doping distribution we consider both the doping agent and the corresponding charge neutrality defect since their electronic effects cannot be considered separately. This is because typically they are at interacting distances of less than 5 Å and, thus, their electronic states are mutually related in the majority of the cases. This has been shown to be the case, for example, for the cation<sup>170</sup> and anion<sup>584</sup> doping of anatase. The charge handling consequences of localized vs band-type states are obvious. These are based mainly on the fact that localized states have an increased likelihood of being recombination centers if located at bulk positions.

Starting with anatase- $TiO_2$ , section 2 considered the fact that doping can lead to localized/band-type electronic states for doping quantities below/above ca. 5 atom % respectively. Any doping of the anatase structure must avoid, as a general rule, the creation of oxygen bulk vacancies if optimization of the photoactivity for sunlight is desired. This arises from the fact that oxygen-defect distribution is always spread over a large energy range (around 1 eV). Hence even for a large number of defects, the presence of some localized, bulk-type electronic states strongly affecting charge recombination is assured.<sup>67</sup> On the other hand, oxygen vacancies leading to band-type gap states as well as those (anionic/cationic) defect states located at the surface can lead to the creation of valuable systems as discussed in sections 2 and 6. In spite of this, the combination of two simple rules, namely, (i) the absence of oxygen-related bulk,

localized-type defects and the presence of defect-related electronic states merged with anatase bands, together with (ii) a high degree of local/long-range structural homogeneity (which allows real control of the doping process and minimize energy dispersion of electronic states and potential presence of localized gap states), should then drive to the adequate modification of the anatase electronic structure with minimal perturbation of other physicochemical characteristics, particularly those related to charge mobility.

Only substitutional cation doping with specific metals such as Mo and W can lead to anatase systems having optimum and general photodegradation and/or photosynthesis behavior suitable for sunlight. These metals fulfill the necessary requirements of no oxygen bulk, localized-type vacancies, long anatase and strict  $-M-O-Ti-$  local orders as well as the modification and tuning of the anatase band structure within a significant range of M:Ti compositions. To date, all optimum high-loaded cation-doped systems known alter the anatase electronic properties by mainly controlling the conduction band end/edge.<sup>19,112,170,274,303</sup> Other cations such as Ce or less likely Nd also appear to be potentially useful candidates although they do tend to present relatively low solubility limits on the anatase structure. These relatively low solubility limits reduce the potential influence on the electronic properties and thus the corresponding decrease in the band gap energy. This in turn restricts the use of sunlight photons. Of course, cations such as Cr typically lead to the presence of anion vacancies. This (and other low-doping cations as Co, Sn<sup>2+</sup>, etc.) can be useful for sunlight operation conditions if oxygen-defect bulk-localized states are avoided by carefully controlling the alien oxidation state and the alien radial distribution. But this is no easy task. Fe represents an example of a different, complex case where a significant variability in the electronic situation can be encountered in doped samples due to the high number of local structural situations present in synthesized samples. This, together with the complex chemistry of Fe present at anatase surfaces, already discussed in section 6.1.2, certainly limits the extraction of useful information, at least for the present.<sup>301,302,317,580–582</sup>

There are also anion highly doped systems. But, possibly, the only real alternatives are those taking into account the N,F-codoping system obtained using the few synthetic methods that guarantee the presence of specific chemical species above 4 atom % together with adequate control of the structural situation.<sup>239–242</sup> As pointed out previously, although the S and specific N-containing materials lead to useful highly loaded sunlight-active systems, they are less than well established from a structural point of view. This is due to the high number of simultaneously present species, with respect to both N-/S- and charge neutrality vacancy-related species, as well as the need for an improved understanding of local-middle range structures.

In the case of anion-doped materials, one unresolved question concerning the general view just described is whether the localized states, that is the most important states likely near the valence band, constitute the exclusive physicochemical characteristic responsible for the enhancement of visible light. Such localized states are characteristic of the low doping level region as previously discussed for N-doped materials but irrespective of the N-content their importance has been discussed.<sup>6,53,75,194,198,200,508</sup> As detailed in section 2.2, sample heterogeneity as well as the ubiquitous presence of surface N-species and/or oxygen-vacancies (potentially a photosensitizer when at the surface) can decisively contribute to the enhancement of photoactivity

observed for visible light.<sup>6,75,248,251,508</sup> It should also be remembered that anion-doped materials are visible-light active but, for example, very few N-doped materials improve P25 or titania samples with sunlight. This is a fact that is neglected in the current literature although it clearly restricts the usefulness of the anion-doped materials in the context of sunlight operation.

Concerning the low loading region, it merits highlighting that low loading cations can also produce positive photoactivity effects. Apart from cases such as V, Co, Ce or Sn<sup>2+</sup> which have already been mentioned where a clear effect on band gap energy is possible (for low/medium concentrations, e.g. below/around 5 atom %), the paradigmatic case of grafted cations into anatase surfaces described in detail in section 6.1.2 exemplifies the situation.<sup>291,326,570</sup> This latter system involves localized electronic states, which can lead to a positive influence on photoactivity if adequately engineered at the surface. Grafted cations make multielectron capture and chemical steps feasible. Optimum energy positions with respect to the anatase band structure are a requirement.

Other alternatives such as, for example, two-photon technologies, made by creating narrow band structures in the anatase gap, are also potentially important for obtaining visible light-active systems. However, to date we are unaware of any serious approach to achieving this within this conceptual framework. However, it should be noted, as discussed in section 2, that the so-called self-reduced (anion vacancy) or Ni-doped TiO<sub>2</sub> materials can be used to realize this concept, although clearly in the case of anion vacancy long-term stability would be an issue. Finally, one idea that has been put forward by Bealac et al. points out that some excited states of doping cations can alter excitonic decay at room temperature in a drastic way. This significantly extends lifetimes in the useful range for the necessary chemistry, e.g. above the microsecond. Hence it could provide a way for improving photocatalytic properties.<sup>605</sup>

A similar approach concerning the key properties controlling the photoactivity of new systems as an alternative to TiO<sub>2</sub> can also be made. As described in depth in previous sections, GaN is a well-known wide band gap semiconductor which exhibits limited photocatalytic performance compared to TiO<sub>2</sub> or ZnO in photodegradation reactions. On the other hand it is well suited for water splitting processes. From DFT calculations, it has been reported that the conduction band of GaN is composed mainly of Ga 4s and 4p orbitals, whereas the valence band is constructed from the N 2p orbitals, which leads to a band separation of 3.4 eV. Ga defect-derived gap states are also observed in nanosized materials.<sup>329,604</sup> In this case, the tailoring of the band structure followed developments as for the TiO<sub>2</sub> doping. For GaN the most successful approach is based on the formation of a solid solution; this strategy was widely studied by Domen's group using the GaN–ZnO system.<sup>443,444,447</sup> The GaN–ZnO solid solution (GaN<sub>1-x</sub>Zn<sub>x</sub>)<sub>(N<sub>1-x</sub>O<sub>x</sub>)</sub> has a notable influence on the position of the valence band of the parent GaN system. The new valence band is formed by mixing the N 2p, Zn 3d and O 2p orbitals. With respect to this new band configuration, density functional studies suggest that this material absorbs visible light via electron transitions from Zn acceptor levels (located near/at the top of the valence band) to the conduction band.<sup>604</sup> Similarly, the solid solution formed by ZnGeN<sub>2</sub> and ZnO exhibits stable photoactivity toward the overall water splitting reaction under visible light irradiation.<sup>448</sup> As is the case for (GaN<sub>1-x</sub>Zn<sub>x</sub>)<sub>(N<sub>1-x</sub>O<sub>x</sub>)</sub>, this new solid solution (Zn<sub>1+x</sub>Ge)<sub>(N<sub>2</sub>O<sub>x</sub>)</sub> involves a band narrowing with respect to the former one. It has also been attributed to the p–d repulsion existing between the N 2p and Zn 3d orbitals at the valence band.

Thus, both the GaN and TiO<sub>2</sub> systems are representative examples of how careful “structural” design can lead to adequate customizing of the band gap energy. This appears to be the most successful general approach for sunlight active materials. In the case of TiO<sub>2</sub>, some cases which lead to localized states for specific conditions of sunlight excitation have already been mentioned.

In addition, some rather less explored alternatives for the above semiconductors which may require attention in the immediate future correspond to the so-called stoichiometric or compensated codoping processes. The presence of two alien species at interacting distances would most likely lead to an absence of charge compensation defects (e.g., compensated codoping). This could make it possible to avoid the most problematic issue already described, namely, expanding the number of useful doping agents to essentially all cations/anions. In anatase, this procedure has been explored for cation doping using Sr/Cr<sup>253</sup> and even more recently using cation–anion (Eu–N, Fe–N and others) doping.<sup>263,264,271</sup> In principle, this option eliminates the existence of anion vacancies in TiO<sub>2</sub>, although structural studies at the local level are required for finding the definitive answer to such a question. For GaN, a similar idea is behind the already mentioned ZnO doping of GaN (Ga<sub>1-x</sub>Cr<sub>x</sub>)(N<sub>1-x</sub>O<sub>x</sub>) ( $x$  above 0.1). However, here the presence of midgap impurity/defect levels (as described in section 6.2) seems to be the key in driving the behavior with visible light. This leads to some complication in the prediction of the optical behavior in the nanometer range.<sup>443,598,604</sup> So, in summary, it should be again stressed that our current understanding of this field indicates that control of the local structure of TiO<sub>2</sub> and GaN-based solid solutions is so complex in the nanostructure region that the necessary systematic structural–electronic–final properties study is yet to be performed. In other words, this alternative of considering useful doping pairs is still not fully exploited.

Noncompensated codoping leading to cation charge-compensating defects can also be envisaged as having the potential to enhance charge density and mobility for semiconductors. This approach would make it possible to simultaneously avoid the most deleterious effects of doping on the photoactivity.<sup>606</sup> Such ideas were initially tested for GaN using CrO doping; the doping level  $x$  was above 0.1 (Ga<sub>1-x</sub>Cr<sub>x</sub>)(N<sub>1-x</sub>O<sub>x</sub>). Although only limited theoretical support has been put forward to support this idea, it may prove a potentially interesting path for future research. In the case of TiO<sub>2</sub>, however, this should not lead to the creation of anion bulk, localized-type vacancies.

As indicated at the start of this section, doping can be used in photoselective processes such as elimination and/or selective oxidation, in conjunction with zeolites, zeotypes, mesoporous and/or nanotube materials/oxides acting as host for the alien agents. All of these systems allow control of the morphological properties but in particular porosity in the 1–5 nm range. This is useful in the context of chemical reactions. In the field of sunlight-excitation the most important applications arise from the use of specific mesoporous oxides. Of particular note are those presenting advanced nanoarchitectures such as membranes (used mainly for water treatment),<sup>607</sup> as well as nanotube materials. Such nanotube materials allow both (i) the efficient drain and collection of charge carriers in specific geometrical configurations and (ii) shape selectivity in chemical processes. Additionally, wall size and surface geometry strongly influence TiO<sub>2</sub> band gap.<sup>608</sup> Since these materials usually consist of composite (for example CdS, metal–TiO<sub>2</sub> nanotubes or C-nanotubes–TiO<sub>2</sub>) systems, a more

in-depth discussion will be presented in the next subsection.<sup>609–612</sup> At this stage of the research, the only work carried out on N and C (among others)-doped TiO<sub>2</sub> nanotubes has mostly (although not exclusively) been devoted to dye-sensitized solar cells and therefore lies outside the scope of this review.<sup>611,613,614</sup> Finally, it should be noted that nanotube morphology is possibly the only 3D ordered structure for high surface area materials that may allow useful or straightforward applications of the antenna concept.<sup>615</sup>

**7.1.1.2. Novel Systems.** Among systems which have undergone limited exploration, C-based materials merit mention in this section. Carbon (black) and other C-containing materials are well-known absorbents and thus are typically used together with titania to optimize photoactivity. However, as single-phase systems with potential usefulness in photocatalysis only three main systems need to be mentioned: multiwalled nanotubes, fullerene and polymeric carbon nitride.

Multiwalled carbon nanotubes are known to produce oxygen radicals on light excitation. But their application as “single phase” systems in the photocatalytic world is almost nonexistent. Fullerenes (C<sub>60</sub>, C<sub>70</sub>) are known to be good hydrogenation photocatalysts with UV light,<sup>616</sup> but, to our knowledge, tests using sunlight-excitation are lacking. This is probably due to the complex modifications required to adequately handle the optical properties. It is possible that the most promising system corresponds to the so-called “polymeric carbon nitride” due to its limited band gap energy (ca. 2.7–2.8 eV). From the first report, it appears that noble-metal promoted carbon nitride together with a RuO<sub>2</sub> cocatalyst (for O<sub>2</sub> handling) showed interesting water-splitting capabilities.<sup>617</sup> The electronic structure of the carbon nitride is particularly adequate for thermodynamically favoring H<sub>2</sub> evolution. A mesoporous version of this system has recently also been reported.<sup>618</sup> Visible-light activity enhancement was subsequently described through the promotion of the graphitic carbon nitride phase with gold and gold rich bimetallic (Au/Pt) phases. This produced a particularly efficient system for hydrogen production from water.<sup>619</sup> A similar enhancement of the photocatalytic activity was achieved by doping with sulfur (C<sub>3</sub>N<sub>4-x</sub>S<sub>x</sub>).<sup>620</sup> Although, as typically observed in anion-doped materials, the material displays several S-containing chemical species. The substitution of N by S appears to drive to the band gap decrease by modifying the valence band structure. This material was tested for hydrogen production as well as for phenol degradation photoprocesses. Other metal promoters, such as Fe, result in systems that are active specifically for benzene partial oxidation to phenol.<sup>621</sup> All cation (Au and Fe) and anion (S) promoted systems are active for both UV and visible light. But unfortunately they require very specific reaction conditions (pressure, temperature and/or ambient/media conditions), at least in the case of partial oxidation reactions. Such conditions therefore demand detailed analysis in order to test the usefulness of such materials with respect to more conventional ones.

An alternative to these C<sub>3</sub>N<sub>4</sub> materials using 1,2,4,5-benzenetetracarboxylic dianhydride (PMDA) coupled to a carbon nitride polymer has also been presented.<sup>622</sup> Such systems outperform both g-C<sub>3</sub>N<sub>4</sub> and N-TiO<sub>2</sub> in methyl orange elimination with visible light under normal (P,T) conditions. Thus, this material can be considered as the most promising C-single phase material reported to date in the literature, although its use with sunlight still needs to be further assessed. Also it should be noted that considering this case as a single or composite material warrants discussion.

Finally, we would like to present a novel system for the water splitting reaction which constitutes one of the most promising candidates with amazing features. Silver orthophosphate has been recently described by Yi et al. as exhibiting an extraordinary performance for water oxidation under visible light.<sup>623</sup> Though  $\text{Ag}_3\text{PO}_4$  is incapable of splitting water to form  $\text{H}_2$ , it possesses a strong photooxidative potential in the presence of a sacrificial agent. In addition, the authors showed that this system also presents an exceptional behavior for methylene blue degradation compared to other visible photoactive systems ( $\text{BiVO}_4$ ,  $\text{TiO}_{2-x}\text{N}_x$ ). The combination with  $\text{AgX}$  forming core–shell heterostructures significantly improves the photocatalytic activity for methyl orange degradation under visible irradiation.<sup>624</sup> Other heterosystems such as  $\text{Ag}_2\text{S}/\text{AgCl}$ ,  $\text{AgCl}/\text{Ag}_2\text{MoO}_4$ ,  $\text{AgBr}/\text{Ag}_2\text{WO}_4$ ,  $\text{AgI}/\text{AgVO}_3$  have been proposed by these authors which would exhibit promising performances for photocatalysis or photoelectric conversion.

The remarkably high efficiency, significantly higher than those previously reported, has been associated with the low recombination rate within the orthophosphate material. From DFT calculations, it has been postulated that the highly dispersive character of the valence and conduction bands strongly favors the photogenerated carrier transport. The considerations made concerning the composition of the bands opened up a new concept for the design of new visible-active photocatalysts. Using this approach, the authors suggest a new pathway open for exploitation, which would consist of the modification of narrow band gap binary oxides ( $\text{Ag}_2\text{O}$ ,  $\text{Bi}_2\text{O}_3$ ,  $\text{Cu}_2\text{O}$ ,  $\text{Fe}_2\text{O}_3$ ,  $\text{Cr}_2\text{O}_3$ ,  $\text{V}_2\text{O}_5$  etc.) by the addition of p block elements, e.g. alkali or alkaline earth ions, into their structures.

**7.1.2. Composite Materials.** As summarized in previous sections, composite materials are typically aimed at improving photoactivity through adequate handling of the electronic, in particular the optical, and/or chemical properties. The optoelectronic properties are mostly concerned with band gap engineering (e.g., controlling light absorption) as well as judicious handling of charge carriers after light excitation. The chemical properties are typically used to enhance the reaction through adequate adsorption and/or activation of the reactant species. Specific trends in electronic and chemical/composition engineering would consider the optimization of these two capital aspects of any photochemical reaction. Any current or future research objective would involve a “physical” separation of both light-handling and chemical centers.<sup>625</sup> With current technologies this is only possible in a multicomponent system. It aims at simplifying the optimum choice/modulation of each of the component characteristics. Ultimately it should end in a fruitful path for the production of future generations of active photocatalysts.

**7.1.2.1. Current Systems.** If the discussion of novel composite materials is started with examples currently being extensively studied and which demonstrate reasonable stability to ensure their long-term use, then there are two which merit mention:

- (i) Oxide–oxide nanomaterials contacting phases such as  $\text{Cu}_2\text{O}/\text{CuO}$ ,  $\text{WO}_3$  and  $\text{Fe}_2\text{O}_3$  with  $\text{TiO}_2$ -anatase. The anatase–rutile system can be used to produce useful sunlight-operating materials if doping of one of both components is possible as detailed in sections 2.1.1 and 2.2.1. Other systems with potential applications and which range from the simple ( $\text{CeO}_2$ ,  $\text{Bi}_2\text{O}_3$ ) to the more complex ( $\text{FeTiO}_3$ ,  $\text{NiTiO}_3$ ,  $\text{LaVO}_4$  and others) have also been described in previous sections.<sup>117–129</sup> Figure 21 summarizes

the current knowledge with respect to size-effects on these systems. In section 2.2 we discussed the fact that surface states can be as important as thermodynamic issues (related to valence/conduction band energy properties) in driving photochemical activity. Phase contact and subsequent charge handling throughout the interfaces are therefore strongly size- and defect-dependent. These need to be carefully analyzed in order to allow definitive conclusions about the usefulness of such systems. Although this limits an unquestionable prediction of the potential of these materials, by using current knowledge some nanosize regions where contact among the phases is expected to be useful can be described. It is therefore possible to put forward the suggestion that core–shell or patchy systems having adequate (i) size (of both the core and the shell) and (ii) anatase-modified surfaces (e.g., with control of acidity and reactant sorption capabilities) could be exploited as advanced materials with potentially fruitful applications in future photocatalysis. Such structures appear, therefore, the most promising candidates for the development of future technologies.

A similar discussion with respect to metal– $\text{TiO}_2$  materials concludes that their relative high cost as well as their limited stability (e.g., oxidation of the metal even in absence of contact with the reaction medium) may restrict the usefulness of these systems. In spite of this, there are current examples of innovative work that merit mention: (i) those handling the metal–nanotube semiconductor interface to reduce charge recombination and/or (ii) novel plasmonic materials including metals, such as  $\text{Ag}–\text{AgX}$  ( $X$  is an halide).<sup>295,297,455,626,627</sup>

- (ii) Systems which incorporate most of the rules mentioned at the beginning of this section such as ternary  $\text{Au}/\text{MS}_x/\text{TiO}_2$  composite materials. A core ( $\text{Au}$ ) shell ( $\text{MS}_x$ ) structure in contact with anatase nanoparticles, as depicted in Figure 6B, appears to be an optimal configuration. The efficiency of such a system would be based on an efficient drain of holes produced by charge evolution on visible light absorption by the chalcogenide phase. Concurrently, efficient charge handling through internal, that is not exposed to the reactant mixture, or external (i.e., exposed), interfaces, is necessary.<sup>139,565</sup> This system is a prototypical example combining all the important concepts for semiconductor–semiconductor and metal–semiconductor systems previously described in this review. It allows the efficient use of both UV and visible parts of sunlight, long-term stability of the system which eliminates the weak facets of both the chalcogenide ( $\text{MS}_x$ ) and the metal ( $\text{Au}$ ) component behavior, effective charge separation for both UV and visible excitations, and adequate surfaces for chemical reactions.

Section 2 described several composites in which the phase-contact metal and/or the visible-light  $\text{MS}_x$  absorber can be replaced by more modern materials. The most exciting composite systems are described below.

**7.1.2.2. Current Less-Explored Systems.** One example of a composite system which has been the subject of research but warrants further study due to clear underexploitation and could in fact become important in the near future is that of carbon- and polymer-oxide ( $\text{TiO}_2$ ,  $\text{ZnO}$ ) nanocomposite materials.

As previously mentioned, the carbon or polymer counterparts of oxides are new materials in the context of this field. Due to the

versatility of these nonoxidic materials, they could lead to exciting new photocatalysts. Among C-containing materials, there have been a significant number of contributions using activated and other high surface carbon materials for improving the limited adsorption capabilities of  $\text{TiO}_2$  and  $\text{ZnO}$  photocatalytic oxides.<sup>628</sup>

More recently, carbon nanotubes (CNTs) have attracted the interest of researchers. Composite materials with photoactive oxides have been recently reviewed.<sup>134,629</sup> Their use in pollutant elimination has been described, although recently they have also been shown to have applications as bactericidal agents.<sup>630</sup> Usually, multiwall CNTs present good conductivity characteristics. Apart from displaying, as do all carbon structures, a high surface area which is beneficial for pollutant adsorption, this nanomorphology also offers spatial confinement, which may be useful for certain reactions such as selective oxidations. In addition, one of the main advantages of carbon nanotubes for photocatalytic applications is related to their high electron storage and visible light absorption capabilities.<sup>631,632</sup> The former contributes to the enhancement of electron–hole separation by receiving electrons from oxides after (UV) light excitation while the latter allows visible light activity for the CNT–oxide composite systems. Apart from the initial excited electron donation from the CNT to the oxide after light excitation, the mechanism for visible light activity is still not clearly established. However, a hypothesis concerning a subsequent electron withdrawal from the oxide valence band and further annihilation with holes present at the positively charged CNT has been postulated. The limited information presently available for such systems restricts the prediction of the importance of CNT–oxide systems for sunlight applications. Finally it should be mentioned that, as with the single oxides, the activity of the CNT–oxide systems is limited by the presence of defects in the carbon counterpart<sup>134</sup> and that their stability for long-term operation may be compromised by oxidation of the CNTs. This requires further input before a definitive conclusion can be reached.

A second C-containing system with significance in the future of the photocatalytic world is the graphene (or graphene oxide)– $\text{TiO}_2$  binary material. Although a few tests concerning hydrogen production<sup>633–636</sup> as well as methanol,<sup>635</sup> rhodamine B<sup>637</sup> and methylene blue<sup>638,639</sup> degradation have been published, the importance of this system for sunlight is still unproven. We, however, note that graphene–gold nanocomposites appear to degrade certain pollutants (rhodamine B; light sensitive) much better than graphene– $\text{TiO}_2$  systems while using visible light. All these results suggest, on the other hand, that an efficient inhibition of the recombination process for all excitation wavelengths is present. In a recent paper, Chen et al. described the preparation of a series of  $\text{TiO}_2$ /graphene oxide composites with a p/n heterojunction.<sup>640</sup> Their study reported a tunable conductivity of graphene oxide which depends on the relative  $\text{TiO}_2$  concentration. The increasing photoactivity for methyl orange under visible irradiation was associated, in this case, with the formation of a p-type heterojunction and subsequent effects on charge handling. Recently, Du et al. reported large-scale density functional calculations of the graphene–rutile- $\text{TiO}_2$  (110) surface interface.<sup>641</sup> They found that there is significant charge transfer from graphene to titania, leading to efficient hole accumulation in the graphene layer and shifting of the Fermi level 0.65 eV below the Dirac point in titania supported graphene. These calculations revealed that an interface charge-transfer mechanism can mediate the direct excitation of electrons from graphene into the

titania conduction band (CB) under visible light irradiation and yield to an improved separation of electron–hole pairs. The versatility of ternary metal/ $\text{MO}_x$ /graphene would be expected to be larger than the binary systems described. They certainly have the potential for further exploitation in the future, but currently there are no reports concerning photocatalysis.<sup>642</sup> Other potential systems explored under visible light correspond to graphene (or graphene oxide)– $\text{BiVO}_4$  or  $\text{BiWO}_6$ .<sup>643,644</sup> Additionally, a ternary system in which graphene acts as a solid electrolyte in the presence of  $\text{BiVO}_4\text{:Ru/SrTiO}_3$  under a direct Z scheme has been recently reported.<sup>645</sup> Such composite material shows a significantly higher activity than the similar system without graphene.<sup>645</sup>

A composite system which has, however, been firmly established for its usefulness with sunlight is that based on polymer–oxide and specifically selected polymer– $\text{TiO}_2$  formulations. Due to the processing versatility of polymers clearly these materials can have significant advantages over conventional, inorganic ones since they can be used as (i) films, (ii) fibers and/or (iii) membranes. Such configurations add beneficial properties to a catalytic system and are optimal for gas and liquid phase (mostly selective) elimination or partial oxidation processes. Additionally, the intimate contact of both phases through a simple heating of the polymer over the glass transition temperature ensures the interdigitation of both components and ultimately a maximized heterointerface.

Where polymer-based films are concerned, those which are homogeneous at a micrometric scale and those corresponding to layered structures can be differentiated. Those that work for both UV and visible light excitation and that correspond to homogeneous systems using EVOH (ethyl–vinyl alcohol copolymer) and PP (polypropylene) have shown high activity in disinfection processes.<sup>135–137,646</sup> In these systems, the organic–inorganic interface is shown to give rise to new electronic states which are not present in the individual components. This allows an efficient charge separation for both UV and visible light excitation. The latter is important since none of the constituents is visible light active. The control of the interface appears critical for obtaining systems that show high activity with sunlight without the need for further modification (doping etc.) of either the oxide or the polymer. Layered polymer–titania structures are more frequently synthesized, but their usefulness is restricted to UV excitation. Their ability to show activity for both UV and visible lights is relatively scarce, at least if compared with the large amount of labor dedicated to UV-active systems. The work carried out with PVA (polyvinyl alcohol)<sup>138</sup> and HA (hyaluronan)<sup>647</sup> and a contribution using  $\text{TiO}_2$  inverse-opal and P3HT (poly-3-hexylthiophene) all merit mention.<sup>648</sup> All the research was devoted to the photoelimination of pollutants and typically showed activities outperforming  $\text{TiO}_2$ -only materials. Another polymer-containing heterostructure presented by Park et al. exhibited enhanced conversion in the  $\text{H}_2$  evolution reaction.<sup>649</sup> This heterostructure is formed by guanidinium cations adsorbed on a Nafion-coated dye-sensitized  $\text{TiO}_2$  thin layer ( $\text{G-Nf/RuL/TiO}_2$ ). The enhanced production of hydrogen in the presence of guanidinium has been ascribed to two parallel effects: a retarded charge recombination and the retarded self-quenching of the excited dyes. We can highlight as future research fields any opened up by the seminal work using photonic inorganic structures. An example is inverse-opal as well as those handling the organic–inorganic interface in order to produce highly efficient systems in the whole UV–visible electromagnetic range. Finally, we should mention polymer-based systems which allow the long-term and

efficient use of  $\text{MS}_x$  semiconductors through judicious handling of the charge carriers generated on visible light excitation of the inorganic matrix.<sup>140</sup>

The second polymer-based “structure” of note corresponds to fibers using polyester, other polymers or natural products of importance in textile and other industrial applications.<sup>650,651</sup> Again, to our knowledge, no specific work devoted to sunlight excitation has been reported using  $\text{TiO}_2$ -based materials, although there are reports using other visible-light assisted oxides, particularly  $\text{CuO}$ .<sup>652</sup> A similar situation is for membrane nanocomposite systems. Although, as detailed in review articles, there has been extensive investigation of polymer– $\text{TiO}_2$  materials with photocatalytic activity, these have been exclusively tested for UV light and would not always be adequate systems for use in sunlight applications.<sup>653</sup> Most of these applications reported are in the field of water treatment. This is because polymer-based membranes allow a complete chemical and biological treatment of liquids while using the so-called “asymmetric pore distributions” ranging from micrometers to nanometers. A photoactive inorganic component significantly improves the behavior of polymer-based membranes. This is done by enhancing the chemical and biological cleaning capabilities, by tuning the organic component hydrophilicity as well as limiting biofouling aging of the polymer component. All these capabilities can be simultaneously attained by using inorganic materials specifically designed for sunlight applications. But surprisingly to date there have been no reports available.

**7.1.2.3. Novel Systems.** One novel composite system with promising potential in photocatalysis is based on metal organic frameworks (MOFs). Such kinds of materials, which most likely will be exponentially developed over the coming years, can be considered as a new alternative to more traditional photoactive systems. Metal organic frameworks can be defined as “a class of crystalline, hybrid inorganic–organic materials presenting a 3D network of metal ions or discrete metal clusters interconnected through multidentate organic molecules”. The metal organic frameworks are a special group of coordination polymers characterized by their particular crystalline and porous structures. This crystalline structure can be compared with that exhibited by zeolite-like ones. Zeolite-based photocatalysts have been extensively described for different applications in both liquid and gas photocatalysis.<sup>2,654,655</sup> The particular textural, structural and electronic properties of zeolites involving transition metals within the zeolite frameworks or cavities have opened up new possibilities in catalysis, in particular those exploiting “shape” selectivity in organic reactions, but also for various photochemical processes. In this context, the disposition of highly dispersed titanium oxide species within a zeolite framework showed improved photocatalytic performance, much higher than that of conventional semiconducting  $\text{TiO}_2$  photocatalysts.<sup>656</sup> However, this option was focused on UV-based applications exclusively. In addition to structural issues, zeolites can also be modified (by dealumination/fluorination) to make strongly hydrophobic materials which have some advantages in aqueous processes.<sup>657</sup>

Important differences between zeolites and MOFs arise from the existence of the organic network. The combination of a 3D order with tunable dimensionality of the cavities, together with their chemical tailoring which induces specific, controlled functionalities, makes MOFs a promising alternative to zeolite-like materials.<sup>658</sup> In addition, a recent review discusses in depth the semiconducting properties of MOFs.<sup>659</sup> Since many MOFs

described are formed by transition metal-containing clusters as structural nodes bridged by organic linkers, a conduction band-type electronic state might be formed if adequate mixing between the empty d metal orbitals and the organic molecule LUMO electronic state takes place. Thus, it can be said that the band gap in MOF systems is closely related (from a simplified point of view) to the HOMO–LUMO gap and can be therefore tuned by varying the functionality of the organic linker.<sup>660,661</sup> In spite of these interesting properties, MOF applications have been mainly restricted to gas separation and storage. In 2004 Yu et al.<sup>662</sup> reported the synthesis of a 3D bimetallic coordination polymer containing uranium and nickel. These authors anticipated that this particular structure should exhibit similar photocatalytic activity as previously reported uranyl units  $\text{UO}_2^{2+}$ . Due to the electronic transitions within the U=O bonds and charge transfer from a ligand to an empty 5f orbital on the U atom upon excitation, uranyl–organic compounds is reported to exhibit attractive photoluminescent, photocatalytic, and photoelectrical properties. However, although the photocatalytic applications of this family of materials have been firmly established, since those first results only a few papers studying their applications in photocatalysis have been reported.<sup>663–666</sup> One of the most analyzed systems is MOF-5, which has a regular, three-dimensional cubic lattice defined by a  $\text{Zn}_4\text{O}$  cluster at each corner of the structure linked by six units of terephthalate (1,4-benzenedicarboxylate). It is reported that MOF-5 gives rise to an absorption spectrum with an onset at 450 nm due to the excitation of the organic linker.<sup>663,667</sup> The calculated band gap for this material is, however, 3.4 eV and presented a similar photoactivity as  $\text{TiO}_2$  or  $\text{ZnO}$  when the activity is compared per metal atom (mol of phenol/metal atom gr.) for phenol degradation on UV irradiation. Since one of the most interesting properties of such materials resides in the possibility of band gap tuning by tailoring the organic linkers and altering the subsequent framework topology,<sup>668</sup> these early results open up a promising field for exploitation within the photocatalytic word.

Other challenging composite configurations, rarely in use but currently under preliminary exploration, consists of the combination of a luminescence material with a photoactive catalyst. Within this configuration the exploitation of the radiation range not absorbed by the photocatalysts is desirable. This approach appears to be a completely new alternative for enhancing the efficiency of the photocatalytic process by judicious handling of the arriving photons. It is clear that the range of non-interacting photons drastically diminishes the quantum yield under solar irradiation conditions. As has been widely described in earlier sections, the extension of the visible absorption using different strategies seeks to increase the photocatalytic process efficiency. Thus, the combination of the photocatalytic system with the so-called “phosphor” material which could handle and transform the incoming sunlight radiation turns out to be an interesting but not yet fully explored highway.<sup>669</sup>

Thus, these combined solutions intended for practical photocatalytic applications would make it possible to profit from the luminescence properties in two ways: the so-called upconversion or downconversion luminescence of a phosphor material. An informed selection of the phosphor material should lead to an extension of the number of photons available within the absorption range of a specific photocatalyst. Thus, an upconverting phosphor would absorb low energy radiation in either the IR or visible range and ultimately emit higher energy radiation in the visible or UV range respectively. In this case, two low-energy

photons are “added together” to give one higher-energy photon.<sup>670</sup> On the contrary, a downconverting phosphor would be excited by high energy radiation (UV light), thus presenting an emission with lower energy in the visible range. Downconversion, which is also known as *quantum cutting*, is the opposite process of upconversion: One high-energy photon is *cut* into two lower-energy photons.<sup>671</sup> Of course, the performance of the composite system requires the interface handling of charge carrier species, and this has not been fully analyzed within this particular situation.

The applications of the upconversion process by phosphor-like systems (e.g., visible to UV) should optimize the photocatalytic performance of traditional UV active photocatalysts.<sup>672</sup> In the same way, using downconverting phosphors (e.g., UV to visible) combined with the new visible active photocatalysts described in previous sections should also result in the improvement of the efficiency of the process.

Among the wide range of reported materials with luminescence properties, several classes of phosphors include (i) mixed metal molybdates, tungstates and vanadates,<sup>673,674</sup> (ii)  $\text{Ln}_3\text{M}_5\text{O}_{12}$  ( $\text{Ln} = \text{Y}, \text{Gd}$ ,  $\text{M} = \text{P}, \text{Al}, \text{Ga}$ ) garnets doped with  $\text{Ce}^{3+}$ ,<sup>675</sup> (iii) new rare earth halide, nitride and oxynitride materials<sup>676,677</sup> and (iv) inorganic–organic framework materials in which the excitation and emission processes would take place at the organic ligand.<sup>678,679</sup> The chemical modification of these organic linkers would allow the preparation of specific polymer networks presenting strong and tunable luminescence activity.

Within this framework, the best option would consist of the coupling of a UV-emitting phosphor with a  $\text{TiO}_2$ -based photocatalyst since the latter provides the best photocatalytic performance over a wide range of applications. Many UV-emitting systems that could be considered for such composite formulation can be found in the literature. Strontium aluminosilicates show a main emission line in the UV region:  $\text{Sr}_2\text{Al}_2\text{SiO}_7:\text{Ce}$  (387 nm) and  $\text{Ca}_{0.5}\text{Sr}_{1.5}\text{Al}_2\text{Si}_2\text{O}_8:\text{Ce,Tb}$  (386 nm). Doping with other rare earth cations results in a shift in the emission line from blue to purple. Other compounds based on borates, silicates, phosphates and sulfates have all been reported to show UV emission. Interesting to mention is  $\text{YF}_3:\text{Yb}^{3+},\text{Tm}^{3+}$ , which allows the use of a near-infrared frequency (980 nm) to obtain a useful UV emission in the 290–365 nm range.<sup>680</sup> In a similar approach, Zhang et al. described a heterosystem formed by  $\text{Bi}_2\text{WO}_6$  with  $\text{Er}^{3+}$  cations which acts as an upconverting phosphor center. This way, the upconverting properties of  $\text{Er}^{3+}$  species can transform visible light beyond the absorption edge of  $\text{Bi}_2\text{WO}_6$  into the UV light region that can activate  $\text{Bi}_2\text{WO}_6$ .<sup>681</sup> These authors demonstrated that such a synergistic system exhibited improved photoactivities for phenol degradation under irradiation at 465 nm by a 3 W LED.

Recently, Li et al. reported an enhancement in the photocatalytic performance of  $\text{TiO}_2$  by coating it with  $\text{Eu}^{2+}, \text{Nd}^{3+}$  codoped  $\text{CaAl}_2\text{O}_4$  phosphor.<sup>682</sup> The  $\text{CaAl}_2\text{O}_4:\text{Eu}^{2+}, \text{Nd}^{3+}$  @  $\text{TiO}_2$  composite synthesized by a sol–gel method showed higher photocatalytic activity than pure  $\text{TiO}_2$  under visible light irradiation for the NO degradation. From these results, the authors claimed that the combination of  $\text{TiO}_2$  with a long afterglow phosphor leads to a composite synergistic system in which phosphor should absorb and store light and then release the energy in the dark period. This would ensure it maintaining its activity in a variety of situations. For  $\text{Sr}_4\text{Al}_{14}\text{O}_{25}:\text{Eu}^{2+},\text{Dy}^{3+}$  phosphor, it has also been reported that the afterglow time strongly depends on the extent of Ca substitution in the

$\text{Sr}$  position.<sup>683</sup> So it appears that this composite configuration would allow the reaction to be extended to a dark regime “à la carte”. This idea will be fully described in section 7.2.

In a recent paper, Ciambelli et al. reported a very interesting synergistic effect between a  $\text{ZnS}$ -based phosphor and  $\text{V}^{3+}\text{-TiO}_2$ .<sup>684</sup> In this case, the downconverting phosphor absorbs radiation at 365 nm presenting the emission band at 440 nm, just within the range in which  $\text{V}^{3+}$  doped catalyst can be activated. For the ethanol photooxidative dehydrogenation reaction, the presence of a luminescence material leads to an increase in the apparent quantum yield from 2 to 30%.

An additional concept within the light-handling approach described above for photoluminescence systems would consist of the consideration of luminescence organic molecules as surface sensitizers. In this case, it would be crucial to protect this luminescence molecule from direct oxidation by the photoactive material. Thus, the phosphor should be embedded or coated by a protective system. On this basis, the production of short wavelength photons in the UV region from low energy light would make it necessary to develop new organic systems to be fitted within the photocatalytic systems in a stable way. Within this scope, one possible methodology could be based on the utilization of the sensitized triplet–triplet annihilation photochemistry.<sup>685</sup> Recently, Singh-Rachford et al. demonstrated the upconversion (visible to UV) process by using two simple organic chromophores. The selective excitation of 2,3-butanedione at 442 nm occurs in the presence of the 2,5-diphenyloxazole dye and results in the observation of a UV fluorescence signal centered at 360 nm.<sup>686</sup> We strongly believe that the sensitization of a photoactive system with a combination of dye molecules will open new strategies for the improvement of photonic efficiency by managing the incoming radiation, as long as the system is sufficiently protected from external chemical attack.

Along these lines, an interesting enhanced luminescence effect has recently been reported for rhodamine heteroaggregates supported on a semiconductor thin film.<sup>687</sup> This effect is achieved by the combination of rhodamine 800 dye with different rhodamine molecules supported on porous thin films ( $\text{SiO}_2$ ,  $\text{TiO}_2$  or  $\text{Ta}_2\text{O}_5$ ). The improved photoluminescence is found in the NIR region. Based on this principle new sensitized systems could be developed by using specific dye-heterostructured surfaces.

Another approach could be based on the handling of the surface chemistry dynamics by the development of a heterosupramolecular  $\text{TiO}_2$ -based hybrid structure in which a close-packed adsorbed bilayer of surfactant molecules covers the  $\text{TiO}_2$  particles.<sup>688</sup> The enhancement in the photocatalytic activity, in this case under UV light, is achieved by confining the organic molecule to be degraded in the hydrophobic nanospace created by the surfactant bilayer. In this way the surface concentration of organic pollutant is increased and water competition for active centers diminished. Based on this mechanism, the authors reported that the photocatalytic activity for naphthol degradation is enhanced as a result of an effective incorporation into the admicellar space. Recently, the same group reported the application of such heterosupramolecular structures for oxidation reactions such as in organic synthetic applications.<sup>689</sup> In these cases, the cationic surfactant bilayer is disposed around  $\text{Au-TiO}_2$  particles which exhibit interesting chemoselectivity for oxidation of alcohols to carbonyl compounds under visible irradiation. The latter situation seems reasonably stable, as opposed to the reaction carried out under UV light. This stability appears to

arise from adequate handling of the physical contact among the components. When the Au component is left free of direct surfactant contact, this appears to limit the degradation of the system with respect to the UV-excited case.

The possibility of developing biomimetic materials for photocatalytic applications should be also mentioned. Recently, biomolecules have been widely used for the modification of semiconductors in order to improve the biocompatibility of these materials.<sup>690</sup> Such hybrid composites have found applications in different solar energy processes as photoelectrochemical cells, photovoltaic technology and photocatalysis. From the data presented in this review it should be clear that one of the most important problems in photocatalysis seeking a solution concerns the recombination process of charge species created on light excitation. Molecules with specific functional groups such as hydroxyl (typically characteristic of oxide materials), carboxyl, silanyl or phosphonate groups present efficient trapping properties, and ultimately this may help in mitigating the problem. As Li et al. described, most of the biomolecules under consideration contain these functional groups and could serve as cocatalysts for photocatalytic applications. Thus, some amino acids (cysteine, arginine, L-hydroxyproline, histidine, alanine), biopolymers (cellulose, chitosan, cyclodextrins) and other small biomolecules (ascorbic acid, citric acid) have all been reported as improving the activity properties of traditional photocatalytic materials.<sup>690</sup>

Following Green Chemistry principles, the driving force in most industrial processes based on heterogeneous catalysis might lie in the development of more selective catalysts that can minimize the use of raw materials and avoid the formation of undesirable byproduct. In this sense, the most selective systems known are enzymes which of course are nature's own catalysts. Recently, many examples involve the development of biomimetic catalysts by assembling enzymes and different catalytic materials.<sup>691–693</sup> The first attempt to combine a photoactive material and enzymes was reported by Kurayama, who described a new photobioreactor formed by TiO<sub>2</sub> and formate dehydrogenase (FDH) as the enzyme for CO<sub>2</sub> fixation and using methylviologen (MV) and diaphorase enzyme (DAH) as electron transfer mediators.<sup>694</sup> In this case, the coupled reaction was designed separately and photocatalytic and biocatalytic reactions were divided by a ceramic membrane. Within this configuration, the inactivation of the enzyme by the UV light was avoided. The immobilization of selective enzymes over a specific support has been recently reported for CO<sub>2</sub> reduction to CH<sub>3</sub>OH.<sup>695</sup> Related to this is the immobilization of the specific enzyme as carbon monoxide dehydrogenase (CODH) onto TiO<sub>2</sub> which has recently been reported by Woolerton et al.<sup>696,697</sup> This novel heterosystem exhibited promising photocatalytic activity for selective reduction of CO<sub>2</sub> to CO. Although only a few examples with both high activity/selectivity and long-term stability while using sunlight are actually reported, the exploration of bioconjugated hybrids and/or bioinspired systems for photocatalytic remediation, selective oxidation or H<sub>2</sub> production is expected to grow in the next few years.

## 7.2. A Summary of Present and Forthcoming Ideas

Section 7.1 presents the conceptual framework where the photoactivity of archetypical single-phase systems such as TiO<sub>2</sub> or GaN can be explained as a function of solid physicochemical characteristics. As a general rule, we detailed the main framework where the simultaneous control of morphology and defect structure could pave the way for future improvements.

In the case of TiO<sub>2</sub>, the morphology parameters affecting the photoactivity include primary and secondary particle size, particle shape and porosity. Although a decrease in primary particle size increases the surface area and has a generally beneficial effect on the photoactivity, a primary particle size decrease can also exert two simultaneous adverse effects: (i) on the enhancement of the geminate recombination and (ii) on the presence of electron traps in the bulk. Of course, doping the anatase structure could alter defect distribution with particularly important but negative consequences on the photoactivity if the oxygen defects responsible for the localized electronic states are created at bulk positions. Particle shape would be expected to affect photoactivity through the presence of kink/edge (and many other) defects as well as by modifying the OH properties. In the case of doped samples surface effects such as these may be combined with those derived from the presence of surface alien species, particularly those altering acidity/basicity. Secondary particle size and porosity affect the light handling properties as well as nonradiative and geminate recombination. Finally, recent results suggest that surface engineering pathways related to the modification or amorphization of surface layers could also lead to useful sun-light-operated systems.<sup>82,698,699</sup> Local arrangements as well as control of defects at surfaces (a highly defective area as described in section 2) are thus important. All of these morphological variables are thus critical to our understanding of the physicochemical basis of photoactivity. However, their exact role and mutual influence need to be systematically addressed in future studies. As previously discussed, where primary particle size is concerned, the distribution involves not only the mean but also higher order moments derived from the important polydispersity of the oxide, and hence the presence of different particle–particle interface situations. These have all received considerable attention, and the presence of three regions with important consequences on photoactivity above/below, respectively, ca. 4–5 and 12–15 nm appears reasonably established.

The photoactivity of the new alternative systems to TiO<sub>2</sub> described in previous sections can also be interpreted within a similar framework where morphological and defect variables might be taken into account. Nevertheless, for pollutant elimination and/or water splitting processes we already mentioned the relatively low importance of morphological variables. Thus, for the specific case of oxides photocatalysts such as perovskite-type catalysts, as well as for nitride photocatalysts, there is evidence for a strong, primary relationship with their inherent electronic features. This is what directly modulates light handling. As widely discussed in previous sections, painstaking studies of both band and defect engineering is therefore a key in the quest to optimizing these systems. Simple morphology properties, in particular one such as the surface area which has been studied to date, thus remain in a secondary plane.

With respect to single-phase materials and morphological control, a final approach could involve the use of suitable bi- or tridimensional structures. Apart from secondary particle size and porosity, which have been already mentioned as the more important interparticle morphological variables, the use of nanomorphologies such as mesostructures with membrane organization or nanotubes must be considered. These were previously mentioned in section 7.1 for TiO<sub>2</sub>-based materials.<sup>607,609–613,615</sup> Nanotube morphology would be expected to add rather interesting properties which could be used to handle noncooperative physical phenomena such as antenna effects. Similarly, it appears that the creation of 2D or 3D superstructures on several perovskite-type

materials have certain influence on the photocatalytic activity, although, as just outlined, the relevance of other morphological variables, particularly primary particle size, appears to be somewhat limited.<sup>359,360,365,366,368,588</sup>

In spite of the advances for single-phase materials just summarized, possibly the most appealing general approach for future improvements probably resides in the use of composite systems. Of course, this takes into consideration that all improvements with respect to single-phase materials could be included in a composite sample. As previously stated, a pathway for future improvement in photocatalysis while essentially using the composite materials described in section 7.1 would also try to uncouple the photo and chemical steps into different phases or surfaces in order to allow for the optimization of each of the properties. This hopefully would lead to eliminating mutual, mostly destructive or noncooperative interferences.

In particular we have emphasized how to use such systems to finely tune the photo steps with a special emphasis on light absorption and/or subsequent charge separation. Novel ideas would require the use of photonic materials and/or plasmonic interfaces. Photonic materials such as inverse opals have been used in, for example, polymer–TiO<sub>2</sub>. While the use of plasmonic interfaces is still in its infancy, some interesting papers working on the control of long-range plasmonic effects on semiconductor surfaces or semiconductor–semiconductor interfaces have already been published.<sup>155,295</sup> Nanotubular morphologies have also been highlighted as rather useful. This is especially true in the context of handling noncooperative phenomena which influence the photo steps<sup>615</sup> and could find application in 3D ordered composite systems.

Some additional ideas suggest the optimization or improvement of chemical activity by using the presence of “smart” interfaces such as would occur with the presence of additional, “inert” porous phases such as polymers, inorganic solid or macromolecules chaining the reaction center. Such interfaces can control reactant diffusion and/or local hydrophilicity near the active center. This then maximizes the chemical activity in both elimination and/or partial oxidation (organic synthesis) processes. Since the current available literature using this approach has already been considered case by case in section 7.1, in summary it is pertinent to point out that such a strategy requires the setting up of rather complex nanoarchitectures. However, it still deserves intensive study as a promising tool for the optimization of the next generation novel photocatalytic systems.

Another important approach involves the so-called “remote photocatalysts”. This includes photocatalytic systems with impact distances outside the normal nanometric region and including distances as long as millimeters.<sup>100</sup> This approach was first proposed by Tatsuma et al.<sup>700</sup> and was rationalized by the presence of gas phase H<sub>2</sub>O<sub>2</sub> and the subsequent production of hydroxyl radicals by UV-photolysis<sup>701</sup> and/or the presence of singlet oxygen.<sup>702</sup> Oxygen diffusion at oxide surfaces has also been shown to be possible at microdistances.<sup>703,704</sup> However, their involvement as leading species in photocatalytic reactions seems only possible in partial oxidation processes. A similar process can account for the main adsorption role of carbon-containing species as previously mentioned for nanocomposite systems. The studies performed, however, show that long distance (mostly in the micro range but up to the millimeter range) charge carrier number decreases about 2 orders of

magnitude with respect to the concentration in the vicinity of the photoactive surface.

A more innovative implementation of this idea would be based on the use of polymer-based composites that could allow charge separation and traveling over long distances without any loss with respect to the photoactivity action of the TiO<sub>2</sub> component alone. This is demonstrated beyond doubt by the high activity, larger than that possible for the inorganic component alone, presented by those systems having the oxide embedded into the bulk of the nanocomposite material. This can be achieved using a range of polymer matrices with semiconductor or even insulating character.<sup>135–138,298,299,646,705</sup> Thus composite systems such as these appear to drive charge carriers a long away from their original production and consequently may open up new alternatives for using photocatalytic systems remotely.

A third interesting option that is still to be fully explored consists of using systems active under dark conditions after an illumination period. The use of phosphors such as Sr<sub>4</sub>Al<sub>14</sub>O<sub>25</sub>: Eu<sup>2+</sup>, Dy<sup>3+</sup> has been discussed in section 7.1.<sup>684</sup> In this case, a suitable component combines both light handling and dark operation capabilities. Outstanding performance was also demonstrated in the case of the PdO (or more probably PdO/Pd) promotion of N-doped TiO<sub>2</sub>.<sup>706,707</sup> The additional presence of Ni(OH)<sub>2</sub> seems to reinforce the dark activity.<sup>708</sup> Such PdO-based systems have shown activity under postillumination conditions both for the elimination of pollutants and in the biosuppression of germs. The Pd-containing phase has an important electron storage capability with release of charge over a period of hours. This discharge period is, normally, in metal–oxide heterojunctions well below a millisecond.<sup>21</sup> It was found that such a singular capability is only operative in the previously mentioned composite case and is not observed when palladium is deposited on titania (anatase) or silica oxides. So although very few examples using this idea have been developed, they really do highlight the beneficial effects potentially obtainable by using light-activated dark-active materials.

Finally, the combination of photocatalysis with other physical and/or chemical processes such as microwave or plasma irradiation, electrochemical treatment, physical adsorption or chemical processes such as ozonization or photophenton must be here mentioned.<sup>709–711</sup>

In summary, the complex combination of all these concepts into a composite system may be possible. If so it would drive the development of optimum systems which would maximize the photoactivity “à la carte” with tools allowing remote, dark activity, plasmonic and/or cooperative effects at interfaces and/or any other physicochemical method already mentioned as required by the specific application. It should, however, be noted that currently the understanding of such composite systems is certainly scarce and probably not only (i) requires exhaustive investigation of structural, particularly morphological, electronic and light handling properties but also (ii) would involve new tools in order to further progress the analysis of the system *in operando* conditions, under the action of light and chemical atmospheres. In this context and together with the already mentioned development of new solid-state tools adapted to the nanometer world such as PDF-XRD, the important efforts summarized by Majima et al. concerning the development of single molecule and single site tools for the seeding of light into optical and chemical steps of relevance in photocatalysis must be recognized.<sup>712</sup>

**AUTHOR INFORMATION****Corresponding Author**

\*E-mail: mfg@icp.csic.es (M.F.-G.); gcolon@icmse.csic.es (G.C.).

**Special Issue**

Part of the thematic issue Solar Photon Conversion.

**BIOGRAPHIES**

Anna Kubacka was born in Poland. She graduated from the Jagiellonian University, Cracow, Poland, with M.Sc. degree in chemistry. Then she started to work in the Institute of Catalysis and Surface Chemistry, Polish Academy of Sciences, Cracow, Poland, where obtained the PhD degree in chemical science in 2004. Afterward she moved to Spain, where she did several years of postdoctoral research at the Institute of Catalysis and Petrochemistry CSIC, Madrid. Now she is a member of Prof. M. Fernández-García's group working as "Ramon y Cajal" research scientist. Her research interests focus on the synthesis of new materials; photocatalysis under UV and visible-light excitation; oxide polymer nanocomposites with biocidal properties; heterogeneous and environmental catalysis on macroporous materials and mixed oxides.



M. Fernández-García was born in Madrid, Spain. He obtained BS and PhD degrees in Physical Chemistry from Complutense University in Madrid in 1989 and 1993, respectively. He conducted postdoctoral work at Yale University with Prof. G. L. Haller during the 1994–1995 period. In 1998, he was awarded a European Fellowship by the Royal Society (London) which funded a visit to Dundee University, U.K. In 1999, he joined the Institute of "Catalysis y Petroleoquímica" (CSIC, Spain),

becoming Professor in 2008. During his carrier he received several awards for studies in environmental sciences. Currently he serves as member of editorial boards of several journals in the fields of catalysis and nanomaterials and is part of the scientific advisory board of the European Synchrotron (ESRF). Main research interest involves solid state chemistry/physics of nanomaterials with industrial application. Subject areas of current interest include material synthesis and preparative methods, deactivation and regeneration, environmental catalysis, and fine chemical synthesis, and also nanocomposite polymer-based systems with application in the field of human health protection, sensors, and membranes.



Gerardo Colón was born in Seville, Spain. He received his BS degree in Chemistry (1992) and PhD degree (1996) from the University of Seville. He then worked as a postdoctoral fellow (1996–1998) at the Università degli Studi di Cagliari (Italy) and Ecole Supérieure des Mines de Saint Étienne (France). He joined the Institute of Materials Science of Seville as a Postdoctoral Researcher (1998–2004). In 2004 he became Tenured Scientist and from 2010 Research Scientist at the same Institute. His research is mainly focused on the development of new photocatalysts for environmental purification.

**ACKNOWLEDGMENT**

Financial support by Projects P09-FQM-4570, CTQ2010-14872/BQU and PLE2009-0037 is fully acknowledged. A.K. thanks the MICINN for a Ramón y Cajal Postdoctoral Fellowship. Authors wish to thanks Profs. Bisquert, Navío and Illas as well as the reviewers for critical reading of the manuscript and/or for helpful comments.

**REFERENCES**

- (1) Hoffmann, M. R.; Martin, B. T.; Choi, W.; Bahnemann, D. W. *Chem. Rev.* **1995**, *95*, 69.
- (2) Anpo, M.; Tacheuchi, M. *J. Catal.* **2003**, *216*, 505.
- (3) Hermann, J. M. *Topics Catal.* **2005**, *34*, 49.
- (4) Bahnemann, D. W.; Anpo, M. *Sol. Energy* **2004**, *77*, 445.
- (5) Thompson, T. L.; Yates, J. T. *Chem. Rev.* **2006**, *106*, 4428.
- (6) Serpone, N. *J. Phys. Chem. B* **2006**, *110*, 24287.
- (7) Colón, G.; Belver, C.; Fernández-García, M. Nanostructured oxides in Photocatalysis. In *Synthesis, Properties and Applications of Solid Oxides*; Rodríguez, J. A., Fernández-García, M., Eds.; Wiley: New York, 2007.
- (8) Carp, O.; Huisman, C. L.; Reller, A. *Prog. Solid State Chem.* **2004**, *32*, 33.

- (9) Di Valentin, C.; Diebold, U.; Selloni, A. *Chem. Phys. Lett.* **2007**, *339*, and articles therein.
- (10) Zhang, H.; Chen, G.; Bahnemann, D. W. *J. Mater. Chem.* **2009**, *19*, 5085.
- (11) Fox, M. A.; Dulay, M. T. *Chem. Rev.* **1993**, *93*, 341.
- (12) Hincapié, M.; Maldonado, M. I.; Oller, I.; Gernjak, W.; Sánchez-Pérez, J. A.; Ballesteros, M. M.; Malato, S. *Catal. Today* **2005**, *101*, 203.
- (13) Fujishima, A.; Rao, T. N.; Tryk, D. A. *J. Photochem. Photobiol. C* **2000**, *1*, 1.
- (14) Diebold, U.; Ruzicka, N.; Herman, G. S.; Selloni, A. *Catal. Today* **2003**, *85*, 93.
- (15) Barnard, A. S.; Xu, H. *ACS Nano* **2008**, *2*, 2237.
- (16) Burdett, J. K.; Hughbands, T.; Gordon, J. M.; Richardson, J. W.; Smith, J. *J. Am. Chem. Soc.* **1987**, *109*, 3639.
- (17) Asahi, R.; Taga, Y.; Mannstadt, W.; Freeman, A. *J. Phys. Rev. B* **2000**, *61*, 7459.
- (18) Sousa, C.; Illas, F. *J. Chem. Phys.* **1994**, *50*, 13974.
- (19) Kubacka, A.; Fernández-García, M.; Colón, G. *J. Catal.* **2008**, *254*, 272.
- (20) Hermann, J. M. *Topics Catal.* **2006**, *39*, 3.
- (21) Kamat, P. V. *J. Phys. Chem. C* **2007**, *111*, 2834.
- (22) Kamat, P. V. *J. Phys. Chem. C* **2008**, *112*, 18737.
- (23) Kiyonaga, T.; Akita, T.; Tada, H. *Chem. Commun.* **2009**, *2011*.
- (24) Mattesini, M.; Almeida, J. S.; Dubrovinsky, L.; Dubrovinskaia, N.; Johansson, B.; Ahuja, R. *Phys. Rev. B* **2004**, *70*, 115101.
- (25) Malato, S.; Fernández-Ibáñez, P.; Maldonado, M.; Blanco, J. *Catal. Today* **2009**, *147*, 1.
- (26) Maeda, K.; Domen, K. *J. Phys. Chem. Lett.* **2010**, *1*, 2655.
- (27) Joshi, U. A.; Palasyuk, A.; Arney, D.; Maggard, P. A. *J. Phys. Chem. Lett.* **2010**, *1*, 2719.
- (28) Penn, L. R.; Banfield, J. F. *Geochim. Cosmochim. Acta* **1999**, *63*, 1549.
- (29) Chen, X.; Mao, S. S. *Chem. Rev.* **2007**, *107*, 2891.
- (30) Catlow, C. R. A.; Bromley, S. T.; Hamad, S.; Mora-Fonz, M.; Sokol, A. A.; Woodley, S. M. *Phys. Chem. Chem. Phys.* **2010**, *12*, 786.
- (31) Dzwigaj, S.; Arrouvel, C.; Breysse, M.; Geantet, C.; Inoue, S.; Toulhoat, H.; Raybaud, P. *J. Catal.* **2005**, *236*, 245.
- (32) Digne, M.; Sautet, P.; Breysse, M.; Toulhoat, H. *J. Catal.* **2002**, *211*, 1.
- (33) Digne, M.; Sautet, P.; Raybaud, P.; Euzen, P.; Toulhoat, H. *J. Catal.* **2004**, *226*, 54.
- (34) Usseglio, S.; Calza, P.; Damin, A.; Minero, C.; Bordiga, S.; Lamberti, C.; Pellizzetti, E.; Zecchina, A. *Chem. Mater.* **2006**, *18*, 3412.
- (35) Fernández-García, M.; Wang, X.; Belver, C.; Hanson, J. C.; Rodríguez, J. A. *J. Phys. Chem. C* **2007**, *111*, 674.
- (36) Fernández-García, M.; Wang, X.; Belver, C.; Hanson, J. C.; Rodríguez, J. A. *J. Am. Chem. Soc.* **2007**, *129*, 13604.
- (37) Barnard, A. S.; Zapol, P.; Curtiss, L. A. *Surf. Sci. Lett.* **2005**, *582*, 2173.
- (38) Barnard, A. S.; Curtiss, L. A. *Nano Lett.* **2005**, *5*, 1261.
- (39) Yang, H. G.; Sun, C. H.; Qiao, S. Z.; Zou, J.; Liu, G.; Smith, S. C.; Cheng, M. H.; Lu, G. Q. *Nature* **2008**, *453*, 638.
- (40) Sakai, N.; Ebina, K.; Takada, K.; Sasaki, T. *J. Am. Chem. Soc.* **2004**, *126*, 5851.
- (41) Matsumoto, Y.; Ida, S.; Inoue, T. *J. Phys. Chem. B* **2008**, *112*, 11614.
- (42) Hang, X.; Kuang, Q.; Jin, M.; Xe, Z.; Zheng, L. *J. Am. Chem. Soc.* **2009**, *131*, 3152.
- (43) Marshall, M. S. J.; Castell, M. P. *Phys. Rev. Lett.* **2009**, *102*, 146102.
- (44) Dai, Y. Q.; Cobley, C. M.; Zhang, J.; Sun, Y. M.; Xia, Y. N. *Nano Lett.* **2009**, *9*, 2455.
- (45) Zhang, D.; Li, G.; Wang, H.; Chang, K. M.; Yu, J. C. *Cryst. Growth Des.* **2010**, *10*, 1130.
- (46) Li, G.; Li, L.; Boerio-Goates, J.; Woodfield, B. F. *J. Am. Chem. Soc.* **2005**, *127*, 8659.
- (47) Soria, J.; Sanz, J.; Sobrados, I.; Coronado, J. M.; Hernández-Alonso, M. D.; Fresno, F. *J. Chem. Phys. C* **2010**, *114*, 16534.
- (48) Hummer, D. R.; Kubicki, J. D.; Kent, P. R. C.; Post, J. E.; Heaney, P. J. *J. Chem. Phys. C* **2009**, *113*, 4240.
- (49) Lazzeri, M.; Vittadini, A.; Selloni, A. *Phys. Rev. B* **2001**, *63*, 155409.
- (50) Vittadini, A.; Selloni, A.; Rotzingerand, F. P.; Grätzel, M. *Phys. Rev. Lett.* **1998**, *81*, 2954.
- (51) Lazzeri, M.; Vittadini, A.; Selloni, A. *Phys. Rev. B* **2001**, *63*, 119901.
- (52) Luca, V. *J. Phys. Chem. C* **2009**, *113*, 6367.
- (53) Diebold, U. *Surf. Sci. Rep.* **2003**, *48*, 53.
- (54) Fernández-García, M.; Martínez-Arias, A.; Hanson, J. C.; Rodriguez, J. A. *Chem. Rev.* **2004**, *104*, 4063.
- (55) Martyanov, I. N.; Uma, S.; Rodrihues, S.; Klabunde, K. *J. Chem. Commun.* **2004**, 2476.
- (56) Colón, G.; Hidalgo, M. C.; Munuera, G.; Ferino, I.; Cutrufello, M. C.; Navío, M. A. *Appl. Catal., B* **2006**, *63*, 45.
- (57) Dhumel, S. Y.; Daulon, T. L.; Jiang, J.; Khomami, B.; Biswas, P. *Appl. Catal., B* **2009**, *86*, 145.
- (58) Swamy, V.; Menzies, D.; Muddle, B. C.; Zuznetsov, A.; Dubrovinsky, S.; Dai, Q.; Dimitriev, V. *Appl. Phys. Lett.* **2006**, *88*, 243103.
- (59) Grey, I. E.; Wilson, N. C. *J. Solid State Chem.* **2007**, *180*, 670.
- (60) Na-Phattalung, S.; Smith, M. F.; Kim, K.; Du, M.-H.; Wei, S.-H.; Zhang, S. B.; Limpojumpong, S. *Phys. Rev. B* **2006**, *73*, 125205.
- (61) Karakoli, A. S.; Kochibhala, S. V. N. T.; Bear, D. R.; Therunthanasi, S. T. *Small* **2008**, *4*, 1210.
- (62) Alimohammada, M.; Fichthor, K. A. *Nano Lett.* **2009**, *9*, 4198.
- (63) Enyashin, A. N.; Seifert, G. *Phys. Status Solidi* **2005**, *582*, 173.
- (64) Satoh, N.; Nakashima, T.; Kamikura, K.; Yamamoto, K. *Nanotechnol.* **2008**, *3*, 106.
- (65) Iacomino, A.; Cantele, G.; Ninno, D.; Narri, I.; Ossini, S. *Phys. Rev. B* **2008**, *78*, 075405.
- (66) Tang, H.; Levy, F.; Berger, H.; Schmid, P. E. *Phys. Rev. B* **1995**, *52*, 7771.
- (67) Bisquert, J. *Phys. Chem. Chem. Phys.* **2008**, *10*, 3175.
- (68) Cohen, M. M. *Introduction to the quantum theory of semiconductors*; Gordon: Amsterdam, 1972.
- (69) Knorr, F. J.; Marcado, C. C.; McHale, J. L. *J. Phys. Chem. C* **2008**, *112*, 12786.
- (70) Ikeda, S.; Sugiyama, N.; Murakami, S.; Kominami, H.; Kera, Y.; Noguchi, H.; Uosaki, K.; Torimoto, T.; Ohtani, B. *Phys. Chem. Chem. Phys.* **2003**, *5*, 778.
- (71) Boschloo, G.; Fitsmaurice, D. *J. Phys. Chem. B* **1999**, *103*, 228.
- (72) Durrant, J. R. *J. Photchem. Photobiol. A* **2002**, *148*, 5.
- (73) Movilla, J. L.; García-Belmonte, G.; Bisquert, J.; Planelles, J. *Phys. Rev. B* **2005**, *72*, 153313.
- (74) Nowotny, M. K.; Sheppard, L. R.; Bak, T.; Nowotny, J. *J. Phys. Chem. C* **2008**, *112*, 5275.
- (75) Emeline, A. V.; Kuznetsov, V. N.; Rybchuk, V. N.; Serpone, N. *Int. J. Photoenergy* **2008**, *1*, 258394.
- (76) McKenna, K. P.; Shluger, A. L. *Nature* **2008**, *7*, 859.
- (77) Quian, L.; Jin, Z. S.; Zhang, J. W.; Huang, Y. B.; Zhang, Z. J.; Du, Z. L. *Appl. Phys. A: Mater. Sci. Process.* **2005**, *80*, 1801.
- (78) Wendt, S.; Sprunger, P. T.; Lira, E.; Madsen, G. K. H.; Li, Z.; Hasen, J. O.; Matthiesen, J.; Blekinge-Rasmussen, A.; Laegsgaard, E.; Hammer, B.; Besenbacher, F. *Science* **2008**, *320*, 1755.
- (79) Finazzi, E.; Di Valentin, C.; Pacchioni, G. *J. Phys. Chem. C* **2009**, *113*, 3382.
- (80) Di Valentin, C.; Pacchioni, G.; Selloni, A. *J. Phys. Chem. C* **2009**, *113*, 20543.
- (81) Matsumoto, M.; Ida, S.; Inoue, T. *J. Phys. Chem. C* **2008**, *112*, 11614.
- (82) Chen, X.; Liu, L.; Yu, P.; Mao, S. S. *Science* **2011**, *331*, 746.
- (83) Colombo, D. P., Jr; Bowman, R. M. *J. Phys. Chem.* **1996**, *100*, 18445 and references therein.
- (84) Iwata, K.; Takaya, T.; Hamaguchi, H.; Yamakata, A.; Ishibashi, T.; Unishi, H.; Kuruda, H. *J. Phys. Chem. B* **2004**, *108*, 20233.
- (85) Fujishima, A.; Zhang, X.; Tryk, A. D. *Surf. Sci. Rep.* **2008**, *63*, 515.

- (86) Efros, A. I. L.; Efros, A. L. *Sov. Phys. Semicond.* **1982**, *16*, 772.
- (87) Yoffre, I. *Adv. Phys.* **2001**, *50*, 1.
- (88) Glinka, Y. D.; Lin, S. H.; Hwang, L. P.; Chen, Y. T.; Tolk, N. H. *Phys. Rev. B* **2001**, *64*, 085421.
- (89) Pan, L. K.; Sun, C. Q. *J. Appl. Phys.* **2004**, *95*, 3819.
- (90) Frohlich, H.; Mott, N. *Proc. R. Soc. London, Ser. A* **1939**, *171*, 496.
- (91) Enright, B.; Fritzmaurice, D. *J. Phys. Chem.* **1996**, *100*, 1027.
- (92) Kroese, J. A.; Savenije, T. J.; Warman, J. M. *J. Am. Chem. Soc.* **2004**, *126*, 7608 and references therein.
- (93) Tamaki, Y.; Hara, K.; Katoh, R.; Tachiya, M.; Furube, A. *J. Phys. Chem. C* **2009**, *113*, 11741.
- (94) Van de Lagemaat, J.; Zhu, K.; Benkstein, K. D.; Frank, A. J. *Inorg. Chim. Acta* **2008**, *361*, 620.
- (95) Henderson, M. A. *Surf. Sci. Rep.* **2011**, *66*, 185.
- (96) Cornu, C. J. G.; Colussi, A. J.; Hoffmann, M. R. *J. Phys. Chem. B* **2003**, *107*, 3156 and references therein.
- (97) Green, A. N. M.; Chandler, R. E.; Haque, S. A.; Nelson, J.; Durrant, J. R. *J. Phys. Chem. B* **2005**, *109*, 142.
- (98) Tamaki, Y.; Furube, A.; Murai, M.; Hara, K.; Katoh, R.; Tachiya, M. *J. Am. Chem. Soc.* **2006**, *128*, 416 and references therein.
- (99) Hurum, D. C.; Kimberly, A. G.; Rajh, T.; Thurnauer, M. C. *J. Phys. Chem. B* **2005**, *109*, 977.
- (100) Naito, K.; Tachikawa, T.; Fujitsuka, M.; Majima, T. *J. Phys. Chem. C* **2008**, *112*, 1048.
- (101) Klimov, V. I. *J. Phys. Chem. B* **2000**, *104*, 6112.
- (102) Morello, G.; Giorgi, M.; Kudera, S.; Manna, L.; Cingolani, R.; Anni, M. *J. Phys. Chem. C* **2007**, *111*, 5846.
- (103) Chepic, D.; Efros, A. I. L.; Ekimov, A.; Ivanov, M.; Kharchenko, V. A.; Kudriavtsev, I. J. *Lumin.* **1990**, *47*, 113.
- (104) Efros, A. I. L.; Rosen, M. *Phys. Rev. Lett.* **1997**, *78*, 1110.
- (105) Bisquert, J.; Zaban, A.; Salvador, P. *J. Phys. Chem. B* **2002**, *106*, 8774.
- (106) Serpone, N.; Lawless, D.; Khairutdinov, R. *J. Phys. Chem.* **1995**, *99*, 16555.
- (107) Ke, S.-C.; Wang, T.-C.; Wong, M.-S.; Gopal, N. O. *J. Phys. Chem. B* **2006**, *110*, 11628.
- (108) Du, Y. K.; Rabani, J. *J. Phys. Chem. B* **2003**, *107*, 11970.
- (109) Choi, W. Y.; Termin, A.; Hoffmann, M. R. *J. Phys. Chem.* **1994**, *98*, 13669.
- (110) Fuerte, A.; Hernández-Alonso, M. D.; Maira, A. J.; Martínez-Arias, A.; Fernández-García, M.; Conesa, J. C.; Soria, J. *Chem. Commun.* **2001**, 2718.
- (111) Fuerte, A.; Hernández-Alonso, M. D.; Maira, A. J.; Martínez-Arias, A.; Fernández-García, M.; Conesa, J. C.; Soria, J. *J. Catal.* **2002**, *212*, 1.
- (112) Kubacka, A.; Colón, G.; Fernández-García *Catal. Today* **2009**, *143*, 286.
- (113) Kitano, M.; Matsuoka, M.; Ueshima, M.; Anpo, M. *Appl. Catal., A* **2007**, *325*, 1.
- (114) Rajeshwar, K.; de Tacconi, N. R.; Chenthamarakshan, C. R. *Chem. Mater.* **2001**, *13*, 2765.
- (115) Robert, D. *Catal. Today* **2007**, *122*, 20.
- (116) Bessekhouad, Y.; Robert, D.; Weber, Jr. *J. Photochem. Photobiol. A* **2004**, *163*, 569.
- (117) Hurum, D. C.; Agrios, A. G.; Crist, S. E.; Gray, K. A.; Rajh, T.; Thurnauer, M. C. *J. Electron Spectrosc. Relat. Phenom.* **2006**, *150*, 155.
- (118) Li, G.; Gray, K. A. *Chem. Phys.* **2007**, *339*, 173.
- (119) Li, G.; Dimitrijevic, N. M.; Chen, L.; Nichols, J. M.; Rajh, T.; Gray, K. M. *J. Am. Chem. Soc.* **2008**, *130*, 5402.
- (120) Wu, L.; Yu, J. C.; Fu, X. Z. *J. Mol. Catal.* **2006**, *244*, 25.
- (121) Hameed, A.; Montini, T.; Gamboa, V.; Fornasiero, P. *J. Am. Chem. Soc.* **2008**, *130*, 9658.
- (122) Robel, I.; Kuno, M.; Kamat, P. V. *J. Am. Chem. Soc.* **2007**, *129*, 4136.
- (123) Hyun, B.-R.; Zhang, Y.-W.; Bartnik, A. C. *ACS Nano* **2008**, *2*, 2206.
- (124) Li, J.; Zhang, J. F. *Coord. Chem. Rev.* **2009**, *293*, 3015.
- (125) Gao, B.; Kim, Y. J.; Chakrabarty, A. K.; Lee, W. I. *Appl. Catal., B* **2008**, *83*, 202.
- (126) Kim, D. H.; Park, H. S.; Kim, S.-J.; Lee, K. S. *Catal. Lett.* **2005**, *106*, 29.
- (127) Huang, H.; Li, D.; Lin, Q.; Zhang, W.; Shao, Y.; Chen, Y.; Sun, M.; Fu, X. *Environ. Sci. Technol.* **2009**, *43*, 4164.
- (128) Ban, Z.; Zhu, J.; Wang, S.; Cao, Y.; Quian, X.; Li, H. *J. Phys. Chem. C* **2008**, *112*, 6258.
- (129) Zhang, X.; Zhang, L.; Xie, T.; Wang, D. *J. Phys. Chem. C* **2009**, *113*, 7371.
- (130) Tachikawa, T.; Fujitsuka, M.; Majima, T. *J. Phys. Chem. B* **2006**, *106*, 29.
- (131) Fu, N.; Lu, G. *Chem. Commun.* **2009**, 3591.
- (132) Li, L.; Wu, Y. Q.; Guo, Y. H.; Hu, C. W. *Microporous Mesoporous Mater.* **2005**, *87*, 1.
- (133) Yang, Y.; Wu, Q. Y.; Gou, Y. H.; Hu, C. W.; Wang, E. *J. Mol. Catal. A* **2005**, *225*, 203.
- (134) Woan, K.; Pyrgiotakis, G.; Sigmund, W. *Adv. Mater.* **2009**, *21*, 1.
- (135) Kubacka, A.; Serrano, C.; Ferrer, M.; Lundsford, H.; Bieleck, P.; Cerrada, M. L.; Fernández-García, M.; Fernández-García, M. *Nano Lett.* **2007**, *7*, 2529.
- (136) Cerrada, M. L.; Serrano, C.; Sánchez-Chaves, M.; Fernández-Martín, F.; de Andrés, A.; Jiménez-Riobóo, R. J.; Kubacka, A.; Ferrer, M.; Fernández-García, M.; Fernández-García, M. *Adv. Funct. Mater.* **2008**, *18*, 1949.
- (137) Kubacka, A.; Serrano, C.; Cerrada, M. L.; Fernández-García, M.; Ferrer, M.; Fernández-García, M. *J. Phys. Chem. C* **2009**, *113*, 9182.
- (138) Wang, Y.; Zhang, M.; Cheng, F.; Yang, J. *Appl. Catal., B* **2009**, *90*, 249.
- (139) Kudo, A. *Pure Appl. Chem.* **2007**, *79*, 1917.
- (140) Zhang, H.; Zhu, Y. *J. Phys. Chem. C* **2010**, *114*, 5822.
- (141) Graetzel, M. *Nature* **2001**, *414*, 338.
- (142) Sayama, K.; Musaka, R.; Abe, Y.; Arakawa, H. *J. Photochem. Photobiol. A* **2002**, *148*, 71.
- (143) Deskins, N. A.; Kerisit, S.; Rosso, K. M.; Dupuis, M. *J. Phys. Chem. C* **2007**, *111*, 9290.
- (144) Zhang, J.; Xu, Q.; Feng, Z.; Li, M.; Li, C. *Angew. Chem., Int. Ed.* **2008**, *47*, 1766.
- (145) Zachariach, A.; Baiju, K. V.; Suukla, S.; Deepa, K. S.; James, J.; Warrier, K. G. K. *J. Phys. Chem. C* **2008**, *112*, 11345.
- (146) Lu, L.; Li, L.; Wang, X.; Li, G. *J. Phys. Chem. B* **2005**, *109*, 17151.
- (147) Machela, L.; Tucek, J.; Zboril, R. *Chem. Mater.* **2011**, *11*, 3255.
- (148) Boulora, M.; Lucaleau, G. *J. Solid State Chem.* **2000**, *167*, 425.
- (149) Song, H.; Jiung, H.; Liu, X.; Meng, G. *J. Photochem. Photobiol. A* **2006**, *181*, 421.
- (150) Yin, M.; Wu, C. K.; Lon, Y. B.; Burda, C.; Koberstein, J. T.; Zhu, Y. M.; Ó'Brien, S. *J. Am. Chem. Soc.* **2005**, *127*, 9506.
- (151) Testino, A.; Bellobono, I. R.; Buscaglia, V.; Canevali, C.; D'Arienzo, M.; Polizzio, S.; Scotti, R.; Morazzoni, F. *J. Am. Chem. Soc.* **2007**, *129*, 3564.
- (152) Hernández-Alonso, M. D.; Coronado, J. M.; Bachiller-Baeza, B.; Fernández-García, M.; Soria, J. *Chem. Mater.* **2007**, *19*, 4283.
- (153) Fuji, H.; Ohtaki, M.; Eguchi, K.; Arai, H. *J. Photochem. Photobiol. A* **1998**, *129*, 61.
- (154) Lee, S. K.; Mills, A. *Platinum Met. Rev.* **2003**, *47*, 61.
- (155) Awazu, K.; Fujimaki, M.; Rockstuhl, C.; Tominga, J.; Morakami, H.; Ohki, Y.; Yoshida, N.; Watanabe, T. *J. Am. Chem. Soc.* **2008**, *130*, 1676.
- (156) López, N.; Illas, F. Theoretical description of the Metal-Oxide Interface by First Principle Methods. In *Supported Metal Catalysts*; Anderson, J. A., Fernández-García, M., Eds.; Imperial College Press: London, 2005.
- (157) Gong, X.-Q.; Selloni, A.; Dulub, O.; Jacobson, P.; Diebold, U. *J. Am. Chem. Soc.* **2008**, *130*, 370.
- (158) Osterloh, F. E. *Chem. Mater.* **2008**, *20*, 35.
- (159) Abe, R.; Takami, H.; Murakami, N.; Ohtani, B. *J. Am. Chem. Soc.* **2008**, *130*, 7780.

- (160) Arai, T.; Yanagida, M.; Konishi, Y.; Ikura, A.; Iwasaki, Y.; Sugihara, H.; Sayama, K. *Appl. Catal., B* **2008**, *84*, 42.
- (161) Luca, V.; Thompson, S.; Howe, R. F. *J. Chem. Soc., Faraday Trans.* **1997**, *93*, 219S.
- (162) Wilke, K.; Brever, H. D. *J. Photochem. Photobiol. A* **1999**, *121*, 49.
- (163) Lin, J.; Yu, J. C.; Lo, D.; Lam, S. K. *J. Catal.* **1999**, *183*, 168.
- (164) Salim, N. I.; Bagshaw, S. A.; Bittar, A.; Kemmit, T.; McQuillan, A. J.; Mills, A. M.; Ryan, M. J. *J. Mater. Chem.* **2000**, *10*, 2358.
- (165) Wang, J. A.; Limas-Ballesteros, R.; López, T.; Moreno, A.; Gómez, R.; Novaro, O.; Bokhimi, X. *J. Phys. Chem. B* **2001**, *105*, 6292.
- (166) Guidi, V.; Carotta, M. C.; Ferroni, M.; Martinelli, G.; Sacerdoti, M. *J. Phys. Chem. B* **2003**, *107*, 120.
- (167) Wu, J.-C.-S.; Chen, C.-H. *J. Photochem. Photobiol. A* **2004**, *163*, 509.
- (168) Gracia, F.; Holgado, J. P.; Caballero, A.; González-Elipe, A. R. *J. Phys. Chem. B* **2004**, *108*, 17466.
- (169) Nagavendi, K.; Hedge, M. S.; Madras, G. *J. Phys. Chem. B* **2004**, *108*, 20204.
- (170) Fernández-García, M.; Martínez-Arias, A.; Fuerte, A.; Conesa, J. C. *J. Phys. Chem. B* **2005**, *109*, 6075.
- (171) Kim, D. H.; Park, H. S.; Kim, S.-J.; Lee, K. S. *Catal. Lett.* **2005**, *100*, 49.
- (172) Chartterjee, D.; Dasgupta, S. *J. Photochem. Photobiol. C* **2005**, *6*, 186.
- (173) Shi, J.; Leng, W.; Cao, J.; Zhang, J.; Cao, C. *Chin. J. Chem. Phys.* **2006**, *19*, 643.
- (174) Kubacka, A.; Martínez-Arias, A.; Fuerte, A.; Fernández-García, M. *Appl. Catal., B* **2007**, *74*, 26.
- (175) Fang, J.; Bao, H.; He, B.; Wang, F.; Si, D.; Jiang, Z.; Pan, Z.; Wei, S.; Huang, W. *J. Phys. Chem. C* **2007**, *111*, 19078.
- (176) Knauth, P.; Chadwick, A. V.; Lippens, P. E.; Auer, G. *Phys. Chem. Phys. Chem.* **2009**, *10*, 1238.
- (177) Wang, Y.; Zhang, L.; Li, S.; Jena, P. *J. Phys. Chem. C* **2009**, *113*, 9210.
- (178) Steng, V.; Bakardjieva, S.; Murafa, N. *Mater. Chem. Phys.* **2009**, *114*, 217.
- (179) Kim, D.-S.; Yang, J. H.; Balaji, S.; Cho, H.-J.; Kim, M. K.; Kang, D.-O.; Dajaoued, Y.; Kwon, Y.-U. *CrystEngComm* **2009**, *11*, 1621.
- (180) Wang, E.; Yang, W.; Cao, Y. *J. Phys. Chem. C* **2009**, *113*, 20912.
- (181) Shah, S. I.; Li, W.; Huang, C. P.; Jung, O.; Ni, C. *Proc. Natl. Acad. Sci. U.S.A.* **2002**, *99*, 6482.
- (182) Xie, Y.; Yuan, C. *Appl. Catal., B* **2003**, *46*, 251.
- (183) Otsuka, Y. M. S.; Omata, T.; Yoshimura, M. *J. Alloys Compd.* **2004**, *376*, 262.
- (184) Nowotny, B. M. K.; Sheppard, L. R.; Bak, T.; Nowotny, J. *J. Phys. Chem. C* **2008**, *112*, 5275.
- (185) Rodríguez-Torres, C. E.; Cabreras, A. I.; Errico, L. A.; Adán, C.; Requejo, F. G.; Weissmann, M.; Stewart, S. J. *J. Phys.: Condens. Matter* **2008**, *20*, 135210.
- (186) Bechstein, R.; Kitta, M.; Schutte, J.; Kuhnle, A.; Onishi, H. *J. Phys. Chem. C* **2009**, *113*, 3277.
- (187) Ruiz, A. M.; Dezanneau, G.; Arbiol, J.; Cornet, A.; Morante, J. R. *Chem. Mater.* **2004**, *16*, 862.
- (188) Márquez, A. M.; Plata, J. J.; Ortaga, Y.; Fdez. Sanz, J. *J. Phys. Chem. C* **2011**, *115*, 16970.
- (189) Chen, X.; Low, Y.; Samia, A. C. S.; Burda, C.; Gole, J. L. *Adv. Funct. Mater.* **2005**, *15*, 41.
- (190) Kitano, M.; Funatsu, K.; Matsuoka, M.; Ueshima, M.; Anpo, M. *J. Phys. Chem. B* **2006**, *110*, 25266.
- (191) Colón, G.; Sampedro, P.; Fernández-García, M.; Chen, H.; Hanson, J. C.; Rodríguez, J. A. *Langmuir* **2008**, *24*, 11111.
- (192) Asahi, R.; Morikawa, T.; Ohwaki, T.; Aoki, K.; Ega, Y. *Science* **2001**, *293*, 269.
- (193) Gole, J. L.; Stout, J. D.; Burda, C.; Lou, Y. B.; Chen, X. B. *J. Phys. Chem. B* **2004**, *108*, 1230.
- (194) Di Valentini, C.; Pacchioni, G.; Selloni, A.; Livraghi, S.; Giamello, E. *J. Phys. Chem. B* **2005**, *109*, 11414.
- (195) Mrowetz, M.; Balcerksi, W.; Colussi, A. J.; Hoffmann, M. R. *J. Phys. Chem. B* **2004**, *108*, 17269.
- (196) Asahi, R.; Morikawa, T. *Chem. Phys.* **2007**, *339*, 57.
- (197) Chen, C.; Bai, H.; Chang, C. *J. Phys. Chem. C* **2007**, *111*, 15228.
- (198) Finazzi, E.; Di Valentini, C.; Selloni, A.; Pacchioni, G. *J. Phys. Chem. C* **2007**, *111*, 9275.
- (199) Yay, K.; Dai, Y.; Huang, B. *J. Phys. Chem. C* **2007**, *111*, 12086.
- (200) Graciani, J.; Álvarez, L. J.; Rodríguez, J. A.; Fernández-Sanz, J. *J. Phys. Chem. C* **2008**, *112*, 2624.
- (201) Livraghi, S.; Chierotti, M. R.; Magnacca, G.; Paganini, M. C.; Capalletti, G.; Bianchi, C. L. *J. Phys. Chem. C* **2008**, *112*, 17244.
- (202) Russo, S. P.; Grey, I. E.; Wilson, N. C. *J. Phys. Chem. C* **2008**, *112*, 7653.
- (203) Belver, C.; Bellod, R.; Steward, S. J.; Requejo, F. G.; Fernández-García, M. *Appl. Catal., B* **2006**, *65*, 309.
- (204) Nakano, Y.; Morikawa, T.; Ohwaki, T.; Taga, Y. *Appl. Phys. Lett.* **2005**, *86*, 132104.
- (205) Steward, S. J.; Fernández-García, M.; Belver, C.; Mun, B. S.; Requejo, F. G. *J. Phys. Chem. B* **2006**, *110*, 16482.
- (206) Batzill, M.; Morales, E. H.; Diebold, U. *Phys. Rev. Lett.* **2006**, *96*, 026103.
- (207) Braum, A.; Akurchi, K. K.; Fortunato, G.; Reifler, F. A.; Ritter, A.; Harvey, A. S.; Vital, A.; Graule, T. *J. Phys. Chem. C* **2010**, *114*, 516.
- (208) Khan, S. U. M.; Al-Shahry, M.; Ingler, W. B. *Science* **2002**, *297*, 2243.
- (209) Sakthivel, S.; Kisch, H. *Angew. Chem., Int. Ed.* **2003**, *42*, 4908.
- (210) Irie, H.; Watanabe, Y.; Hashimoto, K. *Chem. Lett.* **2003**, *32*, 772.
- (211) Zhao, J.; Chen, C.; Ma, W. *Topics Catal.* **2005**, *35*, 267.
- (212) Kamisaka, H.; Adachi, T.; Yamashita, K. *J. Chem. Phys.* **2005**, *123*, 084704.
- (213) Di Valentini, C.; Pacchioni, G.; Selloni, A. *Chem. Mater.* **2005**, *17*, 6656.
- (214) Treschev, S. Y.; Chou, P.-W.; Tseng, Y.-H.; Wang, J.-B.; Perevedentseva, E. V.; Cheng, C.-L. *Appl. Catal., B* **2008**, *79*, 8.
- (215) Graciani, J.; Ortega, Y.; Fernández-Sanz, J. *Chem. Mater.* **2009**, *21*, 1431.
- (216) Hattori, A.; Yamamoto, M.; Tada, H.; Ito, S. *Chem. Lett.* **1998**, *27*, 707.
- (217) Yu, J. C.; Yu, J. G.; Ho, W. K.; Jiang, Z. T.; Zhang, L. Z. *Chem. Mater.* **2002**, *14*, 3808.
- (218) Li, D.; Haneda, H.; Labhsetwar, N. K.; Hishita, S.; Ohashi, N. *Chem. Phys. Lett.* **2005**, *401*, 579.
- (219) Czoska, A. M.; Livraghi, S.; Chiesa, M.; Giamello, E.; Agnoli, S.; Granozzi, G.; Finazzi, E.; Di Valentini, C.; Pacchioni, G. *J. Phys. Chem. C* **2008**, *112*, 8951.
- (220) Yang, H.; Dai, Y.; Huang, B.; Whangbo, M.-H. *Chem. Mater.* **2008**, *20*, 6528.
- (221) Umebayashi, T.; Yamaki, T.; Tanaka, S.; Asai, K. *Chem. Lett.* **2003**, *32*, 330.
- (222) Ohno, T.; Akiyosi, M.; Umebayashi, T.; Asai, K.; Mitsui, T.; Matsumura, M. *Appl. Catal., A* **2004**, *265*, 115.
- (223) Yang, Q.; Xie, C.; Gao, Z.; Du, Y. *J. Phys. Chem. B* **2005**, *109*, 5554.
- (224) Takeshita, K.; Yamakata, A.; Ishibashi, T.; Onishi, H.; Nishijima, K.; Ohno, T. *J. Photochem. Photobiol. A* **2006**, *177*, 269.
- (225) Tian, F.; Liu, C. B. *J. Phys. Chem. B* **2006**, *110*, 17866.
- (226) Izumi, Y.; Itoi, T.; Peng, S.; Oka, K.; Shivata, Y. *J. Phys. Chem. C* **2009**, *113*, 6706.
- (227) Zhao, W.; Ma, W.; Chen, C.; Zhao, J.; Shuai, Z. *J. Am. Chem. Soc.* **2004**, *126*, 4782.
- (228) Chen, D.; Yang, D.; Wang, Q.; Jiang, Z. Y. *Ind. Eng. Chem. Res.* **2006**, *45*, 4110.
- (229) Geng, H.; Yin, S. W.; Yang, Z. G.; Shuai, B. G.; Lui, J. *J. Phys.: Condens. Matter* **2006**, *18*, 87.
- (230) In, S.; Orlov, A.; Berg, R.; García, F.; Pedrosa-Jiménez, S.; Tikhov, M. S.; Wright, D. S.; Lambert, R. M. *J. Am. Chem. Soc.* **2007**, *129*, 13790.

- (231) Luo, H.; Takata, T.; Lee, Y.; Zhao, J.; Domen, K.; Yan, Y. *Chem. Mater.* **2004**, *16*, 846.
- (232) Lin, L.; Lin, W.; Zhu, Y.; Zhao, B.; Xie, Y. *Chem. Lett.* **2005**, *34*, 284.
- (233) Lin, L.; Lin, W.; Xie, J. L.; Zhu, Y. X.; Zhao, B. Y.; Chie, Y. C. *Appl. Catal., B* **2007**, *75*, 52.
- (234) Korou, L.; Papp, S.; Bertoli, I.; Dékány, I. *Chem. Mater.* **2007**, *19*, 4811.
- (235) Hong, X.; Wang, Z.; Cai, W.; Lu, F.; Zhang, J.; Yang, M.; Ma, N.; Liu, Y. *Chem. Mater.* **2005**, *17*, 1548.
- (236) Su, W.; Zhang, Y.; Li, Z.; Wu, L.; Wang, X.; Li, J.; Fu, X. Z. *Langmuir* **2008**, *24*, 3422.
- (237) Tojo, S.; Tachikawa, M.; Fujishita, M.; Majima, T. *J. Phys. Chem. C* **2008**, *112*, 14948.
- (238) Liu, G.; Sun, C.; Cheng, L.; Chen, Z.; Wang, X.; Wang, L.; Smith, S. C.; Lu, G. Q. M.; Chern, H.-M. *J. Mater. Chem.* **2009**, *19*, 2822.
- (239) Li, D.; Haneda, H.; Hishita, S.; Ohashi, N. *Mater. Sci. Eng., B* **2005**, *117*, 67.
- (240) Li, D.; Haneda, H.; Hishita, S.; Ohashi, N. *Chem. Mater.* **2005**, *17*, 2588.
- (241) Maeda, K.; Shimodaira, Y.; Lee, B.; Teramura, K.; Lu, D.; Kobayashi, H.; Domen, K. *J. Phys. Chem. C* **2007**, *111*, 18270.
- (242) Di Valentin, C.; Finazzi, E.; Pacchioni, G. *Chem. Mater.* **2008**, *20*, 3706.
- (243) Seibel, H. A.; Karen, P.; Wagner, T. R.; Woodward, P. M. *J. Mater. Chem.* **2009**, *19*, 471.
- (244) Long, M.; Cai, W.; Wang, Z.; Liu, G. *Chem. Phys. Lett.* **2006**, *420*, 71.
- (245) Maeda, K.; Lee, B.; Lu, D.; Domen, K. *Chem. Mater.* **2009**, *21*, 2286.
- (246) Gombac, V.; De Rogatis, L.; Gasporotto, A.; Vicario, G.; Montini, T.; Barreca, D.; Baldacci, G.; Fornasiero, P.; Tondello, E.; Graziani, M. *Chem. Phys.* **2007**, *339*, 111.
- (247) Liu, G.; Zhao, Y.; Sun, C.; Li, F.; Lu, G. Q.; Cheng, H.-M. *Angew. Chem., Int. Ed.* **2008**, *47*, 4516.
- (248) Liu, G.; Sun, C.; Cheng, L.; Jin, Y.; Lu, H.; Wang, L.; Smith, S. C.; Lu, G. Q.; Cheng, H.-M. *J. Phys. Chem. C* **2009**, *113*, 12317.
- (249) Feng, N.; Zheng, A.; Wang, Q.; Ren, P.; Gao, X.; Liu, S. B.; Shen, Z.; Chen, T.; Deng, F. *J. Phys. Chem. C* **2011**, *115*, 2709.
- (250) Noguchi, D.; Kawamata, Y.; Nagatomo, T. *J. Electrochem. Soc.* **2005**, *152*, D124.
- (251) Zabek, P.; Ebert, J.; Kirsch, H. *Photochem. Photobiol. Sci.* **2009**, *8*, 264.
- (252) Yun, H. J.; Lee, H.; Joo, J. B.; Kim, N. D.; Kang, M. Y.; Yi, J. *Appl. Catal., B* **2010**, *94*, 241.
- (253) Ikeda, T.; Nomoto, T.; Eda, K.; Mizutani, Y.; Kato, H.; Kudo, A.; Onishi, H. *J. Phys. Chem. C* **2008**, *112*, 1167.
- (254) Nishiro, R.; Sato, H.; Kudo, A. *Phys. Chem. Chem. Phys.* **2005**, *7*, 2241.
- (255) Ahamd, A.; Shah, J. A.; Buzby, S.; Shah, S. I. *Eur. J. Inorg. Chem.* **2008**, 948.
- (256) Dai, X. Q.; Xiao, H. Y.; Li, W. S.; Na, Y. Q.; Zhou, X. P. *J. Comb. Chem.* **2005**, *7*, 539.
- (257) Sasikala, R.; Sudasan, V.; Sudakar, C.; Naik, R.; Sakuntala, T.; Bharadway, S. R. *Int. J. Hydrogen Energy* **2008**, *33*, 4966.
- (258) Jian, J.; Song, W.; Zhou, Z.; Liu, X. *J. Phys. Chem. Solids* **2007**, *68*, 1830.
- (259) Liu, S.; Yu, J.; Mann, S. *J. Phys. Chem. C* **2009**, *113*, 10712.
- (260) Zhang, J.; Pan, C.; Wei, J.; Xiong, R. *ACS Appl. Mater. Interfaces* **2010**, *2*, 1173.
- (261) Xu, J. J.; Ao, Y. H.; Fu, D. G. *Appl. Surf. Sci.* **2009**, *256*, 884.
- (262) Isimjan, T. T.; Rubby, A. E.; Rohani, S.; Ray, A. K. *Nanotechnology* **2010**, *21*, 055706.
- (263) Cong, Y.; Zhang, J. L.; Chen, F.; Anpo, M. *J. Phys. Chem. C* **2007**, *111*, 10618.
- (264) Xin, M. Y.; Zhang, J. L.; Chen, F. *J. Phys. Chem. C* **2009**, *113*, 12848.
- (265) Gu, D. E.; Yang, B. C.; Hu, Y. D. *Catal. Commun.* **2008**, *9*, 1472.
- (266) Liu, J.; Han, R.; Zhao, Y.; Yang, H.; Lu, W.; Zhang, Y. *J. Phys. Chem. C* **2011**, *115*, 4507.
- (267) Kubacka, A.; Bachiller-Baeza, B.; Colón, G.; Fernández-García, M. *J. Phys. Chem. C* **2009**, *113*, 8553.
- (268) Sasikala, R.; Shirole, A. R.; Sudasan, V.; Rao, R.; Bharadway, S. R. *Appl. Catal., A* **2010**, *377*, 47.
- (269) Wang, E. J.; He, T.; Zhao, L. S.; Chen, Y. M.; Cao, Y. A. *J. Mater. Chem.* **2011**, *21*, 144.
- (270) Liu, C.; Tang, X.; Mo, C.; Qiang, Z. *J. Solid State Chem.* **2008**, *181*, 913.
- (271) Xu, J. J.; Ao, Y. H.; Fu, D. G. *J. Colloid Interface Sci.* **2008**, *328*, 447.
- (272) Shen, Y.; Xiong, T.; Li, T.; Yang, K. *Appl. Catal., B* **2008**, *83*, 177.
- (273) Kubacka, A.; Bachiller-Baeza, B.; Colón, G.; Fernández-García, M. *Appl. Catal., B* **2010**, *93*, 274.
- (274) Gao, Y.; Li, J.; Xia, J.-B.; Wei, S.-H. *Phys. Rev. Lett.* **2009**, *102*, 036402.
- (275) Chen, C.; Ma, W.; Zhao, J. *Curr. Org. Chem.* **2010**, *14*, 630.
- (276) Xu, Y.; Schoonen, M. A. A. *Am. Mineral.* **2000**, *85*, 543.
- (277) Nolan, M.; Elliot, S. D. *Thin Solid Films* **2008**, *516*, 1468.
- (278) Scanlon, D. O.; Watson, G. W. *J. Phys. Chem. Lett.* **2010**, *1*, 2582.
- (279) Borgohain, K.; Morase, N.; Mahumani, S. *J. Appl. Phys.* **2002**, *92*, 1292.
- (280) Filippetti, A.; Fiorentini, V. *Phys. Rev. B* **2005**, *72*, 035128.
- (281) Rafea, M. A.; Roushdy, N. *J. Appl. Phys. D* **2009**, *42*, 015413.
- (282) Kubo, T.; Nishikitani, Y. *J. Electrochem. Soc.* **1998**, *145*, 1729.
- (283) Karazhanov, S. Zh.; Zhang, Y.; Wang, L.-W.; Mascarenhas, A.; Deb, S. *Phys. Rev. B* **2003**, *68*, 233204.
- (284) Higashimoto, S.; Sakiyana, M.; Azuma, M. *Thin Solid Films* **2006**, *503*, 201.
- (285) Iwamoto, M.; Abe, T.; Tachibana, Y. *J. Mol. Catal. A* **2000**, *55*, 143.
- (286) Salazar, J. S.; Pérez, L.; Abril, O.; Pouvoy, G. *Chem. Mater.* **2011**, *23*, 1379.
- (287) Yagi, I.; Mikami, K.; Ebina, K.; Okamura, M.; Uosaki, K. *J. Phys. Chem. B* **2006**, *110*, 14197.
- (288) Moreals, I.; Lambert, K.; Smetas, D.; Moynek, D. D.; Martins, J. C.; Vanhaecke, F.; Vantomme, A.; Delirue, C.; Allan, G.; Heis, Z. *ACS Nano* **2009**, *3*, 3023 and references therein.
- (289) Mora-Seró, I.; Bisquert, J. *Nano Lett.* **2003**, *3*, 945.
- (290) Teoch, W. Y.; Madder, L.; Avel, R. J. *Catal.* **2007**, *251*, 271.
- (291) Di Paola, A.; García-López, E.; Ikeda, S.; Marci, C.; Ohtani, B.; Palmisano, L. *Catal. Today* **2002**, *75*, 87.
- (292) Mie, G. *Ann Phys. (Leipzig)* **1908**, *25*, 377.
- (293) Chen, X.; Zhan, H.-Y.; Zao, J. C.; Zheng, Z.-F. *Angew. Chem., Int. Ed.* **2008**, *47*, 5353.
- (294) Potje-Kamloth, K. *Chem. Rev.* **2008**, *108*, 367.
- (295) Atwater, H. A.; Polman, A. *Nat. Mater.* **2010**, *9*, 205.
- (296) Ismael, A. A.; Bahnemann, D. W.; Bannat, I.; Wak, M. *J. Phys. Chem. C* **2009**, *113*, 7429.
- (297) Gao, S.; Ueno, K.; Misawa, H. *Acc. Chem. Res.* **2011**, *44*, 251.
- (298) Zhiyong, Y.; Laub, D.; Bensimon, M.; Kiwi, J. *Inorg. Chim. Acta* **2008**, *361*, 589.
- (299) Zhang, Y.; Wei, S.; Zhang, W.; Xu, Y.-J.; Su, D. S.; Xiao, F.-S. *ChemSusChem* **2009**, *2*, 867.
- (300) Luque, A.; Martín, A.; Antolín, E.; Tablero, C. *Physica B* **2006**, *382*, 320.
- (301) Adan, C.; Martínez-Arias, A.; Malato, S.; Bahamonde, A. *Appl. Catal., B* **2009**, *93*, 96.
- (302) Araña, J.; Herrero-Melián, J. A.; Pérez-Peña, J. *Appl. Catal., B* **2002**, *36*, 113.
- (303) Ubemayashi, T.; Yamaki, T.; Itoh, H.; Asai, K. *J. Phys. Chem. Solids* **2002**, *63*, 1909.
- (304) Vittadini, A.; Casarin, M.; Sambi, M.; Selloni, A. *J. Phys. Chem. B* **2005**, *109*, 21766.
- (305) Thimsen, E.; Biwas, S.; Lo, C. S.; Biwas, P. *J. Phys. Chem. C* **2009**, *113*, 2014.

- (306) Shao, G. *J. Phys. Chem. C* **2009**, *113*, 6800.
- (307) Wang, Y.; Doren, D. *J. Solid State Commun.* **2005**, *136*, 142.
- (308) Li, W.; Wang, W.; Lin, H.; Shah, S. I.; Huang, C. P.; Doren, D. J.; Rykov, S. A.; Chen, J. G.; Barreau, M. A. *Appl. Phys. Lett.* **2003**, *83*, 4143.
- (309) Zhao, D.; Peng, T.; Xiao, J.; Yan, C.; Ke, X. *Mater. Lett.* **2007**, *61*, 105.
- (310) Sensato, F. R.; Custodio, R.; Longo, E.; Beltrán, A.; Andrés, J. *Catal. Today* **2003**, *85*, 145.
- (311) Long, R.; Dai, Y.; Huang, B. *J. Phys. Chem. C* **2009**, *113*, 650.
- (312) Long, R.; Dai, Y.; Huang, B. *Phys. Chem. Chem. Phys.* **2009**, *11*, 8165.
- (313) Oropenza, F. E.; Davies, B.; Palgrave, R. G.; Eggleton, R. G. *Phys. Chem. Chem. Phys.* **2011**, *13*, 7882.
- (314) Boppan, V. B. R.; Lobo, R. F. *J. Catal.* **2011**, *281*, 156.
- (315) Wang, D.-Y.; Lin, H.-C.; Yen, C.-C. *Thin Solid Films* **2006**, *512*, 1047.
- (316) Mattsson, A.; Leideburg, M.; Larsson, K.; Westin, G.; Osterlund, L. *J. Phys. Chem. B* **2006**, *110*, 1210.
- (317) Adán, C.; Bahamonde, A.; Fernández-García, M.; Martínez-Arias, A. *Appl. Catal., B* **2007**, *72*, 11.
- (318) Ambrus, Z.; Balazs, N.; Alapi, T.; Wittmann, G.; Sipos, P.; Dombi, A.; Mogorosi, K. *Appl. Catal., B* **2008**, *81*, 27.
- (319) Yu, J.; Xiang, Q.; Zhou, M. *Appl. Catal., B* **2009**, *90*, 595.
- (320) Morokawa, T.; Asashi, R.; Ohwaki, T.; Aoki, A.; Taga, Y. *Jpn. J. Appl. Phys.* **2001**, *40*, L561.
- (321) Lin, Z.; Orlov, A.; Lambert, R. M.; Payne, R. C. *J. Phys. Chem. B* **2005**, *105*, 20948.
- (322) Chen, X.; Burda, C. *J. Am. Chem. Soc.* **2008**, *130*, 5018.
- (323) Bonch-Bruyevich, V. L. *The Electronic Theory of Heavily Doped Semiconductors*; Elsevier: New York, 1966.
- (324) Xie, Y.; Yuan, C. *Appl. Surf. Sci.* **2004**, *221*, 17.
- (325) Kim, C.; Kim, K.-S.; Kim, H. Y.; Han, Y. S. *J. Mater. Sci.* **2008**, *18*, 5809.
- (326) Yu, H.; Irie, H.; Hashimoto, K. *J. Am. Chem. Soc.* **2010**, *132*, 6898.
- (327) Wang, H.; Lewis, J. P. *J. Phys.: Condens. Matter* **2006**, *18*, 421.
- (328) Kudo, A.; Kato, H.; Tsuji, I. *Chem. Lett.* **2004**, *33*, 1534.
- (329) Maeda, K.; Domen, K. *J. Phys. Chem. C* **2007**, *111*, 7851.
- (330) Hur, S. G.; Kim, T. W.; Hwang, S. J.; Choy, J. H. *J. Photochem. Photobiol. A: Chem.* **2006**, *183*, 176.
- (331) Tang, J.; Zou, Z.; Ye, J. *Chem. Mater.* **2004**, *16*, 1644.
- (332) Peña, M. A.; Fierro, J. L. G. *Chem. Rev.* **2001**, *101*, 1981.
- (333) King, G.; Thimmaiah, S.; Dwivedi, A.; Woodward, P. M. *Chem. Mater.* **2007**, *19*, 6451.
- (334) Kako, T.; Zou, Z.; Katajiri, M.; Ye, J. *Chem. Mater.* **2007**, *19*, 198.
- (335) Tang, J.; Zou, Z.; Ye, J. *J. Phys. Chem. C* **2007**, *111*, 12779.
- (336) Cox, D. E.; Sleight, A. W. *Solid State Commun.* **1976**, *19*, 969.
- (337) Yang, Y.; Cao, Z.; Jiang, Y.; Liu, L.; Sun, Y. *Mater. Sci. Eng., B* **2006**, *132*, 311.
- (338) Yang, Y.; Sun, Y.; Jiang, Y. *Mater. Chem. Phys.* **2006**, *96*, 234.
- (339) Li, L.; Jing, W.; Fu, L.; Yang, Xin, B.; Fu, H. *Mater. Res. Bull.* **2007**, *42*, 203.
- (340) Joshi, U. A.; Jang, J. S.; Borse, P. H.; Lee, J. S. *Appl. Phys. Lett.* **2008**, *92*, 242106.
- (341) Gao, F.; Chen, X.; Yin, K.; Dong, S.; Ren, Z.; Yuan, F.; Yu, T.; Zou, Z.; Liu, J. M. *Adv. Mater.* **2007**, *19*, 2889.
- (342) Li, S.; Lin, Y. H.; Zhang, B. P.; Wang, Y.; Nan, C. W. *J. Phys. Chem. C* **2010**, *114*, 2903.
- (343) Catalán, G.; Scott, J. F. *Adv. Mater.* **2009**, *21*, 2463.
- (344) Das, S.; Basu, S. *J. Nanosci. Nanotechnol.* **2009**, *9*, 5622.
- (345) Ruan, Q. J.; Zhang, W. D. *J. Phys. Chem. C* **2009**, *113*, 4168.
- (346) Sun, S.; Wang, W.; Zhang, L.; Shang, M. *J. Phys. Chem. C* **2009**, *113*, 12826.
- (347) Borse, P. H.; Lee, J. S. *J. Appl. Phys.* **2006**, *100*, 124915.
- (348) Hur, S. G.; Kim, T. W.; Hwang, S. J.; Park, H.; Choi, W.; Kim, S. J.; Choy, J. H. *J. Phys. Chem. B* **2005**, *109*, 15001.
- (349) Wang, D.; Kako, T.; Ye, J. *Am. Chem. Soc.* **2008**, *130*, 2724.
- (350) Domen, K.; Kondo, J. N.; Hara, M.; Takata, T. *Bull. Chem. Soc. Jpn.* **2000**, *73*, 1307.
- (351) Domen, K.; Yoshimura, J.; Sekine, T.; Tanaka, A.; Onishi, T. *Catal. Lett.* **1990**, *4*, 339.
- (352) Takata, T.; Tanaka, A.; Hara, M.; Kondo, J. N.; Domen, K. *Catal. Today* **1998**, *44*, 17.
- (353) Kendall, K. R.; Navas, C.; Thomas, J. K.; Loye, H. C. *Chem. Mater.* **1996**, *8*, 642.
- (354) Zhang, C.; Zhu, Y. *Chem. Mater.* **2005**, *17*, 3537.
- (355) Amano, F.; Nogami, K.; Abe, R.; Ohtani, B. *Chem. Lett.* **2007**, *36*, 1314.
- (356) Fu, H.; Zhang, L.; Yao, W.; Zhu, Y. *Appl. Catal., B* **2006**, *66*, 100.
- (357) Zhang, L.; Wang, W.; Chen, Z.; Zhou, L.; Zhu, W. *J. Mater. Chem.* **2007**, *17*, 2526.
- (358) Zhang, L.; Wang, W.; Zhou, L.; Xu, H. *Small* **2007**, *3*, 1618.
- (359) Kato, H.; Kudo, A. *Chem. Phys. Lett.* **1998**, *295*, 487.
- (360) Tang, J.; Zou, Z.; Je, Y. *Catal. Lett.* **2004**, *92*, 53.
- (361) Wu, J.; Duan, F.; Zheng, Y.; Xie, Y. *J. Phys. Chem. C* **2007**, *111*, 12866.
- (362) Hou, J.; Qu, Y.; Kršmanović, D.; Ducati, C.; Eder, D.; Kumar, R. V. *J. Mater. Chem.* **2010**, *20*, 2418.
- (363) Zhao, X.; Xu, T.; Yao, W.; Zhang, C.; Zhu, Y. *Appl. Catal., B* **2007**, *72*, 92.
- (364) Saison, T.; Chemin, N.; Chaneac, C.; Durupthy, O.; Ruaux, V.; Mariey, L.; Maugé, F.; Beaunier, P.; Jolivet, J. P. *J. Phys. Chem. C* **2011**, *115*, 5657.
- (365) Cui, Z.; Zeng, D.; Tang, T.; Liu, J.; Xie, C. *Catal. Commun.* **2010**, *11*, 1054.
- (366) Murcia López, S.; Hidalgo, M. C.; Navío, J. A.; Colón, G. *J. Hazard. Mat.* **2011**, *185*, 1425.
- (367) Colón, G.; Murcia López, S.; Hidalgo, M. C.; Navío, J. A. *Chem. Comm.* **2010**, 4809.
- (368) Shimodaira, Y.; Kato, H.; Kobayashi, H.; Kudo, A. *J. Phys. Chem. B* **2006**, *110*, 17790.
- (369) Bi, J. H.; Wu, L.; Li, H.; Li, L. H.; Wang, X. X.; Fu, X. Z. *Acta Mater.* **2007**, *55*, 4699.
- (370) Long, M.; Cai, W.; Kisch, H. *Chem. Phys. Lett.* **2008**, *461*, 102.
- (371) Xie, H.; Shen, D.; Wang, X.; Shen, G. *Mater. Chem. Phys.* **2008**, *110*, 332.
- (372) Martínez de la Cruz, A.; Obregón Alfaro, S. *J. Mol. Catal. A: Chem.* **2010**, *320*, 85.
- (373) Martínez de la Cruz, A.; Obregón Alfaro, S.; López Cuellar, E.; Ortiz Méndez, U. *Catal. Today* **2010**, *129*, 194.
- (374) Man, Y.; Zong, R.; Zhu, Y. *Acta Phys.-Chim. Sin.* **2007**, *23*, 1671.
- (375) Zhou, L.; Wang, W.; Zhang, L. *J. Mol. Catal. A: Chem.* **2007**, *268*, 195.
- (376) Zheng, Y.; Duan, F.; Wu, J.; Liu, L.; Chen, M.; Xie, Y. *J. Mol. Catal. A: Chem.* **2009**, *303*, 9.
- (377) Lin, X.; Huang, T.; Huang, F.; Wang, W.; Shi, J. *J. Phys. Chem. B* **2006**, *110*, 24629.
- (378) Ye, L.; Zan, L.; Tian, L.; Peng, T.; Zhang, J. *Chem. Commun.* **2011**, *47*, 6951.
- (379) Lin, X.; Shan, Z.; Li, K.; Wang, W.; Yang, J.; Huang, F. *Solid State Science* **2007**, *9*, 944.
- (380) Shan, Z.; Wang, W.; Lin, X.; Ding, H.; Huang, F. *J. Solid State Chem.* **2008**, *181*, 1361.
- (381) Wang, W. D.; Huang, F. Q.; Lin, X. P. *Scr. Mater.* **2007**, *56*, 669.
- (382) Wang, W. D.; Huang, F. Q.; Lin, X. P.; Yang, J. H. *Catal. Commun.* **2008**, *9*, 8.
- (383) An, H.; Du, Y.; Wang, T.; Wang, C.; Hao, W.; Zhang, J. *Rare Met.* **2008**, *3*, 243.
- (384) Wang, Y.; Deng, K.; Zhang, L. *J. Phys. Chem. C* **2011**, *115*, 14300.
- (385) Lin, X.; Huang, T.; Huang, F.; Wang, W.; Shi, J. *J. Mater. Chem.* **2007**, *17*, 2145.

- (386) Frost, R. L.; Henry, D. A.; Weier, M. L.; Marten, W. *J. Raman Spectrosc.* **2006**, *37*, 722.
- (387) Zhang, L.; Chen, D.; Jiao, X. *J. Phys. Chem. B* **2006**, *110*, 2668.
- (388) Zhao, Y.; Xie, Y.; Zhu, X.; Yan, S.; Wang, S. *Chem.—Eur. J.* **2008**, *14*, 1601.
- (389) Zhou, L.; Wang, W.; Xu, H. *Cryst. Growth Des.* **2008**, *8*, 728.
- (390) Tokunaga, S.; Kato, H.; Kudo, A. *Chem. Mater.* **2001**, *13*, 4624.
- (391) Zhang, X.; Ai, Z.; Jia, F.; Zhang, L.; Fan, X.; Zou, Z. *Mater. Chem. Phys.* **2007**, *103*, 162.
- (392) Martínez de la Cruz, A.; García Pérez, U. M. *Mater. Res. Bull.* **2010**, *45*, 135.
- (393) Yin, W.; Wang, W.; Zhou, L.; Sun, S.; Zhang, L. *J. Hazard. Mater.* **2010**, *173*, 194.
- (394) Zhou, L.; Wang, W.; Liu, S.; Zhang, L.; Xu, H.; Zhu, W. *J. Mol. Catal. A: Chem.* **2006**, *252*, 120.
- (395) Guo, Y.; Yang, X.; Ma, F.; Li, X.; Xu, L.; Yuan, X.; Guo, Y. H. *Appl. Surf. Sci.* **2010**, *256*, 2215.
- (396) Zhou, Y.; Vuille, K.; Heel, A.; Probst, B.; Kontic, R.; Patzke, G. R. *Appl. Catal. A* **2010**, *375*, 140.
- (397) Xi, G.; Ye, J. *Chem. Commun.* **2010**, *46*, 1893.
- (398) Wang, D.; Jiang, H.; Zong, X.; Xu, Q.; Ma, Y.; Li, G.; Li, C. *Chem.—Eur. J.* **2011**, *17*, 1275.
- (399) Zheng, Y.; Wu, J.; Duan, F.; Xie, Y. *Chem. Lett.* **2007**, *36*, 520.
- (400) Zhou, L.; Wang, W.; Zhang, L.; Xu, H.; Zhu, W. *J. Phys. Chem. C* **2007**, *111*, 13659.
- (401) Yao, W.; Iwai, H.; Ye, J. *Dalton Trans.* **2008**, 1426.
- (402) Park, H. S.; Kweon, K. E.; Ye, H.; Paek, E.; Hwang, G. S.; Bard, A. J. *J. Phys. Chem. C* **2011**, *115* (36), 17870.
- (403) Subramanian, M. A.; Aravamudan, G.; Subba Rao, G. V. *Prog. Solid State Chem.* **1983**, *15*, 55.
- (404) Zou, Z.; Ye, J.; Arakawa, H. *J. Mol. Catal. A: Chem.* **2001**, *168*, 289.
- (405) Garza-Tovar, L. L.; Torres-Martínez, L. M.; Bernal Rodríguez, D.; Gómez, R.; del Angel, G. *J. Mol. Catal. A: Chem.* **2006**, *247*, 283.
- (406) Luan, J. F.; Hao, X. P.; Zheng, S. R.; Luan, G. Y.; Wu, X. S. *J. Mater. Sci.* **2006**, *41*, 8001.
- (407) He, Y.; Zhu, Y. *Chem. Lett.* **2004**, *33*, 900.
- (408) Kako, T.; Kikugawa, N.; Ye, J. *Catal. Today* **2008**, *131*, 197.
- (409) Tang, J.; Zou, Z.; Yin, J.; Ye, J. *Chem. Phys. Lett.* **2003**, *382*, 175.
- (410) Tang, J.; Zou, Z.; Katagiri, M.; Kako, T.; Ye, J. *Catal. Today* **2004**, *93*–95, 885.
- (411) Tang, J.; Zou, Z.; Ye, J. *Angew. Chem., Int. Ed.* **2004**, *43*, 4463.
- (412) Tang, J.; Zou, Z.; Ye, J. *Chem. Mater.* **2004**, *16*, 1644.
- (413) Ni, M.; Leung, M. K. H.; Leung, D. Y. C.; Sumathy, K. *Renewable Sustainable Energy Rev.* **2007**, *11*, 401.
- (414) Kudo, A.; Miseki, Y. *Chem. Soc. Rev.* **2009**, *38*, 253.
- (415) Chen, X.; Shen, S.; Guo, L.; Mao, S. S. *Chem. Rev.* **2010**, *110*, 6503.
- (416) Abe, R. *J. Photochem. Photobiol. C* **2010**, *11*, 179.
- (417) Maeda, K. *J. Photochem. Photobiol. C: Photochem. Rev.*, doi: 10.1016/j.jphotochemrev.2011.07.001.
- (418) Osterloh, F. E. *Chem. Mater.* **2008**, *20*, 35.
- (419) Woodhouse, M.; Parkinson, B. A. *Chem. Soc. Rev.* **2009**, *38*, 197.
- (420) Sato, S.; White, J. M. *Chem. Phys. Lett.* **1980**, *72*, 83.
- (421) Yamaguti, K.; Sato, S. *J. Chem. Soc., Faraday Trans. 1* **1985**, *81*, 1237.
- (422) Zong, X.; Yan, H.; Wu, G.; Ma, G.; Wen, F.; Wang, L.; Li, C. *J. Am. Chem. Soc.* **2008**, *130*, 7176.
- (423) Leung, D. Y. C.; Fu, X.; Wang, C.; Ni, M.; Leung, M. K. H.; Wang, X.; Fu, X. *ChemSusChem* **2010**, *3*, 681.
- (424) Hu, C. C.; Teng, H. J. *Catal.* **2010**, *272*, 1.
- (425) Maeda, K.; Abe, R.; Domen, K. *J. Phys. Chem. C* **2011**, *115*, 3057.
- (426) Hondow, N. S.; Chou, Y. H.; Sader, K.; Douthwaite, R. E.; Brydson, R. *ChemCatChem* **2011**, *3*, 990.
- (427) Kudo, A. *Mater. Res. Bull.* **2011**, *36*, 32.
- (428) Maeda, K.; Teramura, K.; Lu, D.; Takata, T.; Saito, N.; Inoue, Y.; Domen, K. *J. Phys. Chem. B* **2006**, *110*, 13753.
- (429) Maeda, K.; Teramura, K.; Lu, D.; Takata, T.; Saito, N.; Inoue, Y.; Domen, K. *Nature* **2006**, *440*, 295.
- (430) Maeda, K.; Teramura, K.; Lu, D.; Saito, N.; Inoue, Y.; Domen, K. *J. Phys. Chem. C* **2007**, *111*, 7554.
- (431) Maeda, K.; Teramura, K.; Lu, D.; Saito, N.; Inoue, Y.; Domen, K. *Angew. Chem. Int.* **2006**, *118*, 7970.
- (432) Maeda, K.; Sakamoto, N.; Ikeda, T.; Ohtsuka, H.; Xiong, A.; Lu, D.; Kanehara, M.; Teranishi, T.; Domen, K. *Chem.—Eur. J.* **2010**, *16*, 7750.
- (433) Kim, J.; Hwang, D. W.; Kim, H. G.; Bae, S. W.; Lee, J. S.; Li, W.; Oh, S. H. *Top. Catal.* **2005**, *35*, 295.
- (434) Takata, T.; Furumi, Y.; Shinohara, K.; Tanaka, A.; Hara, M.; Kondo, J. N.; Domen, K. *Chem. Mater.* **1997**, *9*, 1063.
- (435) Kato, H.; Kudo, A. *Catal. Lett.* **1999**, *58*, 153.
- (436) Hu, C. H.; Teng, H. J. *Catal.* **2010**, *172*, 1.
- (437) Yamakata, A.; Ishibashi, T.; Kato, H.; Kudo, A.; Onishi, H. *J. Phys. Chem. B* **2003**, *107*, 14383.
- (438) Machida, M.; Murakami, S.; Kijima, T.; Matsushima, S.; Arai, M. *J. Phys. Chem. B* **2001**, *105*, 3289.
- (439) Zhou, X.; Shi, J.; Li, C. *J. Phys. Chem. C* **2011**, *115*, 8305.
- (440) Zou, Z. G.; Ye, J. H.; Sayama, K.; Arakawa, H. *Nature* **2001**, *414*, 625.
- (441) Zou, Z. G.; Arakawa, H. *J. Photochem. Photobiol. A* **2003**, *158*, 145.
- (442) Maeda, K.; Teramura, K.; Saito, N.; Inoue, Y.; Kobayashi, H.; Domen, K. *Pure Appl. Chem.* **2006**, *78*, 2267.
- (443) Sato, J.; Saito, N.; Yamada, Y.; Maeda, K.; Takata, T.; Kondo, J. N.; Hara, M.; Kobayashi, H.; Domen, K.; Inoue, Y. *J. Am. Chem. Soc.* **2005**, *127*, 4150.
- (444) Maeda, K.; Teramura, K.; Saito, N.; Inoue, Y.; Domen, K. *Bull. Chem. Soc. Jpn.* **2007**, *80*, 1004.
- (445) Maeda, K.; Takata, T.; Hara, M.; Saito, N.; Inoue, Y.; Kobayashi, H.; Domen, K. *J. Am. Chem. Soc.* **2005**, *127*, 8286.
- (446) Maeda, K.; Teramura, K.; Takata, T.; Hara, M.; Saito, N.; Toda, K.; Inoue, Y.; Kobayashi, H.; Domen, K. *J. Phys. Chem. B* **2005**, *109*, 20504.
- (447) Tessier, F.; Maillard, P.; Lee, Y.; Bleugat, C.; Domen, K. *J. Phys. Chem. C* **2009**, *113*, 8526.
- (448) Lee, Y.; Terashima, H.; Shimodaira, Y.; Teramura, K.; Hara, M.; Kobayashi, H.; Domen, K.; Yashima, M. *J. Phys. Chem. C* **2007**, *111*, 1042.
- (449) Ishikawa, A.; Yamada, Y.; Takata, T.; Kondo, J. N.; Hara, M.; Kobayashi, H.; Domen, K. *Chem. Mater.* **2003**, *15*, 4442.
- (450) Ogisu, K.; Ishikawa, A.; Shimodaira, Y.; Takata, T.; Kobayashi, H.; Domen, K. *J. Phys. Chem. C* **2008**, *112*, 11978.
- (451) Kudo, A.; Sekizawa, M. *Chem. Commun.* **2000**, *15*, 1371.
- (452) Xing, C. J.; Zhang, Y. J.; Yan, W.; Guo, L. *J. Int. J. Hydrogen Energy* **2006**, *31*, 2018.
- (453) Zhang, W.; Zhong, Z.; Wang, Y.; Xu, R. *J. Phys. Chem. C* **2008**, *112*, 17635.
- (454) Shen, Z.; Chen, G.; Li, Y.; Wang, X.; Zhou, A. *Catal. Lett.* **2009**, *132*, 454.
- (455) Amirav, L.; Alivisatos, A. P. *J. Phys. Chem. Lett.* **2010**, *1*, 1051.
- (456) Zhang, W.; Xu, R. *Int. J. Hydrogen Energy* **2009**, *34*, 8495.
- (457) Sayama, K.; Yoshida, R.; Kusama, H.; Okabe, K.; Abe, Y.; Arakawa, H. *Chem. Phys. Lett.* **1997**, *277*, 387.
- (458) Abe, R.; Sayama, K.; Domen, K.; Arakawa, H. *Chem. Phys. Lett.* **2001**, *344*, 339.
- (459) Bard, A. J. *J. Photochem.* **1979**, *10*, 59.
- (460) Kato, H.; Hori, M.; Konta, R.; Shimodaira, Y.; Kudo, A. *Chem. Lett.* **2004**, *33*, 1348.
- (461) Wang, X.; Liu, G.; Chen, Z. G.; Li, F.; Lu, G. Q.; Cheng, H. M. *J. Mater. Res.* **2010**, *25*, 39.
- (462) Maeda, K.; Higashi, M.; Lu, D.; Abe, R.; Domen, K. *J. Am. Chem. Soc.* **2010**, *132*, 5858.
- (463) Tada, H.; Mitsui, T.; Kiyonaga, T.; Akita, T.; Tanaka, K. *Nat. Mater.* **2006**, *5*, 782.
- (464) Wang, X.; Liu, G.; Chen, Z. G.; Li, F.; Wang, L.; Lu, G. Q.; Cheng, H. M. *Chem. Commun.* **2009**, 3452.

- (465) Sasaki, Y.; Nemoto, H.; Saito, K.; Kudo, A. *J. Phys. Chem. C* **2009**, *113*, 17536.
- (466) Wang, D. F.; Zhou, Z. G.; Ye, J. H. *Chem. Mater.* **2005**, *17*, 3255.
- (467) Yun, H. J.; Lee, H.; Kim, N. D.; Lee, D. M.; Yu, S.; Yi, J. *ACS Nano* **2011**, *5*, 4084.
- (468) Jing, D.; Liu, H.; Zhang, X.; Zhao, L.; Guo, L. *Energy Convers. Manage.* **2009**, *50*, 2919.
- (469) Inoue, T.; Fujishima, A.; Konishi, S.; Honda, K. *Nature* **1979**, *277*, 637.
- (470) Koci, K.; Obalova, L.; Lacny, Z. *Chem. Pap.* **2008**, *62*, 1.
- (471) Roy, S. C.; Varghese, O. K.; Paulose, M.; Grimes, C. A. *ACS Nano* **2010**, *4*, 1259.
- (472) Zhou, H.; Fan, T.; Zhang, D. *ChemCatChem* **2011**, *3*, 513.
- (473) Jiang, Z.; Xiao, T.; Kuznetsov, V. L.; Edwards, P. P. *Philos. Trans. R. Soc. London* **2010**, *368*, 3343.
- (474) Koppenol, W. H.; Rush, J. D. *J. Phys. Chem.* **1987**, *91*, 4429.
- (475) Teramura, T.; Okuoka, S. I.; Tsuneoka, H.; Shishido, T.; Tanaka, T. *Appl. Catal., B* **2010**, *96*, 565.
- (476) Canfield, D.; Frese, K. W. *J. Electrochem. Soc.* **1983**, *130*, 1772.
- (477) Blajeni, B. A.; Halmann, M.; Manassen, J. *Sol. Energy Mater.* **1983**, *8*, 425.
- (478) Egging, B. R.; Irvine, J. T. R.; Murphy, E. P.; Grimshaw, J. *J. Chem. Soc., Chem. Commun.* **1988**, 1123.
- (479) Fujiwara, H.; Hosokawa, H.; Murakoshi, K.; Wada, Y.; Yanagida, S. *Langmuir* **1998**, *14*, 5154.
- (480) Kuwabata, S.; Nishida, K.; Tsuda, R.; Inoue, H.; Yoneyama, H. *J. Electrochem. Soc.* **1994**, *141*, 1498.
- (481) Anpo, M.; Yamashita, H.; Ichihashi, Y.; Fujii, Y.; Honda, M. *J. Phys. Chem. B* **1997**, *101*, 2632.
- (482) Tseng, I. H.; Wu, J. C. S.; Chou, H. Y. *J. Catal.* **2004**, *221*, 432.
- (483) Tan, S. S.; Zou, L.; Hu, E. *Sci. Technol. Adv. Mater.* **2007**, *9*, 89.
- (484) Lo, C. C.; Hung, C. H.; Yuan, C. S.; Wu, J. F. *Sol. Energy Mater. Sol. Cells* **2007**, *91*, 1765.
- (485) Zhao, Z. H.; Fan, J. M.; Liu, S. H.; Wang, Z. Z. *Chem. Eng. J.* **2009**, *151*, 134.
- (486) Kočí, K.; Matějů, K.; Obalová, L.; Krejčíková, S.; Lacný, Z.; Plachá, D.; Čapek, L.; Hospodková; Šolcová, O. *Appl. Catal., B* **2010**, *96*, 239.
- (487) Hwang, J. S.; Chang, J. S.; Park, S. E.; Ikeue, K.; Anpo, M. *Top. Catal.* **2005**, *35*, 311.
- (488) Yang, H. C.; Lin, H. Y.; Chien, Y. S.; Wu, J. C. S.; Wu, H. H. *Catal. Lett.* **2009**, *131*, 381.
- (489) Varghese, O. K.; Paulose, M.; La Tempa, T. J.; Grimes, C. A. *Nano Lett.* **2009**, *9*, 731.
- (490) Pan, P. W.; Chen, Y. W. *Catal. Commun.* **2007**, *8*, 1546.
- (491) Liu, Y.; Huang, B.; Dai, Y.; Zhang, X.; Qin, X.; Jiang, M.; Whangbo, M. H. *Catal. Commun.* **2009**, *11*, 210.
- (492) Yang, C.; Thompson, R. L.; Baltrus, J.; Matranga, C. *J. Phys. Chem. Lett.* **2010**, *1*, 48.
- (493) Hirano, K.; Inoue, K.; Yatsu, T. *J. Photochem. Photobiol., A* **1992**, *64*, 255.
- (494) Adachi, K.; Ohta, K.; Mizuno, T. *Sol. Energy* **1994**, *53*, 187.
- (495) Tseng, I. S.; Chang, W.-C.; Wu, J. C. S. *Appl. Catal., B* **2002**, *37*, 37.
- (496) Tseng, I. S.; Wu, J. C. S. *Catal. Today* **2004**, *97*, 113.
- (497) Tseng, I. H.; Wu, J. C. S.; Chou, H. Y. *J. Catal.* **2004**, *221*, 432.
- (498) Richardson, R. D.; Holland, E. J.; Carpenter, B. K. *Nat. Chem.* **2011**, *3*, 301.
- (499) Michl, J. *Nat. Chem.* **2011**, *3*, 268.
- (500) Yang, C. C.; Yu, Y. H.; van der Linden, B.; Wu, J. C. S.; Mul, G. *J. Am. Chem. Soc.* **2010**, *132*, 8398.
- (501) Yun, H. J.; Lee, H.; Joo, J. B.; Kim, W.; Yi, J. *J. Phys. Chem. C* **2009**, *113*, 3050.
- (502) Hu, X.; Zhang, T.; Jin, Z.; Huang, S.; Fang, M.; Wu, Y.; Zhang, L. *Cryst. Growth Des.* **2009**, *9*, 2324.
- (503) Wang, Z.; Lv, K.; Wang, G.; Deng, K.; Tang, D. *Appl. Catal., B* **2010**, *100*, 378.
- (504) Pan, J.; Liu, G.; Quing, G.; Lu, M.; Chang, H.-M. *Angew. Chem., Int. Ed.* **2011**, *50*, 2133.
- (505) Liu, G.; Yu, J. C.; Lu, G. Q.; Chen, H.-M. *Chem. Commun.* **2011**, *6763*.
- (506) Araña, J.; Doña-Rodríguez, J. M.; Protillo-Carrizo, D.; Fernández-Rodríguez, C.; Peña-Peña, J.; González-Díaz, O.; Navío, J. A.; Macías, M. *Appl. Catal., B* **2010**, *100*, 346.
- (507) Kamat, P. *J. Phys. Chem. B* **2002**, *106*, 7729.
- (508) Kuznetsov, V. V.; Serpone, N. *J. Phys. Chem. C* **2009**, *113*, 9510.
- (509) Begin-Colin, S.; Gadalla, A.; Gillot, P. *J. Phys. Chem. C* **2009**, *113*, 16589.
- (510) Zhang, Z.; Yates, J., Jr. *J. Phys. Chem. C* **2010**, *114*, 3008.
- (511) De Sario, P.; Chen, L.; Graham, M. E.; Gray, K. A. *J. Vac. Sci. Technol.* **2011**, *A29*, 031568.
- (512) Schaller, R. D.; Klimov, V. I. *Phys. Rev. Lett.* **2004**, *92*, 186601.
- (513) Zhang, H. *J. Mater. Chem.* **2009**, *19*, 5089.
- (514) Tada, H.; Kiyonaga, T.; Naya, S.-i. *Chem. Soc. Rev.* **2009**, *38*, 1849.
- (515) Cao, L.; Huang, A.; Spiess, F. J.; Suib, S. L. *J. Catal.* **1999**, *188*, 48.
- (516) Maira, J.; Yeung, K. L.; Lee, C. Y.; Yue, P. L.; Chan, C. K. *J. Catal.* **2000**, *192*, 185.
- (517) Maira, J.; Yeung, K. L.; Soria, J.; Coronado, J. M.; Belver, C.; Lee, C. Y.; Augugliaro, V. *Appl. Catal., B* **2001**, *29*, 327.
- (518) Anpo, M.; Shima, T.; Kodama, S.; Kubokawa, Y. *J. Phys. Chem.* **1987**, *91*, 4305.
- (519) Hao, W. C.; Zheng, S. K.; Wang, C.; Wang, T. M. *J. Mater. Sci. Lett.* **2002**, *21*, 1627.
- (520) Damm, C.; Voltzke, D.; Abicht, H.-P.; Israel, G. *J. Photochem. Photobiol., A* **2005**, *174*, 171.
- (521) Wang, C. C.; Zhang, Z.; Ying, J. Y. *Nano Struct. Mater.* **1997**, *9*, 583.
- (522) Wu, L.; Yu, C. J.; Zhang, L.; Wang, X.; Ho, W. *J. Solid State Chem.* **2004**, *177*, 2584.
- (523) Koci, K.; Obalova, L.; Matejova, L.; Placha, D.; Lacny, Z.; Jirkovsky, J.; Solcova, O. *Appl. Catal., B* **2009**, *89*, 494.
- (524) Rivera, P.; Tanak, K.; Hisanaga, T. *Appl. Catal., B* **1993**, *3*, 37.
- (525) Deng, X.; Yue, Y.; Gao, Z. *Appl. Catal., B* **2002**, *39*, 135.
- (526) Ohtani, B.; Ogawa, Y.; Nishimoto, S.-i. *J. Phys. Chem. B* **1997**, *101*, 3746.
- (527) Almquist, C. B.; Biswas, P. *J. Catal.* **2002**, *212*, 145.
- (528) Siemon, U.; Bahnemann, D.; Testa, J. J.; Rodríguez, D.; Litter, M. I.; Bruno, N. *J. Photochem. Photobiol., A* **2002**, *148*, 247.
- (529) Chen, G.; Luo, G.; Yang, X.; Sun, Y.; Wang, J. *Mater. Sci. Eng. A* **2004**, *380*, 320.
- (530) Wang, Q.; Zhang, M.; Chen, C.; Ma, W.; Zhao, J. *Angew. Chem., Int. Ed.* **2010**, *49*, 7976.
- (531) Emilio, C. A.; Litter, M. I.; Kunst, M.; Bouchard, M.; Colbeau-Justin, C. *Langmuir* **2006**, *22*, 3606.
- (532) Kim, M. R.; Ah, C. S.; Shin, D.; Lee, S. K.; Lee, W. I.; Jang, D.-J. *J. Nanosci. Nanotechnol.* **2008**, *8*, 3197.
- (533) Vamathevan, V.; Amal, R.; Beydoun, D.; Low, G.; McEnvoy, S. *Chem. Eng. J.* **2004**, *98*, 127.
- (534) Baba, R.; Nakabayashi, S.; Fujishima, A.; Honda, K. *J. Phys. Chem.* **1985**, *89*, 1902.
- (535) Du, L.; Furube, A.; Yamamoto, K.; Hara, K.; Katoh, R.; Tachiya, M. *J. Phys. Chem. C* **2009**, *113*, 6454.
- (536) Noguez, C. *J. Phys. Chem. C* **2007**, *111*, 3806.
- (537) Zhang, J. Z.; Noguez, C. *Plasmonics* **2008**, *3*, 127.
- (538) Kowalska, E.; Abe, R.; Ohtani, R. *Chem. Commun.* **2009**, 241.
- (539) Hou, W.; Liu, Z.; Pavaskar, P.; Hung, W. H.; Cronin, S. B. *J. Catal.* **2011**, *277*, 149.
- (540) Murakami, N.; Chiyyoda, T.; Tsubota, T.; Ohno, T. *Appl. Catal., A* **2008**, *348*, 148.
- (541) Lahiri, D.; Subramanian, V.; Bunker, B. C.; Kamat, P. V. *J. Chem. Phys.* **2006**, *124*, 204720.
- (542) Naya, S.; Teranishi, M.; Isobe, T.; Tada, H. *Chem. Commun.* **2010**, *46*, 815.

- (543) Di Paola, A.; García-López, E.; Marci, C.; Martín, C.; Palmisano, L.; Rives, V.; Venezia, A. M. *Appl. Catal., B* **2004**, *48*, 223.
- (544) Arakawa, H.; Sayama, K. *Res. Chem. Intermed.* **2000**, *26*, 145.
- (545) Fernández-García, M.; Fuerte, A.; Hernández-Alonso, M. L.; Soria, J.; Martínez-Arias, A. *J. Catal.* **2007**, *245*, 84.
- (546) Graciani, J.; Nambu, A.; Evans, J.; Rodríguez, J. A.; Sanz, J. F. *J. Am. Chem. Soc.* **2008**, *130*, 12056.
- (547) Cao, Y.; He, T.; Chen, Y.; Cao, Y. *J. Phys. Chem. C* **2010**, *114*, 3627.
- (548) Senevirathna, M. K. I.; Pitigada, P. K. D. P. P.; Tennekona, K. *J. Photochem. Photobiol., A* **2005**, *171*, 257.
- (549) Li, G.; Dimitrijevic, N. M.; Rajh, T.; Gray, K. M. *J. Phys. Chem. C* **2008**, *112*, 19040.
- (550) Lalitha, K.; Sadanandam, G.; Kumari, V. D.; Subrahmanyam, M.; Sreedar, B.; Hebalkar, N. Y. *J. Phys. Chem. C* **2010**, *114*, 22181.
- (551) Kuo, C. H.; Huang, M. H. *Nano Today* **2010**, *5*, 106.
- (552) Higashimoto, S.; Ushiroda, Y.; Azuma *Topics Catal.* **2008**, *47*, 148.
- (553) Akurati, K. K.; Vital, A.; Delleman, J. P.; Michallow, K.; Graule, T.; Ferri, D.; Baiker, A. *Appl. Catal., B* **2008**, *112*, 53.
- (554) Li, X. Z.; Li, F. B.; Yang, C. L.; Ge, W. K. *J. Photochem. Photobiol., A* **2001**, *141*, 209.
- (555) Smith, W.; Zhao, Y. *J. Phys. Chem. C* **2008**, *112*, 19635.
- (556) Sajjad, A. K. K.; Shamila, D.; Tian, B.; Chen, F.; Zhang, J. F. *Appl. Catal., B* **2009**, *91*, 397.
- (557) Way, C.; Yin, L.; Zhang, L.; Kang, L.; Wang, X.; Gao, R. *J. Phys. Chem. C* **2009**, *113*, 4008.
- (558) Libera, J. A.; Elen, J. W.; Saiter, N. I.; Rajh, T.; Dimitrijevic, N. D. *Chem. Mater.* **2010**, *22*, 409.
- (559) Tada, H.; Jin, Q.; Niijima, H.; Yamamoto, H.; Fujishima, M.; Okuoka, S.-L.; Hattori, T.; Sumida, Y.; Kobayashi, H. *Angew. Chem., Int. Ed.* **2011**, *50*, 3501.
- (560) Li, G.; Zhang, D.; Yu, J. *C. Phys. Chem. Chem. Phys.* **2009**, *11*, 3775.
- (561) Piris, J.; Ferguson, A. J.; Blackbrun, J. L.; Norman, A. G.; Rumble, G.; Salmatem, D. C.; Kopidakis, N. *J. Phys. Chem. C* **2008**, *112*, 7742.
- (562) Hyun, B. R.; Zhong, Y.-W.; Batnik, A. C.; Sun, L.; Abruna, H. D.; Wise, F. S.; Goodreau, J. D.; Mattheus, J. R.; Leslie, T. M.; Borrel, N. F. *ACS Nano* **2008**, *2*, 2206.
- (563) Fuji, H.; Ohtaki, M.; Eguuchi, K.; Arai, H. *J. Mol. Catal. A* **1998**, *129*, 61.
- (564) Hsu, M. C.; Sun, Y. M.; Hon, H. M. *J. Cryst. Growth* **2005**, *215*, 642.
- (565) Taida, H.; Mitsui, T.; Kiyonaga, T.; Akita, T.; Tanaka, K. *Nat. Mater.* **2006**, *5*, 782.
- (566) Wang, D.; Zhao, H.; Wen, N.; El-Khakare, M. A.; Ma, D. *J. Phys. Chem. Lett.* **2010**, *1*, 1030.
- (567) Chakrapani, V.; Turdy, K.; Kamat, P. V. *J. Am. Chem. Soc.* **2010**, *132*, 1228.
- (568) Doong, R. A.; Chen, C. H.; Maithreepala, R. A.; Chen, S. M. *Water Res.* **2001**, *351*, 12873.
- (569) Bahnemann, D. W.; Hilgendorff, M.; Memming, R. *J. Phys. Chem.* **1997**, *101*, 4265.
- (570) Yu, H.; Irie, H.; Shimodaira, H.; Hosogi, Y.; Kuroda, Y.; Miyauchi, M.; Hashimoto, H. *J. Phys. Chem. C* **2010**, *110*, 16481.
- (571) Salmi, M.; Kachenko, N. T.; Lamminmaki, R.-J.; Karvinen, S.; Vehmanan, V.; Lemmettyinen, H. *J. Photochem. Photobiol., A* **2005**, *175*, 8.
- (572) Xu, A.-W.; Gao, Y. *J. Catal.* **2002**, *207*, 151.
- (573) Xin, B.; Ren, Z.; Wang, P.; Liu, J.; Jing, L.; Fu, H. *Appl. Surf. Sci.* **2007**, *253*, 4390.
- (574) Graetzel, M.; Howe, R. F. *J. Phys. Chem.* **1990**, *94*, 2566.
- (575) Di Paola, A.; Marci, G.; Palmisano, L.; Schiavello, M.; Osaki, K.; Ikeda, S.; Ohtani, B. *J. Phys. Chem. B* **2002**, *106*, 637.
- (576) Zhang, Z.; Wang, C. C.; Zakaria, R.; Ying, J. T. *J. Phys. Chem. B* **1998**, *102*, 10871.
- (577) Wang, C.; Bottcher, C.; Bahnemann, D. W.; Dorhmann *J. Mater. Sci.* **2003**, *13*, 2322.
- (578) Wang, X. H.; et al. *J. Phys. Chem. B* **2006**, *110*, 6801.
- (579) Zu, J.; Chen, F.; Zhan, J.; Chen, H.; Anpo, M. *J. Photochem. Photobiol., A* **2006**, *180*, 196.
- (580) Yalcin, Y.; Kilic, M.; Line, Z. *Appl. Catal., B* **2010**, *99*, 469.
- (581) Araña, J.; Díaz, O. G.; Rodríguez, J. M. D.; Melián, J. H.; Cabo, C. G. I.; Peña, J. P.; Hidalgo, M. C.; Navío, J. A. *J. Mol. Catal. A* **2003**, *197*, 157.
- (582) Liu, S.; Liu, X. P.; Chen, Y. S.; Jian, Y. R. *J. Alloys Compd.* **2010**, *506*, 877.
- (583) Spadavecchia, F.; Cappelletti, G.; Ardizzone, S.; Bianchi, C. L.; Oliva, S.; Scarda, P.; Leoni, M.; Fermi, P. *Appl. Catal., B* **2010**, *96*, 314.
- (584) Zhang, Z.; Wang, X.; Long, J.; Gu, Q.; Ding, Z.; Fu, X. *J. Catal.* **2010**, *276*, 201.
- (585) Tachikawa, T.; Fujitsuka, M.; Majima, T. *J. Phys. Chem. B* **2007**, *111*, 5259.
- (586) Kim, M. J.; Kim, K. D.; Seo, H. O.; Luo, Y.; Dey, N. K.; Kim, Y. D. *Appl. Surf. Sci.* **2011**, *257*, 2489.
- (587) Tachikawa, T.; Tojo, S.; Kawai, K.; Endo, M.; Fujitsuka, M.; Ohno, T.; Nishima, K.; Miyamoto, Z.; Majima, T. *J. Phys. Chem. B* **2004**, *108*, 19299.
- (588) Zhang, L.; Wang, H.; Chen, Z.; Wong, P. K.; Liu, J. *Appl. Catal., B* **2011**, *106*, 1.
- (589) Kato, H.; Asakura, K.; Kudo, A. *J. Am. Chem. Soc.* **2003**, *125*, 3082.
- (590) Kudo, A.; Omori, K.; Kato, H. *J. Am. Chem. Soc.* **1999**, *121*, 11459.
- (591) Wang, D. F.; Zou, Z. G.; Ye, J. H. *Chem. Phys. Lett.* **2005**, *411*, 285.
- (592) Yashima, M.; Ogisu, K.; Domen, K. *Acta Crystallogr., B* **2008**, *B64*, 291.
- (593) Zhang, W.; Xu, R. *Int. J. Hydrogen Energy* **2009**, *34*, 8495.
- (594) Oshikiri, M.; Boero, M.; Ye, J.; Zou, Z.; Kido, G. *J. Chem. Phys.* **2002**, *117*, 7313.
- (595) Sato, J.; Kobayashi, H.; Inoue, Y. *J. Phys. Chem. B* **2003**, *107*, 7970.
- (596) Wang, D.; Zou, Z.; Ye *Res. Chem. Intermed.* **2005**, *31*, 433.
- (597) Inoue, Y. *Energy Environ. Sci.* **2009**, *2*, 364.
- (598) Maeda, K.; Teramura, K.; Takata, T.; Hara, M.; Saito, N.; Toda, K.; Inoue, Y.; Kobayashi, H.; Domen, K. *J. Phys. Chem. B* **2005**, *109*, 20504.
- (599) Maeda, K.; Takata, T.; Hara, M.; Saito, N.; Inoue, Y.; Kobayashi, H.; Domen, K. *J. Am. Chem. Soc.* **2005**, *127*, 8286.
- (600) Jensen, L. L.; Muckerman, J. T.; Newton, M. D. *J. Phys. Chem. C* **2008**, *112*, 3439.
- (601) Wei, W.; Dai, Y.; Yang, K.; Guo, M.; Huang, B. *J. Phys. Chem. C* **2008**, *112*, 15915.
- (602) Huda, M. N.; Yan, Y.; Wei, S. H.; Al-Jassim, M. M. *Phys. Rev. B* **2008**, *78*, 195204.
- (603) Di Valentini, C. *J. Phys. Chem. C* **2010**, *114*, 7054.
- (604) Yoshida, M.; Hirai, T.; Maeda, K.; Saito, N.; Kubota, J.; Kobayashi, H.; Inoue, Y.; Domen, K. *J. Phys. Chem. C* **2010**, *114*, 15510.
- (605) Beaulac, R.; Arhcer, P. I.; van Rijssel, J.; Meijerink, A. M.; Gamelin, D. R. *Nano Lett.* **2008**, *8*, 2949.
- (606) Pan, H.; Gu, B.; Eres, G.; Zhang, Z. *J. Chem. Phys.* **2010**, *132*, 104501.
- (607) Ma, N.; Zhang, Y.; Quan, X.; Fan, X.; Zhao, H. *Water Res.* **2010**, *44*, 6104.
- (608) He, T.; Hu, Z. S.; Li, J. L.; Yang, G. W. *J. Phys. Chem. C* **2011**, *115*, 13837.
- (609) Shiraishi, Y.; Hirai, T. *J. Photochem. Photobiol., C* **2008**, *9*, 157.
- (610) Zhou, W.; Liu, H.; Boughton, R.; Du, G.; Lin, J.; Wang, J.; Liu, D. *J. Mater. Chem.* **2010**, *20*, 5993.
- (611) Primo, A.; Corma, A.; García, H. *Phys. Chem. Chem. Phys.* **2010**, *13*, 886.
- (612) Grandcolas, M.; Ye, J.; Hanagata, N. *Mater. Lett.* **2011**, *65*, 236.
- (613) Mor, G. K.; Varghese, O. K.; Paulose, M.; Shankar, K.; Grimes, C. A. *Sol. Energy Mater. Sol. Cells* **2006**, *90*.
- (614) Mohammed, A. E.; Rohani, S. *Energy Environ. Sci.* **2011**, *4*, 1065.

- (615) Likodimos, V.; Stargiopoulos, T.; Falaras, P.; Kunge, J.; Schmuki, P. *J. Phys. Chem. C* **2008**, *112*, 12687.
- (616) Li, B.; Xih, Z. *J. Am. Chem. Soc.* **2009**, *131*, 1638.
- (617) Wang, X.; Maeda, K.; Thomas, A.; Takanabe, K.; Xin, G.; Carlsoon, J. M.; Domen, K.; Antonietti, M. *Nat. Mater.* **2009**, *8*, 76.
- (618) Su, F.; Matheu, S. C.; Lipier, G.; Fu, X.; Antonietti, M.; Bwchert, S.; Wang, X. *J. Am. Chem. Soc.* **2010**, *132*, 16299.
- (619) Di, Y.; Wang, X.; Thomas, A.; Antonietti, M. *ChemCatChem* **2010**, *2*, 834.
- (620) Liu, G.; Niu, P.; Sun, C.; Smith, S. C.; Chen, Z.; Lu, G. C.; Cheng, H.-M. *J. Am. Chem. Soc.* **2010**, *132*, 11642.
- (621) Chen, X.; Zhang, J.; Fu, X.; Antonietti, M.; Wang, X. *J. Am. Chem. Soc.* **2009**, *131*, 11658.
- (622) Guo, Y.; Chi, S.; Yang, S.; Wang, Y.; Zou, Z. *Chem. Commun.* **2010**, *7325*.
- (623) Yi, Z.; Ye, J.; Kikugawa, N.; Kako, T.; Ouyang, S.; Stuart-Williams, H.; Yang, H.; Cao, J.; Luo, W.; Li, Z.; Liu, Y.; Whitters, R. L. *Nat. Mater.* **2010**, *9*, 559.
- (624) Bi, Y.; Shuin, O.; Cao, J.; Ye, J. *Phys. Chem. Chem. Phys.* **2011**, *13*, 10071.
- (625) Peng, X. *Acc. Chem. Res.* **2010**, *43*, 1387.
- (626) Hu, C.; Peng, T.; Hu, X.; Nie, Y.; Zhou, X.; Qu, J.; Hong, H. *J. Am. Chem. Soc.* **2010**, *132*, 857.
- (627) Wang, P.; Huang, B.; Qin, X.; Da, Y.; Wang, Z. *ChemCatChem* **2011**, *3*, 360.
- (628) Zhang, W.; Zou, L.; Wang, L. *Appl. Catal., A* **2009**, *371*, 9.
- (629) Zhang, W. D.; Xu, B.; Jiang, L.-C. *J. Mater. Chem.* **2010**, *20*, 6383.
- (630) Ahkavan, O.; Azimirad, R.; Safa, S.; Larijani, M. M. *J. Mater. Chem.* **2010**, *20*, 7386.
- (631) Kongkanad, A.; Kamat, P. V. *ACS Nano* **2007**, *1*, 13.
- (632) Wang, W. D.; Serp, P.; Kalack, P.; Faria, J. L. *J. Mol. Catal. A* **2005**, *235*, 199.
- (633) Zhang, H.; Lv, X.; Li, Y.; Wang, Y.; Li, J. *ACS Nano* **2009**, *4*, 380.
- (634) Zhang, X. Y.; Li, H. P.; Cun, X. L.; Lin, Y. *J. Mater. Chem.* **2010**, *20*, 2801.
- (635) Li, N.; Liu, G.; Zhen, C.; Li, F.; Zhang, L.; Cheng, H.-M. *Adv. Funct. Mater.* **2011**, *21*, 1717.
- (636) Park, Y.; Kang, S.-H.; Choi, W. *Phys. Chem. Chem. Phys.* **2011**, *13*, 9425.
- (637) Xiong, Z.; Zhang, L. L.; Ma, J.; Zhan, X. L. *Chem. Commun.* **2010**, *6099*.
- (638) Liu, J.; Bai, H.; Wang, Y.; Liu, Z.; Zhang, X.; Sun, D. D. *Adv. Funct. Mater.* **2010**, *20*, 4175.
- (639) Du, J.; Lai, X.; Zhai, J.; Kisailus, D.; Su, F.; Wang, D.; Jiang, L. *ACS Nano* **2011**, *5*, 590.
- (640) Chen, C.; Cai, W.; Long, M.; Zhou, B.; Wu, Y.; D., W.; Feng, Y. *ACS Nano* **2010**, *4*, 6425.
- (641) Du, A.; Ng, Y. H.; Bell, N. J.; Zhu, Z.; Amal, R.; Smith, S. C. *J. Phys. Chem. Lett.* **2011**, *2*, 894.
- (642) Kamat, P. V. *J. Phys. Chem. Lett.* **2010**, *1*, 520.
- (643) Ng, M. H.; Iwasa, A.; Kudo, A.; Amal, R. *J. Phys. Chem. Lett.* **2010**, *1*, 2607.
- (644) Gao, E.; Wang, W.; Shang, M.; Xu, J. *Phys. Chem. Chem. Phys.* **2011**, *13*, 2887.
- (645) Iwase, A.; Ng, Y.; Ishiguro, Y.; Kudo, A.; Amal, R. *J. Am. Chem. Soc.* **2011**, *134*, 11054.
- (646) Kubacka, A.; Ferrer, M.; Serrano, C.; Cerrada, M. L.; Sánchez-Chaves, M.; Fernández-García, M.; de Andrés, A.; Jiménez-Riobóo, R. J.; Fernández-Martín, F.; Fernández-García, M. *Appl. Catal., B* **2009**, *89*, 441.
- (647) Pasqui, D.; Atrei, A.; Barbucci, R. *Nanotechnology* **2009**, *20*, 015703.
- (648) Liao, C.; Chen, S.; Quan, X.; Chen, H.; Zhang, Y. *Environ. Sci. Technol.* **2010**, *94*, 3481.
- (649) Park, J.; Yi, J.; Tachikawa, T.; Majima, T.; Choi, W. *J. Phys. Chem. Lett.* **2010**, *1*, 1351.
- (650) Mejía, M. I.; Marín, J. M.; Restrepo, G.; Ríos, L. A.; Pulgarín, C.; Kiwi, J. *Appl. Catal., B* **2010**, *94*, 166.
- (651) Tryba, B. *J. Hazard. Mater.* **2008**, *151*, 623.
- (652) Torres, A.; Ruales, C.; Pulgarín, C.; Aimable, A.; Bowen, P.; Sarria, V.; Kiwi, J. *ACS Appl. Mater. Interfaces* **2010**, *2*, 2547.
- (653) Kim, J.; van der Brugger, B. *Environ. Pollut.* **2010**, *158*, 2335.
- (654) Anpo, M.; Zhang, S. G.; Mishima, H.; Matsuoka, M.; Yamashita, H. *Catal. Today* **1997**, *39*, 159.
- (655) Dutta, D. K.; Severance, M. *J. Phys. Chem. Lett.* **2011**, *2*, 467.
- (656) Kitano, M.; Matsuoka, M.; Ueshima, M.; Anpo, M. *Appl. Catal., A* **2007**, *325*, 1.
- (657) Kuwacher, Y.; Yamashita, H. *J. Mater. Chem.* **2011**, *21*, 2407.
- (658) Corma, A.; García, H.; Llabrés i Xamena, F. X. *Chem. Rev.* **2010**, *110*, 4606.
- (659) Silva, C. G.; Corma, A.; García, H. *J. Mater. Chem.* **2010**, *20*, 3141.
- (660) Fuentes-Cabrera, M.; Nicholson, D. M.; Sumpter, B. G.; Widom, M. *J. Chem. Phys.* **2005**, *123*, 124713.
- (661) Gascon, J.; Hernández-Alonso, M. D.; Almeida, A. R.; van Klink, G. P. M.; Kapteijn, F.; Mul, G. *ChemSusChem* **2008**, *1*, 981.
- (662) Yu, Z. T.; Liao, Z. L.; Jiang, Y. S.; Li, G. H.; Li, G. D.; Chen, J. S. *Chem. Commun.* **2004**, *1814*.
- (663) Yu, Z. T.; Liao, Z. L.; Jiang, Y. S.; Li, G. H.; Chen, J. S. *Chem.—Eur. J.* **2005**, *11*, 2642.
- (664) Alvaro, M.; Carbonell, E.; Ferrer, B.; Labrés i Xamena, F. X.; García, H. *Chem.—Eur. J.* **2007**, *13*, 5106.
- (665) Farruseng, D.; Aguado, S.; Pinel, C. *Angew. Chem., Int. Ed.* **2009**, *48*, 7502.
- (666) Wang, K. X.; Chen, J. S. *Acc. Chem. Res.* **2011**, *44*, 531.
- (667) Bordiga, S.; Lamberti, C.; Ricchiardi, G.; Regli, L.; Bonino, F.; Damin, A.; Lillerud, K. P.; Bjorgen, M.; Zecchina, A. *Chem. Commun.* **2004**, *2300*.
- (668) Yaghi, O. M.; Ókeeffe, M.; Ockwig, N. W.; Chae, H. K.; Eddaoudi, M.; Kim, J. *Nature* **2003**, *423*, 705.
- (669) Gutierrez-Martín, F.; Fernández-Martínez, F.; Díaz, P.; Colón, C.; Alonso-Medina, A. J. *Alloys Compd.* **2010**, *501*, 193.
- (670) Auzel, F. *Chem. Rev.* **2004**, *104*, 139.
- (671) Wegh, R. T.; Donker, H.; van Loef, E. V. D.; Oskam, K. D.; Meijerink, A. *J. Lumin.* **2000**, *87–89*, 1017.
- (672) Gharavi, A.; McPherson, G. L. *Appl. Phys. Lett.* **1992**, *61*, 2635.
- (673) Neeraj, S.; Kijima, N.; Cheetham, A. K. *Chem. Phys. Lett.* **2004**, *387*, 2.
- (674) Neeraj, S.; Kijima, N.; Cheetham, A. K. *Solid State Commun.* **2004**, *131*, 65.
- (675) Nuñez, N. O.; Liviano, S. R.; Ocaña, M. *J. Colloid Interface Sci.* **2010**, *349*, 484.
- (676) Le Toquin, R.; Cheetham, A. K. *Chem. Phys. Lett.* **2006**, *423*, 352.
- (677) Nuñez, N. O.; Quintanilla, M.; Cantelar, E.; Cusso, F.; Ocaña, M. *J. Nanopart. Res.* **2010**, *12*, 2553.
- (678) Llabrés i Xamena, F. X.; Corma, A.; García, H. *J. Phys. Chem. C* **2007**, *111*, 80.
- (679) Furman, J. D.; Warner, A. Y.; Teat, S. J.; Mikhailovsky, A. A.; Cheetham, A. K. *Chem. Mater.* **2010**, *22*, 2255.
- (680) Qin, W.; Zhang, D.; Zhao, D.; Wang, I.; Zhen, K. *Chem. Commun.* **2010**, *2304*.
- (681) Zhang, Z.; Wang, W.; Yin, W.; Shang, M.; Wang, L.; Sun, S. *Appl. Catal., B* **2010**, *101*, 68.
- (682) Li, H.; Wang, Y. *Res. Chem. Intermed.* **2010**, *36*, 51.
- (683) Dacyl, D.; Uhlich, D.; Jüstel, T. *Cent. Eur. J. Chem.* **2009**, *7*, 164.
- (684) Ciambelli, P.; Sannino, D.; Palma, V.; Vaiano, V.; Mazzei, R. S. *Photochem. Photobiol. Sci.* **2011**, *10*, 414.
- (685) Parker, C. A. *Photoluminescence of Solutions*; Elsevier: Amsterdam, 1968.
- (686) Tenya, N.; Singh-Rachford, T. N.; Castellano, F. N. *J. Phys. Chem. A* **2009**, *113*, 5912.
- (687) Sánchez-Valencia, J. R.; Toudert, J.; González-García, L.; González-Elipe, A. R.; Barranco, A. *Chem. Commun.* **2010**, *46*, 4372.

- (688) Tada, H.; Matsui, H.; Shiota, F.; Nomura, M.; Seishiro, I.; Masakuni, Y.; Kunio, E. *Chem. Commun.* **2002**, 1678.
- (689) Naya, S.; Inoue, A.; Tada, H. *J. Am. Chem. Soc.* **2010**, 132, 6292.
- (690) Li, C.; Wang, F.; Yu, J. C. *Energy Environ. Sci.* **2011**, 4, 100 and references therein.
- (691) Vennestrom, P. N. R.; Christensen, C. H.; Pedersen, S.; Grunwaldt, J. D.; Woodley, J. M. *ChemCatChem* **2010**, 2, 249.
- (692) Vennestrom, P. N. R.; Taarning, E.; Christensen, C. H.; Pedersen, S.; Grunwaldt, J. D.; Woodley, J. M. *ChemCatChem* **2010**, 2, 943.
- (693) Krassen, H.; Otta, S.; Heberle, J. *Phys. Chem. Chem. Phys.* **2011**, 13, 47.
- (694) Kurayama, F.; Matsuyama, T.; Yamamoto, H. *Adv. Powder Technol.* **2005**, 16, 517.
- (695) Sun, Q.; Jiang, Y.; Jiang, Z.; Zhang, L.; Sun, X.; Li, J. *Ind. Eng. Chem. Res.* **2009**, 48, 4210.
- (696) Woolerton, T. W.; Sheard, S.; Reisner, E.; Pierce, E.; Ragsdale, S. W.; Armstrong, F. A. *J. Am. Chem. Soc.* **2010**, 132, 21132.
- (697) Woolerton, T. W.; Sheard, S.; Pierce, E.; Ragsdale, S. W.; Armstrong, F. A. *Energy Environ. Sci.* **2011**, 4, 2393.
- (698) Tao, J.; Luttrell, T.; Batzill, M. *Nat. Chem.* **2011**, 3, 296.
- (699) Dietbold, U. *Nat. Chem.* **2011**, 3, 271.
- (700) Tatsuma, T.; Tachibana, S.-I.; Miwa, T.; Tryk, D. A.; Fujushima, A. *J. Phys. Chem. B* **1999**, 103, 8033.
- (701) Tatsuma, T.; Tachibana, S.-I.; Fujushima, A. *J. Phys. Chem. B* **2001**, 105, 6987.
- (702) Naito, K.; Tachikawa, T.; Cui, S. C.; Sugimoto, A.; Fujitsuka, M.; Majima, T. *J. Am. Chem. Soc.* **2006**, 128, 16430.
- (703) Kawahara, K.; Ohko, T. T.; Fujushima, A. *Phys. Chem. Chem. Phys.* **2003**, 5, 4764.
- (704) Haick, H.; Paz, Y. *Chem. Phys. Chem.* **2003**, 4, 617.
- (705) Kubacka, A.; Ferrer, M.; Fernández-García, M.; Serrano, C.; Cerrada, M. L.; Fernández-García, M. *Appl. Catal., B* **2011**, 104, 346.
- (706) Li, Q.; Li, Y. W.; Wu, P.; Xie, R.; Shang, J. K. *Adv. Mater.* **2008**, 20, 3017.
- (707) Li, Q.; Li, Y. W.; Liu, Z.; Xie, R.; Shang, J. K. *J. Mater. Chem.* **2010**, 20, 1068.
- (708) Yang, F.; Takahashi, Y.; Sakai, N.; Tatsuma, T. *J. Mater. Chem.* **2011**, 21, 2283.
- (709) Augliaro, V.; Litter, M.; Palmisano, L.; Soria, J. *J. Photochem. Photobiol., C* **2006**, 7, 127.
- (710) Martínez-Huitel, C.; Brillas, E. *Appl. Catal., B* **2009**, 87, 105.
- (711) Serpone, N.; Horikoshi, S.; Emeline, A. V. *J. Photochem. Photobiol., C* **2011**, 11, 114.
- (712) Majima, T.; Tachikawa, T. *Chem. Soc. Rev.* **2010**, 39, 4802.